Prediction of NMR J-coupling in condensed matter

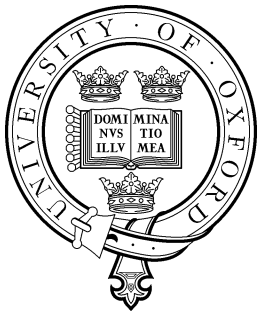

Timothy Green

Lincoln College

University of Oxford

A thesis submitted for the degree of

Doctor of Philosophy

Trinity 2014

Prediction of NMR J-coupling in condensed matter

Timothy Green

Lincoln College

University of Oxford

A thesis submitted for the degree of

Doctor of Philosophy

Trinity 2014

Nuclear magnetic resonance (NMR) is a popular spectroscopic method and has widespread use in many fields. Recent developments in solid-state NMR have increased interest in experiment and, alongside simultaneous developments in computational theory, have led to the field dubbed 'NMR crystallography.' This is a suite of methodologies, complementing the capabilities of other crystallographic methods in the determination of atomic structure, especially when large crystals cannot be made and when exploring materials with phenomena such as compositional, positonal and dynamic disorder. NMR J-coupling is the indirect coupling between nuclear spins, which, when measured, can reveal a wealth of information about structure and bonding.

This thesis develops and applies the method of Joyce for the prediction of NMR J-coupling in condensed matter systems using plane-wave pseudopotential density-functional theory, an important requirement for efficient treatment of finite and infinite periodic systems. It describes the first-ever method for the use of ultrasoft pseudopotentials and inclusion of special relativistic effects in J-coupling prediction, allowing for the treatment of a wider range of materials systems and overall greater user friendliness, thus making the method more accessible and attractive to the wider scientific community.

Acknowledgements

Above all, I would like to thank my supervisor Jonathan for giving me the opportunity to come to Oxford and for supporting and guiding me for the last four years.

I thank my scientific collaborators Pierre Florian, John Hanna, Scott King, Charlotte Martineau, and Vaida Arcisauskaite for assisting the work that led to this thesis. I also thank Bi-Ching and Dan for being brave and offering to give it a read through.

I'd like to thank my officemates Harry, Chris, Keian, Henry, Miguel, Hannes and Marina for entertainment over the years, including Only Connect, rows about cluster queues, and forays of dubious success into gimmicky cryptocurrencies and algorithmic gambling. It could still work, Henry. I'd also like to thank my friends in the wider MML for the strong academic environment, lunchtimes, cake and nights out.

I give my appreciation to my excellent housemates, in order of number of years suffered: Callum (4), Harry (again, 3), Kate (2), and Bex (1), for the pubbing, dinners, holidays, boats and generally being present in my life. I'd also like to thank my other friends in Oxford who made it what it was, including Kieran, Kirstin, Casmir, Ruth and George, along with the Lincoln College MCR.

Finally I would like to thank Mum, Dad and my sister Rosie for supporting everything that I have done that has brought me to this point.

Publications

This thesis is based, in part, on the following publications.

1. Pierre Florian, Emmanuel Veron, Timothy F. G. Green, Jonathan R. Yates, and Dominique Massiot. Elucidation of the Al/Si Ordering in Gehlenite $Ca_2Al_2SiO_7$ by Combined ^{29}Si and ^{27}Al NMR Spectroscopy/Quantum Chemical Calculations. *Chem. Mater.*, 2012, 24 (21), 4068–4079

2. Timothy F. G. Green and Jonathan R. Yates. Relativistic nuclear magnetic resonance J-coupling with ultrasoft pseudopotentials and the zeroth-order regular approximation. *J. Chem. Phys.*, 2014, 140, 234106

Contents

Chapter 1

Introduction

Nuclear magnetic resonance (NMR) is a popular spectroscopic method and has widespread use in many fields. Modern high resolution solid-state NMR experiments[1,2] are a valuable tool for materials characterisation due to their sensitivity to the local atomic environment. Importantly, solid-state NMR can provide information on materials with compositional, positional or dynamic disorder.[3] However, there is no straight-forward analytic technique to obtain atomic-level structure directly from an NMR spectrum; a 'Bragg's law' for NMR. Instead, one must pursue computational-theoretical prediction of the NMR parameters that influence a spectrum in order to fully take advantage of the information present to interpret and assign spectra. First principles predictions of NMR parameters can also assist in the design of NMR experiments, such as determining observability and orientation of tensors. Overall, first-principles calculations offer the ability to fully exploit the information in experimental NMR data.

The sensitivity of NMR experiments to molecular geometry and electronic structure is a 'double-edged sword,' being both an important chemical probe and a challenge

to the computational theorist. For small, finite, systems, NMR parameters such as magnetic shielding, electric field gradients and J-coupling can be routinely calculated with quantum chemical methods based on local orbitals and have demonstrated value in assigning solution-state spectra.[4] Treatment of solid-state NMR systems with these methods requires the creation of finite-clusters, which need careful convergence with respect to the size of the cluster to ensure that the appropriate electronic environment is reconstructed. They also require careful selection of the basis set used to represent the wave function to ensure numerical convergence. A plane wave approach with pseudopotentials is appealing for its algorithmic efficiency, automatic inclusion of periodic boundary conditions and easy systematic convergence of basis sets via the maximum kinetic energy of the plane waves used. However, since such calculations require the use of pseudopotentials, the calculated pseudo-wave function is non-physical near the nucleus, the very region that is so influential to NMR parameters. The development of the gauge-including projector augmented-wave (GIPAW) method[5] has enabled calculations of magnetic shielding in extended systems using pseudopotentials by reconstructing the form of the all-electron wave function near the nucleus. Extensive reviews are available in Refs. 6 and 7.

This thesis concerns itself with the theoretical prediction of NMR J-coupling, or indirect spin-spin coupling, particularly in solid-state systems with heavy ions. J-coupling is the indirect magnetic coupling between two nuclei mediated via the bonding electrons. It manifests in NMR spectra as fine structure splitting of resonant peaks, providing information on bonds such as strength, angles and the connectivity network. J-coupling has been well-studied in the gas and solution state for many decades, as the multiplet splitting in peaks is well resolved due to molecular tumbling decoupling anisotropic interactions. In contrast, solid-state J-coupling studies are more challenging due to broader line widths obscuring fine structure, even when

broadening anisotropic interactions are mostly decoupled with techniques such as magic-angle spinning (MAS). While solid-state NMR experiments have measured J-coupling historically,[8–10] recent advances, such as higher MAS spinning rates (up to 90 kHz) and ultra-high magnetic field strengths (up to 23.3 T), have resulted in increased experimental and theoretical interest[11] in measurements of J.

Joyce *et al.*[12,13] developed a method to calculate J-coupling constants from first principles in extended systems within a plane-wave pseudopotential density functional theory (DFT) framework, using the projector augmented-wave (PAW) method to reconstruct the all-electron properties of the system. This method has been validated for a small number of systems containing light atoms against quantum chemical calculations and against experimental data.[14–18] There is great interest in making this a 'full periodic table' method, i.e. being able to reliably treat systems containing any elements, and so make it a general purpose tool within NMR crystallography.

This thesis is organised as follows. Chapters 2 and 3 outline the background and theory of NMR and plane-wave pseudopotential DFT.

Chapter 4 develops some important improvements to the non-relativistic method of Joyce *et al.*,[13] removing some of the numerical difficulties present in that approach, and generalising the method to use state-of-the-art ultrasoft pseudopotentials.[19] Careful benchmarks of the new ultrasoft plane-wave pseudopotential implementation are provided against both experiment and existing quantum chemical calculations.

Chapter 5 describes and develops the method to allow treatment of systems containing heavy nuclei. It is known[20,21] that J-coupling in systems containing heavy ions is extremely sensitive to the effects of special relativity. This is because both core states and valence states near the nucleus attain high kinetic energy and so should be treated using the Dirac equation, leading to contraction in the wave function and corrections to the operators representing electromagnetic (EM) interactions. Scalar

relativistic effects (i.e. ignoring spin-orbit terms) in particular have been found to be the dominant correction in full four-component Dirac equation calculations,[21] at least for one-bond couplings. It is hence crucial to incorporate relativistic corrections if one wants to approach the reliable treatment of the full periodic table.

Here, the chosen approach develops that of Autschbach and Ziegler,[22,23] which uses the zeroth-order regular approximation (ZORA), an approximation to the Dirac equation, and DFT for the prediction of J-coupling in an all-electron, local orbital framework. Combining this with the insights of Yates et al.[24] into the use of ZORA with pseudopotentials and PAW for the calculation of NMR chemical shifts in systems containing heavy ions, a highly efficient method for predicting J-coupling within extended systems containing heavy ions is created, at negligible extra computational cost as compared to the non-relativistic method.

Chapter 6 is a study of an aluminosilicate glass, gehlenite, demonstrating how disorder in condensed matter systems can be investigated by a combination of solid-state NMR experiments and first-principles calculations, finding correlations between measured experimental NMR parameters and detailed local structural information.

Chapter 7 is a study into a family of silver-containing molecular crystals, looking at ^{31}P-^{107,109}Ag J-couplings and the relevance of relativity in correctly predicting experimental measurements in such systems. In addition, in collaboration with Vaida Arcisauskaite, of the Department of Chemistry at the University of Oxford, further local-orbital calculations are performed to determine the remaining sources of error with respect to experiment and indicate the most important directions for future development.

Chapter 8 is a study into the lead fluoride glass Pb_2ZnF_6, beginning with a basic comparison of experimental and calculated J-couplings on structures of Pb_2ZnF_6

reported in the literature and ending with, for the first time, a detailed investigation combining both ab-initio molecular dynamics and relativistic ultrasoft J-coupling.

Appendix A gives the motivation for and definition of a standardised computer file format for reporting the output of ab-initio magnetic resonance calculations.

Appendix B describes a library for the Python programming for processing the output of ab-initio magnetic resonance calculations.

Together, these new methods developed and applications made demonstrate the high utility of ab-initio NMR J-coupling prediction within the field of NMR crystallography and point towards possible future developments.

Chapter 2

Nuclear magnetic resonance

2.1 NMR theory

Nuclear magnetic resonance (NMR) is the physical phenomena of the resonance of atomic nuclei with radio-frequency electromagnetic waves when subject to an external magnetic field. Consider an atomic nucleus: atomic nuclei possess the property of quantum spin, which in some respects is analogous to classical angular momentum. Like a classical dipole, a nuclear spin precesses at its Larmor frequency when in a magnetic field:

$$\omega = \gamma|\mathbf{B}|, \tag{2.1}$$

where γ is the gyromagnetic ratio of the nucleus and $\mathbf{B}$ is the magnetic field experienced by the nucleus. This is alternatively expressed as the splitting of energy levels

when in a static magnetic field, the Zeeman effect:

$$\hat{H}_Z = -\gamma\hbar\hat{S}\cdot\mathbf{B} \tag{2.2}$$

where $\hat{S}$ is the nuclear spin operator. Magnetic dipole transitions then allow photons to be absorbed and emitted between the energy levels. In the case of a $I = \frac{1}{2}$ spin, e.g. for ^{1}H, the spin eigenstates are parallel and anti-parallel to a magnetic field; one is higher and the other is lower in energy, depending on the sign of the gyromagnetic ratio. The energy difference between the Zeeman energy levels in a typical magnetic field (order of 1 T in strength) is of the order of radio-frequency photons.

This proportionality to the magnetic field means that whenever there is an environmental change that changes the magnetic field experienced by a nucleus, there is a corresponding shift in its precession frequency. This also means that, unlike many other crystallographic techniques, NMR investigates a localised phenomena.

NMR was first observed by groups at Harvard University and Stanford University,[25,26] and soon after it was found that the resonant frequencies of nuclei depended on their chemical environment,[27,28] such as the observation that ethanol contains three chemically distinct protons,[29] in agreement with its predicted structure. Further experiments confirmed the structural predictions of many other simple molecules. NMR was thus established as a key technique in chemistry, biochemistry and related subjects, allowing detailed investigations of various systems.

In an NMR experiment the goal is to measure the response of an ensemble of nuclear spin systems to an external perturbation and so learn about the environment of the nuclei in the system. This is done by placing the system in a static magnetic field and then exposing it to some pulse of radio waves, of varying complexity, driving transitions between different states, and then recording the radio waves emitted by

the precession and decay of the response.

The relative ensemble population difference in the excited state of a $I = \frac{1}{2}$ nuclear magnetic moment is thermodynamically described by the Boltzmann factor:

$$\frac{N_\uparrow}{N_\downarrow} = \exp(-\beta \Delta E), \tag{2.3}$$

where ΔE is the energy difference between the two energy levels, and $\beta = \frac{1}{k_\mathrm{B} T}$, with k_B the Boltzmann constant and T the temperature.

For a fixed temperature, the stronger the external static magnetic field, the greater the energy difference between the Zeeman states and so the greater the population difference between the states. This means more spins can be detected undergoing the transition and it is easier to measure resonance.

Historically, the first experiments would sweep the frequency of electromagnetic radiation, or more conveniently and equivalently the external magnetic field strength in *continuous-wave spectroscopy*, over a range and determine when the nuclei were in resonance. When at resonance, nuclear spins are excited from the lower Zeeman energy levels to the higher energy levels and relax back while emitting radio-frequency photons. Modern experiments use the more efficient *Fourier-transform spectroscopy* by emitting a short pulse of broad spectrum radio waves and then measuring the decay signal of the nuclei as they decohere and relax to thermal equilibrium. To use a common analogy, this is like hitting a bell with a hammer and listening to its sound as the ringing decays.

The relevant parameters that determine the spectrum that an NMR experiment will observe are those that describe the nuclear spin system ensemble and relate to how the spin of a nucleus interacts with the surrounding magnetic field and electronic

structure. The main interactions involved are *magnetic shielding*, quadrupolar coupling to the *electric field gradient*, *dipolar coupling*, and *indirect spin-spin coupling* — also known as *J-coupling*.

2.1.1 Magnetic shielding

The clearest and earliest of these interactions to be observed in experiments is the *chemical shift*, which is due to nuclei in different chemical environments experiencing different induced magnetic fields and thus having different resonant frequencies. In diamagnetic materials the induced magnetic field is caused by shielding of the nucleus by currents induced in the surrounding electron cloud. The magnetic shielding has the form of a dimensionless rank-2 tensor:

$$\mathbf{B}_{\mathbf{R}}^{\text{in}} = -\sigma_{\mathbf{R}} \cdot \mathbf{B}_{\text{ext}}. \tag{2.4}$$

and can be expressed as the second derivative of the system energy with respect to the nuclear magnetic moment and external field:

$$\sigma_{\mathbf{R}} = \frac{\partial^2 E}{\partial \mathbf{B}_{\text{ext}} \partial \boldsymbol{\mu}_{\mathbf{R}}}. \tag{2.5}$$

The chemical shift, δ, is defined by referencing the magnetic shielding to the magnetic shielding experienced by another reference nucleus, as this is typically how it is measured in experiment:

$$\delta = 10^6 \frac{\sigma_{\text{ref}} - \sigma_{\text{iso}}}{1 - \sigma_{\text{ref}}}. \tag{2.6}$$

Typical reference nuclei would be the ^{1}H, ^{13}C and ^{29}Si resonances in tetramethyl-

silane (TMS, $Si(CH_3)_4$). In calculations, the magnetic shielding values are not usually referenced against a similar calculation on the reference molecule as solvent and temperature effects can confound such comparisons. Instead, shielding values are compared to experimental shifts by internal referencing, i.e. taking differences between peaks, or by linear regression of one against the other.

2.1.2 Electric field gradient

This is not a magnetic interaction but still manifests in NMR spectra due to the spins of nuclei with a quadrupole moment ($I > \frac{1}{2}$) interacting with the gradient of the electric field in the system. In solid-state systems it often has the effect of broadening and distorting spectra, making them difficult to interpret, while in a liquid the interaction is, to first order, averaged to zero but contributes to line broadening relaxation processes. The electric field gradient tensor, G_{ij}, is defined as

$$G_{ij} = \frac{\partial^2 V}{\partial x_i \partial x_j}, \tag{2.7}$$

where V is the electric potential as a function of position. G is, by construction, traceless as, assuming that all charge generating the electric potential is external to the nucleus, $\nabla^2 V = 0$ due to Gauss' law.

We can diagonalise G, where S is a unitary matrix of eigenvectors and Λ is a diagonal matrix of eigenvalues:

$$G = S^\dagger \Lambda S. \tag{2.8}$$

Experimentally what is usually measured is the quadrupole coupling frequency, C_Q,

defined as

$$C_Q = \frac{eQ\Lambda_{11}}{h}, \tag{2.9}$$

where e is the electron charge, Q is the quadrupole moment of the nucleus in question and h is the Planck constant. C_Q is typically in the range of MHz.

In addition, one can define the asymmetry, η_Q, as

$$\eta_Q = \frac{\Lambda_{22} - \Lambda_{33}}{\Lambda_{11}}, \tag{2.10}$$

where the eigenvalues have been ordered as:

$$|\Lambda_{11}| \geq |\Lambda_{22}| \geq |\Lambda_{33}|. \tag{2.11}$$

2.1.3 Dipolar coupling

A straight forward and easy to calculate effect is the *dipolar coupling*. The dipolar coupling is the interaction between the magnetic field generated by one nucleus' magnetic moment and another nucleus' magnetic moment. It has the form of a traceless rank-2 tensor, which means it is usually averaged out by molecular tumbling in liquids and as such is difficult to observe. However, it does contribute to spin relaxation processes. In solid-state systems it is not averaged out and causes significant difficulties in obtaining clear spectra.

The dipolar coupling adds the following term to the spin Hamiltonian for every pair

of nuclei:

$$\hat{H}_{\mathrm{A,B}} = \mathbf{I}_{\mathrm{A}} \cdot D_{\mathrm{A,B}} \cdot \mathbf{I}_{\mathrm{B}}, \tag{2.12}$$

where the dipolar coupling tensor D is

$$D_{\mathrm{A,B}} = \frac{\gamma_{\mathrm{A}}\gamma_{\mathrm{B}}\hbar^2}{|\mathbf{r}|^3}(1 - 3\mathbf{r} \otimes \mathbf{r}), \tag{2.13}$$

in which γ_{A} is the gyromagnetic ratio of nucleus A and the internuclear separation vector is $\mathbf{r}$.

2.1.4 J-coupling

The indirect spin-spin coupling, also known as J-coupling, is due to the magnetic field generated by one magnetic moment interacting with its surrounding electron cloud, which goes on to generate a magnetic field at another nucleus. It was first observed as splitting of spectral resonance peaks in liquid NMR experiments,[31] one not dependent on the external magnetic field strength and so not a chemical shift effect. This was unexpected, as the dipolar interaction between nuclear spins is traceless and in a liquid should average to zero over all orientations of a tumbling molecule. These observations thus indicated that there was a new interaction, with a non-zero trace, between nuclear spins. Ramsey[32,33] developed the theory of second-order indirect coupling between nuclear spins via electrons to account for this.

From the experimental behaviour, it can be determined that terms in the spin Hamiltonian that give rise to inter-nuclear coupling are products of two nuclear

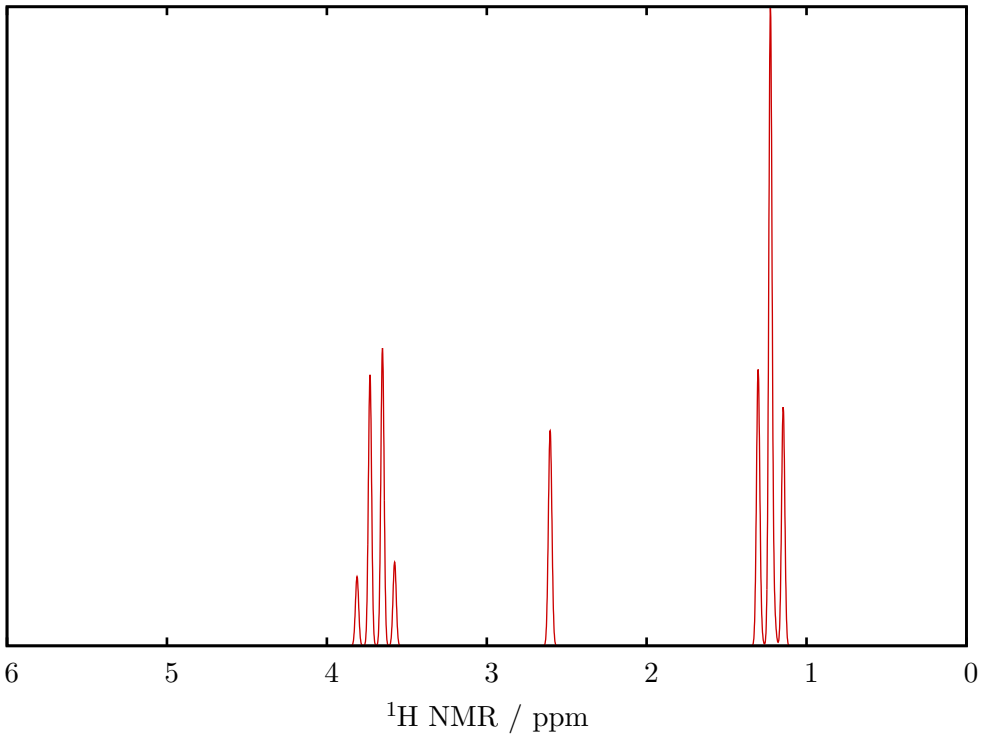

Figure 2.1: Simulated ^{1}H NMR spectrum of ethanol (C_2H_6O), showing splitting of the three inequivalent proton environments by J-coupling to neighbouring protons, based on experimental peak data.[30] The vertical scale is intensity in arbitrary units. The peaks can be thus assigned, left to right, as CH_2, OH and CH_3.

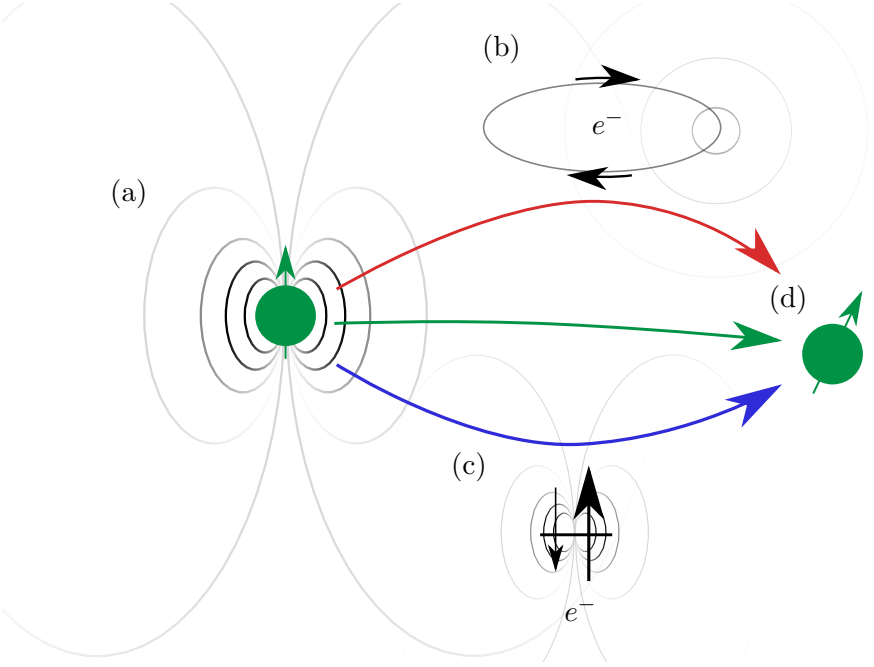

Figure 2.2: Illustration of the mechanisms behind NMR indirect spin-spin coupling, J-coupling. The perturbing nucleus' magnetic moment (a) has a magnetic field, which induces currents (b) in the surrounding electron cloud by paramagnetic and diamagnetic mechanisms, as well as interacting with the electrons' spins via the Fermi-contact and spin-dipole mechanisms to create a spin polarisation (c). Finally, both the induced current and spin polarisation generate a magnetic field at the receiving nucleus (d). In addition, the magnetic fields of the nuclei directly interact to give the dipolar coupling.

spins:

$$\hat{H}_{\mathrm{A},B} = \mathbf{I}_{\mathrm{A}} \cdot (D_{\mathrm{A,B}} + J_{\mathrm{A,B}}) \cdot \mathbf{I}_{\mathrm{B}}, \tag{2.14}$$

where J is the J-coupling tensor and D is the dipolar coupling tensor. Experimentally, these two couplings can be difficult to disentangle, although D is traceless, but theoretically these are defined and calculated entirely separately.

It is usually the isotropic J-coupling that is measured, $J_{\mathrm{iso}} = \mathrm{Tr}[J]/3$, manifesting in simple 1D NMR experiments as the splitting of peaks between inequivalent nuclei. A simulated ^{1}H NMR spectrum of ethanol (C_2H_6O) is shown in Fig. 2.1, based on experimental peak data. Splitting of the resonances corresponding to the three inequivalent proton environments can be observed and ascribed to J-coupling to neighbouring protons — hence the OH resonance has no splitting, the CH_3 resonance is split in three in a 1:2:1 ratio by the two neighbouring CH_2 protons and the CH_2 resonance is split in four in a 1:3:3:1 ratio by the three neighbouring CH_3 protons.

For theoretical purposes, J-coupling is most usefully expressed as a 'reduced' rank-2 tensor, K,

$$K_{\mathrm{A,B}} = \frac{\partial^2 E}{\partial \boldsymbol{\mu}_{\mathrm{A}} \partial \boldsymbol{\mu}_{\mathrm{B}}}, \tag{2.15}$$

where $\boldsymbol{\mu}_{\mathrm{A}}$ is the magnetic moment of nucleus A. The K tensor is only dependent on the electronic structure, not on the type of nucleus. It is worth noting that the symmetric part of the interaction tensor is symmetric under interchange of nuclear indices; this is a good test of numerical codes, because numerical imprecision and certain types of model error can break this symmetry. The J tensor is then related

to K by

$$K_{\mathrm{A,B}} = \frac{2\pi}{\hbar\gamma_{\mathrm{A}}\gamma_{\mathrm{B}}} J_{\mathrm{A,B}}, \tag{2.16}$$

where γ_{A} is the nuclear gyromagnetic moment of nucleus A.

The four Ramsey mechanisms[32,33] involved are illustrated in Fig. 2.2 and outlined more comprehensively in Chapter 4. A current density, $\mathbf{j}^{(1)}(\mathbf{r})$, is created by a sum of the diamagnetic and paramagnetic interactions. The induced current density produces a magnetic field, calculated using the Biot–Savart law. A spin density, $\mathbf{m}^{(1)}(\mathbf{r})$, is created by the Fermi-contact and spin-dipole mechanisms at the perturbing nucleus; the Fermi-contact term is proportional to the electron density at the nucleus and is generally the dominant contribution. The induced spin polarisation produces a magnetic field by symmetric mechanisms at the receiving nucleus. The total K tensor is then

$$K_{ij} = K_{ij}^{\mathrm{spin}} + K_{ij}^{\mathrm{orb}} \tag{2.17}$$

$$K_{ij}^{\mathrm{spin}} = \alpha^2 \int \mathrm{d}\mathbf{r} \left[\left(\frac{3\mathbf{r}_{A;i}\mathbf{r}_{A;j} - |\mathbf{r}_A|^2\delta_{ij}}{|\mathbf{r}_A|^5} \right) + \frac{8\pi}{3}\delta(\mathbf{r}) \right] \mathbf{m}_j(\mathbf{r}) \tag{2.18}$$

$$K_{ij}^{\mathrm{orb}} = \alpha^2 \int \mathrm{d}\mathbf{r} \left(\mathbf{j}_j^{(1)}(\mathbf{r}) \times \frac{\mathbf{r}_A}{|\mathbf{r}_A|^3} \right)_i . \tag{2.19}$$

2.2 Solid-state NMR

Solid-state NMR is the collection of experimental techniques relating to the application of NMR to solid substances, as opposed to liquid or gas. There are problems experienced in solid-state NMR that are not usually experienced in NMR experi-

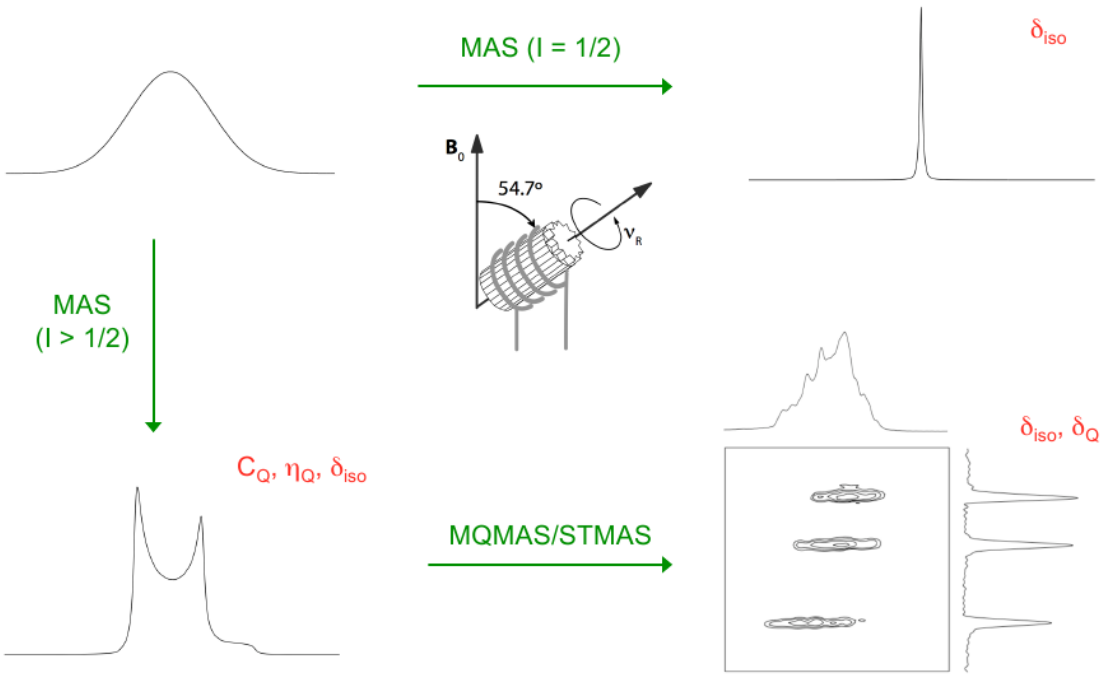

Figure 2.3: Illustration of magic angle spinning (MAS) revealing obscured detail in the solid-state spectrum. [Credit Dr Sharon Ashbrook, University of St. Andrews.]

ments on liquids or gases. As mentioned, traceless interactions are averaged out by the molecular tumbling in liquids, leaving a clean spectrum of peaks and line splittings caused by the isotropic components of the interaction tensors. In solids, there is no such tumbling and so anisotropic interactions remain. Firstly, each nucleus will experience the direct dipolar interaction at many different orientations, leading to a broad and featureless spectrum. Also experienced is the *chemical shift anisotropy* (CSA); that there is an anisotropic component to the magnetic shielding means it varies according to the molecule's orientation relative to the magnetic field, normally averaged out by molecular tumbling in liquids. Finally, the quadrupolar coupling of nuclei to the electric field gradient is no longer suppressed and causes broadening of spectral peaks.

The main approach to solving these problems in solid-state NMR is *magic angle spinning* (MAS).[34] In magic angle spinning, the sample is spun at a high frequency — higher than the frequency of the anisotropic interactions involved — with the rotation axis at a particular angle relative to the magnetic field, θ. This angle is chosen so that a second-rank anisotropic interaction, for example the direct dipolar coupling between two nuclei, varies between negative and positive maxima when spun and averages to zero, revealing obscured detail (Fig. 2.3). The rotational average of an anisotropic interaction when spun at an angle θ is proportional to $3\cos^2\theta - 1$; setting this to zero and solving finds that $\theta = 54.7°$, the 'magic angle'.

Magic angle spinning, however, creates spinning 'side bands' in the spectrum as the spinning speed (kHz) is not much greater than the interaction frequencies (Hz–kHz). The higher the spinning speed, the further away these side bands are in the spectrum and the lower their intensity. In the limit of full secular decoupling they disappear.

Modern NMR experiments use 'pulse sequences' to describe the electromagnetic radiation that the sample is exposed to. These can be of varying complexity and cover a whole range of different purposes. A few of the more common ones, mentioned in later chapters, will now be briefly explained.

The most basic pulse sequence is a single pulse of radiation, corresponding to a rotation of the sample's magnetisation to perpendicular to the external magnetic field (a '90° pulse'), followed by allowing it to precess freely and generate an electromagnetic radio-frequency signal that can be detected.

Double-quantum filtered (DQF) experiments use pulse sequences that excite pairs of coupled nuclei and, in effect, only show resonances from directly bonded nuclei. This can be used, for example, when one wants to suppress singlet signals from molecules with only a single NMR-active isotope of the element in question in order to improve resolution of doublet peaks and higher.

Experiments using the INADEQUATE pulse sequence perform DQF in J-coupled homonuclear systems (i.e. two alike nuclei), using the J-coupling network to couple pairs of nuclei. INEPT pulse sequence experiments are used to transfer magnetisation from a highly NMR sensitive nucleus, i.e. large γ, to a less sensitive nucleus in order to enhance spectra and edit heteronuclear multiplets.

Cross-polarisation (CP, CP-MAS in solid-state NMR) is a method commonly used in solid-state NMR that is similar to INEPT, in that it first creates magnetisation of the ^{1}H nuclei and transfers it to some other nucleus which is then observed.

The J-coupling between nuclei allows decoherence of spins to occur, contributing to the T_2 spin-spin relaxation time. This can be measured with a *Hahn-echo*, or spin-echo, experiment. This applies a pulse to a sample, allows the magnetisation to precess under the chemical shift in time and then applies a second pulse to 'mirror' the magnetisation, which then precesses back to its original state and is 'refocused'. However, if there is an isotropic J-coupling present, it is not necessarily fully refocused and this can be used to measure the coupling strength. The first detection of J-coupling was between two protons in dichloroacetaldehyde by Hahn and Maxwell[31] using a spin echo experiment.

2.3 Recent solid-state J-coupling developments

Solid-state NMR measurements of J-coupling are more challenging due to broader line widths obscuring fine structure, even when broadening anisotropic interactions are mostly decoupled with techniques such as MAS. Measurements of J-coupling in specific solid-state systems have existed for a number of years, such as the observation of ^{1}J(N−C) and ^{2}J(Cd−C) indirect spin-spin couplings by Eichele and Wasylishen[8] in cadmium thiocyanates with ^{13}C CP-MAS spectroscopy, and the ob-

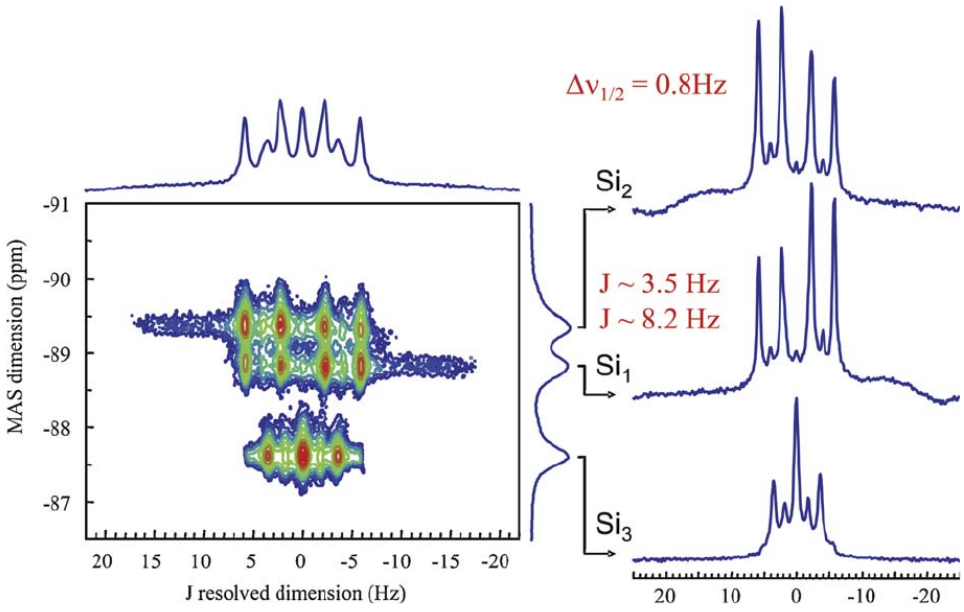

Figure 2.4: Example spectra of crystalline wollastonite, showing J-couplings of a few hertz using a 2D J-resolved experiment. [Credit Ref. 11.]

servation of ^{2}J(P−P) by Wu and Wasylishen[9] in $Hg(PPh_3)_2(NO_3)_2$ with ^{31}P MAS. However, these observations were reliant on spectra described only by high perturbation order behaviour specific to the studied systems.

More recently, better solid-state NMR methods, such as ultrahigh magnetic fields, up to 23.3 T, high MAS spinning speeds, up to 90 kHz, accurate magic angle setting ($\pm 0.01^\circ$)[35] and improved experimental protocols have improved the ability to measure J-couplings in organic and inorganic structures, making it a popular tool in materials science for investigating ordered and disordered materials at the sub-nanometer length scales. In particular, new developments have enhanced the detection and measurement of small J-couplings in solid-state NMR experiments,[1,11] even when quadrupolar nuclei are present.[2] Two-dimensional NMR methods, where two resonance axes are probed, also make significant used of J-coupling to correlate connected nuclei, manifesting as off-diagonal peaks in the 2D spectrum.[1]

For example, Figure 2.4 shows J-couplings in an inorganic material, $CaSiO_3$ calcium silicate polymorphs, being measured down to a few hertz.[36] This was a 2D J-resolved experiment, which correlates a 1D spectrum to individual coupling multiplets from a J-resolved Hahn-echo experiment. J-couplings can be used to establish atomic level descriptions of structures of various organic and inorganic materials, for both homonuclear and heteronuclear couplings.

For homonuclear couplings there are examples of small one bond couplings, ^{1}J, for ^{13}C$-^{13}$C[37–39] and ^{31}P$-^{31}$P.[40,41] There are also examples of homonuclear two bond couplings, ^{2}J, for ^{31}P$-$O$-^{31}$P,[42–49] ^{31}P$-$N$-^{31}$P[50] and ^{29}Si$-$O$-^{29}$Si[51,52] in ordered and disordered materials. For heteronuclear couplings there are examples of one-bond couplings for ^{19}F$-^{207}$Pb,[53] ^{31}P$-^{113}$Cd and ^{31}P$-^{77}$Se[54,55] and two-bond couplings ^{29}Si$-$O$-^{31}$P.[56,57]

Also of interest for solid-state NMR is interactions involving quadrupolar nuclei. Usually in solution, fluctuating quadrupolar interactions cause signification relaxation broadening of spectral peaks and so prevent observation of J-coupling. In solid-state NMR quadrupolar interactions do not fluctuate and so do not induce relaxation, allowing observation of small J-couplings between quadrupolar nuclei and others. Examples of spin-$\frac{1}{2}$ nuclei coupling to quadrupolar nuclei include ^{13}C and ^{35,37}Cl[58] and ^{63,65}Cu.[40,41,59–61]

Solid-state NMR has significant applications in the investigation of disordered materials, i.e. going 'beyond periodicity'[3,62] and including information that is difficult to acquire using other crystallographic techniques. Many materials, such as oxide glasses,[18,63,64] rather than being totally disordered are in fact made up of a distribution of locally ordered structures. As NMR is a short-range effect, it can identify these locally ordered structures. In particular, in order to characterise them, it can measure J-couplings within distinct disordered sites. Studies of amorphous

materials[11] show spectra containing superpositions of different disordered sites and clearly measurable J-coupling trends, with implications for understanding of their local structure.[65]

Chapter 3

First-principles methodologies

First-principles methodologies hope to model and predict the behaviour of real systems with nothing other than the known laws of physics, without fitting to experimental data. For properties that are strongly dependent on quantum mechanical behaviour, such as NMR, this means using quantum theory.

A starting point for many quantum calculations is knowledge of the ground state of a system, i.e. the quantum state with the lowest energy. In order to correctly find the ground state of a particular system the many-body wave function, a complex function of dimension $3N$ for N particles in the system, would have to be represented in a basis and, in some fashion, the Schrödinger equation variationally minimised. This is only possible for small N before the exponential growth in the wave function size swamps any available computing resources and prevents a proper variational exploration of its configuration space, the 'exponential wall'.[66] To illustrate this, suppose we have p parameters per dimension of the wave function, e.g. if we were representing the wave function on a Cartesian grid we might be quantising it with

p grid points per axis. This means we have

$$M = p^{3N} - 1 \tag{3.1}$$

parameters in total to minimise with respect to, including normalisation. Even for small p, e.g. 10, this rapidly becomes intractable. For example, with $p = 10$ and $N = 50$, a reasonably sized molecule one might want to look at, $M = 10^{150}$ — unlikely to ever be possible with conventional computers as this vastly exceeds the estimated number of particles in the known universe!

This exponential wall forces theorists to consider restricted spaces for the wave function to live in: for example Hartree–Fock theory[67] which considers only a single Slater determinant and no electron correlation, or more recent post-Hartree–Fock theories, such as coupled-cluster (CC) theory[68,69] or multi-configurational self-consistent field (MCSCF), which only mix in certain extra parts of the full Fock space,[70] or add in electron correlation effects by perturbation theory, e.g. Møller–Plesset perturbation theory (MP) to various orders.[71]

3.1 Density functional theory

Density functional theory (DFT) takes an alternative route to finding the ground state by focusing on real physical 3-dimensional quantities; principally the electron density of the system. This allows a significant computational speed up by reducing the number of variational parameters. DFT is, in theory, an exact method for finding the ground state of quantum systems, allowing the prediction of many important properties. Its creation was a key development in computational quantum mechanics, providing a route to vastly simplify the solution of the Schrödinger equation.

Typically, the Born–Oppenheimer approximation is used. Due to the much higher mass of the nuclei relative to the electrons, the full many-body wave function is assumed to factorise into separate nuclear and electronic wave functions. The nuclear degrees of freedom are then treated classically. The electrons experience an electrostatic potential corresponding to the nuclei at fixed coordinates:

$$v(\mathbf{r}) = -\sum_{\mathbf{R}} \frac{Z_{\mathbf{R}}}{|\mathbf{R} - \mathbf{r}|}. \tag{3.2}$$

We'd like to describe the ground-state energy of a system as a universal functional of the electron density; which we can then minimise with respect to:

$$E[n(\mathbf{r})] = \int \mathrm{d}\mathbf{r}\, n(\mathbf{r}) v(\mathbf{r}) + F[n(\mathbf{r})], \tag{3.3}$$

$$n(\mathbf{r}) = N\langle\psi| \prod_{i=0}^{N} \delta(\mathbf{r} - \mathbf{r}_i)|\psi\rangle, \tag{3.4}$$

where $F[n(\mathbf{r})]$ is a universal functional containing the kinetic energy and self-interaction of the electron gas and $v(\mathbf{r})$ is the external potential. We would like to express $E[n(\mathbf{r})]$ as a universal functional. However, it still contains a dependence on the external potential.

3.1.1 The Hohenberg–Kohn theorem

Hohenberg and Kohn[72] proved that the external potential, $v(\mathbf{r})$, is a unique functional of the ground-state density. This proof proceeds by demonstrating a variational contradiction if there exists another potential, $v'(\mathbf{r})$, giving rise to the same

ground-state density, $n(\mathbf{r})$, as $v(\mathbf{r})$.

Given two ground-state wave functions and system Hamiltonians we have

$$\langle\Psi|\hat{H}|\Psi\rangle = \langle\Psi|\hat{T} + \hat{V} + \hat{U}|\Psi\rangle = E, \tag{3.5}$$

$$\langle\Psi'|\hat{H}'|\Psi'\rangle = \langle\Psi'|\hat{T} + \hat{V}' + \hat{U}|\Psi'\rangle = E', \tag{3.6}$$

where $\hat{H}$ is the system Hamiltonian, $\hat{T}$ is the kinetic energy operator, $\hat{V} = v(\mathbf{r})$ and $\hat{V}' = v'(\mathbf{r})$ are the external potential operators where

$$v(\mathbf{r}) \neq v'(\mathbf{r}) \tag{3.7}$$

and $\hat{U}$ is the internal potential operator, Ψ is the ground-state wave function of $\hat{H}$ and Ψ' is the ground-state wave function of $\hat{H}'$, both with the same density.

By the variational principle, as Ψ is not the ground-state of $\hat{H}'$, the expectation of the energy must be greater than the ground-state energy, so

$$E' < \langle\Psi|\hat{T} + \hat{U} + v'(\mathbf{r})|\Psi\rangle, \tag{3.8}$$

$$E < \langle\Psi'|\hat{T} + \hat{U} + v(\mathbf{r})|\Psi'\rangle. \tag{3.9}$$

Expanding both and expressing as integrals over density, which is equal for both, gives

$$E' < E + \int \mathrm{d}\mathbf{r}\, (v'(\mathbf{r}) - v(\mathbf{r}))n(\mathbf{r}) \tag{3.10}$$

$$E < E' + \int \mathrm{d}\mathbf{r}\, (v(\mathbf{r}) - v'(\mathbf{r}))n(\mathbf{r}). \tag{3.11}$$

Summing the two equations gives the inequality

$$E + E' < E + E', \tag{3.12}$$

hence there cannot exist another external potential not equal to v that gives rise to the same ground-state density. This implies that the external potential must be a unique functional of the ground-state density. This means that the system Hamiltonian is uniquely determined by the ground-state density, and so the many-body wave function is also uniquely defined by the ground-state density, and so all ground-state expectation values of operators are uniquely defined by the ground-state density

$$\langle \hat{O} \rangle = \langle \Psi[n(\mathbf{r})] | \hat{O} | \Psi[n(\mathbf{r})] \rangle. \tag{3.13}$$

Now that we have demonstrated that $v(\mathbf{r})$ is a functional of $n(\mathbf{r})$, we can write the expectation value of the Hamiltonian as a universal functional:

$$E[n(\mathbf{r})] = \int \mathrm{d}\mathbf{r}\, v[n(\mathbf{r})](\mathbf{r})n(\mathbf{r}) + E_H + G[n(\mathbf{r})], \tag{3.14}$$

where E_H is the classical Coulomb self-interaction of the electron density

$$E_H = \frac{1}{2} \int \int \mathrm{d}\mathbf{r}\mathrm{d}\mathbf{r}' \, \frac{n(\mathbf{r})n(\mathbf{r}')}{|\mathbf{r} - \mathbf{r}'|} \tag{3.15}$$

and $G[n(\mathbf{r})]$ contains kinetic, exchange, and correlation functionals of the electron density.

Hohenberg and Kohn then proved that the ground-state energy can be minimised variationally, and that the density of the system with the minimal ground-state energy is the ground-state density.

The overall effect has been to move the complexity of the many-body wave function into the complexity of an unknown functional, the remaining G functional:

$$G[n(\mathbf{r})] = T[n(\mathbf{r})] + E_{\mathrm{int}}[n(\mathbf{r})], \tag{3.16}$$

where T is the kinetic energy functional, which is unknown but significant, and E_{int} is the electronic interaction energy functional, excluding the Hartree energy, which is unknown and expected to be small compared to the other terms in the Hamiltonian. However, this extra energy is large enough to be necessary to include in calculations and hence represents the main challenge in the application of density functional theory, alongside estimating the kinetic energy.

3.1.2 The Kohn–Sham equation

Kohn and Sham[73] provided a way forward in minimising the functional $E[n(\mathbf{r})]$ by demonstrating that, as the ground-state energy of a system is determined by the ground-state density, without the nature of the electron–electron interaction

specified, one can map the problem of interacting electrons in an external potential to one of non-interacting electrons in an effective potential. This allows a good estimate of the kinetic energy, the main difficulty in applying the Hohenberg–Kohn theorem in practice, from the non-interacting electrons' orbitals.

The wave function of the non-interacting electrons is a determinant of single particle orbitals,

$$\Psi = \frac{1}{N!} \det \left[\psi_1, \psi_2, \ldots, \psi_N \right], \tag{3.17}$$

and the density is a simple sum of squares of the orbitals

$$n(\mathbf{r}) = \sum_{i=1}^{N} \psi_i(\mathbf{r})^* \psi_i(\mathbf{r}). \tag{3.18}$$

We want to construct a fictitious non-interacting electronic Hamiltonian which generates exactly the same ground-state density as the equivalent many-body interacting Hamiltonian.

The non-interacting kinetic energy, T_S, is then:

$$T_S = -\frac{1}{2} \sum_i \int \mathrm{d}\mathbf{r}\, \psi_i^*(\mathbf{r}) \nabla^2 \psi_i(\mathbf{r}) \tag{3.19}$$

and the total energy of the system can be written

$$E_{\mathrm{KS}} = T_S + E_H + E_{\mathrm{xc}}[n(\mathbf{r})] + \int \mathrm{d}\mathbf{r}\, v(\mathbf{r}) n(\mathbf{r}) \tag{3.20}$$

where $E_{\mathrm{xc}}[n(\mathbf{r})]$ is

$$E_{\mathrm{xc}}[n(\mathbf{r})] = \langle \hat{T} \rangle - T_S + \langle \hat{U} \rangle - E_H, \tag{3.21}$$

where $\langle \hat{T} \rangle$ is the kinetic energy of the true, many-body system and $\langle \hat{U} \rangle$ is the electron self-interaction energy of the real, many-body system.

3.1.3 The exchange-correlation functional

The E_{xc} functional is unknown and there is no known systematic approach to approximating it, so the remaining challenge is to find a good guess. Although the true exchange-correlation functional must necessarily be non-local, it is highly computationally favourable to keep it as a local potential. This is theoretically supported to some extent by the short-rangeness of electron–electron interactions.[74]

Kohn and Sham approximated E_{xc} by assuming a slowly varying $n(\mathbf{r})$,

$$E_{\mathrm{xc}}^{\mathrm{LDA}}[n(\mathbf{r})] = \int \mathrm{d}\mathbf{r}\, n(\mathbf{r}) \epsilon_{\mathrm{xc}}(n(\mathbf{r})), \tag{3.22}$$

where $\epsilon_{xc}(n)$ is the exchange correlation energy per electron of a uniform electron gas with density n. This is known as the *local-density approximation* (LDA). Kohn and Sham then derived a one-particle Schrödinger equation, the Kohn–Sham equation,

$$[-\frac{1}{2}\nabla^2 + v(\mathbf{r}) + \int \mathrm{d}\mathbf{r}' \, \frac{n(\mathbf{r}')}{|\mathbf{r} - \mathbf{r}'|} + v_{\mathrm{xc}}(\mathbf{r})]\psi_i(\mathbf{r}) = \epsilon_i \psi_i(\mathbf{r}), \tag{3.23}$$

where

$$v_{\mathrm{xc}}(\mathbf{r}) = \frac{\partial E_{\mathrm{xc}}}{\partial n(\mathbf{r})} \tag{3.24}$$

which when solved self-consistently for $n(\mathbf{r})$ gives the correct ground-state density for the many-body interacting electron system with external potential $v(\mathbf{r})$. They also examine including exchange effects exactly, using the exchange energy from Hartree–Fock theory, which they note is more complex as the effective potential is now non-local.

Taking the LDA form suggested by Kohn and Sham for the exchange-correlation functional, Ceperley and Alder[75] presented a Monte Carlo method to solve the ground-state of the uniform electron gas, giving an estimate for the electron exchange-correlation functional for use in density functional theory, which was then parameterised by Perdew and Zunger[76] and others.

Further extensions to the LDA have been made, such as including spin polarisation, giving the local spin density approximation (LSDA),

$$E_{\mathrm{xc}}^{\mathrm{LSDA}}[n_\uparrow, n_\downarrow] = \int \mathrm{d}\mathbf{r}\, n(\mathbf{r}) \epsilon_{\mathrm{xc}}(n_\uparrow(\mathbf{r}), n_\downarrow(\mathbf{r})), \tag{3.25}$$

of which there are a number of analytic expressions.[77]

An extension to the LDA/LSDA scheme is the semi-local *generalised gradient approximation* (GGA):[78]

$$E_{\mathrm{xc}}^{\mathrm{GGA}}[n_\uparrow, n_\downarrow] = \int \mathrm{d}\mathbf{r}\, n(\mathbf{r}) \epsilon_{\mathrm{xc}}(n_\uparrow(\mathbf{r}), n_\downarrow(\mathbf{r}), \nabla n_\uparrow(\mathbf{r}), \nabla n_\downarrow(\mathbf{r})), \tag{3.26}$$

two parameterisations of which are the Perdew–Wang 1991 (PW91) functional[79] and

the Perdew–Burke–Ernzerhof (PBE) functional.[78] 'Meta' functionals go further and include the Laplacian of the electron density in addition to its derivatives.

The use of a GGA functional can improve certain properties such as total energies, barriers and structural energy differences. However, they tend to favour softened bonds, sometimes excessively, compared to the LDA, and do not necessarily represent a systematic improvement over the LDA. In particular GGAs do not satisfy the electron correlation sum rule, that the implied pair density should integrate to one missing electron, while the LDA does.

Overall, (semi-)local exchange-correlation functionals suffer from issues such as non-physical electron self-interaction, failing to reproduce the discontinuity in v_{xc} for integer particle occupation numbers,[80] exclusion of dispersion effects, and generally systematically underestimating the HOMO–LUMO/band gap.

Some functionals which attempt to fix some of these issues include exact-exchange functionals — which compute exactly the Hartree–Fock exchange part of the energy using the Kohn–Sham orbitals, $E_{\mathrm{x}}^{\mathrm{HF}}$, usually mixed with some correlation energy in a hybrid functional, e.g. the PBE0 functional,

$$E_{\mathrm{xc}}^{\mathrm{PBE0}} = E_{\mathrm{xc}}^{\mathrm{PBE}} + \frac{1}{4}\left(E_{\mathrm{x}}^{\mathrm{HF}} - E_{\mathrm{x}}^{\mathrm{PBE}}\right), \tag{3.27}$$

or the popular B3LYP functional (Becke, three-parameter, Lee–Yang–Parr),[81]

$$E_{\mathrm{xc}}^{\mathrm{B3LYP}} = E_{\mathrm{xc}}^{\mathrm{LSDA}} + a_0(H_{\mathrm{x}}^{\mathrm{HF}} - E_{\mathrm{x}}^{\mathrm{LSDA}}) + a_{\mathrm{x}}\Delta E_{\mathrm{x}}^{\mathrm{B88}} + a_{\mathrm{c}}\Delta E_{\mathrm{c}}^{\mathrm{PW91}}, \tag{3.28}$$

where the empirical coefficients a_0, a_{x} and a_{c} are fitted to experimental data, $\Delta E_{\mathrm{x}}^{\mathrm{B88}}$ is Becke's 1988 gradient correction to LSDA exchange[82] and $\Delta E_{\mathrm{c}}^{\mathrm{PW91}}$ is Perdew and Wang's 1991[79] gradient correction to correlation. Some hybrid functionals, such as

HSE,[83] include screened Coulomb effects in the exchange energy.

A low cost approach to fixing deficiencies in local functionals is the DFT+U method,[84] which introduces an interaction between localised electrons in d and f orbitals and, while not solving the self-interaction error directly, can correct for some of its effects. A higher cost approach is many-body perturbation theory methods such as GW,[85] which eliminates electron self-interaction and correctly reproduces the non-analytic behaviour of the true v_{xc} on addition of a fractional electron to the system. However, the high cost of GW generally means it cannot be solved self-consistently, and is instead performed as the one-shot G_0W_0 method.[86] In addition, properties beyond the total energy and orbital eigenvalues are difficult to calculate.

Finally, there exist exchange correlation functionals which attempt to, at varying levels of cost, include non-local van der Waals dispersion effects that are otherwise missed by local functionals[87] and can be important for the accurate calculation of properties such as crystal lattice parameters and molecular binding energies.

3.1.4 Periodic systems and Bloch's theorem

Bloch's theorem is an important result for the theoretical treatment of systems with periodic boundary conditions, and will now be outlined and explained below following Martin.[88]

Consider a crystal with lattice vectors $\mathbf{a}_1$, $\mathbf{a}_2$, $\mathbf{a}_3$. These vectors form a primitive unit cell. One can place an integer number of such primitive unit cells, N_i, next to one another to form a $N_1 \times N_2 \times N_3$ supercell, shown in Fig. 3.1. Although no real crystal system is actually infinite in size, they are well approximated by an indefinitely large supercell.

One can also define a set of reciprocal basis vectors, $\mathbf{b}_i$, which are dual to the lattice

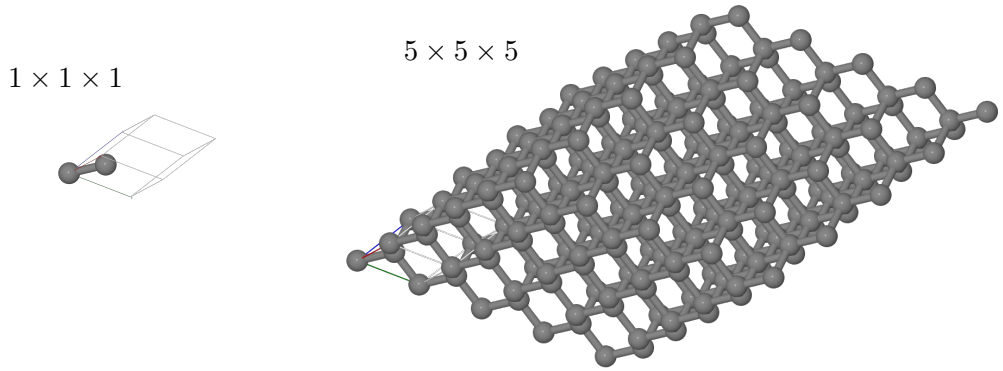

Figure 3.1: Illustration of two equivalent cells of diamond, on the left is the primitive cell, and on the right is a $5\times5\times5$ supercell created by creating copies of the primitive cell.

vectors $\mathbf{a}_i$,

$$\mathbf{a}_i \cdot \mathbf{b}_j = 2\pi\delta_{ij}. \tag{3.29}$$

These allow the definition of inner products in a non-orthonormal basis.

A periodic operator, $\hat{O}$, such as the Hamiltonian $\hat{H}$, must be invariant to all lattice translations $\mathbf{T_n} = n_1\mathbf{a}_1 + n_2\mathbf{a}_2 + n_3\mathbf{a}_3$. These are represented by the translation operator, $\hat{T}_\mathbf{n}$:

$$\hat{T}_\mathbf{n}\psi(\mathbf{r}) = \psi(\mathbf{r} + n_1\mathbf{a}_1 + n_2\mathbf{a}_2 + n_3\mathbf{a}_3). \tag{3.30}$$

The fact that $\hat{T}_\mathbf{n}$ and $\hat{H}$ must commute implies that eigenstates of $\hat{H}$ can be chosen

to be eigenstates of $\hat{T}_{\mathbf{n}}$ for all $\mathbf{n}$:

$$\hat{T}_{\mathbf{n}}\psi(\mathbf{r}) = t_{\mathbf{n}}\psi(\mathbf{r}). \tag{3.31}$$

As the product of any two translation operators is a third translation operator with the sum of translation vectors,

$$\hat{T}_{\mathbf{n}_1}\hat{T}_{\mathbf{n}_2} = \hat{T}_{\mathbf{n}_1+\mathbf{n}_2}, \tag{3.32}$$

so must the eigenvalues $t_{\mathbf{n}}$ obey

$$t_{\mathbf{n}_1+\mathbf{n}_2} = t_{\mathbf{n}_1}t_{\mathbf{n}_2} \tag{3.33}$$

and so, breaking down a translation into translations by the lattice vectors,

$$t_{\mathbf{n}} = (t_{\mathbf{a}_1})^{n_1}(t_{\mathbf{a}_2})^{n_2}(t_{\mathbf{a}_3})^{n_3}. \tag{3.34}$$

In order for ψ to be bounded, $|t_{\mathbf{a}_i}| = 1$ and so we can always write

$$t_{\mathbf{a}_i} = \mathrm{e}^{2\pi \mathrm{i} m_i y_i}, \tag{3.35}$$

where $y_i = 1/N_i$, m_i is an integer and N_i is the number of cells being considered in the direction i. Alternatively this can be written

$$t_{\mathbf{n}} = \mathrm{e}^{\mathrm{i}\mathbf{k}\cdot\mathbf{T}_{\mathbf{n}}}, \tag{3.36}$$

where the reciprocal space vector $\mathbf{k}$ is

$$\mathbf{k} = \frac{m_1}{N_1}\mathbf{b}_1 + \frac{m_2}{N_2}\mathbf{b}_2 + \frac{m_3}{N_3}\mathbf{b}_3. \tag{3.37}$$

$\mathbf{k}$ can be restricted to the primitive cell of the reciprocal lattice, as you can add an arbitrary reciprocal lattice vector $\mathbf{G}$, such that $\mathbf{G} \cdot \mathbf{T} = 2\pi m$, and not change the phase.

We hence have

$$\hat{T}_{\mathbf{n}}\psi(\mathbf{r}) = \mathrm{e}^{\mathrm{i}\mathbf{k}\cdot\mathbf{T_n}}\psi(\mathbf{r}). \tag{3.38}$$

We can write the eigenfunction ψ in terms of a spatial phase factor and a periodic function $u_{i,\mathbf{k}}$,

$$\psi_{i\mathbf{k}}(\mathbf{r}) = \mathrm{e}^{\mathrm{i}\mathbf{k}\cdot\mathbf{r}}u_{i,\mathbf{k}}(\mathbf{r}). \tag{3.39}$$

where $u_{i,\mathbf{k}}$ is periodic in the crystal lattice,

$$u_{i,\mathbf{k}}(\mathbf{r}) = u_{i,\mathbf{k}}(\mathbf{r} + \mathbf{T_n}). \tag{3.40}$$

The periodic function u is then an eigenvalue of the Bloch Hamiltonian:

$$\hat{H}_{\mathbf{k}}u_{i,\mathbf{k}}(\mathbf{r}) = \left[-\frac{1}{2}(\nabla + \mathrm{i}\mathbf{k})^2 + V(\mathbf{r})\right] u_{i,\mathbf{k}}(\mathbf{r}) = \epsilon_{i,\mathbf{k}}u_{i\mathbf{k}}(\mathbf{r}). \tag{3.41}$$

Per-cell properties, such as the electron density $\rho(\mathbf{r})$, can be expressed as sums over

k:

$$\rho(\mathbf{r}) = \frac{1}{N_k} \sum_{\mathbf{k}} \sum_{i} u^*_{i,\mathbf{k}}(\mathbf{r}) u_{i,\mathbf{k}}(\mathbf{r}), \tag{3.42}$$

where N_k is the number of **k**-vectors considered, i.e. the number of cells in the supercell. In the limit of an infinitely large supercell this becomes an integral over the Brillouin Zone,

$$\rho(\mathbf{r}) = \frac{1}{\Omega_{\mathrm{BZ}}} \int_{\Omega_{\mathrm{BZ}}} \mathrm{d}\mathbf{k} \sum_{i} u^*_{i,\mathbf{k}}(\mathbf{r}) u_{i,\mathbf{k}}(\mathbf{r}). \tag{3.43}$$

3.1.5 Plane-wave basis sets

The periodic function $u(\mathbf{r})$ can be written

$$u(\mathbf{G}) = \frac{1}{\Omega_{\mathrm{cell}}} \int_{\Omega_{\mathrm{cell}}} \mathrm{d}\mathbf{r}\, u(\mathbf{r}) \mathrm{e}^{\mathrm{i}\mathbf{G}\cdot\mathbf{r}} \tag{3.44}$$

where Ω_{cell} is the volume of the unit cell and the **G** vectors are a lattice in reciprocal space,

$$\mathbf{G_m} = m_1\mathbf{b}_1 + m_2\mathbf{b}_2 + m_3\mathbf{b}_3. \tag{3.45}$$

In addition to being a natural orthogonal function basis for a periodic function, representing the u function in terms of plane waves is attractive as the kinetic energy operator, amongst others, is diagonal in reciprocal space. While the potential operator $v(\mathbf{r})$ is diagonal in real space, converting between real space representations and reciprocal space representations is is cheap with a Fast-Fourier Transform

(FFT), for which the cost scales favourably as $n \log n$, where n is the number of plane waves. These properties allow calculations using plane wave basis sets to have a smaller computational cost than calculations using similarly sized non-plane-wave basis sets.

In calculations, the plane-wave basis set used is typically determined by the maximum kinetic energy it can describe, i.e. a sphere of $\mathbf{G}$ for every $\mathbf{k}$ with

$$E_{\text{cut}} > \frac{1}{2}|\mathbf{k} + \mathbf{G}|^2, \tag{3.46}$$

where E_{cut} is the *cut-off energy*. As the only free parameter in the basis set, this can be systematically converged to minimise basis set error for the calculation at hand.

Plane-wave basis sets have drawbacks in poor representation of rapidly changing functions, for example wave functions near the nucleus of an atom, and expensive, non-sparse, representation of vacuum regions (e.g. inside and outside a nanotube). In addition, the large number of basis functions make the calculation of exact-exchange integrals expensive.

3.1.6 Numerical approach to finding the ground state

In order to find the ground-state wave functions of an N electron system we need to find the N lowest eigenstates of the one-particle effective Hamiltonian (the Kohn–Sham equation). A significant difficulty is that the Kohn–Sham equation is, in fact, a non-linear eigenproblem, dependent on the electron density, which itself depends on the wave functions. The most common method for solving this is by *self-consistent field* (SCF), whereby an approximate density and Hamiltonian is constructed, solved, and then a new density constructed from the Kohn–Sham states. This is then

iterated until the changes in the density, states and Hamiltonian are considered sufficiently small and approximate convergence to a self-consistent ground state is achieved.

One could construct the matrix elements of the Hamiltonian and directly diagonalise it, generate the electron density from the N lowest eigenstates, and then iterate until convergence is achieved. The amount of memory required to store the matrix scales as M^2, with M the number of basis states per electron, so a full representation is clearly undesirable for more than a few electrons or basis states. This method also wastes considerable resources calculating eigenstates when the system is far from self-consistency.

Numerical solution of the Kohn–Sham equations has been greatly enhanced by iterative minimisation methods,[89] where one minimises the electronic states and density simultaneously. In the molecular dynamics method, the electronic degrees of freedom are given fictitious masses and a second-order differential equation, constrained to ensure that the orbitals remain orthogonal, is integrated. Although introduced by Car and Parrinello[90] as a method for molecular dynamics, by freezing the atoms this method will iteratively converge to the electronic ground state. One of the key disadvantages is that the fictitious electron mass, μ, must by carefully tuned to avoid systematic errors in calculated forces and ensure convergence.[91]

It is preferable to directly minimise the energy functional,[89] as it has a well defined minimum and avoids instabilities in the evolution of the electronic configuration. A method of directly minimising the energy functional of the system, and the one conventionally preferred in modern codes, is the conjugate gradient algorithm[92,93] and its descendants. This attempts to make optimal steps around the functional energy surface, avoiding discontinuous changes in the charge density, and improves on the basic steepest-descent algorithm by using information from previous minimisation

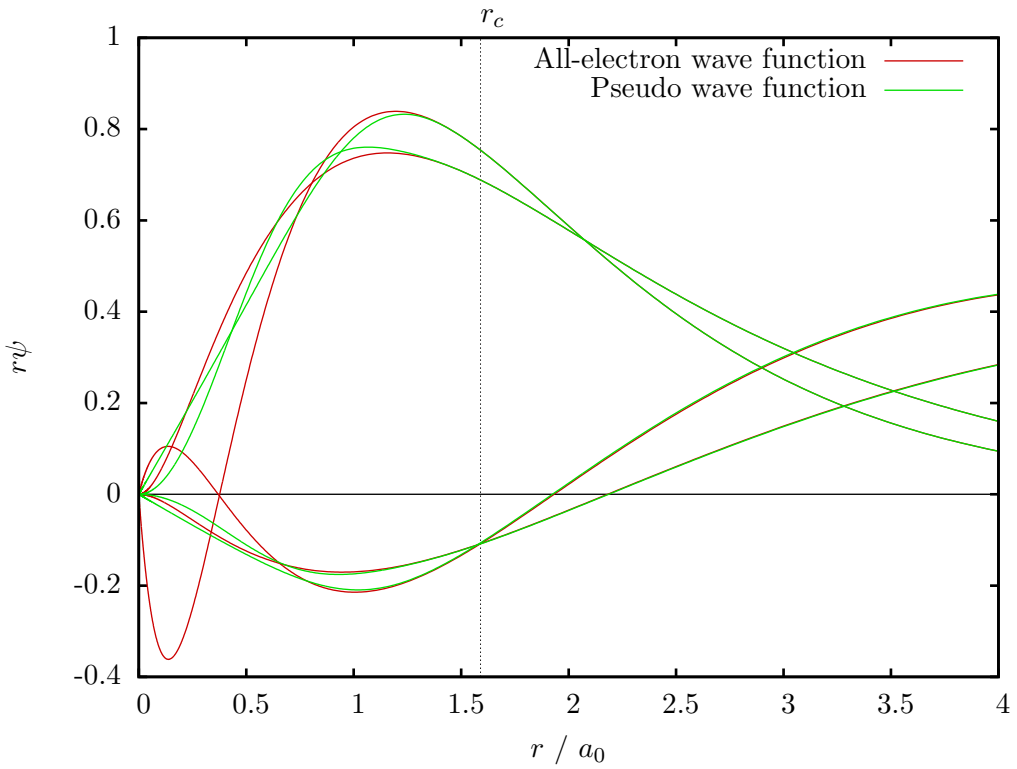

Figure 3.2: Illustration of the all-electron and pseudised valence wave functions in a norm-conserving carbon pseudopotential. Note that they are equal to one another for radii larger than the cut-off radius, r_c.

steps to chose the optimum direction of movement.

In both methods one applies the Hamiltonian multiple times to a set of trial wave functions to discover the next step to take. As mentioned, using a plane-wave basis set enables efficient application of the kinetic part of the Hamiltonian diagonally in reciprocal space, and the local potential diagonally in real space, eliminating the need to store the full matrix representation of the Hamiltonian.

3.1.7 The pseudopotential approximation

In quantum mechanical simulations it is desirable that the electronic wave functions should be well represented by the smallest basis set possible in order to minimise the memory storage needs and the cost of computational operations such as FFTs and application of operators. For a plane-wave basis set this means minimising the energy cut-off (E_{cut}), i.e. the maximum spatial frequency component of the wave function, effectively requiring that the wave functions be as smooth as possible. The primary source of high frequency components in wave functions is the sharp nuclear Coulomb potential — the strong potential and enforced orthogonalisation to lower lying eigenstates means the wave functions of valence electrons possess a large curvature.

In quantum mechanical calculations it is also desirable to simulate a minimum number of electrons, as the computational cost increases with each. In the case of plane-wave DFT, computational cost scales as the cube of the system size.[89] In many typical systems a change in an atom's chemical environment leaves the core electrons of the atom largely unchanged. By not updating the degrees of freedom relating to the core electrons, the 'frozen core approximation', the computational cost is significantly reduced.[94]

We want calculations to reproduce the chemical properties of a system, such as the bonding and dynamics. These properties primarily depend on the overlap of valence wave functions outside the core region, $r > r_c$, where the wave function is typically representable by a small energy cut-off, so it might be the case that we can modify the valence wave functions in the core region without affecting the accuracy of the calculation. The requirement to reproduce chemical properties implies that we need to retain the scattering properties of the nuclear potential around the energy range of chemical interactions (low eV) and thus retain the form of the wave functions in

the bonding region.

To achieve this we replace the nuclear Coulomb potential by a smoother *pseudopotential* and remove the core electrons. The smoother potential and removal of the orthogonality constraint to the core electrons smooths the valence wave functions in the core region, allowing a description with a smaller basis cut-off energy, while retaining a good description of chemical properties.

Early pseudopotentials, e.g. Fermi pseudopotentials,[95] were strictly local potentials,

$$\tilde{V} = V_{\text{eff}}(\mathbf{r}), \tag{3.47}$$

generated by fitting to experimental data. These give approximate wave functions and can't be systematically improved.

The most common approach in modern first-principles calculations is to use non-local pseudopotentials of the form

$$\tilde{V} = V_{\text{eff}}(\mathbf{r}) + \sum_{ij} |p_i\rangle D_{ij} \langle p_j|, \tag{3.48}$$

where $|p_i\rangle$ are localised atomic projectors and D_{ij} is a pseudopotential-specific matrix representing the non-local potential for different projector channels.

Typically such pseudopotentials are generated from an all-electron (AE) atomic calculation. A reference calculation is performed on the radial Kohn–Sham equation to extract atomic eigenvalues and wave functions, ϕ, and then matching pseudo-wave functions, $\tilde{\phi}$, are generated within the afforded freedom using one of various methods to satisfy certain desirable features, shown in Fig. 3.2.

From the given pseudo-wave functions, the screened potential is recovered by in-

verting the radial Schrödinger equation, and then de-screened by subtracting the Hartree and exchange-correlation potentials of the valence electrons to give an ionic pseudopotential.

There are a number of ways to generate the pseudo-wave functions.[96–98] Hamann *et al.*[97] outlined the following properties as being desirable: exact agreement of eigenvalues between the pseudo and real valence wave functions for a reference atomic configuration; that the pseudo and real wave functions are equal beyond the core radius, r_c; that the integral of real and pseudo charges for each orbital within the core region are equal; that the logarithmic derivatives of the pseudo and real wave functions are equal outside the core region, as well as their first energy derivatives — this minimises the error when states are shifted in a new environment (e.g. when bonding). Pseudopotentials satisfying these properties are more likely to be accurate and transferable.

The requirement that the integrals of the real and pseudo charges inside the core region are equal is called the norm-conserving constraint. Troullier and Martins[96] described a procedure to construct a smooth norm-conserving pseudopotential, satisfying the generalised norm-conservation constraint

$$0 = \langle \phi_{\mathbf{R},n} | \phi_{\mathbf{R},m} \rangle - \langle \tilde{\phi}_{\mathbf{R},n} | \tilde{\phi}_{\mathbf{R},m} \rangle, \tag{3.49}$$

for $\phi_{\mathbf{R},n}$ the all-electron wave functions of atom $\mathbf{R}$ and $\tilde{\phi}_{\mathbf{R},n}$ are the equivalent pseudo-wave functions.

However, the norm-conserving constraint means that for elements with 1s, 2p, 3d or 4f valence states, which are nodeless radially, the pseudo-wave function still contains high frequency components. This makes these pseudopotentials 'hard' and necessitates a higher cut-off energy than other pseudopotentials.

3.1.8 Ultrasoft pseudopotentials

The so-called 'ultrasoft' pseudopotential formalism introduced by Vanderbilt[19] is the most computationally efficient form of pseudopotential, generally providing numerically converged results with significantly smaller basis sets. This is particularly important for elements which require semi-core states to be treated as valence for accurate results e.g. '3p' states in the 3d transition metal series. While ultrasoft potentials are efficient from a user's point of view, there is some additional complexity when implemented in an electronic-structure code. The key ingredient of the ultrasoft scheme is that the norm of the pseudo partial-waves in the augmentation region can be different from that of the corresponding all-electron partial waves. We can thus define a non-zero charge augmentation term $\mathrm{Q}_{\mathbf{R},nm}(\mathbf{r})$:

$$\mathrm{Q}_{\mathbf{R},nm}(\mathbf{r}) = \langle\phi_{\mathbf{R},n}|\mathbf{r}\rangle\langle\mathbf{r}|\phi_{\mathbf{R},m}\rangle - \langle\tilde{\phi}_{\mathbf{R},n}|\mathbf{r}\rangle\langle\mathbf{r}|\tilde{\phi}_{\mathbf{R},m}\rangle. \tag{3.50}$$

The norm of a pseudo-wave function can be computed as the expectation value of the pseudo operator $\tilde{1} = S$. Using Eqn. 3.50,

$$S = 1 + \sum_{\mathbf{R},n,m} |p_{\mathbf{R},n}\rangle \mathrm{q}_{\mathbf{R},nm} \langle p_{\mathbf{R},m}| \tag{3.51}$$

where

$$\mathrm{q}_{\mathbf{R},nm} = \langle\phi_{\mathbf{R},n}|\phi_{\mathbf{R},m}\rangle - \langle\tilde{\phi}_{\mathbf{R},n}|\tilde{\phi}_{\mathbf{R},m}\rangle. \tag{3.52}$$

As a result, a normalised eigenstate of the pseudo Hamiltonian obeys the generalised

equations:

$$\tilde{H}|\tilde{\psi}_o\rangle = \varepsilon_o S|\tilde{\psi}_o\rangle, \tag{3.53}$$

and

$$\langle\tilde{\psi}_o|S|\tilde{\psi}_{o'}\rangle = \delta_{o,o'}. \tag{3.54}$$

The pseudo-Hamiltonian $\tilde{H}$ can be derived using Eqn. 3.63 as

$$\tilde{H} = -\nabla^2 + V_{\text{eff}} + \sum_{\mathbf{R},n,m} |p_{\mathbf{R},n}\rangle \mathrm{D}_{\mathbf{R},nm} \langle p_{\mathbf{R},m}| \tag{3.55}$$

where $\mathrm{D}_{\mathbf{R},nm}$ is given by

$$\mathrm{D}_{\mathbf{R},nm} = \mathrm{D}^0_{\mathbf{R},nm} + \int \mathrm{d}\mathbf{r}\, V_{\text{eff}}(\mathbf{r}) \mathrm{Q}_{\mathbf{R},nm}(\mathbf{r}). \tag{3.56}$$

$\mathrm{D}^0_{\mathbf{R},nm}$ is obtained from the construction of the pseudopotential,[99] and V_{eff} is the screened local potential. The norm-conserving pseudopotential scheme can be regarded as special case in which $\mathrm{q}_{\mathbf{R},nm} = 0$ by definition, and in all norm-conserving implementations the terms $\mathrm{Q}_{\mathbf{R},nm}$ are ignored. The charge density in the ultrasoft scheme is given by

$$n(\mathbf{r}) = \sum_{o\sigma} [\psi^*_{o\sigma}(\mathbf{r})\psi_{o\sigma}(\mathbf{r}) \tag{3.57}$$

$$+ \sum_{\mathbf{R},n,m} Q_{\mathbf{R},nm}(\mathbf{r}) \langle p_{\mathbf{R},n}|\psi_{o\sigma}\rangle\langle\psi_{o\sigma}|p_{\mathbf{R},m}\rangle]. \tag{3.58}$$

In practice $Q_{\mathbf{R},nm}$, and hence $n(\mathbf{r})$, would be prohibitively expensive to represent in a plane-wave basis or on a real-space grid, and so $Q_{\mathbf{R},nm}$ is replaced by a pseudised augmentation charge $\tilde{Q}_{\mathbf{R},nm}$, where the pseudisation conserves the electrostatic moments of the charge.[99] The pseudised augmentation charge is represented on a larger grid than the standard density grid, often called called the 'fine grid', at a memory cost for every density grid needed. The grid-representable charge density $\bar{n}(\mathbf{r})$ is given by

$$\bar{n}(\mathbf{r}) = \sum_{o\sigma} [\psi^*_{o\sigma}(\mathbf{r})\psi_{o\sigma}(\mathbf{r}) \tag{3.59}$$

$$+ \sum_{\mathbf{R},n,m} \tilde{Q}_{\mathbf{R},nm}(\mathbf{r})\langle p_{\mathbf{R},n}|\psi_{o\sigma}\rangle\langle\psi_{o\sigma}|p_{\mathbf{R},m}\rangle]. \tag{3.60}$$

3.1.9 The projector augmented-wave method

As discussed, the use of pseudopotentials is highly desirable as they allow the use of plane-wave basis sets. The use of pseudopotentials, however, implies that the valence wave functions have a non-physical form in the region close to the nucleus; this means that theories expressed in terms of all-electron operators that are sensitive to the precise form of the wave functions near to the nuclei, such as NMR, will give incorrect results. This is solved in the projector augmented-wave (PAW) formalism introduced by Van de Walle and Blöchl.[100,101] PAW provides a practical way to transform an operator acting on the AE wave function $|\psi\rangle$ into an operator acting on the pseudo-wave function $|\tilde{\psi}\rangle$, allowing pseudopotentials to be used in calculations of properties that are sensitive to the form of the wave function near the nucleus.

In particular, PAW proposes a linear transformation $\mathcal{T}$,

$$\mathcal{T} = 1 + \sum_n (|\phi_n\rangle - |\tilde{\phi}_n\rangle)\langle p_n|, \tag{3.61}$$

such that $\mathcal{T}|\tilde{\psi}\rangle = |\psi\rangle$ where ϕ_n and $\tilde{\phi}_n$ are atomic-like AE and PS partial waves at each atomic site for the spherically symmetric atom and pseudo-atom. The AE and PS partial waves form a complete basis within the augmentation region ($r < r_c$) and are equal outside. The functions p_n are the corresponding projectors to $\tilde{\phi}_n$, defined such that $\langle p_n|\tilde{\phi}_m\rangle = \delta_{nm}$ and that they vanish outside the augmentation region.

So, for a (semi-)local AE operator $\hat{O}$,

$$\langle\psi|\hat{O}|\psi\rangle = \langle\tilde{\psi}|\mathcal{T}^\dagger\hat{O}\mathcal{T}|\tilde{\psi}\rangle, \tag{3.62}$$

thus we can derive the equivalent pseudo-operator $\widetilde{O} = \mathcal{T}^\dagger\hat{O}\mathcal{T}$. The explicit form of $\widetilde{O}$ is

$$\widetilde{O} = \hat{O} + \sum_{nm} |p_n\rangle(\langle\phi_n|\hat{O}|\phi_m\rangle - \langle\tilde{\phi_n}|\hat{O}|\tilde{\phi_m}\rangle)\langle p_m|. \tag{3.63}$$

This allows us to calculate all-electron properties from pseudopotential calculations. Expectation values of operators with the partial waves are typically calculated on a log-radial grid, and in practice the number of partial waves used is truncated.

3.1.10 Density functional perturbation theory

Many observable properties, such as phonon spectra, electric polarisation and NMR parameters are defined theoretically as the response of a quantum system to a small

perturbation. Gonze[102,103] and Baroni[104,105] outlined the use of perturbation theory within DFT, *density functional perturbation theory* (DFPT), including the requirement of corrections for the self-consistency of the exchange-correlation potential with any change in the density.

The variation in the wave functions, $|\psi_n^{(1)}\rangle$, is a self-consistent solution of:

$$(\hat{H}^{(0)} - \epsilon_n^{(0)})|\psi_n^{(1)}\rangle = -(\hat{H}^{(1)} - \epsilon_n^{(1)})|\psi_n^{(0)}\rangle, \tag{3.64}$$

where $\hat{H}^{(0)}$ is the unperturbed Kohn–Sham Hamiltonian and

$$\hat{H}^{(1)} = V^{(1)}(\mathbf{r}) + \left.\frac{\mathrm{d}v_{\mathrm{xc}}(n)}{\mathrm{d}n}\right|_{n=n(\mathbf{r})} n^{(1)}(\mathbf{r}) + \int \mathrm{d}\mathbf{r}' \, \frac{n^{(1)}(\mathbf{r}')}{|\mathbf{r} - \mathbf{r}'|}, \tag{3.65}$$

where

$$n^{(1)}(\mathbf{r}) = 4\,\mathrm{Re}\sum_{n=1}^{N/2} \psi_n^{(0)*}(\mathbf{r})\psi_n^{(1)}(\mathbf{r}). \tag{3.66}$$

This is analogous to the Sternheimer equation[106] with corrections for self consistency.[107] This system of equations is solved self-consistently in a way similar to the Kohn–Sham equation, as $\hat{H}^{(1)}$ itself depends on $n^{(1)}$ and $n^{(1)}$ on $|\psi^{(1)}\rangle$.

This can be difficult computationally to solve, as $\psi_n^{(1)}$ depends on all unoccupied $\psi_m^{(0)}$ for $n \neq m$, while normally only the occupied states of the system are known. As the perturbation only couples occupied to unoccupied states, the self-consistent Eqn. 3.64 can be modified with projectors onto the empty and occupied state man-

ifolds, P_{c} and P_{v}:

$$(\hat{H}^{(0)} + \alpha P_{\mathrm{v}} - \epsilon_n^{(0)})|\psi_n^{(1)}\rangle = -P_{\mathrm{c}}\hat{H}^{(1)}|\psi_n^{(0)}\rangle, \tag{3.67}$$

in practice the P_{v} on the left hand side is achieved by selecting trial solutions that are orthogonal to the occupied states.

3.2 Relativity

The methods described thus far are all based on the non-relativistic Schrödinger equation. It's well known[20,108–110] that a proper description of the chemistry of heavier elements requires the inclusion of relativistic effects. In particular, it has been found that in order to properly predict NMR parameters in systems containing heavy nuclei, relativistic effects must be included.[22,24,111–116] An overview is given in Ref. 117. In pseudopotential methods, special relativitic effects are usually trivially included in the ground-state Hamiltonian by using orbital eigenvalues from relativistic free atom calculations. However, this isn't sufficient if relativistic all-electron wave functions or operators are needed, such as when calculating properties with PAW.

3.2.1 The Dirac equation

The equation that Dirac proposed in his 1928 paper, Ref. 118, in time-independent form, for an electron and in Hartree atomic units, is:

$$[c\alpha \cdot \hat{\mathbf{p}} + \beta c^2 + V]\psi = E\psi, \tag{3.68}$$

where V is an external potential, and α_i and β are 4×4 matrices and satisfy the following properties:

$$\alpha_i^2 = \beta^2 = I_4, \tag{3.69}$$

$$\alpha_i \alpha_j - \alpha_j \alpha_i = \delta_{ij}, \tag{3.70}$$

$$\alpha_i \beta - \beta \alpha_i = 0. \tag{3.71}$$

The wave function ψ is a complex four-component spinor, alternatively expressed in terms of the small component χ and the large component ϕ:

$$\psi = \begin{pmatrix} \phi \\ \\ \chi \end{pmatrix}. \tag{3.72}$$

The Dirac equation admits solutions with negative energy, which were poorly understood at the time, but are now known to correspond to antiparticle states. Darwin,[119] while finding solutions of the Dirac equation for a hydrogen-like atom, notes that in order to get a complete basis set of states one must include the negative energy states. This continuum of negative energy states can cause variational collapse when numerical solutions of the Dirac equation are attempted and so methods to do so must be considered carefully, in addition to the extra computational memory cost of storing the four-component spinor wave functions.

3.2.2 Zeroth-order regular approximation

It's desirable to come up with an effective Hamiltonian which captures the main relativistic effects, while being variationally stable and not energy dependent. We

start with the Dirac equation, Eqn. 3.68. In the case of DFT, V represents the nuclear, Hartree and exchange-correlation potentials. We can eliminate the small component (esc) χ by substitution,

$$\chi = \hat{X}\phi = \frac{c\sigma \cdot \hat{\mathbf{p}}}{2c^2 + E - V}\phi, \tag{3.73}$$

and retrieve an energy-dependent Hamiltonian in the large component ϕ only:

$$\hat{H}^{esc}\phi = E\phi = V\phi + \frac{1}{2}\sigma \cdot \hat{\mathbf{p}}(1 + \frac{E - V}{2c^2})^{-1}\sigma \cdot \hat{\mathbf{p}}. \tag{3.74}$$

To normalise ϕ we introduce a normalisation operator $\hat{O} = \sqrt{1 + \hat{X}^\dagger \hat{X}}$ and so we find the transformed Hamiltonian:

$$\hat{H} = (1 + \hat{X}^\dagger \hat{X})^{\frac{1}{2}}[V + c\sigma \cdot \hat{\mathbf{p}}\hat{X}](1 + \hat{X}^\dagger \hat{X})^{-\frac{1}{2}} \tag{3.75}$$

The standard expansion of $\hat{X}$ and $\hat{H}^{esc}$ in $(E - V)/(2c^2)$ to give the relativistic Pauli approximation is appropriate when the classical velocity of the electrons is small compared to the speed of light. This breaks down for a nuclear Coulomb potential. Instead, following van Lenthe,[120,121] we expand in $1/(2c^2 - V)$, which is justified even near the singularity of a nuclear Coulomb potential, to lowest order to give the *zeroth-order regular approximation* (ZORA). This gives

$$\hat{H}^{esc} \approx V + \sigma \cdot \hat{\mathbf{p}}\frac{c^2}{2c^2 - V}\sigma \cdot \hat{\mathbf{p}} - \sigma \cdot \hat{\mathbf{p}}\frac{c^2}{2c^2 - V}\frac{E}{2c^2 - V}\sigma \cdot \hat{\mathbf{p}} + \ldots. \tag{3.76}$$

To lowest order the expansion of $\hat{O}$ in $1/(2c^2 - V)$ gives the identity, so we find that

the first two terms of Eqn. 3.76 are the ZORA Hamiltonian:

$$\hat{H}^{ZORA} = V + \frac{1}{2}\sigma \cdot \hat{\mathbf{p}}\mathcal{K}\sigma \cdot \hat{\mathbf{p}}, \tag{3.77}$$

where $\mathcal{K}$ effectively determines the local influence of relativity on the system (Fig. 3.3),

$$\mathcal{K} = \frac{2c^2}{2c^2 - V}. \tag{3.78}$$

It is known that ZORA describes valence states in many-electron systems well,[121,122] and core states less so. However, as valence states are the main contributors to J-coupling it should provide an appropriate level of theory for the present work.

Substituting the canonical momentum for a magnetic vector potential $\mathbf{A}$, $\hat{\mathbf{p}} \rightarrow \pi = \hat{\mathbf{p}} + \mathbf{A}$, and expanding we obtain the ZORA Hamiltonian in an EM field:

$$\hat{H}^{\mathrm{ZORA}} = \hat{V} + \frac{1}{2}(\hat{\mathbf{p}}\mathcal{K}\hat{\mathbf{p}} + \mathrm{i}\sigma(\hat{\mathbf{p}}\mathcal{K}) \times \hat{\mathbf{p}} \tag{3.79a}$$

$$+ \hat{\mathbf{p}}\mathcal{K}\mathbf{A} + \mathbf{A}\mathcal{K}\hat{\mathbf{p}} + \mathrm{i}\sigma\left[\hat{\mathbf{p}} \times (\mathcal{K}\mathbf{A}) + \mathbf{A} \times (\mathcal{K}\hat{\mathbf{p}})\right] \tag{3.79b}$$

$$+ \mathcal{K}\mathbf{A} \cdot \mathbf{A}) \tag{3.79c}$$

It can be observed that for $\mathcal{K} = 1$ the ZORA Hamiltonian reduces to the non-relativistic Levy–Leblond Hamiltonian[123] plus spin-orbit coupling. The right hand side of 3.79a corresponds to the EM-free ZORA Hamiltonian.

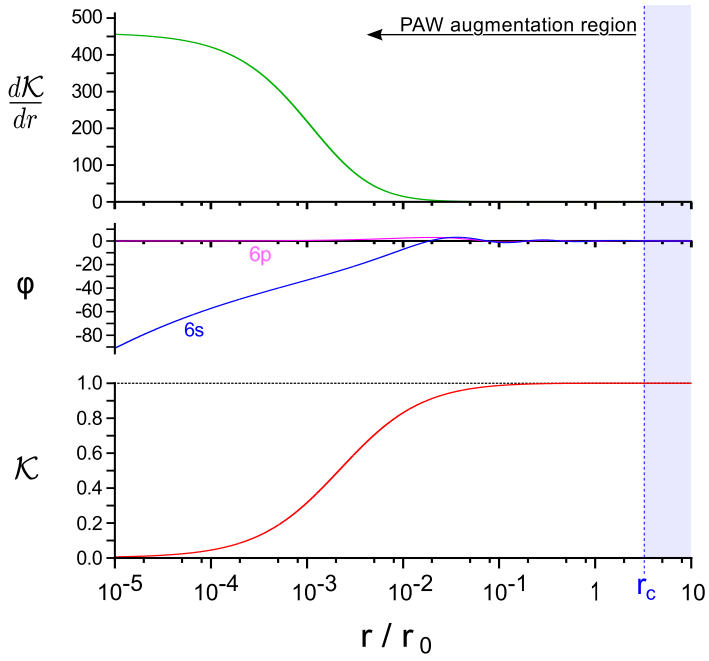

Figure 3.3: Plot of $\mathcal{K}(r)$, the 6s and 6p all-electron partial waves ϕ, and $\frac{\mathrm{d}\mathcal{K}}{\mathrm{d}r}$ for a scalar-relativistic lead atom. Note that $\mathcal{K}(r)$ quickly reaches unity and $\frac{\mathrm{d}\mathcal{K}}{\mathrm{d}r}$ quickly reaches zero for $r \ll r_c = 2.36a_0$, the pseudopotential cut off radius. Also note that only the 6s orbital has significant character in the region where $\frac{\mathrm{d}\mathcal{K}}{\mathrm{d}r} \gg 0$ while the 6p has none.

3.3 Prediction of NMR parameters

As all the interaction terms involved in NMR are weak, they can be treated as a perturbation to the ground state of the system. This means that DFT is a viable approach to their calculation. In addition, it would be desirable to be able to calculate NMR parameters in the solid-state using density functional theory with a plane-wave basis set and pseudopotentials. This would greatly improve the computational efficiency of the calculation and would allow straightforward treatment of infinite solids. There is a depth of literature on calculations of NMR parameters using local basis set methods,[10,124] so this will mainly concentrate on pseudopotential methods.

3.3.1 Magnetic shielding

To allow the treatment of extended systems with plane-wave basis sets, Mauri *et al.*[125] presented a method for ab-initio computation of NMR chemical shifts in periodic systems. This allows more efficient treatment of crystals, surfaces, polymers and non-periodic systems such amorphous solids and defects within supercells. Previously such studies were confined to molecules and clusters.

Mauri *et al.* describe the electron exchange-correlation with LSDA, ignoring current density contributions to the exchange-correlation energy. Previous studies[126] have found the contribution to be negligible. They also neglect errors caused by the difference between the pseudo-wave functions for the valence electrons in the core regions and the all-electron wave functions. As the pseudo-wave functions differ significantly from the all-electron wave functions in the core region, expectation values of operators in this region will be incorrect. They find that, with norm-conserving pseudopotentials, this error for first row elements is minor, but far from perfect, and gives good agreement with experiment for hydrogen, which is the least affected

by pseudopotential errors. Pickard and Mauri[5] corrected this ab-initio theory to properly take into account the nature of the pseudo-wave function near the nucleus.

In a magnetic field, translating the system by a vector $\mathbf{t}$ means the wave functions pick up a phase factor $\mathrm{e}^{(\mathrm{ic}/2)\mathbf{r}\cdot\mathbf{t}\times\mathbf{B}}$. Blöchl's original PAW method does not have the required translational invariance in a magnetic field. This means that, if the vector potential $\mathbf{A}$ is chosen in the symmetric gauge,

$$\mathbf{A} = \frac{1}{2}\mathbf{B} \times (\mathbf{r} - \mathbf{d}), \tag{3.80}$$

where $\mathbf{d}$ is the gauge origin, although the expectation values of observable operators do not depend on $\mathbf{d}$, the number of partial waves required to accurately describe the all-electron valence wave function does. A choice that places $\mathbf{d}$ at the centre of the augmentation region minimises the number of partial waves required. This is only possible in PAW when the system contains just one augmentation region.

Placing the translational phase factor into the PAW transformation operator, $\mathcal{T}$, restores exact translational invariance, allowing the presence of many augmentation regions while maintaining good convergence with respect to the number of partial waves used:

$$\mathcal{T}_B = 1 + \sum_n \mathrm{e}^{(\mathrm{ic}/2)\mathbf{r}\cdot\mathbf{R}\times\mathbf{B}}(|\psi_n\rangle - |\psi_n\rangle)\langle\tilde{p}_n|\mathrm{e}^{-(\mathrm{ic}/2)\mathbf{r}\cdot\mathbf{R}\times\mathbf{B}}. \tag{3.81}$$

This is the *gauge-including projector augmented-wave* (GIPAW) generalisation of the PAW transformation operator, introduced by Pickard and Mauri. This approach is related to the GIAO,[127] IGAIM[128] and IGLO[126] methods. Pickard and Mauri went on to demonstrate the theory and implementation within GIPAW of the prediction of NMR chemical shifts, treating the magnetic field as a perturbation using DFPT

and solved with conjugate-gradient minimisation. This gives a cost equivalent to calculating the electronic ground state.

Isotropic chemical shifts calculated using the GIPAW method gave good agreement with those calculated using the IGAIM approach. A comparison of the calculated quantities confirms the importance of the GIPAW corrections to the bare shielding.

3.3.2 Electric field gradients

Profeta *et al.*[129] developed a method for the calculation of EFG tensors in a plane-wave basis set, also using PAW. The EFG tensor at spatial position $\mathbf{r}$ is determined by the total charge density:

$$G_{\alpha\beta}(\mathbf{r}) = \int \mathrm{d}\mathbf{r}' \, \frac{n(\mathbf{r}')}{|\mathbf{r}-\mathbf{r}'|^3} \left[\delta_{\alpha\beta} - 3\frac{(r_\alpha - r'_\alpha)(r_\beta - r'_\beta)}{|\mathbf{r}-\mathbf{r}'|^2} \right]. \tag{3.82}$$

The density is a sum of ionic and electronic densities,

$$n(\mathbf{r}) = n^{\mathrm{ION}}(\mathbf{r}) + n^{\mathrm{El}}(\mathbf{r}), \tag{3.83}$$

where the ionic charge distribution is

$$n^{\mathrm{ION}}(\mathbf{r}) = \sum_n Z_n \delta(\mathbf{r} - \mathbf{R}_n) \tag{3.84}$$

and $n^{\mathrm{El}}(\mathbf{r})$ is the electronic charge distribution, calculated using a plane-wave pseudopotential approach. In a calculation using pseudopotentials the charge density near the nucleus differs from the true-all electron value. As Profeta *et al.* determined, correcting this is particularly import for calculation of the EFG as it is sensitive to

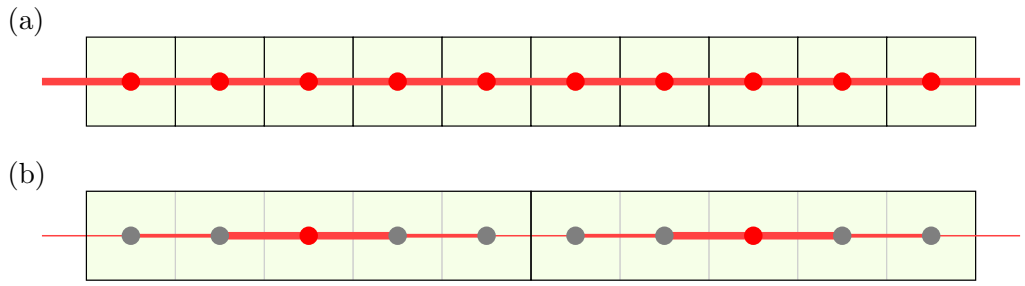

Figure 3.4: Illustration of a J-coupling perturbing site (dark red) in a one-dimensional system and its periodic images with lines showing the coupling strength in (a) a small unit cell, and (b) a supercell of five unit cells, demonstrating the need for a supercell when periodic images are too close to ensure proper decay of the coupling.

the charge density around the nucleus. Their solution was to augment the density with PAW:

$$n^{\text{El}}(\mathbf{r}) = n^{\text{El-PS}}(\mathbf{r}) + n^{\text{El-AUG}}(\mathbf{r}). \tag{3.85}$$

The PAW augmentation charge, $n^{\text{El-AUG}}$, is

$$n^{\text{El-AUG}}(\mathbf{r}) = 2 \sum_{\mathbf{R},o,n,m} \langle \tilde{\psi}_o | p_{\mathbf{R},m} \rangle \left[\langle \phi_{\mathbf{R},m} | \mathbf{r} \rangle \langle \mathbf{r} | \phi_{\mathbf{R},n} \rangle - \langle \tilde{\phi}_{\mathbf{R},m} | \mathbf{r} \rangle \langle \mathbf{r} | \tilde{\phi}_{\mathbf{R},n} \rangle \right] \langle p_{\mathbf{R},n} | \tilde{\psi}_o \rangle. \tag{3.86}$$

When using ultrasoft pseudopotentials, the ultrasoft augmentation charge for the atomic site $\mathbf{R}$ must be subtracted from the pseudo-density before adding the PAW augmentation at $\mathbf{R}$.

3.3.3 J-coupling

To enable the use of plane-wave basis sets in the calculation of NMR J-coupling, Joyce *et al.*[13] developed a method to calculate J-coupling parameters using pseudopotentials with the PAW method to reconstruct all-electron core properties.

The reduced J-coupling tensor $K_{A,B}$ is the magnetic field at the site of nucleus B caused by a magnetic moment at nucleus A. In order to calculate the magnetic field, first the electronic current density, $\mathbf{j}(\mathbf{r})$, and spin density, $\mathbf{m}(\mathbf{r})$, induced by nucleus K are calculated and then the magnetic field created by the current and spin density at every nuclear position in the system is calculated. A more detailed explanation is given in Chapter 4, including the PAW augmentation of the perturbation operators.

As we are using periodic boundary conditions, we must use a supercell of sufficient size[130] to ensure decay of the induced quantities within the cell and prevent a perturbation from interacting with its periodic images, as shown in Fig. 3.4.

Joyce goes on to compare the new method to pre-existing quantum-chemical methods, finding good agreement with experiment and favourable comparison to more computationally expensive methods (Fig 3.5).

3.3.4 Relativistic effects in NMR

As noted, it has been found that the inclusion relativistic effects can be important for the prediction of NMR parameters in systems containing heavy nuclei. In Ref. 113 Visscher *et al.* perform full, four-component calculations on a range of hydrogen halides, HF to HI, and find the importance of including relativistic spin-orbit effects for correctly predicting the halogen magnetic shielding trend. In addition, relativistic effects are found to be important in the prediction of the isotropic J-coupling.

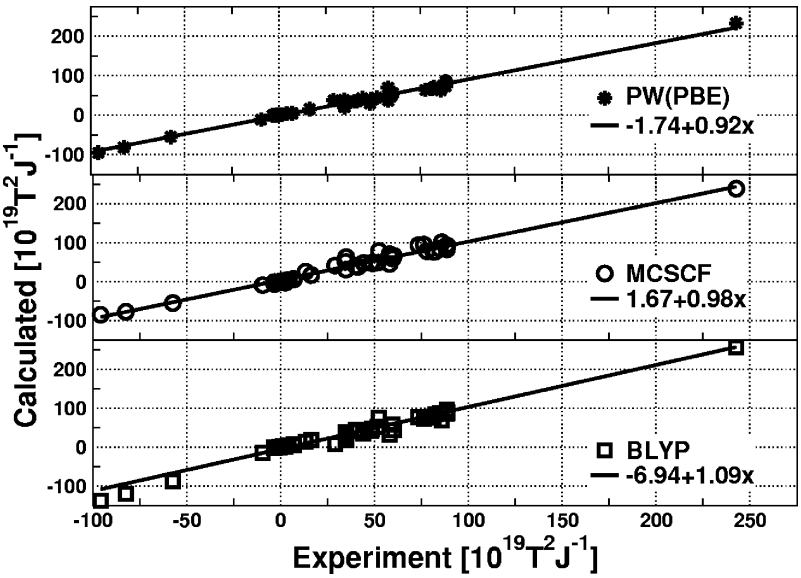

Figure 3.5: Comparison of experimentally measured J-couplings to J-couplings calculated with the plane-wave pseudopotential method using the PBE exchange-correlation functional, 'PW(PBE)', and to MCSCF and BLYP results for a range of molecules. [Reprinted with permission from Ref. 13. Copyright 2007, AIP Publishing LLC.]

Autschbach *et al.* outlines in Ref. 22 the theory of the calculation of J-coupling for heavy elements, including relativity at the ZORA scalar-relativistic level, finding that for some couplings the correction can be of the same magnitude as the original non-relativistic coupling. The method is benchmarked again in Ref. 116 for a wide range of sixth row element containing molecules, along with the effects of hybrid functionals, finding a good level of agreement at the scalar-relativistic ZORA level but that spin-orbit effects can be important in some elements, for example thallium, though giving less improvement than the use of hybrid functionals.

Wodyński *et al.* also finds in Ref. 131 that relativistic effects are important in the calculation of shieldings and J-coupling for sixth row elements, comparing non-relativistic theory, four-component Dirac–Kohn–Sham (DKS) DFT and two component ZORA calculations. They find that, for the heavy metal shieldings, two-

component ZORA calculations recover roughly between 75% and 90% of the DKS result, while there is a smaller discrepancy between ZORA and DKS J-couplings.

3.4 Applications of plane-wave DFT to NMR

Although a fairly recently developed method, plane-wave pseudopotential DFT has been used to predict NMR parameters in a wide range of systems.[14,17,132–143] An extensive review is available in Ref. 6, here we shall concentrate on applications of PAW J-coupling. Two examples are outlined below, showing the typical process and insights given into the theory and experiment.

In Ref. 14 Joyce *et al.* applied the J-coupling PAW method to the calculation of hydrogen bond mediated J-couplings in two 6-aminofulvene-1-aldimine derivatives, pyrrole and triazole. By making use of an inherently periodic solid-state method, the difficulty in determining an adequate cluster, as is necessary in standard quantum-chemical methods, is avoided. There have been previous quantum-chemical studies into the differences in intramolecular hydrogen bonding, but only on a smaller scale than the systems examined by Joyce.[144,145]

A full geometry relaxation was performed on the given structures. These optimised structures were then used to calculate the J-coupling with the `Castep` plane-wave DFT code,[146] using norm-conserving Troullier–Martins pseudopotentials and the PBE functional. The plane-wave energy cut-off was converged with J-coupling to 80 Ry, similar to other investigations, with an error of ± 0.1 Hz.

The calculated crystal results were then compared to MAS INADEQUATE NMR experiments, showing good agreement. The isolated molecule results were also compared to solution-state experiments, showing reasonable agreement, though differences are expected due to solvent effects.[147,148]

In order to determine the role of long-range electrostatic effects in the crystal, they also compare the effects of taking an unrelaxed molecule from the structure and calculating the J-coupling in a vacuum and relaxing the same molecule and calculating the J-coupling in a vacuum. It is expected that the relaxed structure corresponds better to the solution-state experiment as the molecule in the crystal will be hindered by its neighbours. Comparing the crystal, relaxed and unrelaxed calculations will determine the contributions from J-coupling arising from local structural differences and the contributions from crystal interactions.

For the one-bond couplings between nitrogen nuclei in the pyrrole and triazole structures there was little difference found in the couplings between the constrained and relaxed molecules, but there is a 0.5 Hz increase between the constrained molecule and the full crystal, which might be ascribed to long-range electrostatic effects. For the two-bond couplings it is found that both structural and long-range effects are present, possibly due to change in the hydrogen bond length and angle. It is concluded that there is about a 0.9 Hz average difference compared to experiment in J-coupling across the structures when including long-range effects or not, compared to about 0.3 Hz, within experimental error, for the full crystal structure in general.

It is thus apparent that proper treatment of crystal effects is necessary for the accurate prediction of J-couplings in solid-state systems, and that changes in molecular structure are insufficient. Noted is that one calculation, of guanosine ribbons, contained 192 atoms, in excess of anything previously examined in quantum-chemical investigations, demonstrating the value of the plane-wave pseudopotential method for big systems. Also noted is the value of comparing solid-state experiments and calculations when evaluating techniques, as uncontrolled solvent effects make the standard technique of comparing solution-state and vacuum calculations potentially unreliable.

Another PAW J-coupling investigation was performed by Bonhomme *et al.*[16] in to a number of phosphates. Some of the structures were experimental, and some of them were relaxed from experimental structures using DFT. For J-coupling some structures required supercells of varying sizes to ensure that periodic images of the perturbation did not interact.

Excellent agreement (± 0.70 ppm RMS error compared to experiment) is found for prediction of the chemical shifts, and it is suggested that for unknown structures it is reasonable to use the calculations as a constraint for structural determination. It was found that the calculated J-coupling constants are also consistent with data from the INEPT experiment, validating the structural models.

Chapter 4

J-coupling with ultrasoft pseudopotentials

4.1 NMR J-coupling theory

As a starting point we will use the method of Joyce *et al.*[12,13] for the calculation of NMR J-coupling tensors using plane-wave pseudopotential DFT. This method has been validated for a small number of systems containing light atoms against quantum chemical calculations and against experimental data.[14–18] This method was originally implemented to use norm-conserving pseudopotentials. As these can be tricky to construct, use, and limit the ability to include semi-core atomic orbitals explicitly as valence electrons, it is preferable to be able to use state-of-the-art ultrasoft pseudopotentials as first developed by Vanderbilt.[19] The relaxation of the norm-conserving constraint reduces the highest necessary plane-wave frequency in the basis-set, $|\mathbf{G}_{\max}|$, and allows more robust construction of pseudopotentials, especially when including semi-core atomic states in the valence, at the expense of

complicating the theory and implementation.

As explained in Chapter 3, following Ramsey's second-order perturbation analysis,[32,33] the reduced spin coupling tensor K^{AB}, between nuclei A and B, can be expressed as a second derivative of the system energy with respect to the two interacting nuclear moments, $\boldsymbol{\mu} = \gamma\hbar\mathbf{I}$, where γ is the nucleus' gyromagnetic ratio and $\mathbf{I}$ is the nucleus' spin:

$$K^{AB} = \left.\frac{\partial^2 E}{\partial\boldsymbol{\mu}_A\partial\boldsymbol{\mu}_B}\right|_{\boldsymbol{\mu}_N=0\forall N} \tag{4.1}$$

We can then express the observed J tensor in terms of the reduced spin coupling tensor, $J^{AB} = \frac{\hbar}{2\pi}\gamma_A\gamma_B K^{AB}$.

For our system of nuclear dipole moments the magnetic vector potential is, in the symmetric gauge with ($\mathbf{r}_N = \mathbf{r} - \mathbf{R}_N$), $\mathbf{A} = \sum_N \alpha^2 \frac{\boldsymbol{\mu}_N \times \mathbf{r}_N}{|\mathbf{r}_N|^3}$, where α is the fine-structure constant. Determining the derivatives of the Schrödinger Hamiltonian in this $\mathbf{A}$-field with respect to the interacting nuclear magnetic moments will allow us to use second-order perturbation theory to calculate K^{AB}:

$$E^{(1,1)} = 2\,\mathrm{Re}\langle\psi^{(0,1)}|\hat{H}^{(1,0)}|\psi^{(0,0)}\rangle + \langle\psi^{(0,0)}|\hat{H}^{(1,1)}|\psi^{(0,0)}\rangle, \tag{4.2}$$

using superscripts to represent order of perturbation with respect to the perturbation parameters $\boldsymbol{\mu}_A$ and $\boldsymbol{\mu}_B$:

$$X^{(n,m)} = \left(\frac{\partial}{\partial\boldsymbol{\mu}_A}\right)^n \left(\frac{\partial}{\partial\boldsymbol{\mu}_B}\right)^m X\Bigg|_{\boldsymbol{\mu}_N=0\forall N}. \tag{4.3}$$

It was found by Ramsey,[32,33] when neglecting spin-orbit coupling, that the induced

field is caused by two mechanisms. The first is the nuclear magnetic moment interacting with the charge density to create orbital currents, which in turn create a magnetic field. The second is the nuclear magnetic moment inducing an electronic spin polarisation. This spin density then creates a magnetic field.

The relevant derivatives of the Schrödinger equation in the **A**-field are:

$$\hat{H}^{(1,1)}_{\text{dia};i,j} = \alpha^4 \frac{\delta_{ij}(\mathbf{r}_A \cdot \mathbf{r}_B) - \mathbf{r}_{A;i}\mathbf{r}_{B;j}}{|\mathbf{r}_A|^3 |\mathbf{r}_B|^3}, \tag{4.4a}$$

which is the diamagnetic current term and

$$\hat{H}^{(1,0)}_{\text{para};i} = \frac{\alpha^2}{2\text{i}} \left[\frac{1}{|\mathbf{r}_A|^3} (\mathbf{r}_A \times \nabla)_i + (\mathbf{r}_A \times \nabla)_i \frac{1}{|\mathbf{r}_A|^3} \right] \tag{4.5a}$$

$$= \frac{\alpha^2}{\text{i}} \frac{1}{|\mathbf{r}_A|^3} (\mathbf{r}_A \times \nabla)_i, \tag{4.5b}$$

which is the paramagnetic current term, which combine to make the orbital current contribution;

$$\hat{H}^{(1,0)}_{\text{FC};i} = \frac{4\pi\alpha^2}{3} \sigma_i \delta(\mathbf{r}_A), \tag{4.6a}$$

which is the Fermi-contact (FC) term and

$$\hat{H}^{(1,0)}_{\text{SD};i} = \frac{\alpha^2}{2} \left(\frac{3(\sigma \cdot \mathbf{r}_A)\mathbf{r}_{A;i}}{|\mathbf{r}_A|^5} - \frac{\sigma_i}{|\mathbf{r}_A|^3} \right), \tag{4.7a}$$

which is the spin-dipolar (SD) term, which combine to make the spin magnetisation contribution, with $\mathbf{r}_A$ the displacement vector to nucleus A, σ the Pauli spin operator. The FC and SD terms give rise to the spin magnetisation density and the diamagnetic and paramagnetic terms give rise to the induced current.

We can now proceed to calculate K by separating it into contributions from the interactions of the nuclear magnetic moments mediated by the electron spin, K^{spin}, Eqns. 4.6 and 4.7, and from the interactions of the nuclear magnetic moments mediated by the electron charge current, K^{orb}, Eqns. 4.4 and 4.5.

4.1.1 Spin magnetisation

To calculate the contribution from the electron spin density to K, K^{spin}, we first find an expression for the magnetisation induced by a perturbing nuclear moment. From this we can compute the magnetic field induced at all of the other nuclei in the system.

We take the wave function to be a product of spin-restricted independent electron orbitals ψ, with a spin index σ. The magnetisation induced by a nuclear magnetic moment aligned along the $\mathbf{u}_j$ direction, $\mathbf{m}_j$, is calculated by summing the magnetisation induced when applying the perturbation with the spin quantised along each direction $\mathbf{u}_k$.

$$\mathbf{m}_j(\mathbf{r}) = \sum_k m_{jk}(\mathbf{r})\mathbf{u}_k \tag{4.8}$$

where $m_{jk}(\mathbf{r})$ is given by

$$m_{jk}(\mathbf{r}) = 4g\beta \sum_o \langle \psi^{(1)}_{o\uparrow jk} | \mathbf{r} \rangle \langle \mathbf{r} | \psi^{(0)}_{o\uparrow} \rangle, \tag{4.9}$$

and the first order response in the wave function, $|\psi^{(1)}_{o\sigma jk}\rangle$, is given by

$$|\psi^{(1)}_{o\sigma jk}\rangle = \mathcal{G}(\epsilon)|\psi^{(0)}_{o\sigma}\rangle. \tag{4.10}$$

$\mathcal{G}(\epsilon)$ is Green's function,

$$\mathcal{G}(\epsilon) = \sum_e \frac{|\psi^{(0)}_e\rangle\langle\psi^{(0)}_e|}{\epsilon_o - \epsilon_e}(\hat{H}^{(0,1)}_{\mathrm{spin};j} + \hat{H}^{(1)}_{\mathrm{xc}}), \tag{4.11}$$

where ϵ_o and ϵ_e are the eigenvalues of the occupied and empty bands respectively, $\sum_e$ is a sum over empty bands and $\hat{H}^{(1)}_{\mathrm{xc}}$ is the self-consistent first order variation in the Kohn–Sham exchange-correlation potential due to the first order change in the spin density:

$$\hat{H}^{(1)}_{\mathrm{xc}} = V^{(1)}_{\mathrm{xc}}[m^{(1)}], \tag{4.12}$$

where $m^{(1)}$ is the first order magnetisation. We evaluate $V^{(1)}_{\mathrm{xc}}[m^{(1)}]$ with a numerical derivative:

$$V^{(1)}_{\mathrm{xc}}[m^{(1)}] = \frac{V_{\mathrm{xc}}[n^{(0)}, \lambda m^{(1)}] - V_{\mathrm{xc}}[n^{(0)}, -\lambda m^{(1)}]}{2\lambda}, \tag{4.13}$$

noting that $n^{(1)} = 0$ and $m^{(0)} = 0$.

As there is a first-order change in the Hamiltonian, we solve Eqn. 4.10 self-consistently by iteration.

Given the first order variation in the wave functions, the full expression for the spin

term contribution to K is, with an implicit rotation over the spin axes,

$$K_{ij}^{\text{spin}} = 2\text{Re}\sum_{o,\sigma}\int \mathrm{d}\mathbf{r}\ \psi_o^{(0)}(\mathbf{r})^\dagger \hat{H}_{\text{spin};i}^{(1,0)}\psi_{o\sigma j}^{(1)}(\mathbf{r}). \tag{4.14}$$

We can rearrange this expression to get the effective spin coupling in terms of the induced magnetisation, including an implicit rotation over the spin axes,

$$K_{ij}^{\text{spin}} = \alpha^2\int \mathrm{d}\mathbf{r}\ \left[\left(\frac{3\mathbf{r}_{A;i}\mathbf{r}_{A;j} - |\mathbf{r}_A|^2\delta_{ij}}{|\mathbf{r}_A|^5}\right) + \frac{8\pi}{3}\delta(\mathbf{r})\right]\mathbf{m}_j(\mathbf{r}). \tag{4.15}$$

4.1.2 Current density

To calculate the contribution from the electron charge current density, K^{orb}, we first find an expression for the current density induced by a perturbing nuclear moment and subsequently the magnetic field induced at the receiving magnetic moment. As with the induced magnetisation, we can calculate the induced magnetic field at all the receiving nuclei from this induced current density.

To first order the current perturbation term, $\hat{H}_{\text{para},j}^{(0,1)}$, does not modify the magnetisation or the charge density so there is no first order change in the self-consistent potential. The first order variation in the orbitals is therefore

$$|\psi_{oj}^{(1)}\rangle = \mathcal{G}(\epsilon)|\psi_o^{(0)}\rangle, \tag{4.16}$$

where $\mathcal{G}(\epsilon)$ is Green's function,

$$\mathcal{G}(\epsilon) = \sum_e \frac{|\psi_e^{(0)}\rangle\langle\psi_e^{(0)}|}{\epsilon_o - \epsilon_e}\hat{H}_{\text{para};j}^{(0,1)}, \tag{4.17}$$

in which ϵ_o and ϵ_e are the eigenvalues of the occupied and empty bands respectively and $\sum_e$ is a sum over empty bands.

From second order perturbation theory we can write down K^{orb}:

$$\begin{aligned} K_{ij}^{\mathrm{orb}} = \sum_{o,\sigma} \int \mathrm{d}\mathbf{r}\, \psi_o^{(0)}(\mathbf{r})^\dagger \hat{H}_{\mathrm{para};i}^{(1,0)} \psi_{oj}^{(1)}(\mathbf{r}) + c.c. \\ + \psi_o^{(0)}(\mathbf{r})^\dagger \hat{H}_{\mathrm{dia},ij}^{(1,1)} \psi^{(0)}(\mathbf{r}). \end{aligned} \tag{4.18}$$

From the first order variation in the orbitals we can re-arrange Eqn. 4.18 to find the induced current:

$$\mathbf{j}_j^{(1)}(\mathbf{r}) = 2 \sum_o \left[2\,\mathrm{Re}\langle \psi_o^{(0)} | \mathbf{J}^{\mathrm{P}}(\mathbf{r}) | \psi_{oj}^{(1)} \rangle + \langle \psi_o^{(0)} | \mathbf{J}_j^{\mathrm{D}}(\mathbf{r}) | \psi_o^{(0)} \rangle \right], \tag{4.19}$$

where our modified paramagnetic and diamagnetic current operators have the form

$$\mathbf{J}^{\mathrm{P}}(\mathbf{r}) = -(\hat{\mathbf{p}}|\mathbf{r}\rangle\langle\mathbf{r}| + |\mathbf{r}\rangle\langle\mathbf{r}|\hat{\mathbf{p}})/2 \tag{4.20}$$

$$\mathbf{J}_j^{\mathrm{D}}(\mathbf{r}) = -\alpha^2 \frac{\mathbf{r}_B \times \hat{\mu}^j}{|\mathbf{r}_{kB}|^3} \tag{4.21}$$

and so the orbital current contribution to K is simply the Biot–Savart law acting on the induced current:

$$K_{ij}^{\mathrm{orb}} = \alpha^2 \int \mathrm{d}\mathbf{r} \left(\mathbf{j}_j^{(1)}(\mathbf{r}) \times \frac{\mathbf{r}_A}{|\mathbf{r}_A|^3} \right)_i. \tag{4.22}$$

4.1.3 Ultrasoft pseudopotential augmentation

The majority of the J-coupling methodology developed by Joyce *et al.*[12,13] is still valid for ultrasoft pseudopotentials, as the PAW formulation made no assumption regarding the norm of the partial waves used in the PAW transformation. However, changes are required when computing the first order induced current and magnetisation. Firstly, we note that to avoid a costly sum over unoccupied states the first-order change in the wave functions is computed using a conjugate-gradient minimisation.[13] For ultrasoft pseudopotentials the minimisation routines must be adapted to allow for the generalised orthonormality condition, Eqn. 3.54. This can be done straight-forwardly following the method outlined in Appendix B of Ref. 149. Secondly, care must be taken in computing the induced magnetisation. Following the ultrasoft charge density in Eqn. 3.59 we introduce the magnetisation $\bar{m}^{(1)}$

$$\bar{m}^{(1)}(\mathbf{r}) = 2\sum_{o}[\psi_o^{*(1)}(\mathbf{r})\psi_o^{(0)}(\mathbf{r}) + c.c. \tag{4.23}$$

$$+ \sum_{\mathbf{R},n,m} \tilde{Q}_{\mathbf{R},nm}(\mathbf{r}) \left(\langle p_{\mathbf{R},n}|\psi_o^{(1)}\rangle\langle\psi_o^{(0)}|p_{\mathbf{R},m}\rangle + c.c. \right)] \tag{4.24}$$

In addition, the self-consistent exchange-correlation term, Eqn. 4.12, should also be augmented to reflect the first order change in the D matrix (Eqn. 3.56):[150]

$$\hat{H}_{\mathrm{xc}}^{(1)} = V_{\mathrm{xc}}^{(1)}[\bar{m}^{(1)}] + \sum_{\mathbf{R},n,m} |p_{\mathbf{R},n}\rangle \left[\int \mathrm{d}\mathbf{r}\; V_{\mathrm{xc}}^{(1)}[\bar{m}^{(1)}](\mathbf{r})\tilde{Q}_{\mathbf{R},nm}(\mathbf{r}) \right] \langle p_{\mathbf{R},m}|. \tag{4.25}$$

4.2 J-coupling with PAW

Unlike the calculation of NMR magnetic shielding, which requires the use of GIPAW to preserve translational invariance in a magnetic field,[5] the calculation of J-coupling can use a gauge fixed on the perturbing atom and so only standard PAW is required. We can now apply the PAW operator transformation to the derived non-relativistic J-coupling operators in order to get the pseudo-operators.

4.2.1 Spin magnetisation contribution

In the case of the spin contribution, the sharply localised FC perturbation operator can be written entirely inside augmentation as

$$\widetilde{H}^{(1,0)}_{\mathrm{FC}} = \sum_{\mathbf{R},n,m} |p_{\mathbf{R},n}\rangle\langle\phi_{\mathbf{R},n}|\hat{H}^{(1,0)}_{\mathrm{FC}}|\phi_{\mathbf{R},m}\rangle\langle p_{\mathbf{R},m}|, \tag{4.26}$$

where we have used the on-site approximation. As the FC operator is a Dirac delta function, this simply reduces to sampling the electron spin density at the nucleus.

The SD PAW augmentation is evaluated on a real radial grid, while the un-augmented contribution is calculated in Fourier space from the ultrasoft augmented magnetisation.

$$\widetilde{H}^{(1,0)}_{\mathrm{SD}} = \hat{H}^{(1,0)}_{\mathrm{SD}} + \Delta\hat{H}^{(1,0)}_{\mathrm{SD}}, \tag{4.27}$$

where, using the on-site approximation again,

$$\Delta\hat{H}^{(1,0)}_{\mathrm{SD}} = \sum_{\mathbf{R},n,m} |p_{\mathbf{R},n}\rangle(\langle\phi_{\mathbf{R},n}|\hat{H}^{(1,0)}_{\mathrm{SD}}|\phi_{\mathbf{R},m}\rangle - \langle\tilde{\phi}_{\mathbf{R},n}|\hat{H}^{(1,0)}_{\mathrm{SD}}|\tilde{\phi}_{\mathbf{R},m}\rangle)\langle p_{\mathbf{R},m}|.$$

The total spin contribution to the reduced coupling tensor is then

$$K^{\mathrm{spin}} = \tilde{K}^{\mathrm{spin}} + \Delta K^{\mathrm{spin}} \tag{4.28}$$

$$\tilde{K}^{\mathrm{spin}} = -\frac{\mu_0}{3}\int \mathrm{d}\mathbf{G}\left[\frac{3(\bar{\mathbf{m}}^{(1)}(\mathbf{G})\cdot\mathbf{G})\mathbf{G} - \bar{\mathbf{m}}^{(1)}(\mathbf{G})G^2}{G^2}\right] e^{\mathrm{i}\mathbf{G}\cdot\mathbf{r}_A} \tag{4.29}$$

$$\Delta K^{\mathrm{spin}} = \sum_{oo'\sigma\sigma'} \langle\psi^{(0)}_{o\sigma}|\widetilde{H}^{(1,0)}_{\mathrm{FC}} + \Delta\hat{H}^{(1,0)}_{\mathrm{SD}}|\psi^{(1)}_{o'\sigma'}\rangle, \tag{4.30}$$

where $\bar{\mathbf{m}}^{(1)}(\mathbf{G})$ is the ultrasoft augmented spin density in reciprocal space, to which we apply the spin dipole operator and slow Fourier transform at the position of the receiving nucleus

When computing Eqn. 4.29 using $\bar{\mathbf{m}}^{(1)}(\mathbf{r})$, in order to capture off-site contributions to the spin-dipolar contribution, care should be taken to subtract from every receiving atom the on-site contribution from the ultrasoft augmentation charge so as not to double count with the PAW on-site augmentation, as shown in Fig. 4.1.

4.2.2 Orbital current contribution

The diamagnetic current operators do not receive PAW augmentation, as we cannot make the off-site approximation due to the complexity of calculating the relevant matrix elements, and so only contribute to the bare current. This has the effect of

ignoring the diamagnetic augmented current, although as the diamagnetic contribution is the smallest J-coupling component it may only be really relevant for the calculation of anisotropic couplings.[151]

The PAW augmented paramagnetic operator is

$$\tilde{H}^{(1,0)}_{\text{para}} = \hat{H}^{(1,0)}_{\text{para}} + \Delta\hat{H}^{(1,0)}_{\text{para}} \tag{4.31}$$

$$\Delta\hat{H}^{(1,0)}_{\text{para}} = \sum_{\mathbf{R},n,m} |p_{\mathbf{R},n}\rangle(\langle\phi_{\mathbf{R},n}|\hat{H}^{(1,0)}_{\text{para}}|\phi_{\mathbf{R},m}\rangle \tag{4.32}$$

$$- \langle\tilde{\phi}_{\mathbf{R},n}|\hat{H}^{(1,0)}_{\text{para}}|\tilde{\phi}_{\mathbf{R},m}\rangle)\langle p_{\mathbf{R},m}|. \tag{4.33}$$

The bare contribution of the paramagnetic current is calculated in Fourier space on the pseudo-current density and is PAW augmented on a real radial grid with an on-site approximation, justified by the short-rangeness of the interaction. The total orbital current contribution is then

$$K^{\text{orb}} = \tilde{K}^{\text{orb}} + \Delta K^{\text{orb}} \tag{4.34}$$

$$\tilde{K}^{\text{orb}} = \mu_0 \int \mathrm{d}\mathbf{G}\, \frac{\mathrm{i}\mathbf{G} \times \tilde{\mathbf{j}}^{(1)}(\mathbf{G})}{G^2} e^{\mathrm{i}\mathbf{G}\cdot\mathbf{r}_A} \tag{4.35}$$

$$\Delta K^{\text{orb}} = 2\,\mathrm{Re}\sum_{oo'\sigma}\langle\psi^{(0)}_{o\sigma}|\Delta\hat{H}^{(1,0)}_{\text{para}}|\psi^{(1)}_{o'\sigma}\rangle, \tag{4.36}$$

where $\tilde{\mathbf{j}}^{(1)}(\mathbf{G})$ is the un-augmented induced current density, paramagnetic and diamagnetic, in Fourier space, to which we apply the Biot–Savart law in reciprocal space and slow Fourier transform at the position of the receiving nucleus.

The total indirect coupling tensor between the two nuclei is then the sum of K^{spin}

and K^{orb}.

4.2.3 PAW degree of freedom

Blöchl notes that there is a degree of freedom in Eqn. 3.63 to add a term of the form

$$\hat{B} - \sum_{ij} |p_i\rangle\langle\tilde{\phi}_i|\hat{B}|\tilde{\phi}_j\rangle\langle p_j|, \tag{4.37}$$

where $\hat{B}$ is an arbitrary local operator acting solely within the augmentation region. We might describe an all electron operator $\hat{O}$ in terms of a 'fictitious' operator $\hat{O}_{\mathrm{fict}}$ and a 'real' operator $\hat{O}_{\mathrm{real}}$, which are equal outside the augmentation region:

$$\hat{O} = \hat{O}_{\mathrm{fict}} + f(r)(\hat{O}_{\mathrm{real}} - \hat{O}_{\mathrm{fict}}), \tag{4.38}$$

where $f(r)$ is a cutoff function which is unity for $r < r_c$ and zero otherwise and so $\hat{B} = \hat{O}_{\mathrm{real}} - \hat{O}_{\mathrm{fict}}$. If we apply the PAW operator transform to $\hat{O}$ (Eqn. 3.63) and add Eqn. 4.37 we find:

$$\widetilde{O} = \hat{O}_{\mathrm{fict}} + \sum_{ij} |p_i\rangle(\langle\phi_i|\hat{O}_{\mathrm{real}}|\phi_j\rangle - \langle\tilde{\phi}_i|\hat{O}_{\mathrm{fict}}|\tilde{\phi}_j\rangle)\langle p_j|. \tag{4.39}$$

This allows us to substitute a new operator $\hat{O}_{\mathrm{fict}}$, which is easier to numerically represent, for the pseudo calculation, so long as it is equal to the real operator, $\hat{O}_{\mathrm{real}}$, outside the augmentation region, and perform the correction in the PAW augmentation. Blöchl goes on to use this freedom to set pseudopotential theory within the PAW formalism by substituting the real nuclear Coulomb potential of an atom for a smoothed fictitious potential that is more amenable for evaluation in a

plane-wave basis set.

We can use this technique to better represent the radially divergent part of the magnetic dipole perturbation, $\frac{1}{r^3}$, which when naïvely applied in real space is ill-represented on the Cartesian grid, leading to varying numerical predictions depending on the relative position of the perturbing nucleus to the real space grid. We replace it with a smoothed term,

$$\hat{O}_{\text{fict}} = \frac{1 - \exp(-(r/r_0)^3)}{r^3}, \tag{4.40}$$

plotted in Fig. 4.2, which is well represented on a coarser real-space grid and make the correction using Eqn. 4.39 during PAW augmentation. This function was chosen to smoothly tend towards a small, finite number for small r and exponentially converge to $\frac{1}{r^3}$ for $r > r_0$. As we can only modify the operator within the PAW augmentation region, the error in the approximation should be as close to zero as possible when $r = r_c$, plotted in Fig. 4.3 in terms of r_0. However, a smaller r_0 will mean a ficticious operator that is sharper and more difficult to represent on a real grid. We should hence choose r_0 so as to minimise the numerical error relative to both the pseudopotential radius and real grid spacing.

4.3 Calculations

The methodology as proposed has been implemented in the `Castep` plane wave DFT code[146] with ultrasoft pseudopotentials.[19,99] Modifications were needed to address the issues mentioned in Section 4.1.3. In addition, PAW is also used to smooth the dipole operator and reconstruct it in real space to provide greater numerical stability with respect to real grid spacing, as described in Section 4.2.3.

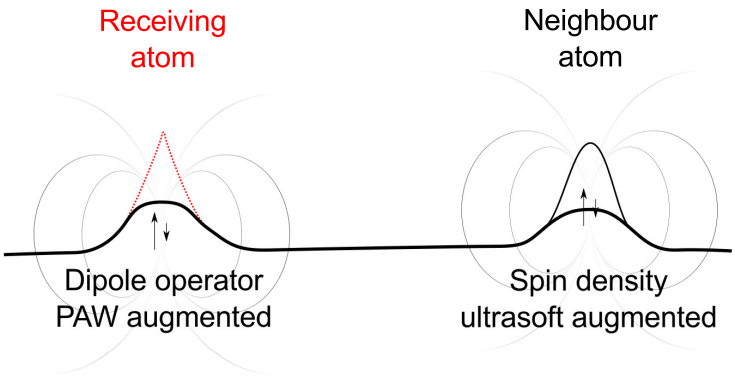

Figure 4.1: Illustration of on-site PAW augmentation and off-site ultrasoft augmentation of the spin magnetisation.

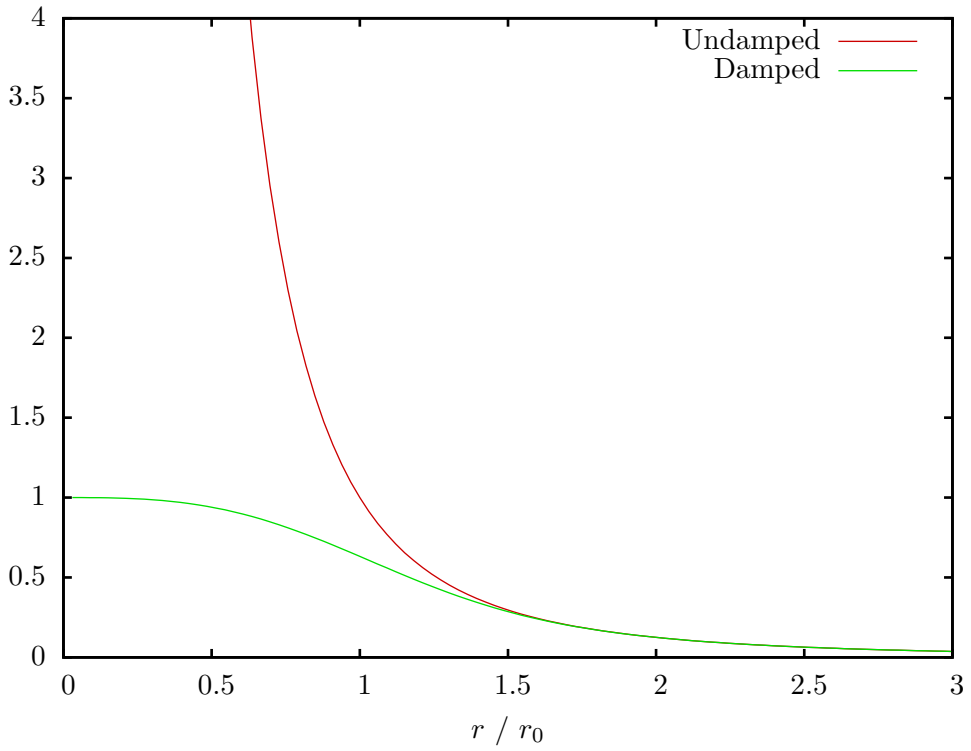

Figure 4.2: Illustration of the damped radial dipole component, $\frac{1-\exp(-(r/r_0)^3)}{r^3}$, versus the undamped radial component, $\frac{1}{r^3}$, as a function of $\frac{r}{r_0}$, in units of $\frac{1}{r_0^3}$.

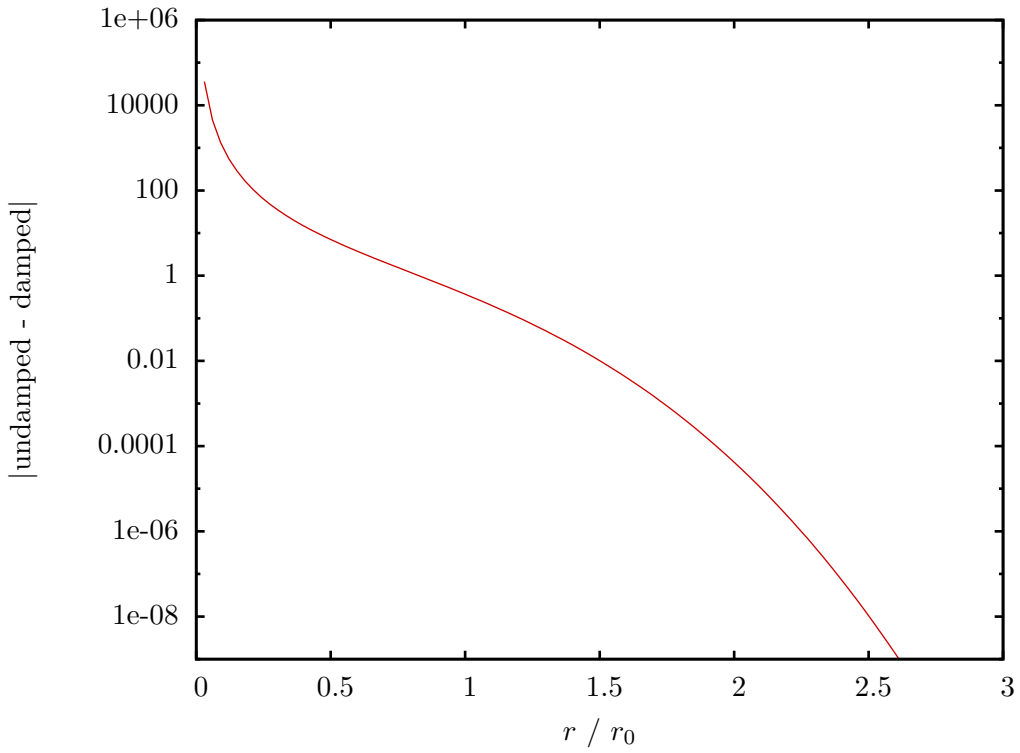

Figure 4.3: Illustration of the difference between radial components of the undamped dipole and the damped dipole as a function of $\frac{r}{r_0}$, in units of $\frac{1}{r_0^3}$. One should choose r_0 such that there is a satisfactorally low error beyond r_c.

4.3.1 Energy and grid scale convergence

One must systematically converge the numerical parameters of a calculation in order to achieve a desired level of numerical precision. Fig. 4.4 shows the convergence of the calculated ^{1}J(C−C) coupling in C_2H_4 as a function of the cut-off energy used, i.e. the energy corresponding to the highest frequency of plane wave in the basis set. In addition, lines are shown for different combinations of standard grid scale and fine grid scales, respectively corresponding to the maximum frequency of the grids used to represent the real space wave function and the ultrasoft augmented density as a multiple of the wave function momentum cut off. One can see that a high fine grid scale is essential for good convergence, but the standard grid scale can be twice the wave function scale, as expected, since the soft density contains maximum frequencies twice that of those in the wave function.

4.3.2 Effect of PAW operator smoothing

As explained in Section. 4.2.3, we can use the freedom afforded to us by PAW to smooth the part of the perturbation operator applied to the wave function represented on a real grid. Here we will demonstrate its ability to reduce numerical noise caused by the relative position of nuclei to the real-space gridpoints due to the poor representation of the $\frac{1}{r^3}$ component of the dipole.

Fig. 4.5 illustrates the dependence of ^{1}K(C−C) in C_2H_4 on the relative offset of the perturbation centre to the origin in a direction perpendicular to the molecular plane, z, against r_0. Small r_0 correspond to small amounts of damping. For small values of r_0, when the perturbation centre approaches a grid point at the origin ($z = 0$) there is a strong divergence in the coupling, more so the smaller r_0 is. Large values of r_0, approaching r_c, also exhibit diminished coupling as PAW can no longer fully

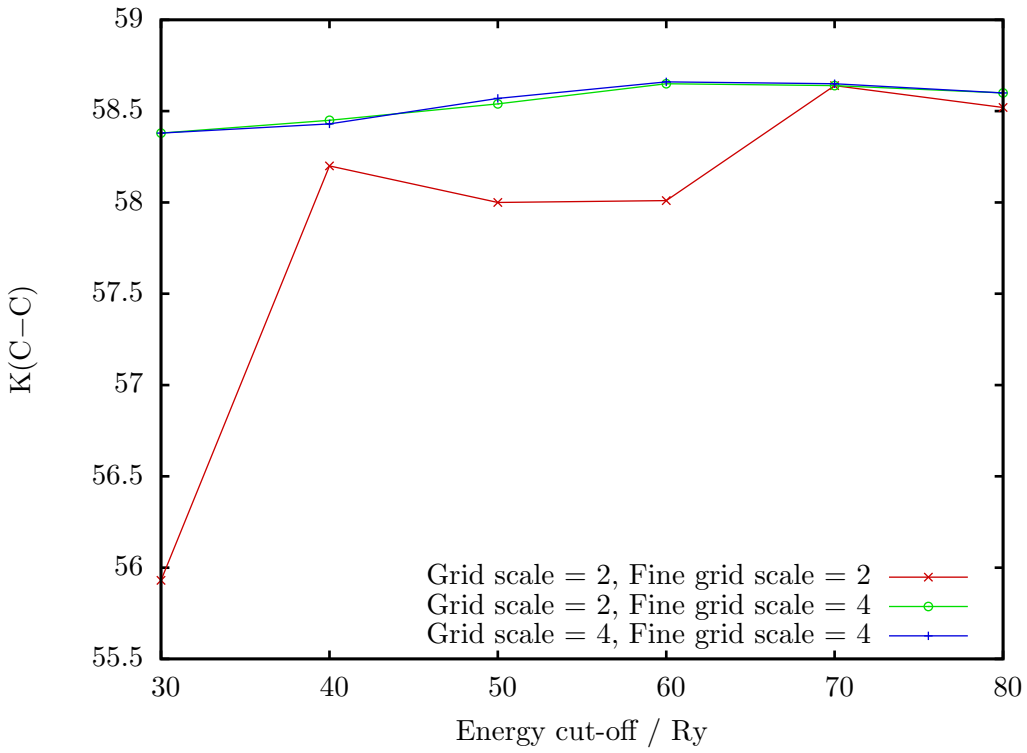

Figure 4.4: Convergence of ^{1}J(C−C) in C_2H_4 with respect to cut-off energy, grid scale and fine grid scale. One can see that a high fine grid scale is essential for good convergence, but a standard grid scale of 2 is sufficient.

reconstruct the significant difference between the two operators. There is still some slight variations in the coupling for intermediate values of r_0 as the damped operator is still not perfectly represented on the real grid. However, Fig. 4.6 shows only slight improvement on increasing the standard grid scales used for $r_0 = 0.5,\ 0.8\,a_0$.

4.3.3 Validation against existing quantum chemistry

Lantto, Vaara and Helgaker[152] provide a benchmark on 34 small molecules containing light atoms with couplings calculated using localised Gaussian orbital basis sets at the LDA, BLYP, B3LYP and MCSCF levels of theory along with some experimental values. Included in the light atoms is fluorine, which is notoriously difficult to treat well with density functional theory.[153] We have run the same calculations at a non-relativistic level of theory using both norm-conserving and ultrasoft pseudopotentials with the LDA functional and present the results in Tables 4.1, 4.2, 4.3 and 4.4 and Figures 4.7, 4.8 and 4.9.

As expected, the fluorine couplings perform poorly compared to experiment, particularly ^{1}J(F−C). In addition, they compare poorly to the Gaussian orbital basis set calculations. The majority of the difference between the pseudopotential calculations and the Gaussian orbital basis set calculations is from the Fermi-contact term contribution, suggesting that the origin of the disagreement might lie in the difficulty of constructing Gaussian basis sets with sufficient flexibility in the core to represent Fermi-contact coupling,[154] a problem that is circumvented with pseudopotentials when using the PAW transformed operator.

The root-mean-square deviation (RMSD) agreements of, where available, unsigned experimental couplings with LDA Gaussian orbital, norm-conserving and ultrasoft calculations was 49.4, 39.7 and 38.4 Hz respectively. Excluding systems including fluorine gives RMSD agreements with experiment of 40.0, 34.4 and 29.7 Hz. Exclud-

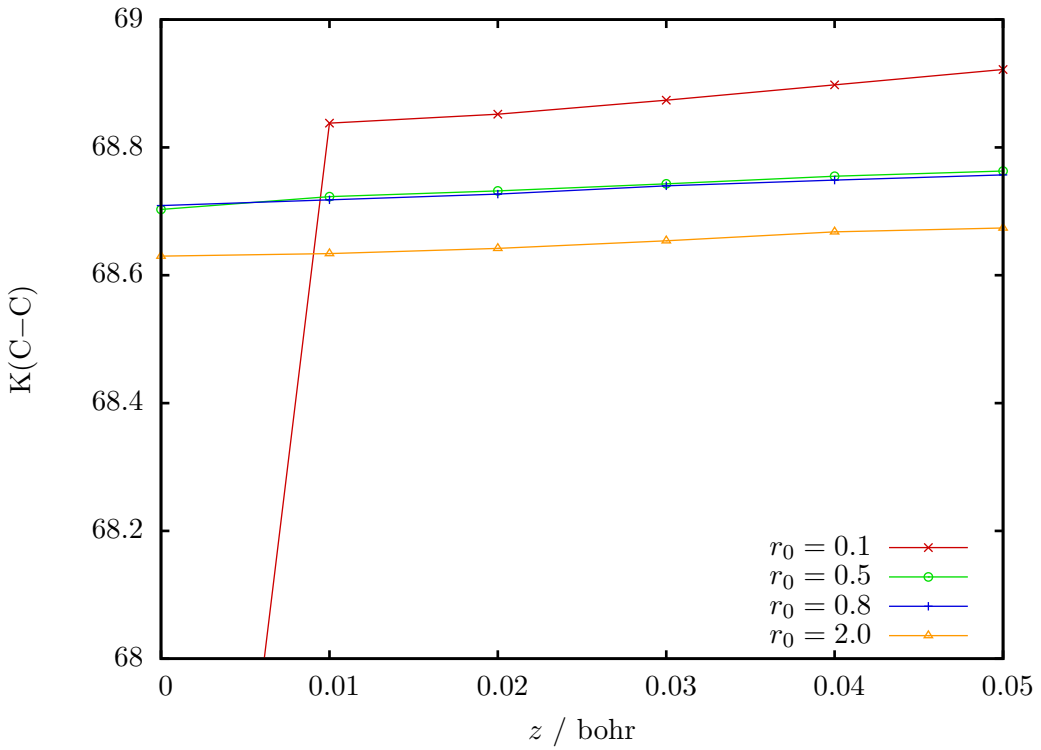

Figure 4.5: Dependence of ^{1}K(C−C) in C_2H_4 on z, the displacement of the perturbation centre from the origin in a direction perpendicular to the molecular plane, as a function of the dipole damping scale r_0 introduced in equation 4.40. Smaller r_0 correspond to less damping and a sharper dipole function, poorly represnted on the real grid, larger r_0 correspond to more damping that spills beyond the r_c that PAW can correct the error within.

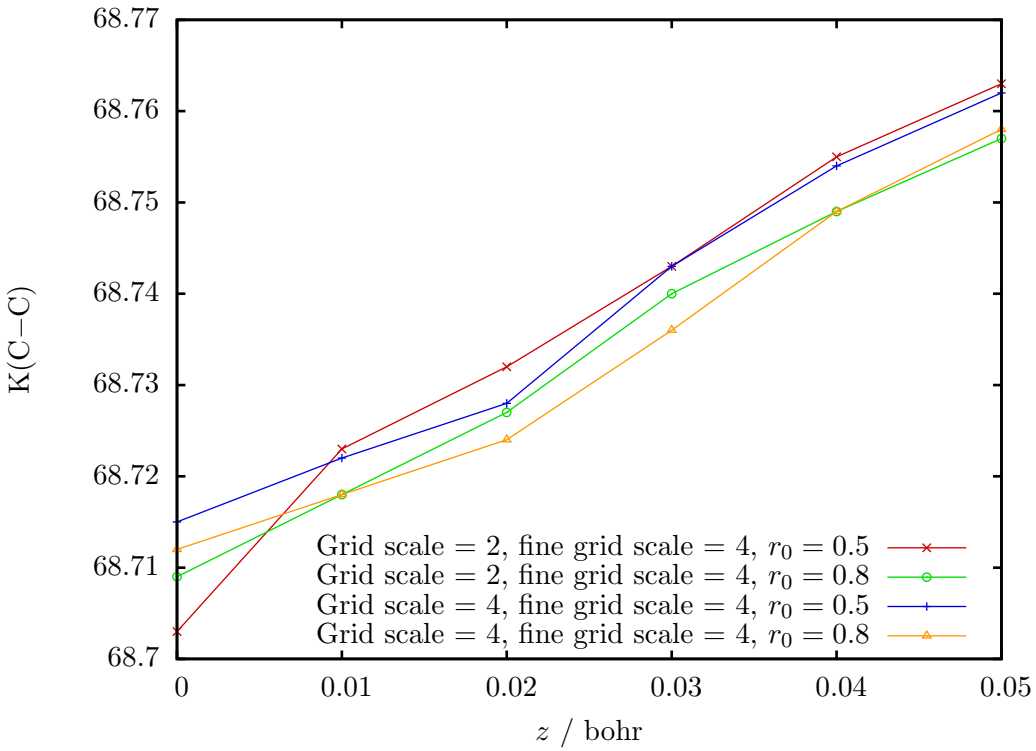

Figure 4.6: Dependence of ^{1}K(C−C) in C_2H_4 on z, the displacement of the perturbation centre from the origin in a direction perpendicular to the molecular plane, on the chosen damping scale, r_0, and on the standard grid scale.

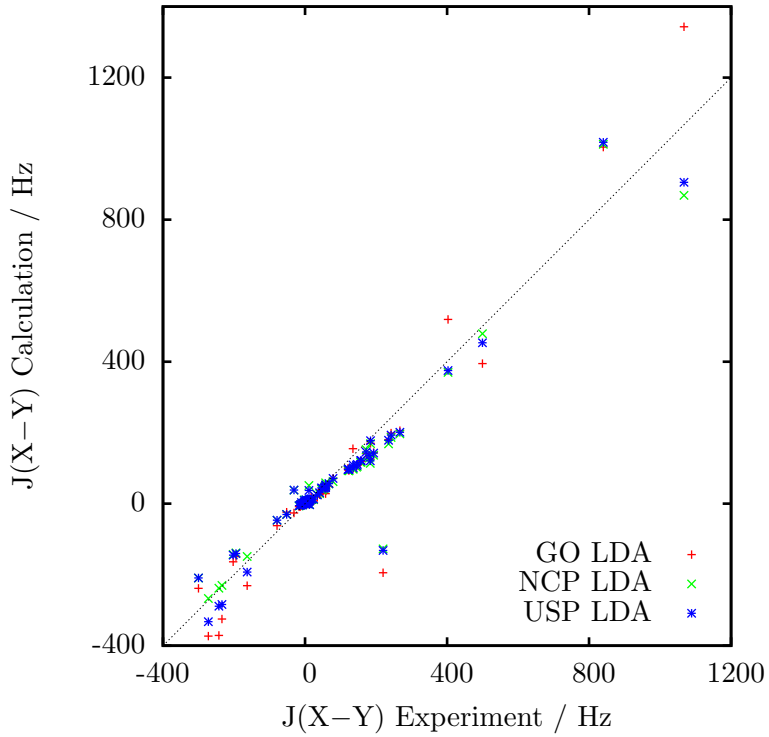

Figure 4.7: Comparison of isotropic J-couplings in a number of small molecules calculated using Gaussian orbital basis sets (red crosses), norm-conserving pseudopotentials (green diagonal crosses) and ultrasoft pseudopotentials (blue stars), all at the non-relativistic level of theory and using the LDA exchange-correlation functional, against experimental values. Gaussian orbital and experimental values are from Ref. 152.

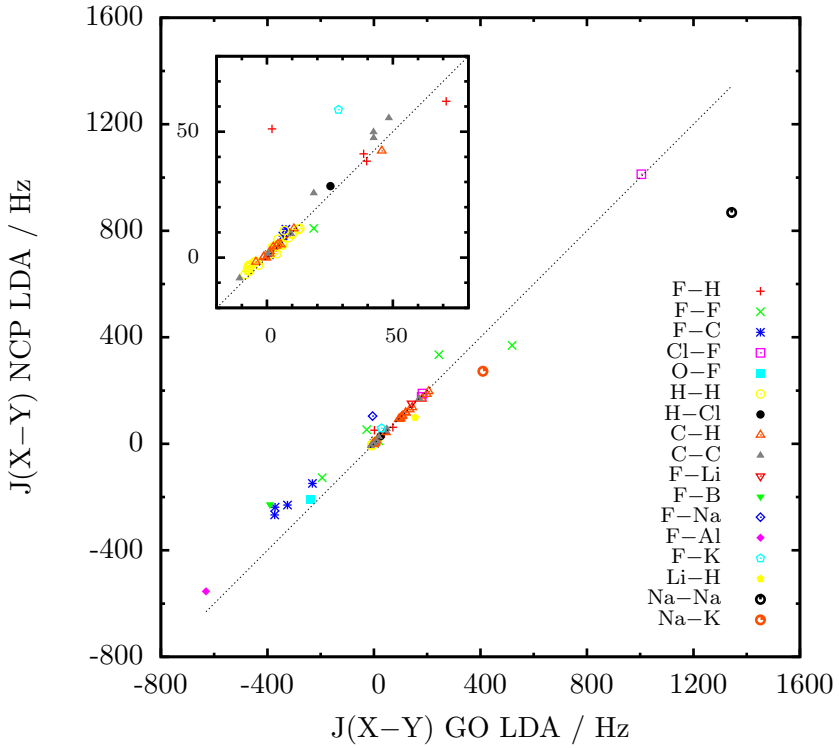

Figure 4.8: Comparison of isotropic J-couplings in a number of small molecules calculated using norm-conserving pseudopotentials against calculations using Gaussian orbital basis sets, both at the non-relativistic level of theory and using the LDA exchange-correlation functional. Gaussian orbital values are from Ref. 152.

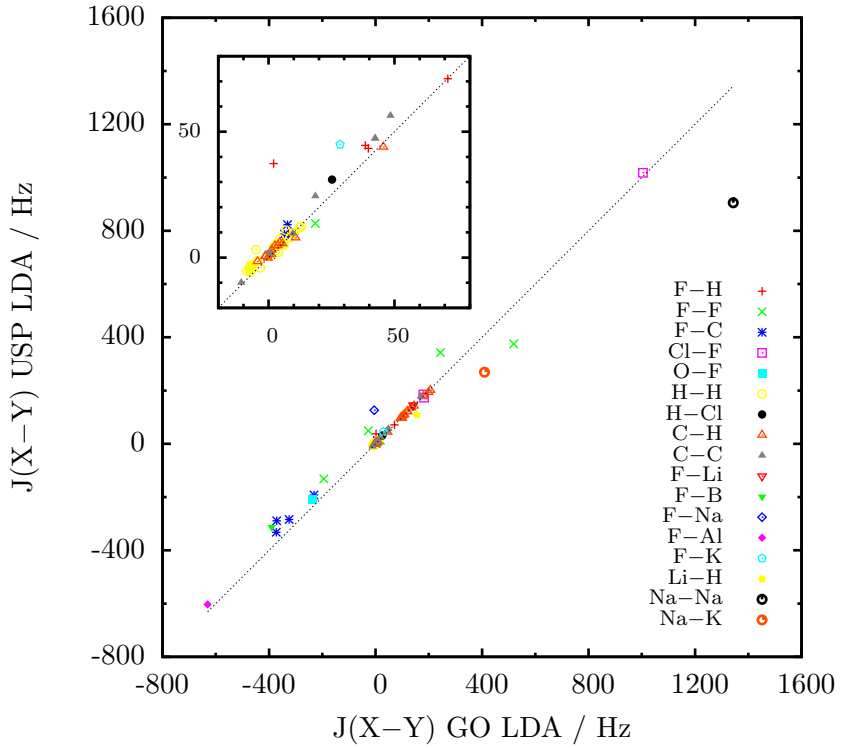

Figure 4.9: Comparison of isotropic J-couplings in a number of small molecules calculated using ultrasoft pseudopotentials against calculations using Gaussian orbital basis sets, both at the non-relativistic level of theory and using the LDA exchange-correlation functional. Gaussian orbital values are from Ref. 152.

ing systems involving sodium, the other significantly poorly performing element, gives RMSD agreements with experiment of 40.0, 33.9 and 34.5 Hz respectively. Excluding systems including both fluorine and sodium gives RMSD agreements of 20.8, 24.2 and 22.0 Hz respectively. Further statistics broken down by group of molecules are given in Tables 4.1–4.4.

The RMSD agreements of Gaussian orbital LDA with norm-conserving and ultrasoft calculations was 57.1 and 49.6 Hz respectively, 54.2 and 50.4 Hz excluding fluorine systems, 33.7 and 23.5 Hz excluding sodium systems and 8.4 and 7.1 Hz excluding both fluorine and sodium systems.

This indicates that, by and large, norm-conserving and ultrasoft pseudopotential calculations give couplings favourably comparable to equivalent localised Gaussian orbital calculations and to experiment.

Table 4.1: Non-relativistic benchmark on fluorine containing molecules. Gaussian orbital LDA, BLYP from Ref. 152, MCSCF calculations and experimental numbers from papers cited. NCP LDA and USP LDA values calculated with the implementation in `Castep`. All values are isotropic J-coupling in hertz.

Structure	Ref.	Site A	Site B	GO LDA	GO BLYP	GO MCSCF	NCP LDA	USP LDA	Exp
BF	155	F1	B1	-390.4	-382.8	-222.4	-227.5	-312.7	
FHF^-	*	F1	F2	-194.5	-124.6	-238.6	-127.1	-131.9	220.0
		F1	H1	2.0	0.5	10.1	51.1	37.3	11.0
ClF_3	156	F1	F1	519.1	558.7	404.0	369.9	375.2	403.0
		Cl1	F2	179.3	168.6	164.4	176.6	185.2	
		Cl1	F1	182.2	176.0	195.3	188.9	173.1	
HF	157	H1	F1	394.6	389.0	539.3	478.7	453.2	499.8
p-$C_6H_4F_2$	158	F1	C1	-375.6	-392.7	-210.7	-245.6	-295.3	-242.6
		F1	C2	21.3	28.8	33.1	25.9	27.8	24.3
		F1	C3	6.8	8.1	7.5	8.7	9.5	8.2
		F1	C4	-0.7	0.3	4.6	0.1	0.3	2.7
		F1	F2	6.4	7.5	11.2	6.6	8.3	17.4
		F1	H1	7.9	7.9	1.1	8.6	9.4	7.9
		F1	H2	2.3	3.4	6.8	2.7	2.9	4.5
ClF	155	Cl1	F1	1004.3	979.1	832.3	1012.4	1018.1	840.0
OF_2	156	O1	F1	-238.6	-249.3	-309.0	-209.5	-209.3	-300.0
AlF	155	F1	Al1	-630.7	-636.6	-627.1	-553.8	-603.1	
CHF_3	159	F1	C1	-344.0	-361.6	-225.6	-239.1	-301.7	-272.2
		F1	F1	-43.3	-16.7	125.9	32.4	30.9	
		F1	H1	71.2	88.2	79.1	62.1	71.0	79.1
		C1	H1	180.5	228.0	236.8	168.3	178.7	235.3
CH_2F_2	159	F1	C1	-325.6	-340.2	-229.0	-233.4	-284.1	-233.9
		F1	F2	-36.8	-3.3	140.0	45.9	54.4	
		F1	H1	39.6	54.3	52.0	38.3	43.4	48.6
		C1	H1	134.3	173.8	175.7	128.4	135.3	180.4
		H1	H2	3.2	4.1	-0.7	4.5	5.3	
CH_3F	159	F1	C1	-293.9	-306.3	-212.4	-216.0	-255.9	-163.0
		F1	H1	38.4	49.7	48.6	41.2	44.6	46.4
		C1	H1	108.3	141.8	141.5	105.4	110.5	147.3
		H1	H1	-4.4	-7.1	-11.5	-1.5	-1.4	
Root-mean-square deviation				71.17	76.98	19.01	53.56	57.58	0.00
Mean absolute deviation				49.70	50.31	11.54	34.15	38.91	0.00
Median absolute deviation				32.25	9.50	5.35	19.06	28.67	0.00
Mean relative deviation				32.76%	31.45%	18.10%	39.90%	35.66%	0.00%
Median relative deviation				24.42%	20.34%	8.04%	21.38%	21.60%	0.00%

* MCSCF calculation performed in Ref. 152 and experimental value estimated from Ref. 160 by authors of Ref. 152.

Table 4.2: Non-relativistic benchmark on nitrogen containing molecules. Gaussian orbital LDA, BLYP from Ref. 152, MCSCF calculations and experimental numbers from papers cited. NCP LDA and USP LDA values calculated with the implementation in `Castep`. All values are isotropic J-coupling in hertz.

Structure	Ref.	Site A	Site B	GO LDA	GO BLYP	GO MCSCF	NCP LDA	USP LDA	Exp
HNC	161	C1	H1	10.7	10.6	16.4	11.5	7.9	
		C1	N1	0.3	3.7	7.5	7.8	5.7	
		N1	H1	68.2	82.9	80.3	66.1	68.9	
$HCONH_2$	162, 163	C1	H1	144.2	183.2	183.2	136.4	142.3	193.1
		C1	H2	4.4	5.2	2.8	5.3	6.0	2.7
		C1	H3	-1.4	-1.8	-4.2	0.1	0.5	-3.7
		H2	H3	6.9	9.0	3.8	10.7	10.9	2.2
		H2	H1	0.9	0.9	0.8	1.2	1.1	2.3
		H3	H1	10.0	14.1	11.8	9.2	9.8	13.9
		C1	N1	4.0	5.9	12.8	9.5	8.4	10.6
		C1	O1	34.5	34.1	20.7	19.6	26.7	
		N1	O1	-1.2	-0.5	-1.3	0.8	0.7	
		N1	H1	9.5	11.5	9.6	11.9	12.9	13.5
		N1	H2	37.3	45.3	65.2	50.8	53.0	58.3
		N1	H3	37.0	45.3	63.2	50.0	52.1	58.3
		O1	H1	-4.7	-6.2	-6.2	-4.3	-4.9	
		O1	H2	-0.3	-0.7	-1.0	-0.2	-0.4	
		O1	H3	1.1	1.3	1.6	1.7	1.7	
HCN	161	C1	H1	205.8	260.8	249.3	196.7	201.2	267.3
		C1	N1	5.7	9.4	14.1	11.8	10.1	13.2
		N1	H1	4.3	4.2	4.6	3.4	2.8	6.2
NH_3	157	H1	H1	-5.0	-9.0	-11.3	-1.8	3.2	-10.0
		N1	H1	-26.3	-31.9	-31.1	38.2	38.5	-31.1
CH_3NC	161	C1	C2	-10.0	-10.8	-5.2	-6.9	-8.4	
		C1	H1	105.4	139.1	143.5	102.7	107.0	145.2
		C2	H1	1.1	2.6	2.6	1.5	1.3	2.7
		H1	H1	-7.5	-11.6	-19.1	-3.9	-4.0	
		N1	C1	-1.2	1.6	9.0	7.5	5.8	6.3
		N1	C2	3.4	6.1	13.7	6.8	4.5	7.6
		N1	H1	-0.6	-0.9	-3.2	0.1	0.3	-2.3
CH_3CN	161	C1	C2	43.5	56.5	72.0	51.0	48.7	58.0
		C1	H1	99.4	130.5	142.4	97.1	101.2	135.7
		C2	H1	-4.4	-6.9	-15.5	-1.8	-1.6	-9.9
		H1	H1	-8.7	-13.8	-22.9	-6.7	-5.4	-16.9
		N1	C1	4.4	7.0	15.4	-2.4	-2.9	12.7
		N1	C2	-3.0	-3.2	-2.0	10.8	8.8	-2.1
		N1	H1	0.4	1.0	1.5	0.6	0.5	1.1
	Root-mean-square deviation			19.82	5.19	5.75	21.33	19.57	0.00
	Mean absolute deviation			11.97	3.81	3.79	11.74	11.04	0.00
	Median absolute deviation			5.00	2.50	2.10	7.02	5.34	0.00
	Mean relative deviation			52.42%	38.32%	23.81%	68.81%	67.19%	0.00%
	Median relative deviation			50.00%	22.26%	15.11%	33.94%	40.50%	0.00%

Table 4.3: Non-relativistic benchmark on lithium, sodium and potassium containing molecules. Gaussian orbital LDA, BLYP from Ref. 152, MCSCF calculations and experimental numbers from papers cited. NCP LDA and USP LDA values calculated with the implementation in `Castep`. All values are isotropic J-coupling in hertz.

Structure	Ref.	Site A	Site B	GO LDA	GO BLYP	GO MCSCF	NCP LDA	USP LDA	Exp
LiF	155	F1	Li1	141.1	160.0	192.9	152.3	145.5	172.3
NaF	155	F1	Na1	-4.8	39.5	193.9	104.2	126.2	
LiH	155	Li1	H1	155.0	223.6	152.7	98.7	109.0	134.9
Na_2	155	Na1	Na2	1343.3	1375.3	1243.9	868.4	905.1	1067.2
KF	155	F1	K1	28.4	43.2	76.6	58.7	44.9	57.8
KNa	155	Na1	K1	409.5	401.3	480.0	272.7	269.0	
			Root-mean-square deviation	140.07	160.59	89.89	101.53	83.43	0.00
			Mean absolute deviation	89.20	105.92	58.48	63.99	56.94	0.00
			Median absolute deviation	30.30	51.65	19.70	28.11	26.37	0.00
			Mean relative deviation	27.44%	31.76%	18.56%	14.67%	18.07%	0.00%
			Median relative deviation	21.99%	27.06%	14.88%	15.13%	17.39%	0.00%

Table 4.4: Non-relativistic benchmark on remaining molecules. Gaussian orbital LDA, BLYP from Ref. 152, MCSCF calculations and experimental numbers from papers cited. NCP LDA and USP LDA values calculated with the implementation in `Castep`. All values are isotropic J-coupling in hertz.

Structure	Ref.	Site A	Site B	GO LDA	GO BLYP	GO MCSCF	NCP LDA	USP LDA	Exp
PH_3	157	H1	H1	-7.7	-12.5	-12.9	-5.0	-4.8	-13.4
		P1	H1	126.1	157.2	190.3	113.5	120.8	184.0
SiH_4	157	H1	H1	2.0	4.1	0.3	4.0	4.2	2.6
		Si1	H1	-163.6	-209.9	-201.3	-142.8	-144.8	-202.5
H_2O	157	H1	H2	-3.3	-6.4	-9.4	-3.0	-4.1	-7.3
		O1	H1	-61.9	-68.1	-78.0	-47.0	-46.5	-78.7
CH_4	157	H1	H1	-7.2	-12.4	-13.9	-3.1	-3.0	-12.6
		C1	H1	99.8	132.7	120.8	93.5	96.4	120.9
CH_3SiH_3	164	C1	H1	94.4	121.3	115.7	93.1	96.6	122.5
		C1	H4	3.7	5.5	3.4	4.6	4.8	4.6
		H1	H1	-7.2	-11.6	15.2	-4.9	-3.9	
		H4	H4	3.8	6.3	2.5	5.0	5.2	
		H1	H4	10.0	12.8	10.1	9.4	9.9	
		H1	H5	0.9	1.2	0.7	1.1	1.1	
		H1	H3	3.9	5.1	3.8	1.5	2.0	4.6
		Si1	C1	-24.1	-40.8	-60.5	-30.3	-30.2	-51.6
		Si1	H4	-149.0	-187.5	-182.9	-138.6	-140.3	-194.4
		Si1	H1	2.6	4.5	9.8	-0.1	-0.1	7.9
C_2H_6	165	C1	C2	17.3	28.3	37.5	24.2	23.1	34.6
		C1	H1	94.0	122.7	119.8	92.4	96.2	124.2
		C1	H4	-1.2	-2.2	-5.3	0.4	0.6	-4.6
		H1	H2	-6.5	-10.4	-14.1	-3.1	-3.3	
		H1	H4	12.4	16.3	14.7	11.2	11.8	
		H1	H5	2.8	3.8	3.5	2.5	2.6	
		H1	H4	6.0	8.0	7.2	5.4	5.7	8.0
C_2H_4	165	C1	C2	56.4	73.5	75.7	64.5	65.4	67.5
		C1	H1	119.2	155.4	147.7	116.4	121.1	156.3
		C1	H3	1.2	0.0	-3.3	2.5	3.0	-2.4
		H1	H2	4.4	4.9	0.9	7.3	7.4	2.2
		H1	H3	8.6	11.3	10.4	7.9	8.0	11.6
		H1	H4	13.0	18.1	17.0	11.6	12.4	19.0
C_2H_2	165	C1	C2	154.5	176.5	166.5	155.4	164.1	184.5
		C1	H2	198.7	254.4	232.1	186.6	193.4	242.4
		C1	H1	45.6	53.1	50.1	42.4	43.9	53.8
		H1	H2	6.2	9.6	10.8	4.9	5.0	10.1
C_6H_6	166	C1	C2	48.4	63.8	75.1	54.2	53.8	55.8
		C1	C3	0.7	0.0	-3.7	1.7	1.9	-2.5
		C1	C4	7.9	8.4	16.8	7.7	7.9	10.1
		C1	H1	119.8	155.0	185.1	117.4	122.0	158.3
		C1	H2	2.5	2.1	-9.8	4.2	4.7	1.0
		C1	H3	5.5	7.2	12.9	5.1	5.5	7.6
		C1	H4	-0.3	-0.8	-6.1	-0.1	-0.2	-1.2
H_2S	157	H1	H2	-7.0	-11.5	-15.4	-5.4	-5.6	
		S1	H1	21.5	23.5	31.9	23.3	22.8	
HCl	157	H1	Cl1	25.2	21.6	36.3	28.4	31.0	41.0
Root-mean-square deviation				21.59	7.40	7.87	25.71	23.52	0.00
Mean absolute deviation				14.66	4.59	5.19	16.81	15.39	0.00
Median absolute deviation				5.85	2.05	2.60	7.58	7.20	0.00
Mean relative deviation				38.48%	24.27%	54.67%	50.77%	50.66%	0.00%
Median relative deviation				25.43%	10.31%	10.99%	31.74%	28.64%	0.00%

Chapter 5

Relativistic J-coupling with pseudopotentials

Autschbach and Ziegler[22] presented a scalar-relativistic *zeroth-order regular approximation* (ZORA)-based method[120] for calculating spin-spin coupling between nuclei in NMR systems. Previous authors[167,168] have derived scaling schemes to account for relativistic effects on the Fermi-contact term. These can be effective, but the authors note that they do not always reproduce the correct trends. Some authors[168,169] suggest that it is necessary to use proper relativistic wave functions to reproduce experimental values, and that simply scaling the orbital contributions is insufficient. Full four-component Dirac equation calculations for magnetic shielding and J-coupling were tested in Ref. 113, showing that the relativistic correction was often of the same size as the original non-relativistic parameter, due to large changes in the valence wave functions near the nucleus.

The use of the full Dirac equation with four-component spinor wave functions would be highly computationally expensive and as such are limited to small systems. Ap-

proximations with two-component spinors have been developed, one of which is ZORA, in which we can also neglect spin-orbit coupling to give a purely scalar theory. Yates *et al.*[24] introduced a method for ab-initio relativistic NMR chemical shifts using GIPAW where relativistic effects are treated with scalar-ZORA entirely within the pseudopotential. The use of pseudopotentials means the treatment of heavy nuclei is no more computationally complex than lighter elements. This motivates a treatment of relativistic J-coupling within the more computationally efficient ZORA.

5.1 Zeroth-order regular approximation

While the effect of spin-orbit coupling on J-coupling can be significant in some compounds,[23] Ref. 116 finds that the inclusion of spin-orbit effects at the PBE level of theory for a collection of Hg, Pt, W, Pb and Tl molecules gives little improvement in the total mean absolute error (513.3 to $476.5 \times 10^{19}\,\mathrm{T^2\,J^{-1}}$) and an actual worsening of the total mean relative absolute error (39.6% to 40.7%). In particular, both the absolute and relative absolute errors worsen for the Pt, W and Pb containing molecules. The main improvement in total relative absolute error is found by going from the PBE functional[78] to the PBE0 functional,[170] with a total relative absolute error of 22.4%, and the main improvement in mean absolute error by both including spin-orbit effects and using the PBE0 functional. Hence, with calculation cost and complexity of implementation in mind, we concentrate on the dominant scalar-relativistic terms, parts 3.79b and 3.79c, and so neglect the third term of 3.79a, representing spin-orbit coupling.

5.1.1 NMR J-coupling

As done for the non-relativistic Schrödinger equation in Chapter 4 we will proceed by taking the derivatives of the scalar ZORA Hamiltonian in a magnetic field, Eqn. 3.79, with respect to pairs of nuclear magnetic moments, and then use second-order perturbation theory to calculate K^{AB}:

$$K^{AB} = \left.\frac{\partial^2 E}{\partial \boldsymbol{\mu}_A \partial \boldsymbol{\mu}_B}\right|_{\boldsymbol{\mu}_A=0,\boldsymbol{\mu}_B=0} \tag{5.1}$$

As before, for our system of nuclear dipole moments the magnetic vector potential is, in the symmetric gauge with ($\mathbf{r}_N = \mathbf{r} - \mathbf{R}_N$), $\mathbf{A} = \sum_N \alpha^2 \frac{\boldsymbol{\mu}_N \times \mathbf{r}_N}{|\mathbf{r}_N|^3}$, where α is the fine-structure constant.

Using the same superscript notation to denote perturbation order, Autschbach[22] obtained the following derivatives of the ZORA Hamiltonian, along with their equivalent $\hat{H}^{(0,1)}$ derivatives, as follows:

$$\hat{H}^{(1,1)}_{\text{Z-dia};i,j} = \mathcal{K}\alpha^4 \frac{\delta_{ij}(\mathbf{r}_A \cdot \mathbf{r}_B) - \mathbf{r}_{A;i}\mathbf{r}_{B;j}}{|\mathbf{r}_A|^3 |\mathbf{r}_B|^3} \tag{5.2a}$$

$$= \mathcal{K} H^{(1,1)}_{\text{dia}} \tag{5.2b}$$

$$\hat{H}^{(1,0)}_{\text{Z-para};i} = \frac{\alpha^2}{2\mathrm{i}} \left[\frac{\mathcal{K}}{|\mathbf{r}_A|^3} (\mathbf{r}_A \times \nabla)_i + (\mathbf{r}_A \times \nabla)_i \frac{\mathcal{K}}{|\mathbf{r}_A|^3} \right] \tag{5.3a}$$

$$= \frac{\alpha^2}{\mathrm{i}} \frac{\mathcal{K}}{|\mathbf{r}_A|^3} (\mathbf{r}_A \times \nabla)_i \tag{5.3b}$$

$$= \mathcal{K} \hat{H}^{(1,0)}_{\text{para}} \tag{5.3c}$$

$$\hat{H}^{(1,0)}_{\text{Z-spin};i} = \frac{4\pi\alpha^2}{3}\mathcal{K}\sigma_i\delta(\mathbf{r}_A) \tag{5.4a}$$

$$+ \frac{\mathcal{K}\alpha^2}{2}\left(\frac{3(\sigma\cdot\mathbf{r}_A)\mathbf{r}_{A;i}}{|\mathbf{r}_A|^5} - \frac{\sigma_i}{|\mathbf{r}_A|^3}\right) \tag{5.4b}$$

$$+ \frac{\alpha^2}{2}\frac{1}{|\mathbf{r}_A|^3}\left[\{(\nabla\mathcal{K})\cdot\mathbf{r}_A\}\sigma_i - (\nabla_i\mathcal{K})(\sigma\cdot\mathbf{r}_A)\right] \tag{5.4c}$$

Here we choose to split the spin term into a spin-dipole analogue, $\mathcal{K}\hat{H}^{(1,0)}_{\text{SD}}$, plus a Fermi-contact analogue:

$$\hat{H}^{(1,0)}_{\text{Z-FC};i} = \frac{8\pi\alpha^2}{6}\mathcal{K}\sigma_i\delta(\mathbf{r}_A) \tag{5.5a}$$

$$+ \frac{\mathrm{d}\mathcal{K}}{\mathrm{d}r}\frac{\alpha^2}{2}\left(\frac{(\sigma\cdot\mathbf{r}_A)\mathbf{r}_{A;i}}{|\mathbf{r}_A|^4} - \frac{\sigma_i}{|\mathbf{r}_A|^2}\right). \tag{5.5b}$$

All the terms reduce to the non-relativistic versions[13] in the limit $c \to \infty$, that is, $\mathcal{K} = 1$ and $\nabla\mathcal{K} = 0$. We see changes for the relativistic case, $\mathcal{K} \neq 1$, especially in the case of the Eqn. 5.4 where term 5.4c is non-zero and the term 5.4a (equivalent to the Fermi-contact term) is zero for a nuclear Coulomb potential, neglecting finite-size nucleus effects. Finite-size nucleus effects have been found[171] to be somewhat significant in certain circumstances, contributing a 10 to 15% reduction in isotropic J-couplings between heavy elements in the sixth row of the periodic table and light elements, and larger between two heavy elements.

We can now proceed to calculate K by separating it into contributions from the interactions of the nuclear magnetic moments mediated by the electron spin, $K^{\text{Z-spin}}$, Eqn. 5.4, and from the interactions of the nuclear magnetic moments mediated by the electron charge current, $K^{\text{Z-orb}}$, Eqn. 5.2b and 5.3c.

5.1.2 Relativistic J-coupling with PAW

As for the ultrasoft non-relativistic case, we will now apply PAW to the derived ZORA-level scalar-relativistic theory of J-coupling to get pseudo-operators in terms of modifications to the non-relativistic operators. The diamagnetic and paramagnetic current operators are simple multiples of $\mathcal{K}$, while the Fermi-contact term disappears for a nuclear Coulomb potential and the spin-dipole term turns into a simple multiple of $\mathcal{K}$ plus a Fermi-contact-like term which is sharply localised by the gradient of $\mathcal{K}$ (Figure 3.3). As the region where $\mathcal{K} \neq 1$ is localised inside the augmentation region, the operators are equal to their non-relativistic equivalents outside, and so we can apply all these corrections accurately in PAW augmentation for no extra computational cost[24] using Eqn. 4.39.

In the case of the spin contribution, the sharply localised Z-FC perturbation operator can be written as

$$\widetilde{H}^{(1,0)}_{\text{Z-FC}} = \sum_{\mathbf{R},n,m} |p_{\mathbf{R},n}\rangle\langle\phi_{\mathbf{R},n}|\hat{H}^{(1,0)}_{\text{Z-FC}}|\phi_{\mathbf{R},m}\rangle\langle p_{\mathbf{R},m}|, \tag{5.6}$$

where we have used the on-site approximation. The Z-SD PAW augmentation is also evaluated on a real radial grid, while the un-augmented contribution is calculated in Fourier space on the ultrasoft augmented magnetisation density.

$$\widetilde{H}^{(1,0)}_{\text{Z-SD}} = \hat{H}^{(1,0)}_{\text{SD}} + \Delta\hat{H}^{(1,0)}_{\text{Z-SD}}, \tag{5.7}$$

where, using the on-site approximation again,

$$\Delta\hat{H}^{(1,0)}_{\text{Z-SD}} = \sum_{\mathbf{R},n,m} |p_{\mathbf{R},n}\rangle(\langle\phi_{\mathbf{R},n}|\mathcal{K}\hat{H}^{(1,0)}_{\text{SD}}|\phi_{\mathbf{R},m}\rangle - \langle\tilde{\phi}_{\mathbf{R},n}|\hat{H}^{(1,0)}_{\text{SD}}|\tilde{\phi}_{\mathbf{R},m}\rangle)\langle p_{\mathbf{R},m}|.$$

The total spin contribution to the reduced coupling tensor is then

$$K^{\text{Z-spin}} = \tilde{K}^{\text{Z-spin}} + \Delta K^{\text{Z-spin}} \tag{5.8}$$

$$\tilde{K}^{\text{Z-spin}} = -\frac{\mu_0}{3}\int \mathrm{d}\mathbf{G}\left[\frac{3(\tilde{\mathbf{m}}^{(1)}(\mathbf{G})\cdot\mathbf{G})\mathbf{G} - \tilde{\mathbf{m}}^{(1)}(\mathbf{G})G^2}{G^2}\right] e^{i\mathbf{G}\cdot\mathbf{r}_A} \tag{5.9}$$

$$\Delta K^{\text{Z-spin}} = \sum_{oo'\sigma\sigma'} \langle\psi^{(0)}_{o\sigma}|\widetilde{H}^{(1,0)}_{\text{Z-FC}} + \Delta\hat{H}^{(1,0)}_{\text{SD}}|\psi^{(1)}_{o'\sigma'}\rangle, \tag{5.10}$$

where $\tilde{\mathbf{m}}^{(1)}(\mathbf{G})$ is the un-augmented spin density in reciprocal space, to which we apply the spin dipole operator and slow Fourier transform at the position of the receiving nucleus

As in the non-relativistic case we do not PAW augment the diamagnetic current operator due to complexity of implementation and the small magnitude of the effect.

The PAW augmented paramagnetic operator is

$$\tilde{H}^{(1,0)}_{\text{Z-para}} = \hat{H}^{(1,0)}_{\text{Z-para}} + \Delta\hat{H}^{(1,0)}_{\text{Z-para}} \tag{5.11}$$

$$\Delta\hat{H}^{(1,0)}_{\text{Z-para}} = \sum_{\mathbf{R},n,m} |p_{\mathbf{R},n}\rangle(\langle\phi_{\mathbf{R},n}|\mathcal{K}\hat{H}^{(1,0)}_{\text{para}}|\phi_{\mathbf{R},m}\rangle \tag{5.12}$$

$$- \langle\tilde{\phi}_{\mathbf{R},n}|\hat{H}^{(1,0)}_{\text{para}}|\tilde{\phi}_{\mathbf{R},m}\rangle)\langle p_{\mathbf{R},m}|. \tag{5.13}$$

The bare contribution of the paramagnetic current is calculated in Fourier space on the pseudo-current density and is PAW augmented on a real radial grid with an on-site approximation, justified by the short-rangeness of the interaction. The total orbital current contribution is then

$$K^{\text{Z-orb}} = \tilde{K}^{\text{Z-orb}} + \Delta K^{\text{Z-orb}} \tag{5.14}$$

$$\tilde{K}^{\text{Z-orb}} = \mu_0 \int \mathrm{d}\mathbf{G}\, \frac{\mathrm{i}\mathbf{G} \times \tilde{\mathbf{j}}^{(1)}(\mathbf{G})}{G^2} e^{\mathrm{i}\mathbf{G}\cdot\mathbf{r}_A} \tag{5.15}$$

$$\Delta K^{\text{Z-orb}} = 2\,\mathrm{Re} \sum_{oo'\sigma} \langle \psi^{(0)}_{o\sigma} | \Delta \hat{H}^{(1,0)}_{\text{Z-para}} | \psi^{(1)}_{o'\sigma} \rangle, \tag{5.16}$$

where $\tilde{\mathbf{j}}^{(1)}(\mathbf{G})$ is the un-augmented induced current density, paramagnetic and diamagnetic, in Fourier space, to which we apply the Biot–Savart law in reciprocal space and slow Fourier transform at the position of the receiving nucleus.

The total indirect coupling tensor between the two nuclei is then the sum of $K^{\text{Z-spin}}$ and $K^{\text{Z-orb}}$.

5.2 Validation against existing quantum chemistry

We make a comparison against a comprehensive benchmark performed by Moncho and Autschbach[116] on a set of 45 molecules containing sixth row elements. For this study they used the Amsterdam Density Functional code (`ADF`) at the scalar-relativistic and spin-orbit levels of ZORA theory and with both the PBE[78] (more precisely a mix of VWN[172] and PBE) and PBE0[170] functionals. As neither PBE0 nor spin-orbit effects have yet been implemented for the calculation of NMR parameters in periodic DFT calculations we compare only to their PBE scalar-relativistic ZORA

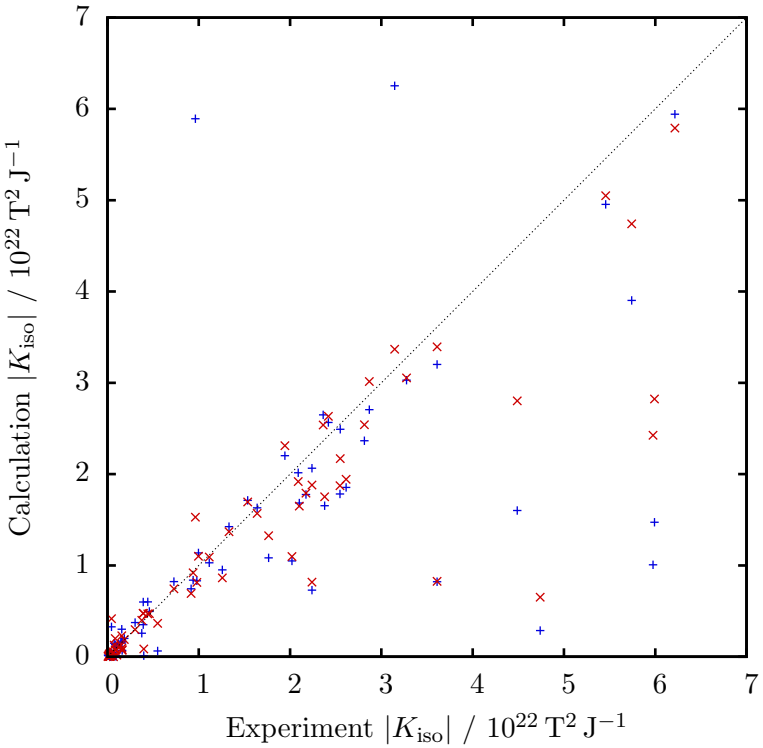

Figure 5.1: Comparison of reduced isotropic J-couplings in a number of small molecules containing row six elements calculated using ADF's implementation of scalar-relativistic ZORA J-coupling (red ×), from Ref. 116, and the new implementation in Castep of the same (blue +), both using the PBE exchange-correlation functional, against experiment. Two points are excluded due to scale: ^{2}J(Hg−Sn) in Hg-Ir-$SnCl_3$; and ^{1}J(Pt−C) in Pt($SnCl_3$).

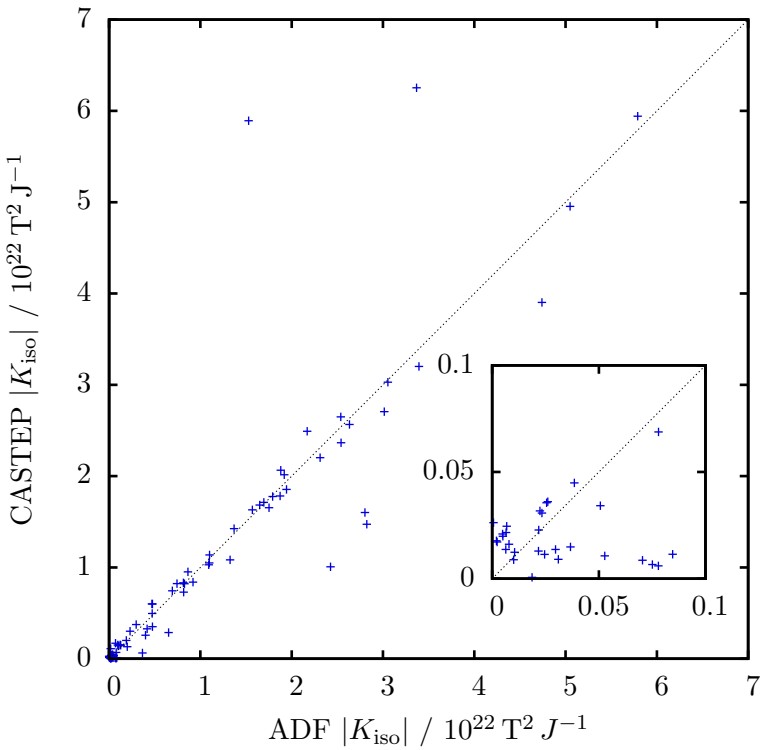

Figure 5.2: Comparison of reduced isotropic J-couplings in a number of small molecules containing row six elements calculated using `ADF`'s implementation of scalar-relativistic ZORA J-coupling, from Ref. 116, against the new implementation in `Castep` of the same, both using the PBE exchange-correlation functional. Two points are excluded due to scale: ^{2}J(Hg−Sn) in Hg-Ir-$SnCl_3$; and ^{1}J(Pt−C) in Pt($SnCl_3$).

calculations.

We now highlight some of the physical and numerical differences between the scalar relativistic approach used in Ref. 116 and our plane-wave pseudopotential formalism. In Ref. 116 the spin-dipole term (the relativistic analog of $\hat{H}_{\mathrm{SD}}$) is neglected in scalar relativistic calculations due to computational expense, however, we include it in our calculations. It is generally less than 1% of the final isotropic value, though in the case of WF_6 it accounts for 24% of the coupling.

The ADF calculations took V from four-component numerical Dirac equation calculations on isolated, neutral atoms. This potential was then used to determine $\mathcal{K}$ for a ZORA Hamiltonian. Similarly, in our implementation, $\mathcal{K}$ for each species of atom is determined by the all-electron potential of a four-component calculation on an isolated, neutral atom. This was then used to construct a scalar ZORA isolated atom and so generate an ultrasoft pseudopotential.

The norm-conserving relativistic potentials were generated with the `atom` code as maintained by José Luís Martins from four-component calculations, with the all-electron partial waves taking the spin-up electron state of the valence orbitals.

By using pseudopotentials we are implicitly using the frozen core approximation. While Moncho and Autschbach do not use the frozen core approximation, Autschbach[22] notes that the frozen core approximation yields almost the same couplings as the respective all-electron computations as long as a sufficiently complete basis set is used. We neglect finite nucleus effects, which can be relevant for row-six elements, as noted in Section 5.1.1. Finally, we also neglect solvent effects, which are included in the ADF calculations with the conductor-like screening model (COSMO).[173] However, Moncho and Autschbach find that the COSMO model does not significantly improve the median relative deviations of couplings with experiment over the gas phase calculations and suggest that explicit solvent models are necessary. We also note that

the main goal of our methodology is to compute J-couplings in solid materials, where solvent effects are not relevant.

The PBE functional was used with a converged plane-wave basis set cut-off of 80 rydberg and a single k-point in each case. As we are implicitly using periodic boundary conditions, we must place the molecules in a supercell of sufficient size to reduce interactions between periodic images. A cubic cell size of $(15\text{Å})^3$ is found to be sufficient in most cases. The calculated isotropic reduced couplings for tungsten, lead, mercury, platinum and thallium are shown alongside statistics on the unsigned values in Tables 5.1, 5.2, 5.3, 5.4 and 5.5 respectively. Fig. 5.1 shows `Castep` and `ADF` calculations against experiment and Fig. 5.2 shows the `Castep` implementation against `ADF`. To be consitent with Ref. 116 in this section we report the reduced coupling constants in S.I. units ($10^{19}\,\mathrm{T}^2\,\mathrm{J}^{-1}$).

Considering the full set of compounds we find that, as expected, the non-relativitistic pseudopotential calculations show large deviation from experiment, with a RMSD of 4529.2, mean absolute deviation of 1352.3 and median absolute deviation of $224.1 \times 10^{19}\,\mathrm{T}^2\,\mathrm{J}^{-1}$. Using relativistic ultrasoft pseudopotentials and the ZORA formalism of Section 5.1.1 significantly improves the agreement with experiment, giving a RMSD of 1215.2, mean absolute deviation of 511.6 and median absolute deviation of 87.6. These results are comparable to the equivalent results of Moncho and Autschbach[116] (1558.7, 517.8, 82.1). We also note that there is good agreement between the norm-conserving and ultrasoft pseudopotential results.

For tungsten containing molecules (Table 5.1), the performance of ultrasoft pseudopotentials was equivalent to the all-electron calculations, with marginally larger RMSD and smaller mean and median absolute deviations from experiment. Lead-containing molecules (Table 5.2) also gave equivalent performance for ultrasoft pseudopotentials, with marginally smaller RMSD, mean and median absolute deviations.

Mercury-containing molecules (Table 5.3) have a significantly smaller RMSD, dominated by the size of the ^{2}J(Hg−Sn) coupling in IrCl($SnCl_3$)(HgCl)(CO)(PH_3)$_2$, and smaller mean and median absolute deviations. Platinum-containing molecules (Table 5.4) have a larger RMSD, mean and median deviations, largely due to the significant error in the ^{1}J(Pt−Pt) coupling in the charged molecules. We believe this error arises from the difficulty in treating charged systems with periodic boundary conditions and the influence of the solvation model on the all-electron couplings.

For thallium containing molecules (Table 5.5), the statistics are poor compared to experiment. It was previously found in Ref. 116 that greater accuracy for couplings in thallium-containing molecules required going to PBE0 and spin-orbit levels of theory. When including just spin-orbit effects, thallium containing molecules are the only set found to experience an improvement in mean relative absolute error, going from 57.0% to 33.1%. They also experience a similar improvement when just using the PBE0 functional. When spin-orbit effects are included and the PBE0 functional is used, the mean absolute error goes from 2226.0 to $737.1 \times 10^{19}\,\mathrm{T^2\,J^{-1}}$ and the mean relative absolute error goes from 57.0% to 22.0%. This indicates that the thallium couplings are unusually sensitive to both functional and spin-orbit effects. In addition, the present results also show some deviations from the all-electron results. The reported couplings in molecules TlF, TlCl, TlBr and TI are taken from gas phase experiments and, except for TlI, are in good agreement with all-electron calculations. The ^{1}J(Tl−I) coupling exhibits a very large orbital current contribution, an order of magnitude larger than the total value, and a large Fermi-contact-like contribution with opposite sign. The couplings in the remaining thallium molecules are measured in solution; $Tl_4(OCH_3)_4$, with a particularly poor ^{2}J(Tl−Tl) coupling was in a toluene solvent and the rest in a water solvent. Calculations presented at the PBE0 and spin-orbit level of theory in Ref. 116 show that, in contrast to

other elements, couplings in thallium containing molecules are significantly affected by the inclusion of solvent, with the mean absolute deviation going from 1163.0 to $737.1 \times 10^{19}\,\mathrm{T^2\,J^{-1}}$ when moving to the COSMO model. Neglect of solvation effects is hence likely to be the main source of disagreement between our results and all-electron couplings.

Table 5.1: Relativistic benchmark on tungsten containing molecules. Local orbital PBE ZORA calculations using `ADF` from Ref. 116, experimental numbers from cited references. Ultrasoft PBE ZORA values calculated with the implementation in `Castep`. All values are isotropic reduced J-coupling in $10^{19}\,T^2\,J^{-1}$.

Structure	Ref.	Site A	Site B	Exp	ADF rel	USP rel
$W(CO)_6$	174	W1	C1	997.0	1099.5	1138.2
$W(CCH_3)(CH_2CH_3)_3$*	175	W1	H10	20.7	-24.6	-11.4
$W(CO)_5PI_3$	176	W1	P1	1639.0	1568.7	1633.1
η^5-$(C_5H_5)W(CO)_3H$	177	W1	H6	72.4	127.4	148.2
$W(CO)_5PF_3$	178	W1	P1	2362.9	2537.3	2651.9
$W(CO)_5PCl_3$	176	W1	P1	2090.0	1918.0	2018.1
WF_6	179	W1	F1	85.4	-198.5	-131.4
			Root-mean-square deviation		114.2	129.1
			Mean absolute deviation		98.7	91.3
			Median absolute deviation		102.5	71.9
			Mean relative deviation		36.8%	33.4%
			Median relative deviation		10.3%	14.2%

* Used as model for $W(CC(CH_3)_3)(CH_2C(CH_3)_3)_3$.

Table 5.2: Relativistic benchmark on lead containing molecules. Local orbital PBE ZORA calculations using `ADF` from Ref. 116, experimental numbers from cited references. Ultrasoft PBE ZORA values calculated with the implementation in `Castep`. All values are isotropic reduced J-coupling in $10^{19}\,\mathrm{T}^2\,\mathrm{J}^{-1}$.

Structure	Ref.	Site A	Site B	Exp	ADF rel	USP rel
$Pb(CH_3)_3CF_3$	180	Pb1	F1	102.0	17.1	109.8
		Pb1	H1	28.7	-4.9	21.0
$PbCl_4$	181	Pb1	Cl1	2868.3	-3014.1	-2709.0
$Pb(CH_3)_2(CF_3)_2$	180	Pb1	F1	160.7	70.4	169.8
		Pb1	H1	33.9	-6.8	24.6
PbH_4	*	Pb1	H1	1115.0	1090.7	1030.0
$Pb(CH_3)_2H_2$	182	Pb1	H1	979.4	814.0	832.6
		Pb1	H3	-30.3	-10.1	8.9
$Pb_2(CH_3)_6$	183	Pb1	C1	44.4	-416.5	-328.1
		Pb1	C6	146.0	121.7	152.7
		Pb1	H1	-16.8	5.0	19.9
		Pb1	H16	9.1	10.5	12.4
$Pb(CH_3)_3H$	182	Pb1	H1	915.9	692.5	744.9
		Pb1	H2	-27.1	-6.4	13.8
$Pb(CH_3)_4$	184	Pb1	C1	396.7	-84.6	-11.5
		Pb1	H1	24.5	-2.3	17.2
			Root-mean-square deviation		148.7	139.9
			Mean absolute deviation		98.1	82.5
			Median absolute deviation		25.7	11.3
			Mean relative deviation		100.2%	66.2%
			Median relative deviation		68.5%	22.8%

* Extrapolated in Ref. 116 from $Pb(CH_3)_3H$ and $Pb(CH_3)_2H_2$.

Table 5.3: Relativistic benchmark on mercury containing molecules. Local orbital PBE ZORA calculations using `ADF` from Ref. 116, experimental numbers from cited references. Ultrasoft PBE ZORA values calculated with the implementation in `Castep`. All values are isotropic reduced J-coupling in $10^{19}\,\mathrm{T^2\,J^{-1}}$.

Structure	Ref.	Site A	Site B	Exp	ADF rel	USP rel
$Hg(CH_3)Cl$	185	Hg1	C1	2614.5	1943.0	1857.1
		Hg1	H1	93.6	-77.9	6.0
$[Hg(CN)_4]^{2-}$	186	Hg1	C1	2814.2	2540.4	2368.4
$Hg(CCCl)_2$	187	Hg1	C1	5456.6	5049.0	4961.6
		Hg1	C3	1535.8	1694.3	1714.7
$Hg(C_6H_5)_2$	187	Hg1	C1	2174.6	1791.5	1778.7
		Hg1	C2	157.0	228.9	301.7
		Hg1	C3	183.7	188.8	199.7
		Hg1	C4	32.0	-29.7	-13.8
$Hg(CH_3)CCH$	187	Hg1	C1	2549.2	2169.9	2493.6
		Hg1	C2	2101.5	1650.0	1685.2
		Hg1	C3	728.0	743.6	823.3
$Hg(CH_3)I$	185	Hg1	C1	2378.0	1751.2	1655.5
		Hg1	H1	84.6	-70.5	8.6
$IrCl(SnCl_3)(HgCl)\ldots$	188	Hg1	Sn1	50,838.5	62,548.2	50,861.4
$\ldots(CO)(PH_3)_2$*		Hg1	P1	375.5	-399.1	-257.2
$Hg(CH_3)(CF_3)$	180	Hg1	F1	459.0	471.7	496.3
		Hg1	H1	64.0	-52.8	10.7
$Hg(CH_3)_2$	185	Hg1	C1	1258.2	863.5	953.0
		Hg1	H1	46.4	-36.7	14.7
$Hg(CH_3)Br$	185	Hg1	C1	2546.7	1873.8	1785.1
		Hg1	H1	90.5	-75.1	6.6
$Hg(CN)_2$	187	Hg1	C1	5741.7	4740.7	3907.1
			Root-mean-square deviation		2470.2	511.4
			Mean absolute deviation		753.4	311.1
			Median absolute deviation		158.5	118.3
			Mean relative deviation		16.9%	37.4%
			Median relative deviation		17.0%	29.0%

* Used as model for $IrCl(SnCl_3)(HgCl)(CO)(P(C_6H_5)_3)_2$.

Table 5.4: Relativistic benchmark on platinum containing molecules. Local orbital PBE ZORA calculations using `ADF` from Ref. 116, experimental numbers from cited references. Ultrasoft PBE ZORA values calculated with the implementation in `Castep`. All values are isotropic reduced J-coupling in $10^{19}\,\mathrm{T}^2\,\mathrm{J}^{-1}$.

Structure	Ref.	Site A	Site B	Exp	ADF rel	USP rel
cis-$PtH_2(P(CH_3)_3)_2$	189	Pt1	H1	392.1	474.2	599.3
		Pt1	P1	1765.2	1324.9	1083.9
$[Pt(CO)_3]_2^{2+}$	190	Pt1	C1	2420.2	2632.3	2576.4
		Pt1	C3	1943.6	2312.0	2204.5
		Pt1	C4	39.7	-38.5	-44.9
		Pt1	C6	302.7	296.8	375.2
		Pt1	Pt2	962.9	1527.9	5893.1
$Pt(PF_3)_4$	191	Pt1	P1	6215.0	5789.7	5949.6
$Pt(P(CH_3)_3)_4$	192	Pt1	P1	3610.5	3393.7	3205.5
trans-$PtI_2(NH_2CH_3)_2$	193	Pt1	C1	22.8	-6.5	21.7
		Pt1	H1	23.3	-21.7	-12.9
cis-$PtCl_2(P(CH_3)_3)_2$	194	Pt1	P1	3276.2	3053.5	3033.2
cis-$PtI_2(NH_2CH_3)_2$	193	Pt1	C1	31.9	-18.7	-0.6
		Pt1	H1	26.3	-23.3	-30.8
$Pt(SnCl_3)(CH_2C\ldots$	195	Pt1	Sn1	28,025.3	23,956.7	26,441.7
$\ldots(CH_3)CH_2)(C_2H_4)$		Pt1	C4	50.1	-50.7	-34.2
		Pt1	C2	65.2	-0.6	26.3
		Pt1	C3	160.8	78.0	68.9
		Pt1	C1	157.7	95.3	151.1
		Pt1	C6	119.8	104.5	141.2
		Pt1	H1	19.5	-22.4	-31.8
		Pt1	H2	16.8	-7.9	-16.2
		Pt1	H3	23.7	-26.1	-36.1
		Pt1	H4	22.5	-25.5	-35.6
		Pt1	H5	6.1	-2.0	-17.8
		Pt1	H6	22.5	31.0	9.1
trans-$PtH_2(P(CH_3)_3)_2$	189	Pt1	H1	392.1	474.2	351.1
trans-$PtCl_2(P(CH_3)_3)_2$	194	Pt1	P1	2239.7	1880.4	2067.0
$[Pt(CN)_5]_2^{4-}$	196	Pt1	C1	1331.7	1369.1	1426.7
		Pt1	C5	937.3	918.8	839.2
		Pt1	C6	30.0	-21.8	-22.9
		Pt1	C10	441.4	468.9	601.9
		Pt1	Pt2	3146.0	3367.4	6254.0
			Root-mean-square deviation		733.1	1065.4
			Mean absolute deviation		231.9	387.2
			Median absolute deviation		27.5	41.0
			Mean relative deviation		23.8%	49.9%
			Median relative deviation		14.5%	23.7%

Table 5.5: Relativistic benchmark on thallium containing molecules. Local orbital PBE ZORA calculations using `ADF` from Ref. 116, experimental numbers from cited references. Ultrasoft PBE ZORA values calculated with the implementation in `Castep`. All values are isotropic reduced J-coupling in $10^{19}\,\mathrm{T}^2\,\mathrm{J}^{-1}$.

Structure	Ref.	Site A	Site B	Exp	ADF rel	USP rel
$Tl(CN)_3$	197	Tl1	C1	4488.5	2802.2	1602.1
TlBr	155	Tl1	Br1	-3610.0	-825.9	-821.1
$Tl(CN)Cl_2$	197	Tl1	C1	5975.5	2424.9	1008.2
$Tl(CN)_2Cl$	197	Tl1	C1	5991.8	2822.9	1474.7
$Tl_4(OCH_3)_4$*	198	Tl1	Tl1	549.8	-365.3	-63.2
TlCl	155	Tl1	Cl1	-2240.0	-817.4	-728.6
TlF	155	Tl1	F1	-2020.0	-1096.7	-1050.0
TlI	155	Tl1	I1	-4740.0	-652.2	-286.8
			Root-mean-square deviation		2570.6	3249.6
			Mean absolute deviation		2226.0	2822.6
			Median absolute deviation		2235.2	2837.6
			Mean relative deviation		57.0%	74.8%
			Median relative deviation		56.2%	76.3%

* Used as model for $Tl_4(OC(CH_3)_3)_4$.

Chapter 6

Disorder in gehlenite

Crystallographic techniques such as X-ray diffraction (XRD) often only provide us with an average topology of a material. However, materials can be disordered, with spatial deviations from the average structure such as disordered chemical occupancy of sites, disorded atomic positions and temporal deviations in the form of dynamics. Solid-state NMR can be an effective local probe of this disorder, revealing more local chemical environments than are present in the average topology.[3] These observed local chemical environments correspond to the range of local electronic environments within the full disordered structural model.

By using ab-initio predictions of the NMR properties of possible local environments, we can piece together the NMR spectrum of a disordered material and quantify the structural model in terms of deviations from average topology. This could be, for example, in terms of probabilities of site occupancies, probabilities of correlated bonding of particular sites or correlations of NMR properties with continuously disordered structural parameters, such as bond angles and strain parameters.

The calculations described in this chapter were done in support of experimental work

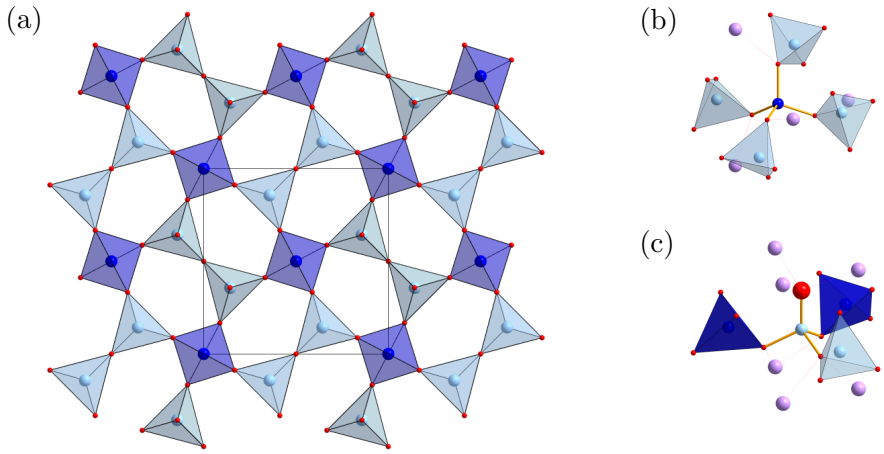

Figure 6.1: (a) A plane of the aluminosilicate structure showing (b) the T_1 environment and (c) the T_2 environment. [Reprinted (adapted) with permission from Ref. 18. Copyright 2012 American Chemical Society.]

by Pierre Florian *et al.* and reported in Ref. 18, which contains further experimental details. In addition, the two sets of model structures for gehlenite were created by Pierre Florian.

6.1 Structure of gehlenite

Gehlenite ($Ca_2Al_2SiO_7$) is one of the principal minerals in the melilite group. Minerals in the melilite group have the general formula $A_2B(T_2O_7)$, where the T_2O_7 are corner-sharing pairs of TO_4 and T=Al,Si,B. The pairs are linked together into sheets by the B cation, often Al. The sheets are then held together by the A cations, usually Ca or Na. The Loewenstein rule[199] predicts that $(O_3Al)-O-(AlO_3)$ linkages are forbidden energetically.

The melitite-type materials can be doped with lanthanide ions, which makes them

attractive for optical applications such as solid-state lasers. Recent studies have reported long lasting phosphoresence (1 s to 10^3 s) of Ce^{3+} doped $Ca_2Al_2SiO_7$ and $CaYAl_3O_7$ melilite crystals, making them candidates for solid-state lasing materials tunable in the violet and blue regions.[200,201] In addition, crystals of $Ca_2Al_2SiO_7$ doped with Tm^{3+}, Er^{3+}, Yb^{3+}, Ce^{3+} exhibit a broad and intense absorption band, making them suitable for use as a laser.[202,203] Furthermore, the Eu^{2+} doped solid solution $Ca_2(1-x)Sr_{2x}Al_2SiO_7$ was recently reported as a potential component of semiconductor-based LEDs.[204]

These studies all note that the Al/Si ordering in gehlenite plays an important role in controlling the electronic structure at the lanthanide Ln^{3+} site,[205] and hence its spectroscopic properties. There is, therefore, a need for a complete description of melilite-type structures in order to explain and predict optical properties.

In addition, in the geophysical sciences, the Al/Si ordering is known to be important when studying aluminosilicates, as adherence to Loewenstein rule affects thermodynamic properties of material.[206] The break-down of Al-avoidance has been suggested to lead to increased fragility[207] — an important factor for industrial glass making.

There have been many previous ^{29}Si NMR studies of minerals using the separation of the spectrum into different tetrahedral units to investigate Al/Si ordering.[208] The relative intensities from the NMR spectrum can be compared to the equivalent frequencies of occurance derived from structural models.[208–211]

Furthermore, ^{17}O NMR studies of aluminosilicates have established that the Loewenstein rule is generally violated many cases. This is because when the Al/Si cation distribution is not fully random, their ordering is incomplete.[212–214]

Gehlenite has not been fully investigated before. However, it is an ideal material for investigation of Loewenstein-rule violation due to the pseudo-isolated T_2O_7 pairs.

Crystalline gehlenite consists of layers of T_1 and T_2 sites bonded by bridging oxygens, and inter-layer calcium cations. One such layer is shown in Fig. 6.1. The tetrahedral T_1 sites are bonded to four T_2 sites via bridging oxygens. The tetrahedral T_2 sites can be Al or Si and have one non-bridging oxygen, two oxygens bonded to a T_1 site and one oxygen bridging to the paired T_2 site.

A T_1 site can hence have five second-coordination-sphere environments, $\mathrm{Al{-}(OSi)_p(OAl)_{4\text{-}p}}$, depending on the occupancy of the neighbouring T_2 sites.

If the Loewenstein rule is obeyed, the T_2 pairs should always have the form $\mathrm{(O_3Al){-}O{-}(SiO_3)}$. By quantifying the population of Al−O−Al and Si−O−Si bonds one can determine the degree of deviation from the Loewenstein rule, and hence build up an accurate structural model of gehlenite.

The T_2 ordering process follows

$$2\,\mathrm{Al{-}O{-}Si} \rightleftharpoons^{\Delta H} \mathrm{Al{-}O{-}Al} + \mathrm{Si{-}O{-}Si} \tag{6.1}$$

where ΔH is the ordering enthalpy. Previous simulations of gehlenite, using empirical interatomic potentials, have suggested that $\Delta H = 50.2\,\mathrm{kJ/mol}$ (0.52 eV).[215]

Long range interaction between pairs is weak,[215] as there is no $T_2{-}T_2$ network, hence the T_2 pairs can be considered disordered. Weak interaction between pairs gives an un-observably low Al/Si ordering temperature, $T_c = 700\,\mathrm{K}$, which is well below the glass transitions temperature (860 °C) below which structural rearrangements are not observable experimentally, contrary to what one would predict, T_c = 5000–10,000 K, from a simple 'Bragg Williams' (BW) mean-field model, explained in Ref. 215.

6.2 Model structures used

The disorder will be treated within a supercell framework. Each supercell has been constructed from $2 \times 2 \times 3$ primitive unit cells, giving 24 T_1 and 48 T_2 sites and a total of 288 atoms. By using a large supercell a single site in the material can feel the average long-range crystal effects at the same time as experiencing a disordered short-range chemical environment.

Given the five chemical environments for each T_1 site, five supercells were created for each by Pierre Florian, with the T_2 sites in the cell either randomly occupied Al/Si (the 'random' set), or randomly occupied but constrained to obey the Loewenstein pairing rule (the 'Loewenstein' set). This gives a total of 25 supercells for each set, plus a fully ordered cell that reflects the average structure. The positions of atoms within the supercells were then optimised to minimise atomic forces using ultrasoft pseudopotentials and an energy cut-off of 32 Ry, with the lattice vectors held constant at their experimental values.

6.3 Ordering enthalpy

6.3.1 Experiment

The Al/Si occupation ratio of a given tetrahedral site is directly related to the change in Gibbs free energy for the ordering process, ΔG, through the equation

$$p_{\mathrm{Al-Al}} = \exp(-\frac{1}{2}\Delta G/k_{\mathrm{B}}T) \tag{6.2}$$

where T is the temperature at which the (partial) ordering took place and a $p_{\mathrm{Al-Al}} \ll 1$ approximation has been made.

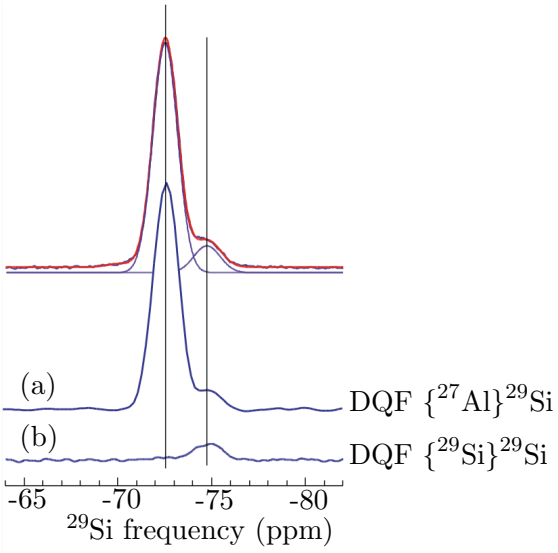

Figure 6.2: Unfiltered spectrum (top) showing all Si sites, and double-quantum filtered (DQF) (a) INADEQUATE and (b) INEPT spectra showing, respectively, (a) Si sites bonded to at least one Al, i.e. both T_2 environments, and (b) Si sites bonded to at least one Si, i.e. Si T_2 in a Loewenstein-rule violating pair. The ratio of the intensities gives $p_{\mathrm{Al-Al}}$ and thus the ordering enthalpy. [Reprinted (adapted) with permission from Ref. 18. Copyright 2012 American Chemical Society.]

In gehlenite, only the T_2 sites are concerned with Al/Si ordering, and hence $p_{\mathrm{Al-Al}}$ is the relative population of aluminum atoms engaged in a T_2Al−O−T_2Al linkage and also, symmetrically, the relative population of silicon atoms engaged in a T_2Si−O−T_2Si linkage.

Using double-quantum filtering (DQF), the relative populations of Si−O−Si bonds can be determined. Fig. 6.2 shows the ^{29}Si MAS spectra of a gehlenite sample treated at 1333 K. The top, unfiltered, spectrum shows two Si sites, presumably corresponding to the two types of T_2 Si sites present in gehlenite. To disambiguate and assign them, DQF 1D spectra were acquired with (a) $\{^{27}\mathrm{Al}\}^{29}$Si INEPT, only showing Si coupled to at least one Al, Fig. 6.2a, and (b) $\{^{29}\mathrm{Si}\}^{29}$Si INADEQUATE, only showing Si coupled to at least one Si, Fig. 6.2b. The INEPT spectrum is

identical to the un-filtered spectrum, as both Si environments are bonded to at least two Al in all cases. The INADEQUATE spectrum, however, only shows the one peak corresponding to the Si$-(OAl)_2(OSi)$ T_2 pair. The largest line is hence Si$-(OAl)_3$ and the smaller line Si$-(OAl)_2(OSi)$.

The relative intensity of the Si$-(OAl)_3$ and Si$-(OAl)_2(OSi)$ components can be measured to determined $p_{\mathrm{Al-Al}}$, and it was found that $p_{\mathrm{Al-Al}}(1333\,\mathrm{K}) = 0.11$ and $p_{\mathrm{Al-Al}}(1823\,\mathrm{K}) = 0.17$.

We can use the Gibbs–Helmholtz relationship with Eqn. 6.2 to show that

$$\frac{\mathrm{d}\ln p_{\mathrm{Al-Al}}}{\mathrm{d}T} = \frac{\Delta H}{2k_{\mathrm{B}}T^2}. \tag{6.3}$$

Assuming that ΔH is independent of T over the experimental temperature range, a linear regression was performed, with Eqn. 6.3, and an enthalpy of ordering $\Delta H = 0.52\,\mathrm{eV}$ with a standard deviation of $0.017\,\mathrm{eV}$ was derived.

6.3.2 Calculations

We can estimate the ordering enthalpy, ΔH, of the Loewenstein rule-violating process, Eqn. 6.1, using DFT total energy calculations. Ground-state calculations were performed at 50 Ry using ultrasoft pseudopotentials, a single k-point $(\frac{1}{4}, \frac{1}{4}, \frac{1}{4})$ and the PBE exchange-correlation functional.

From these ground-state calculations we can plot the total energies versus the number of T_2 pairs that violate the Loewenstein rule present in the supercell, shown in Fig. 6.3. A linear regression finds that $\Delta H = 0.51\,\mathrm{eV}$, consistent with the previous prediction of $0.52\,\mathrm{eV}$ by Thayaparam *et al.*[215] and with the experimental value of $\Delta H = 0.52 \pm 0.017\,\mathrm{eV}$.

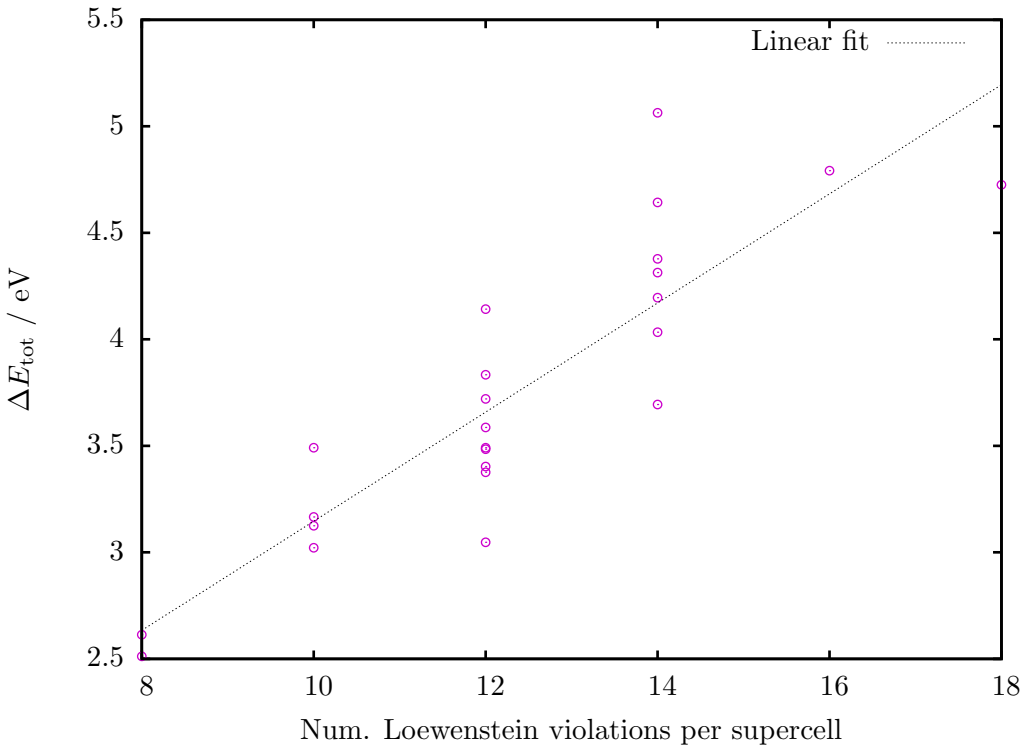

Figure 6.3: Total energy difference between supercells from the 'random' set (i.e. randomly occupied T_2 sites) and the 'ordered' supercell versus number of Loewenstein-rule-violating T_2 pairs in the supercell. A linear regression finds $\Delta H = 0.51226 \pm 0.06098\,\mathrm{eV}$.

6.4 Electric field gradients

6.4.1 Experiment

When performing ^{27}Al MAS and MQMAS at 9.4 T and 17.6 T the spectra, Fig. 6.4, show two main contributions. Fitting seven possible aluminium sites, five T_1 and two T_2, to the four spectra and refining gives NMR parameters, chemical shifts and $|C_Q|$ (see Table 6.1 for the T_1 site $|C_Q|$), for the seven sites. Simulated spectra, shown in Fig. 6.4, are in good agreement with experiment, although this does not guarantee uniqueness of the fitted parameters.

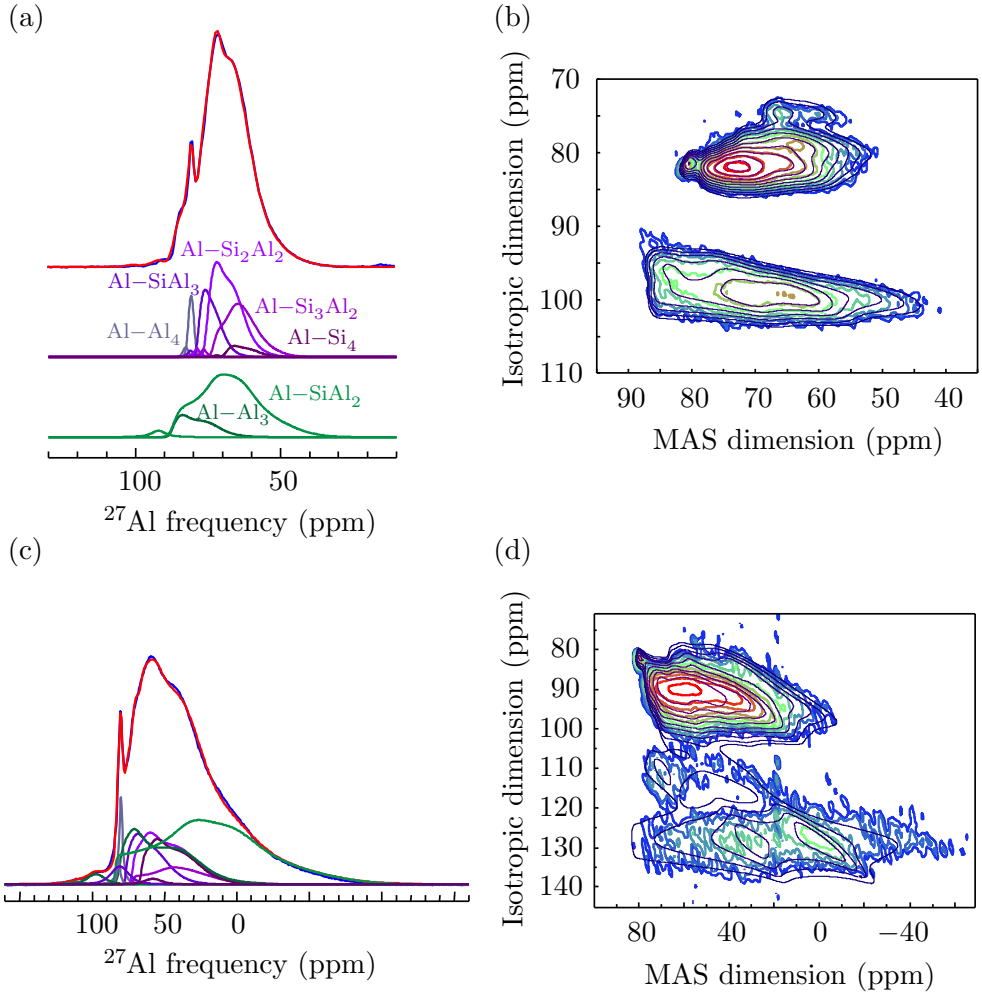

Figure 6.4: ^{27}Al MAS at (a) 9.4 T and (c) 17.6 T and MQMAS at (b) 9.4 T and (d) 17.6 T spectra along with their fitted seven component simulation. [Reprinted (adapted) with permission from Ref. 18. Copyright 2012 American Chemical Society.]

Table 6.1: Mean T_1 Al $|C_Q|$ in MHz versus number of next-nearest neighbour Si atoms, n_{Si}, from experiment and ab-initio calculations on the 'random' structures, the 'Loewenstein' structures and the fully ordered structure.

		Mean $\|C_Q\|$ / MHz			
Site	n_{Si}	Experiment	Random	Loewenstein	Ordered
T_1 Al	0	1.75	2.46	1.05	
T_1 Al	1	5.82	7.44	5.66	
T_1 Al	2	7.27	8.80	7.31	6.02
T_1 Al	3	7.59	8.07	7.09	
T_1 Al	4	6.89	7.65	7.96	

6.4.2 Calculations

Electric field gradients were calculated with ultrasoft pseudopotentials, a 50 Ry cut-off energy and a single k-point. Statistics are given in Table 6.1 and plotted in Fig. 6.5.

The behavior of the ^{27}Al quadrupolar coupling constant C_Q appears to be complex (Fig. 6.5): the 'random' structures systematically overestimate experiment by at least 1 MHz, while the 'Loewenstein' set are close to the experimental values, although we experimentally know that there is some degree of Loewenstein violation, and the ordered structure underestimate C_Q by 1 MHz. This indicates a possible link between the disorder in the T_2 sites and the EFG on the T_1 Al sites.

Decomposition of the EFG tensor

By decomposing the EFG tensors into a sum of local electronic, non-local electronic, and ionic components we can attempt to determine the origin of the variation in C_Q.

First, we separate out the electron charge density contribution to the EFG, Eqn. 3.85, into local (inside the cut-off radius of nucleus $\mathbf{R}$) and non-local (outside the cutoff

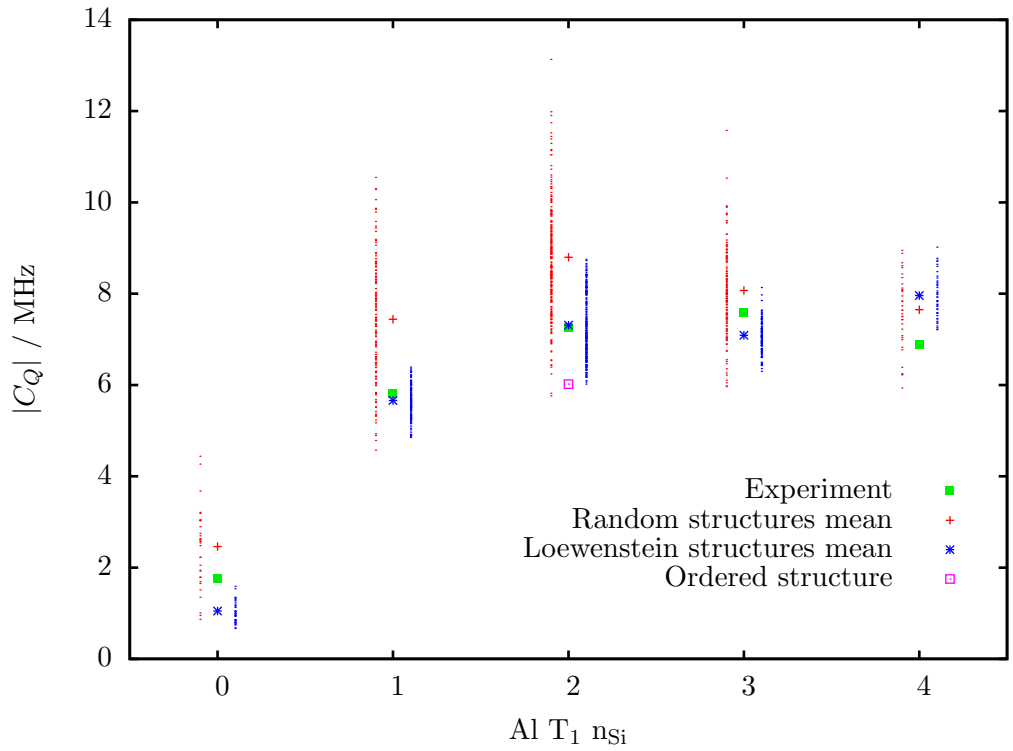

Figure 6.5: The dependence of experimentally measured and calculated EFG C_Q values on the T_1 site as a function of the number of Si next-nearest neighbours.

radius of nucleus $\mathbf{R}$) parts:

$$n_{\mathbf{R}}^{\text{El}} = n_{\mathbf{R}}^{\text{El-L}} + n_{\mathbf{R}}^{\text{El-NL}}, \tag{6.4}$$

where, dropping the augmentation of other nuclei $\mathbf{R}' \neq \mathbf{R}$ (the on-site approximation),

$$n_{\mathbf{R}}^{\text{El-L}} = 2 \sum_{o,n,m} \langle \tilde{\psi}_o | p_{\mathbf{R},m} \rangle \langle \phi_{\mathbf{R},m} | \mathbf{r} \rangle \langle \mathbf{r} | \phi_{\mathbf{R},n} \rangle \langle p_{\mathbf{R},n} | \tilde{\psi}_o \rangle, \tag{6.5}$$

and

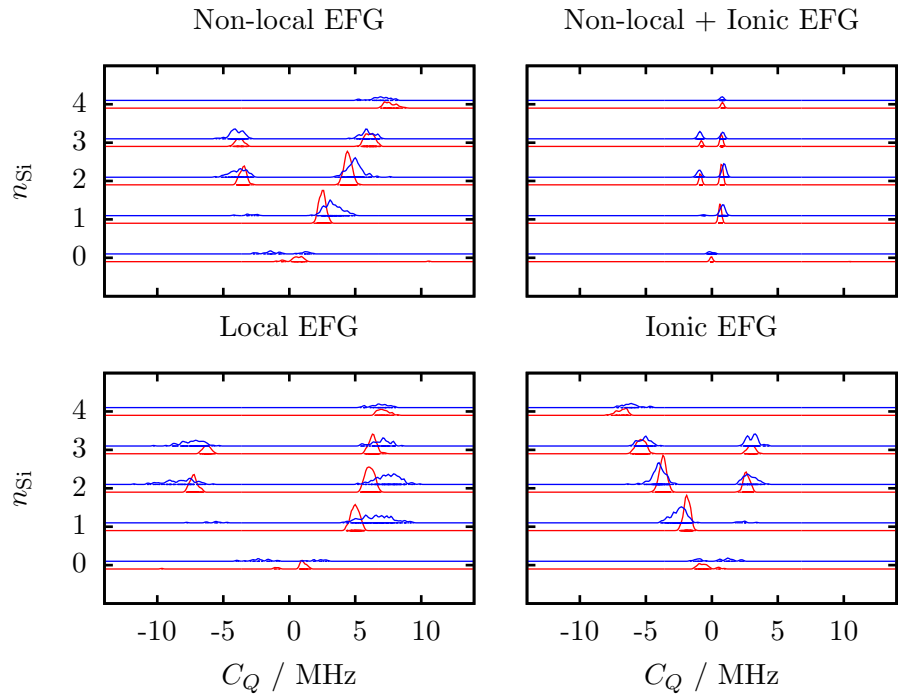

Figure 6.6: Illustration of the distributions of C_Q subcomponent tensors for the Loewenstein and random structure sets, demonstrating that the non-local electronic ($r > r_c$) and ionic contributions largely cancel to leave the local electronic contribution as the dominant part of the total EFG tensor.

$$n_{\mathbf{R}}^{\text{El-NL}} = n^{\text{El-PS}} - 2 \sum_{o,n,m} \langle \tilde{\psi}_o | p_{\mathbf{R},m} \rangle \langle \tilde{\phi}_{\mathbf{R},m} | \mathbf{r} \rangle \langle \mathbf{r} | \tilde{\phi}_{\mathbf{R},n} \rangle \langle p_{\mathbf{R},n} | \tilde{\psi}_o \rangle, \tag{6.6}$$

where $n^{\text{El-PS}}$ is the soft electron pseudo-density.

We then separate the EFG tensor at nuclear site $\mathbf{R}$ into three contributions:

$$G = G^{\text{ions}} + G^{\text{local}} + G^{\text{non-local}}, \tag{6.7}$$

where the individual contributions are calculated from their respective densities:

$$G^{\text{ions}}_{\alpha\beta}(\mathbf{R}) = \sum_n \frac{Z_n}{|\mathbf{R}-\mathbf{R}_n|^3}\left[\delta_{\alpha\beta} - 3\frac{(R_\alpha - R_{n\alpha})(R_\beta - R_{n\beta})}{|\mathbf{R}-\mathbf{R}_n|^2}\right]; \tag{6.8}$$

$$G^{\text{local}}_{\alpha\beta}(\mathbf{R}) = 2\sum_{o,n,m} \langle\tilde{\psi}_o|p_{\mathbf{R},m}\rangle\langle\phi_{\mathbf{R},m}|\frac{1}{r^3}\left[\delta_{\alpha\beta} - 3\frac{r_\alpha r_\beta}{r^2}\right]|\phi_{\mathbf{R},n}\rangle\langle p_{\mathbf{R},n}|\tilde{\psi}_o\rangle \tag{6.9}$$

$$G^{\text{non-local}}_{\alpha\beta}(\mathbf{R}) = G^{\text{pseudo}}_{\alpha\beta} - 2\sum_{o,n,m} \langle\tilde{\psi}_o|p_{\mathbf{R},m}\rangle\langle\tilde{\phi}_{\mathbf{R},m}|\frac{1}{r^3}\left[\delta_{\alpha\beta} - 3\frac{r_\alpha r_\beta}{r^2}\right]|\tilde{\phi}_{\mathbf{R},n}\rangle\langle p_{\mathbf{R},n}|\tilde{\psi}_o\rangle \tag{6.10}$$

where $G^{\text{pseudo}}_{\alpha\beta}$ is the EFG tensor calculated from the soft electron pseudo-density.

Rotating the individual tensors into the eigenspace of the total tensor we can look at which contribute to C_Q. If we diagonalise the total tensor, G:

$$G = S^\dagger \Lambda S, \tag{6.11}$$

taking Λ_{11} to be the largest eigenvalue, then

$$C_Q = \frac{eQ\Lambda_{11}}{h} \tag{6.12}$$

where e is the electron charge, Q is the nuclear quadrupole moment and h is the Planck constant. We can now write the local contribution to C_Q as

$$\Lambda^{\text{local}}_{11} = \left[SG^{\text{local}}S^\dagger\right]_{11} \tag{6.13}$$

$$C_Q^{\text{local}} = \frac{eQ\Lambda_{11}^{\text{local}}}{h}, \tag{6.14}$$

and other contributions similarly.

Plotting the histograms of C_Q contributions to the total C_Q, Fig. 6.6, we can see that non-local electronic and ionic contributions to the EFG largely cancel, leaving only the local ($r < r_c$) component as the main contributor to the total C_Q on the T_1 Al sites. It is hence from this that we investigate the principle cause of the variation in the local electronic structure.

Cause of variation in local environment

The number of T_2 next nearest-neighbors to the T_1 atom which are in Loewenstein-rule violating pairs is positively correlated (see Fig. 6.7) with C_Q on the T_1 atom for all sites except $n_{\text{Si}} = 4$, where it is negatively correlated, indicating the role of Loewenstein violations in the EFG.

This is consistent with the 'random' structures giving systematically higher mean C_Q than the 'Loewenstein' structures for all sites except $n_{\text{Si}} = 4$, where the 'random' structures give a lower mean C_Q. It is also consistent with the broader distribution of C_Q on the 'random' structures, for which a T_1 site may have between 0 and 4 next-nearest neighbours in a Loewenstein rule-violating pair, and 'Loewenstein' structures which have none.

We might suppose that the nearby presence of a Loewenstein rule-violating T_2 pair induces a distortion of the oxygen polyhedron around a T_1 site. This can be quantified in terms of Ghose's tetrahedral shear parameters:[216] the mean tangent of the absolute deviation of the $\angle O{-}T_1{-}O$ bond angles from the tetrahedral angle

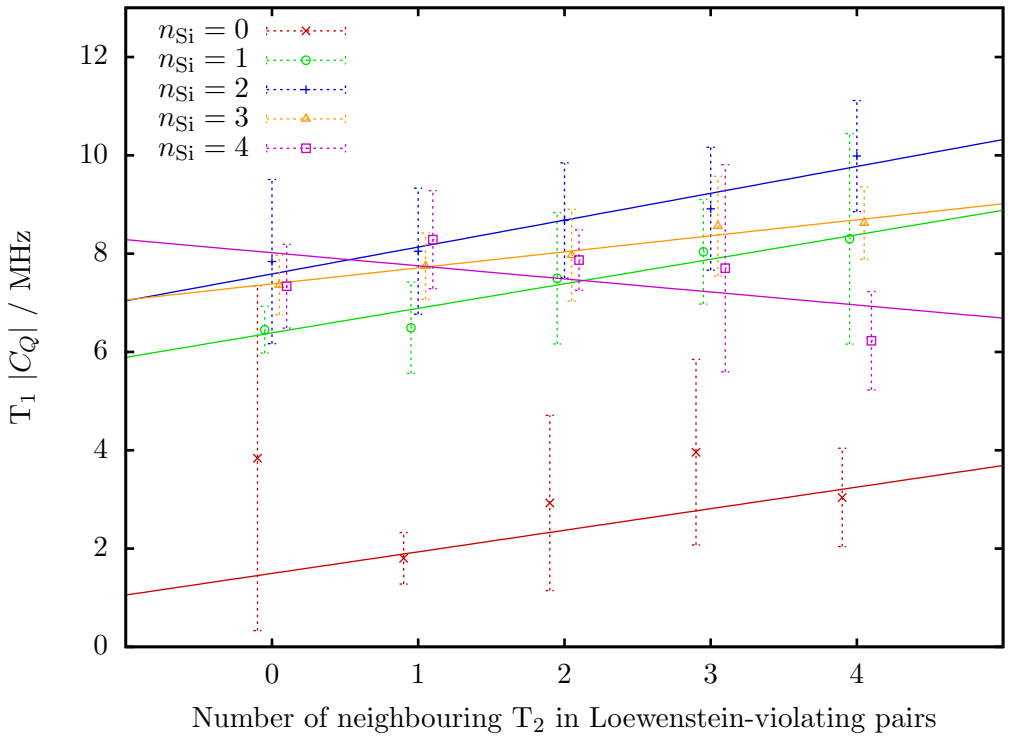

Figure 6.7: Correlation of the T_1 EFG C_Q versus number of neighbouring T_2 sites in Loewenstein rule-violating pairs. Error bars represent the standard deviation in the samples.

(109.47°),

$$|\phi| = \sum_i |\tan(\theta_i - \theta_0)|, \tag{6.15}$$

where $\theta_0 = 2\arctan(\sqrt{2})$, and the mean of the log of the ratio of the T_1−O bond lengths with their mean lengths (l_0),

$$|\alpha| = \sum_i |\ln(l_i/l_0)|. \tag{6.16}$$

Both these parameters are correlated with C_Q on the T_1 atom (see Fig. 6.8 for the

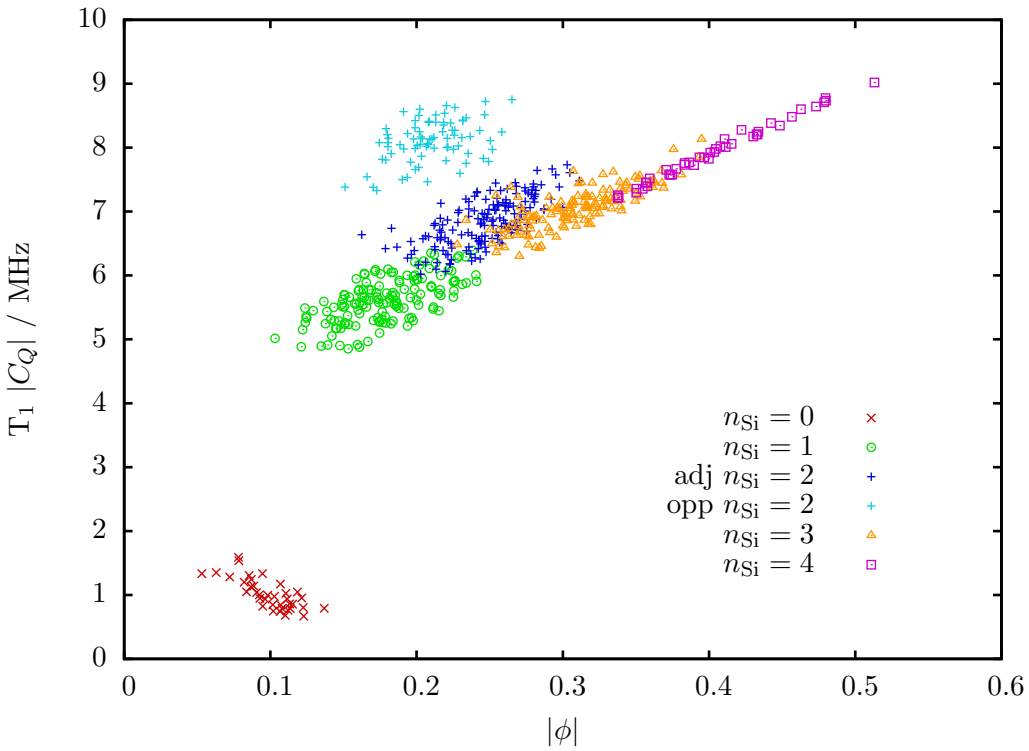

Figure 6.8: Correlation of the Ghose's shear strain parameter,[216] $|\phi|$, on the T_1 site oxygen tetrahedra versus the EFG C_Q on those sites. A clear correlation can be seen of increasing C_Q with increasing tetrahedral strain, except for $n_{Si} = 0$, where it decreases. One can also note a split in population for the $n_{Si} = 2$ environment, corresponding to situations in which (a) the neighbouring Si atoms are on adjacent bonds when projected onto the layer plane, labelled "adj", or (b) are on opposite bonds when projected to the layer plane, labelled "opp".

case of the shear strain).

These tetrahedral shear parameters are also linked to the number of Loewenstein rule-violating T_2 site neighbors to the T_1 site (see Fig. 6.9). This indicates that the increase in EFG may be due to the presence of Loewenstein rule-violating neighbors inducing a shear in the oxygen tetrahedron around the T_1 site.

The increase in the T_1 polyhedrons distortion is certainly an indirect effect of an imbalance in the Al p-type orbitals population from which the EFG is expected to

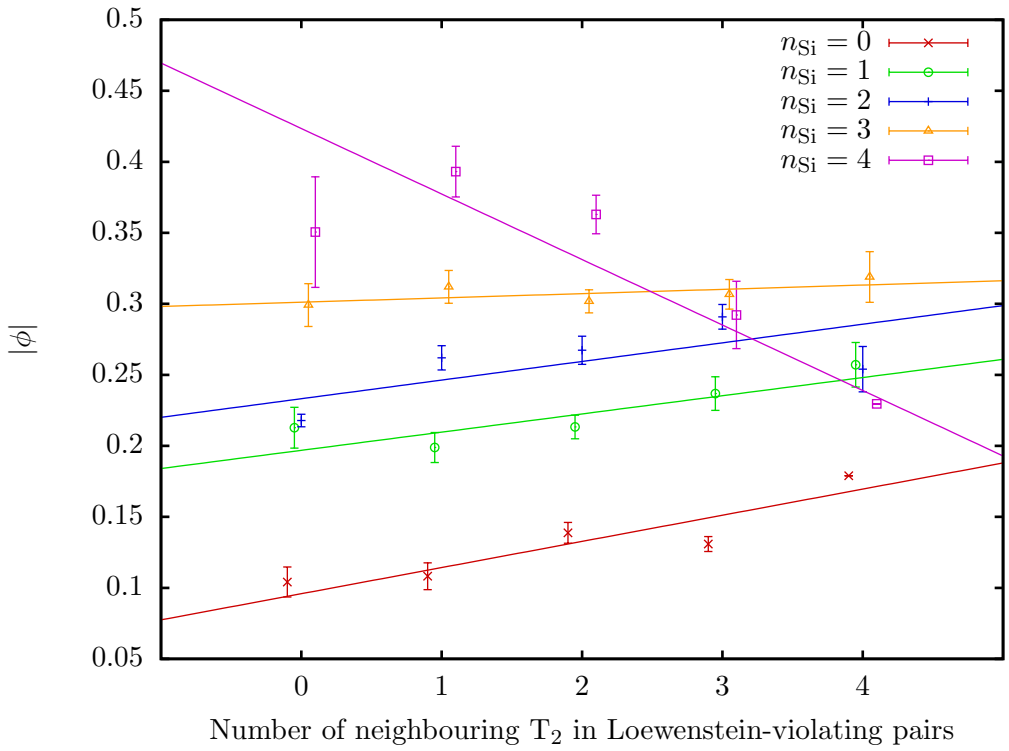

Figure 6.9: Correlation of the number of T_2 sites neighbouring a T_1 in a Loewenstein rule-violating pair and the mean of Ghose's shear strain parameter,[216] $|\phi|$, on the T_1 site oxygen tetrahedra. Error bars represent the error in the mean.

originate.[217]

The distribution of C_Q is significantly smaller in the case of the 'Loewenstein' structures, as there is a smaller range of tetrahedral bond angle and bond length distortion due to lower disorder, evidencing the direct link between the width of the distribution of NMR parameters and the Al/Si ordering.

The best agreement with the (difficult to measure) experimental C_Q distribution would be found intermediate between the random structures and the Loewenstein rule-obeying structures, as the level of Loewenstein rule violation in the random structures is excessively high for the experimental temperature and conversely excessively low for the Loewenstein-rule obeying structures. Indeed, p_{Al-Al} in the

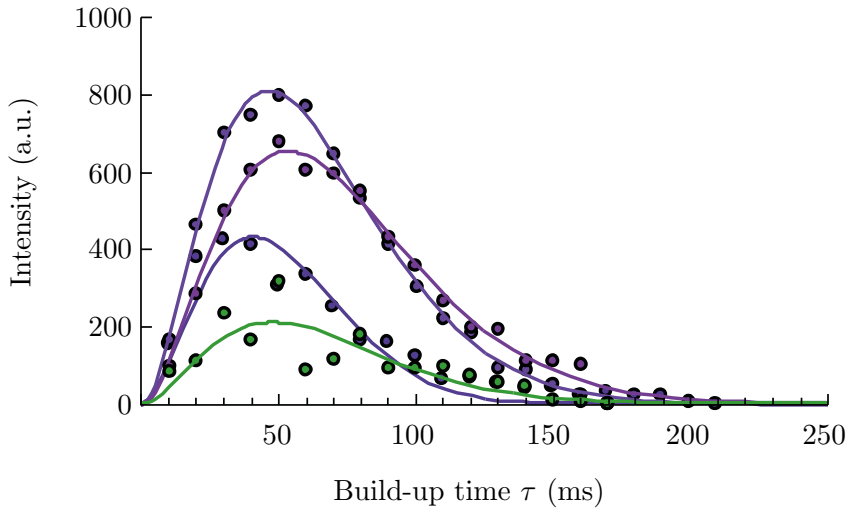

Figure 6.10: $\{^{29}\mathrm{Si}\}^{27}\mathrm{Al}$ double-quantum INEPT spectrum build-up curves. [Reprinted (adapted) with permission from Ref. 18. Copyright 2012 American Chemical Society.]

purely random case (relative populations of Al−Al, Al−Si, and Si−Si linkages in the ratios 1:2:1) approaches a high temperature limit, beyond that of the experimental heat treatments used.

6.5 J-coupling

6.5.1 Experiment

The $^{2}\mathrm{J}(\mathrm{Si}{-}\mathrm{O}{-}\mathrm{Al})$ couplings were estimated for some of the sites with a more intense $\{^{29}\mathrm{Si}\}^{27}\mathrm{Al}$ double-quantum INEPT signal by fitting a curve to the signal build-up, show in Fig. 6.10. The fitted parameters are listed in Table 6.2, finding a range of roughly 1–4 Hz for the $^{2}\mathrm{J}(\mathrm{T}_1\mathrm{Al}{-}\mathrm{O}{-}\mathrm{T}_2)$ couplings.

Table 6.2: Mean ^{2}J(T_1Al−T_2Si) parameters as a function of number of next-nearest neighbour Si atoms, n_{Si}, to the T_1 site, for both experiment and from first-principles calculations on the 'Loewenstein' and 'Random' structure sets.

Site		Mean J_{iso} / Hz		
Coupling	n_{Si}	Experiment	Random	Loewenstein
^{2}J(T_1Al−T_2Si)	1		-3.033 ± 0.225	-2.925 ± 0.484
^{2}J(T_1Al−T_2Si)	2	3.3 ± 0.5	-3.828 ± 0.209	-3.301 ± 0.332
^{2}J(T_1Al−T_2Si)	3	1.5 ± 0.3	-3.979 ± 0.420	-3.951 ± 0.689
^{2}J(T_1Al−T_2Si)	4	1.1 ± 0.4	-4.273 ± 0.316	-4.633 ± 0.463
^{2}J(T_1Al−T_2Al)	0		1.933 ± 0.540	1.793 ± 0.343
^{2}J(T_1Al−T_2Al)	1		2.468 ± 0.513	2.213 ± 0.466
^{2}J(T_1Al−T_2Al)	2		2.673 ± 0.619	2.459 ± 0.323
^{2}J(T_1Al−T_2Al)	3		2.625 ± 0.391	3.093 ± 0.268
^{2}J(T_2Al−T_2Si)	1	3.9 ± 2.3		-5.156 ± 0.210

6.5.2 Calculations

J-coupling constants were calculated for all supercells in the 'random' set, using the plane-wave norm-conserving pseudopotential PAW methodology, between a chosen T_1 site and all other sites in the supercell, and a chosen T_2 site and all other sites in the supercell. Norm-conserving pseudopotentials were used as the ultrasoft methodology had yet to be developed.

Previous work[36] has shown that the scalar ^{2}J(Si−O−Si) coupling constant of calcium silicates is closely related to the Si−O−Si bond angle, Ω, through the following relationship: $\Omega \sim 3.41J + 127$. The 2.8 ± 0.2 Hz range measured for gehlenite can hence be transformed into a $136.5° \pm 0.8°$ angular range, in good agreement with the value of $135.3° \pm 1.74°$ derived from the statistical analysis of the optimised random structures, hence this linear relationship appears to hold for calcium aluminosilicate to a very good approximation.

As seen in Fig. 6.11, calculated values of ^{2}J(Al−O−Si) for T_1 Al sites are found between 1 and 6 Hz, i.e. on a slightly larger range than the experimental values,

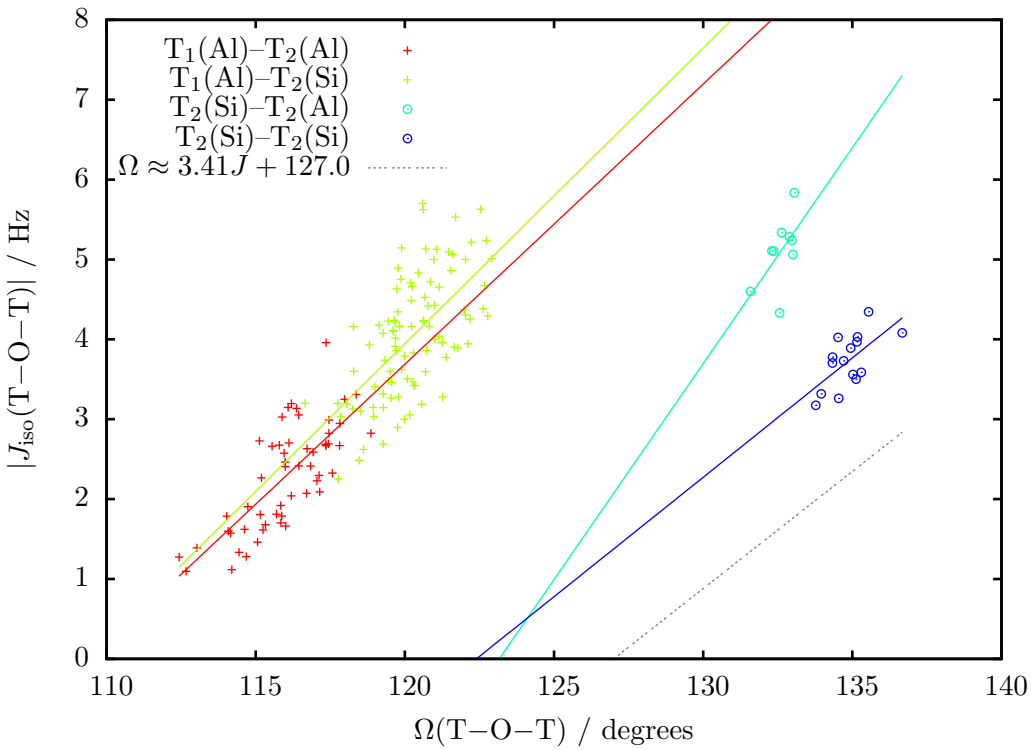

Figure 6.11: ^{2}J(T−O−T) for T_1 and T_2 sites in gehlenite versus the ∠T−O−T bond angle Ω. Good linear correlations between Ω and ^{2}J can be seen, with best fit lines plotted. Also plotted is the ^{2}J(Si−O−Si) relationship found in Ref. 36, $\Omega \sim 3.41J + 127$.

but difficult to measure, 1–4 Hz range. However, when the T_1 sites are broken down by n_{Si}, the calculations predict a different qualitative trend than the experimental estimates for the couplings as a function of n_{Si}. This experimental trend, however, is based on relatively imprecise measurements of small couplings.

The calculated ^{2}J(T_2Al−O−T_2) couplings are found to be similarly correlated with Ω, $\Delta J/\Delta\Omega = 0.351 \pm 0.043$ deg/Hz for ^{2}J(Al−O−Al) and $\Delta J/\Delta\Omega = 0.312 \pm 0.061$ deg/Hz for ^{2}J(Al−O−Si).

The calculated ^{2}J(T_2−O−T_2) couplings are defined on a much smaller range of angles, but the best-fit correlation with Ω finds that $\Delta J/\Delta\Omega = 0.541 \pm 0.279$ Hz/deg

for ^{2}J(Si−O−Al) and $\Delta J/\Delta\Omega = 0.299 \pm 0.101$ Hz/deg for ^{2}J(Si−O−Si), very similar to the 0.293 Hz/deg slope found for Si−O−Si in calcium silicates,[36] although systematically larger, as can be seen in Fig. 6.11.

There is no observable difference between the 'random' and 'Loewenstein' set in the J-coupling, as opposed to the significant difference observed for the EFG. While the T_1 EFG arises from the bonding with the four neighboring oxygen atoms, the scalar coupling depends on the hybridisation state of the Al−O−T_2 linkage, less so to the specifics of the Al-centered polyhedron.

The scalar coupling also seems to be influenced by the number of non-bonding oxygens bonded to the site considered, as opposed to what has been expected for silicates.[36]

Overall, the very small values encountered here will prevent its precise measurement and hence its quantitative use from a structural point of view. However, future developments in experiments that allow more precise measurements of small J-couplings in such materials will increase its relevance for quantitative structural analysis.

6.6 Conclusions

Comparisons of experimental EFGs to ab-initio calculations have been shown to be an effective probe of local disorder, not just by providing a decomposition into local environments but also by allowing us to understand structural trends. By introducing an efficient decomposition of the different contributions to the EFG tensor, using PAW, the local electronic environment was found to be the dominant contribution to T_1 site C_Q values in gehlenite. The local structural strains that affect the local electronic environment appear to be caused by disorder in the T_2 sites, principally the presence of neighbouring Loewenstein rule-violating T_2 pairs.

We have also demonstrated that scalar coupling is a good local probe of continuously disordered parameters, such as bond angles, in agreement with previous empirical trends,[36] through the induced atomic environment. However, its effectiveness is limited by the small scalar couplings in materials such as gehlenite. This means that quantative use of such calculations is only applicable to materials with larger scalar couplings until future experimental techniques that can measure small J with greater precision are developed, though this does demonstrate the value of calculations in determining observability of couplings for experimental design.

Together these demonstrate the power of combining solid-state NMR with ab-initio calculations to explore and build accurate models of disordered materials.

Chapter 7

Silver-phosphine molecular crystal systems

7.1 Introduction

Molecular crystals are a common form of matter in nature, forming many organic and inorganic solids. While conventional local-orbital methods may be able to treat the molecules in isolation for the prediction of NMR parameters, intermolecular effects, beyond structural changes, such as long-range electrostatics can be important.[14] Treatment of such systems using the full crystallographic cell and periodic boundary conditions may be important for achieving a full level of accuracy.

We will examine a family of molecular crystals that consist of a silver atom bonded to a varying complex and to phosphorous atoms, each bonded to three phenyl groups, sometimes with solvent molecules present. Both $^{1}J(^{31}P-^{107,109}Ag)$ and $^{2}J(^{31}P-^{107,109}Ag-^{31}P)$ couplings have been measured using solid-state NMR, making it an ideal test of the current plane-wave pseudopotential methodology, par-

ticularly the relevance of special relativistic effects. These are also experimentally attractive compounds, as each of the ^{31}P and ^{107,109}Ag nuclei are spin-$\frac{1}{2}$, and so there are no electric quadrupole coupling effects to complicate measurements.

7.2 Experiment and structures

The molecules examined are shown in Fig. 7.1, their structures are from a variety of sources given in Table 7.1. The structres were all determined by X-ray diffraction (XRD).

From these experimental structures, geometry optimisations were performed using ultrasoft pseudopotentials with a cut-off energy of 50 Ry on the full crystal unit cell. Atoms of all elements were allowed to move in order to their minimise forces experienced. The experimental cell lattice parameters were kept constant.

The experimental NMR J-coupling values for structures gb1054 and gb1038 are from Bowmaker *et al.*,[224] the others from an unpublished experimental collaboration. The experiments were ^{31}P CPMAS solid-state NMR, and are quoted for both ^{107}Ag ($\gamma = -1.0889181 \times 10^7\,\mathrm{rad\,s^{-1}\,T^{-1}}$) and ^{109}Ag ($\gamma = -1.2518634 \times 10^7\,\mathrm{rad\,s^{-1}\,T^{-1}}$), both of roughly equal natural abundance, when distinguishable. When converted to reduced couplings these should give the same value, neglecting isotope effects such as nuclear motion which, due to the closeness of the atomic masses, are likely to be small. Hence, a difference in reduced couplings could be considered as an indication of the experimental error.

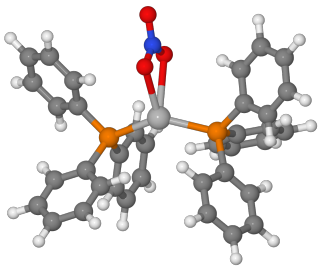

(a) Structure 2

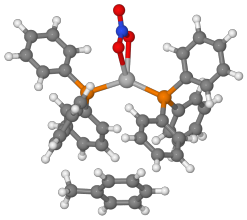

(b) Structure 3

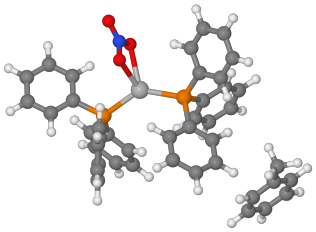

(c) Structure 4

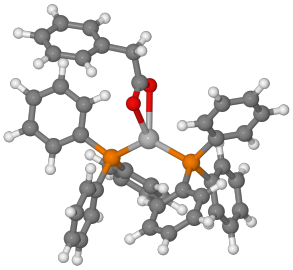

(d) Structure 5

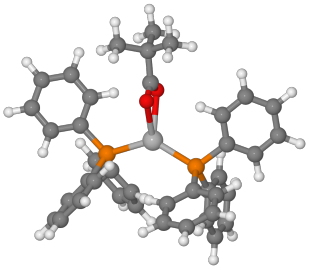

(e) Structure 6

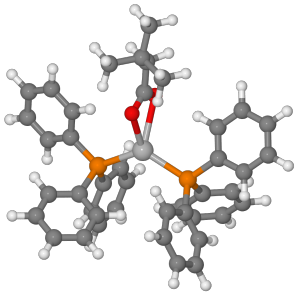

(f) Structure 8

Figure 7.1: The molecules examined in this chapter, shown as isolated molecules rather than in their full crystal. The numbering is for consistency with experimental collaborators.

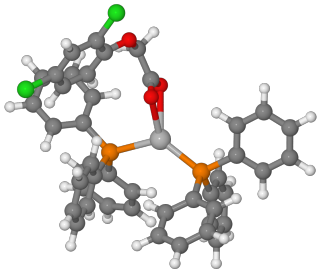

(g) Structure 12

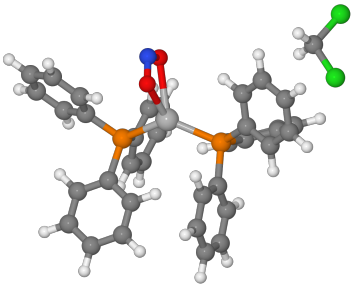

(h) Structure 14

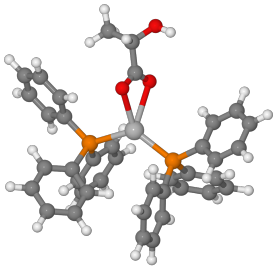

(i) Structure 17

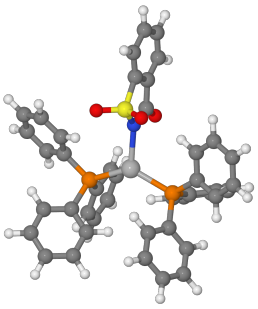

(j) Structure 18

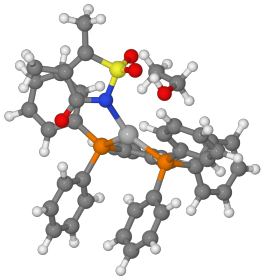

(k) Structure 19

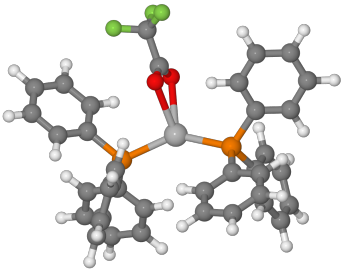

(l) Structure 21

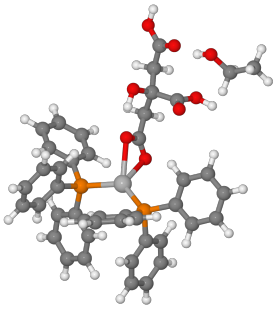

(m) Structure 22

7.3 Calculations

7.3.1 Convergence testing

Energy cut-off

Table 7.2 shows the convergence of calculated couplings in an isolated molecule of structure 2 with respect to the cut-off energy of the plane-wave basis set used (E_{cut}). As good level of convergence is achieved by $E_{\text{cut}} = 50\,\text{Ry}$.

Inclusion of semi-core orbitals in pseudopotential valence

Inclusion of some high lying core orbitals in the valence of a pseudopotential can sometimes improve the accuracy of calculations if they are chemically active. To investigate this, the 4p and 4s orbitals were added to the silver pseudopotential. Table 7.3 illustrates the level of improvement to be had in an isolated molecule of structure 2.

The inclusion of both the 4s and 4p in the silver pseudopotential gives a modest increase in the coupling, approximately $17 \times 10^{19}\,\text{T}^2\,\text{J}^{-1}$. However, this came at the cost of roughly doubling the memory requirements of the calculation due to the extra electrons treated and storage of projector arrays.

7.3.2 Plane-wave pseudopotential calculations

We have calculated J-couplings using both non-relativistic theory and ZORA scalar-relativistic theory with ultrasoft pseudopotentials for all crystals with all atomic positions optimised, a 50 Ry energy cut-off and a single k-point — as all cells were

Table 7.1: The molecular crystals examined, with references, chemical formulae and, if present, solvent. The molecules are illustrated in Fig. 7.1.

Number	Reference	Formula	Solvent	No. atoms in cell
2.	218	$(Ph_3P)_2Ag(NO_3)$	None	146
3.	218	$(Ph_3P)_2Ag(NO_3)$	Toluene (1)	176
4.	218	$(Ph_3P)_2Ag(NO_3)$	Toluene (2)	352
5.	*	$(Ph_3P)_2Ag(O_2CCH_2Ph)$	None	172
6.	*	$(Ph_3P)_2Ag(O_2CC(CH_3)_3)$	None	340
8.	*	$(Ph_3P)_2Ag(O_2CCH_2C(CH_3)_3)$	None	352
12.	219	$(Ph_3P)_2Ag(O_2CCH_2O\text{-}C_6H_3\text{-}2,4Cl_2)$	None	348
14.	220	$(Ph_3P)_2Ag(NO_2)$	CH_2Cl_2	154
17.	221	$(Ph_3P)_2Ag(O_2C(OH)CHCH_3)$	None	160
18.	222	$(Ph_3P)_2Ag(NS(O_2)C_6H_4C(O))$	None	340
19.	222	$(Ph_3P)_2Ag(NS(O_2)C(CH_3)C(CH_3)C(O))$	None	188
21.	223	$(Ph_3P)_2Ag(CF_3CO_2)$	None	608
22.	*	$(Ph_3P)_2Ag(C_6H_7O_7)$	CH_3CH_2OH	196
gb1054	224	$(Ph_3P)_2Ag(O_2COH)$	None	148
gb1038	224	$\{(Ph_3P)_2Ag\}_2(CO_3)$	$2H_2O$	296

* Supplied by collaborator

Table 7.2: Convergence with respect to the cut-off energy of couplings in an isolated molecule of structure 2. Reduced couplings are given in units of $10^{19}\,T^2\,J^{-1}$.

E_{cut} / Ry	^1K(Ag−P1)	^1K(Ag−P2)	^2K(P1−Ag−P2)
20	1986.986	1936.440	60.773
30	2007.986	1956.620	61.662
40	2009.932	1958.332	61.722
50	2010.092	1958.485	61.742
60	2010.135	1958.680	61.758
70	2010.208	1958.752	61.763

Table 7.3: Illustration of improvement by inclusion of semi-core states in the valence of the ultrasoft pseudopotential in an isolated molecule of structure 2. Reduced isotropic couplings are given in units of $10^{19}\,T^2\,J^{-1}$.

Ag valence	P valence	^1K(Ag−P1)	^1K(Ag−P2)
4d5s5p	3s3p3d	2009.805	1958.125
4p4d5s5p	3s3p3d	2005.428	1954.578
4s4d5s5p	3s3p3d	2009.245	1959.292
4s4p4d5s5p	3s3p3d	2026.145	1976.190

of sufficient size to avoid perturbation image effects. Tables 7.4 and 7.5 show the calculated couplings.

The non-relativistic predicted values are in poor agreement with experiment, systematically underestimating both ^{1}K(P−Ag) and ^{2}K(P−Ag−P).

When a relativistic pseudopotential is used on the silver atom both sets of couplings are significantly improved with respect to experiment, although ^{1}K(P−Ag) still systematically underestimates even the lower end of the quoted experimental ranges.

There are two effects that can be discussed separately. The first is the indirect effect of relativity on the couplings by its effect on the ground-state electronic structure, which will be visible in changes in the ^{1}K(P−Ag) and ^{2}K(P−Ag−P) couplings. This effect has previously been noted studies involving two-bond coupling through a heavy ion.[21] The second is the direct effect of relativity due to the modifications to the coupling perturbation operators, which will be visible in the ^{1}K(P−Ag) couplings. Both of these are present, indirect effects are visible in the increase in the ^{2}K(P−Ag−P) couplings, and both direct and indirect effects together, albeit not disentangleable, are in the increase of the ^{1}K(P−Ag) couplings.

7.3.3 Local orbital calculations

In order to determine the source of the remaining source of error with experiment, calculations were performed by including spin-orbit effects and using the PBE0 hyrbid functional. These two extra contributions were shown to be important by Moncho and Autschbach[116] for row six elements. As neither spin-orbit effects nor the use of hybrid functional have been implemented for the calculation of J-coupling tensors in plane-wave pseudopotential codes, a local-orbital code must be used. The

Table 7.4: Calculated and experimental isotropic reduced coupling constants (K), in $10^{19}\,\mathrm{T^2\,J^{-1}}$. For K^{ZORA}_{Calc} silver atoms were treated with relativistic pseudopotentials and ZORA modified operators. Experimental couplings have not been supplied for structures 5–9.

Structure	Site A	Site B	K^{NRel}_{Calc}	K^{ZORA}_{Calc}	$K^{\mathrm{Ag109}}_{\mathrm{Exp}}$	$K^{\mathrm{Ag107}}_{\mathrm{Exp}}$
2.	Ag	P 1	1548.66	2043.54	2485.88	2322.65
	Ag	P 2	1551.78	2046.42	2345.77	2323.11
	P 1	P 2	44.58	61.53	50.75	65.11
3.	Ag	P 1	1574.76	2060.02	2309.15	2491.00
	Ag	P 2	1493.68	1961.37	2201.84	2302.71
	P 1	P 2	43.80	60.30	67.95	60.97
4.	Ag	P 1	1449.08	1903.20	2200.53	2241.58
	Ag	P 2	1560.80	2038.83	2381.60	2400.94
	P 1	P 2	46.27	62.79	67.95	67.33
5.	Ag	P 1	1344.02	1748.86		
	Ag	P 2	1334.55	1749.64		
	P 1	P 2	47.32	61.91		
6.	Ag	P 1	1409.59	1843.57		
	Ag	P 2	1310.08	1702.24		
	P 1	P 2	46.41	60.96		
8.	Ag	P 1	1347.52	1759.11		
	Ag	P 2	1340.53	1744.18		
	P 1	P 2	45.97	60.09		

$*$ ^{107}Ag and ^{109}Ag couplings were not resolved separately in experiment.

Table 7.5: Calculated and experimental isotropic reduced coupling constants, in $10^{19}\,\mathrm{T^2\,J^{-1}}$. For K^{ZORA}_{Calc} silver atoms were treated with relativistic pseudopotentials and ZORA modified operators.

Structure	Site A	Site B	K^{NRel}_{Calc}	K^{ZORA}_{Calc}	$K^{\mathrm{Ag109}}_{\mathrm{Exp}}$	$K^{\mathrm{Ag107}}_{\mathrm{Exp}}$
12.	Ag	P 1	1554.25	2041.21	2132.16	2451.22*
	Ag	P 2	1217.46	1585.89	1671.57	1921.70*
	P 1	P 2	49.58	65.48	70.18	70.18
14.	Ag	P 1	1379.04	1787.23	1990.78	2288.68*
	Ag	P 2	1258.68	1620.05	1802.42	2072.13*
	P 1	P 2	43.16	56.64	60.95	60.95
17.	Ag 1	P 1	1429.28	1887.32	2069.37	2379.03*
	Ag 1	P 2	1170.02	1516.32	1741.38	2001.96*
	Ag 2	P 3	1429.58	1885.33	2069.37	2379.03*
	Ag 2	P 4	1169.63	1514.18	1741.38	2001.96*
	P 1	P 2	49.13	64.18	71.86	71.86
	P 3	P 4	49.13	64.00	71.86	71.86
18.	Ag 1	P 1	1354.17	1767.94	1937.65	2227.60*
	Ag 1	P 2	1425.18	1869.94	2139.63	2459.80*
	Ag 2	P 3	1355.51	1767.33	1937.65	2227.60*
	Ag 2	P 4	1426.34	1868.91	2139.63	2459.80*
	P 1	P 2	50.06	66.23	65.06	65.06
	P 3	P 4	50.06	66.07	65.06	65.06
19.	Ag	P 1	1285.05	1691.45	1725.58	1983.79*
	Ag	P 2	1426.63	1889.36	2038.86	2343.95*
	P 1	P 2	42.84	57.64	60.55	60.55
21.	Ag	P 1	1429.83	1867.77	2129.53	2200.34
	Ag	P 2	1561.66	2039.01	2374.09	2491.60
	P 1	P 2	40.64	55.98	56.03	56.64
22.	Ag	P 1	1291.64	1683.16	1894.18	1982.78
	Ag	P 2	1575.36	2064.07	2371.46	2390.14
	P 1	P 2	43.45	58.64	67.75	66.53
gb1054	Ag	P 1	1481	1952	2059	2398
	Ag	P 2	1492	1958		
	P 1	P 2	53.0	70.6	74.5	74.5
gb1038	Ag 1	P 1	1259	1644	1848	2125*
	Ag 1	P 2	1398	1849		
	Ag 2	P 3	1470	1919		
	Ag 2	P 4	1229	1583		

* ^{107}Ag and ^{109}Ag couplings were not resolved separately in experiment.

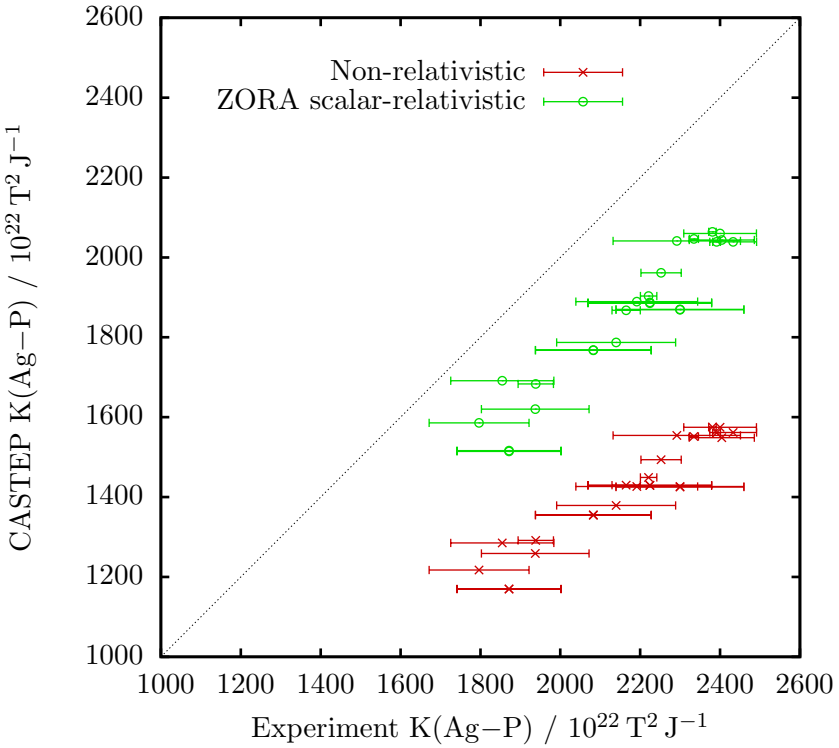

Figure 7.1: Experimental versus calculated K(Ag−P) J-couplings in various silver molecular crystals. The calculations were performed at a non-relativistic and ZORA scalar-relativistic level of theory. The experimental error bars are derived from the spread in K values for ^{107}Ag and ^{109}Ag experiments.

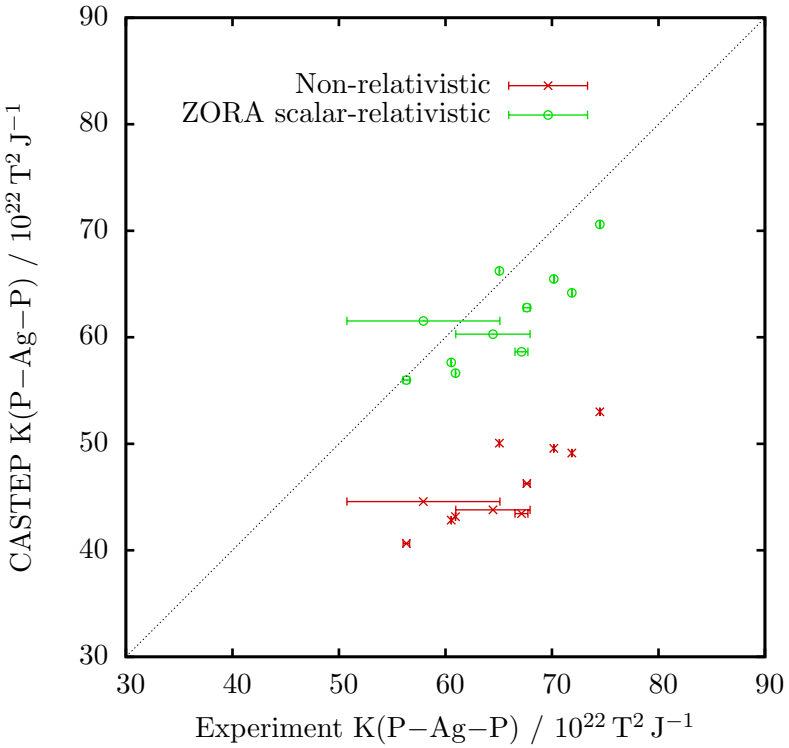

Figure 7.2: Experimental versus calculated K(P−Ag−P) J-couplings in various silver molecular crystals. The calculations were performed at a non-relativistic and ZORA scalar-relativistic level of theory. The experimental error bars are derived from the spread in K values for ^{107}Ag and ^{109}Ag experiments.

Amsterdam density-functional (`ADF`) code was chosen for its mature relativistic J-coupling implementation — allowing both inclusion of spin-orbit effects and use of hybrid functionals.

The `ADF` calculations were performed by Vaida Arcisauskaite, of the Department of Chemistry at the University of Oxford.

To reduce computational cost, only isolated molecules were treated. Three molecules with relatively small complexes and possessing a range of couplings, structures 2, 14 and 21, were chosen to be examined. Their structures were created by extracting single molecules from the relaxed crystal structures, thus still taking into account structural effects of crystal packing. The basis set chosen was QZ4P on the coupled atoms and TZ2P on other atoms, there was no frozen core, and a point-like nucleus was used. The functionals used were PW92/PBE and PW92/PBE0 for the ground-state and VWN/PBE and VWN/PBE0 for the first-order response.

The calculated couplings are displayed in Table 7.6, alongside scalar-relativistic PBE calculations using `Castep` for both the full crystal and for the isolated molecule (including any solvent molecule) for comparison and estimation of the effect of the crystal packing on the couplings, and plotted in Fig. 7.3.

The inclusion of spin-orbit effects has a small effect on the coupling, a reduction of approximately $30 \times 10^{19}\,\mathrm{T^2\,J^{-1}}$ in the ^{1}K(Ag−P) couplings. The use of the PBE0 hyrbid functional, however, has quite a significant effect, increasing the ^{1}K(Ag−P) couplings by approximately $250 \times 10^{19}\,\mathrm{T^2\,J^{-1}}$.

The scalar-relativistic calculations using the PBE0 functional have the best RMSD agreement with experiment, of 29.53 and $3.08 \times 10^{19}\,\mathrm{T^2\,J^{-1}}$ for ^{1}K(Ag−P) and ^{2}K(P−Ag−P) couplings respectively. The next best are the spin-orbit including relativistic calculations using the PBE0 functional, with RMSDs of 50.83 and $3.14 \times 10^{19}\,\mathrm{T^2\,J^{-1}}$

respectively.

One would expect that going from scalar-relativistic to spin-orbit including levels of theory would improve the agreement with experiment, however it hasn't. This can in fact be explained by the calculations being on isolated molecules rather than the full crystal. We can estimate the effect of being packed in a crystal on the couplings by taking the difference between a plane-wave pseudopotential calculation on the crystal and the same calculation on an isolated molecule, which we shall term the "crystal correction" (CC). Adding the CC on to the various levels of local-orbital theory, shown in Table 7.7 and Fig. 7.3, shows that the agreement of the spin-orbit level of theory improves to RMSDs of 29.27 and $2.38 \times 10^{19}\,\mathrm{T^2\,J^{-1}}$ respectively, within the estimated experimental error for the majority of couplings, whereas the agreement of the scalar-relativistic level of theory worsens to RMSDs of 44.30 and $2.47 \times 10^{19}\,\mathrm{T^2\,J^{-1}}$ respectively.

7.4 Conclusions

In this chapter we have demonstrated the ability of the presented plane-wave pseudopotential scalar-relativistic method to predict isotropic NMR J-coupling constants in molecular crystals of moderate size, hundreds of atoms in a unit cell, an advance on methods that, due to computational cost, can only treat small isolated molecules.

We have also examined the source of the remaining errors in the calculations, finding that when spin-orbit effects are included, hybrid functionals are used and crystal packing is accounted for, a within-error agreement with experiment is achieved.

Table 7.6: Reduced isotropic coupling values, in $10^{19}\,\mathrm{T^2\,J^{-1}}$, for selected molecules, showing level of improvement in agreement with experiment when including spin-orbit effects and using the PBE0 hybrid functional. Experimental errors estimated by spread in reported ^{107}Ag and ^{109}Ag couplings. The `ADF` calculations were performed by Vaida Arcisauskaite, of the Department of Chemistry at the University of Oxford.

Structure 2		`Castep`		`ADF` (molecule)				Experiment	
Site A	Site B	Crystal	Molecule	SR PBE	SR PBE0	SO PBE	SO PBE0		
Ag	P 1	2043.00	2010.00	2141.10	2371.77	2115.03	2344.05	2404.27	± 81.62
Ag	P 2	2045.00	1958.00	2060.66	2299.85	2034.72	2272.23	2334.44	± 11.33
P 1	P 2	61.50	61.75	64.90	62.05	64.32	61.54	57.93	± 7.18
Structure 14									
Ag	P 1	1787.23	1705.66	1810.86	2095.87	1783.97	2067.08	2139.73	± 148.95
Ag	P 2	1620.05	1556.92	1668.19	1926.87	1640.80	1897.97	1937.27	± 134.86
P 1	P 2	56.64	55.28	56.32	57.77	55.73	57.25	60.95	± 0.00
Structure 21									
Ag	P 1	1867.77	1829.09	1942.95	2194.92	1917.11	2167.44	2164.94	± 35.41
Ag	P 2	2039.01	2042.68	2167.44	2425.91	2144.97	2398.55	2432.85	± 58.75
P 1	P 2	55.98	54.83	57.44	55.47	56.84	54.94	56.64	± 0.00
RMSD ^{1}J(Ag−P)				272.18	29.53	297.84	50.83		
RMSD ^{2}J(P−P)				4.85	3.08	4.76	3.14		

Table 7.7: Reduced isotropic coupling values, in $10^{19}\,\mathrm{T^2\,J^{-1}}$, for the selected molecules with a "crystal correction" (CC), estimated from the difference between isolated molecule and full crystal `Castep` calculations, added on to calculations using the PBE0 functional at scalar-relativistic (SR PBE0) and spin-orbit (SO PBE0) levels of theory calculated using the `ADF` local-orbital code. Root mean-squared deviations (RMSD) from experiment are shown for ^{1}K(Ag−P) and ^{2}K(P−Ag−P) couplings.

Structure 2		Corrected `ADF` (molecule)		Experiment	
Site A	Site B	SR PBE0 + CC	SO PBE0 + CC		
Ag	P 1	2404.77	2377.05	2404.27	± 81.62
Ag	P 2	2386.85	2359.23	2334.44	± 11.33
P 1	P 2	61.80	61.29	57.93	± 7.18
Structure 14					
Ag	P 1	2177.44	2148.65	2139.73	± 148.95
Ag	P 2	1990.00	1961.10	1937.27	± 134.86
P 1	P 2	59.13	58.61	60.95	± 0.00
Structure 21					
Ag	P 1	2233.60	2206.12	2164.94	± 35.41
Ag	P 2	2422.24	2394.88	2432.85	± 58.75
P 1	P 2	56.62	56.09	56.64	± 0.00
RMSD ^{1}J(Ag−P)		44.30	29.27		
RMSD ^{2}J(P−P)		2.47	2.38		

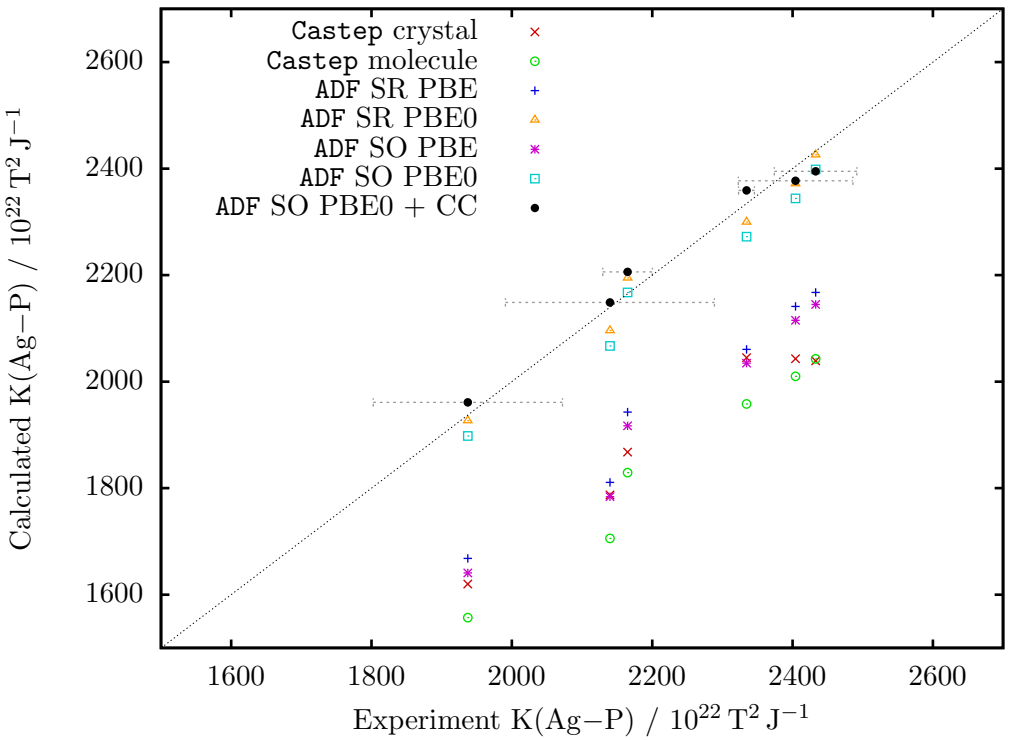

Figure 7.3: Comparison of calculated reduced isotropic coupling values, in 10^{19} T^2 J^{-1}, for the selected molecules at various levels of theory against experimental values.

Chapter 8

J-coupling in Pb_2ZnF_6

In this chapter, a theoretical study of J-coupling in lead fluoride systems is presented, based on published experimental papers. Discrepencies between experimentally measured J-couplings and those calculated with the published structures are found and discussed, with relevance to the experimental and theoretical investigation of dynamics.

8.1 Pb_2ZnF_6 experiments

Pb_2ZnF_6 is a recrystallisation product of the ternary transition metal glass family PbF_2-ZnF_2-GaF_3.[225] It has fluorine mobility and anionic conductivity. It was investigated in Ref. 226, where it was noted that the room temperature structure of Pb_2ZnF_6 had never been fully determined, although it had been previously studied using 1D MAS NMR spectroscopy.[227,228] In addition, they describe a new transition at above room temperature to a new phase, which they name β-Pb_2ZnF_6. They go on to perform X-ray powder diffraction (XRPD), ^{19}F NMR, ^{207}Pb NMR and ^{67}Zn NMR on Pb_2ZnF_6 and, with ab-initio calculations, propose a structure for the β

form.

The XRPD was performed at $T = 25\,^{\circ}\mathrm{C}$ and $90\,^{\circ}\mathrm{C}$. The ^{19}F NMR and ^{207}Pb NMR was performed at $T = 28\,^{\circ}\mathrm{C}$, $57\,^{\circ}\mathrm{C}$, $69\,^{\circ}\mathrm{C}$ and $90\,^{\circ}\mathrm{C}$. The ^{19}F Hahn-echo NMR was performed at $T = 70\,^{\circ}\mathrm{C}$ and the ^{67}Zn Hahn-echo NMR was performed at $T = 100\,^{\circ}\mathrm{C}$.

Their differential thermal analysis (DTA) data suggests that Pb_2ZnF_6 has two phases: a room temperature phase, α-Pb_2ZnF_6; and a higher temperature phase, β-Pb_2ZnF_6. The α phase has a lower symmetry than the β phase, observed as more peaks in the XRPD spectrum of the α phase ($T = 25\,^{\circ}\mathrm{C}$) than the β phase ($T = 90\,^{\circ}\mathrm{C}$) and a reduction in the number of ^{19}F and ^{207}Pb lines in NMR experiments above $T = 60\,^{\circ}\mathrm{C}$.

Two candidate structures were created by the authors of Ref. 226. Structure 1 was derived from the XRPD spectrum and is shown in Fig. 8.1, with the fluorine sites labelled. In this structure of β-Pb_2ZnF_6 there is one lead site, one zinc site, and five fluorine sites. There are alternating layers of corner sharing lead-fluorine tetrahedra and corner sharing zinc-fluorine octahedra. In the zinc-fluorine layers, the Zn and F are arranged in two orthogonal sets of chains, one containing the F2 and the other the F3 fluorine sites. All FX−Zn−FX have an angle of 180°. The F2 chains are described as having a 180° Zn−F2−Zn angle and the F3 chains are described as having a 139.7° Zn−F3−Zn angle.

Structure 2 is the other structure reported in Ref. 226. The density functional forces were minimised using the `Wien2k` linearised augmented plane-wave (LAPW) code with, as reported, a $R_{\mathrm{MT}}K_{\max} = 8$, 100 k-points and with electron exchange-correlation described by the PBE functional. Forces on ions were minimised to below 1.8 mRy per bohr, or approximately 46 meV/Å. The lattice vectors were fixed at their experimental values. It was not specified if symmetry constraints were

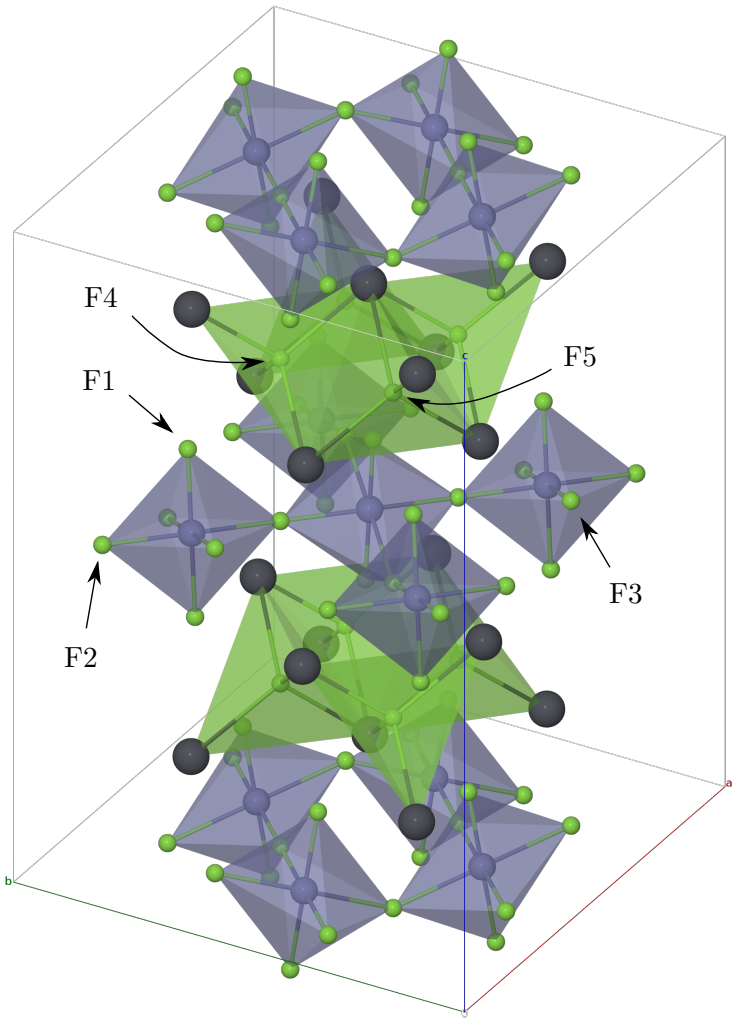

Figure 8.1: Unit cell structure of β-Pb_2ZnF_6 with the fluorine sites labeled, from the XRPD structure (1) determined in in Ref. 226. Grey spheres correspond to lead atoms, green to fluorine and blue to zinc.

Table 8.1: Summary of structural parameters, including standard deviations where appropriate, of the ZnF_6 octahedra in various Pb_2ZnF_6 models. The parameter $|\psi|$ is Ghose and Tsang's[216] polyhedral distortion parameter, Eqn. 6.15.

Parameter	1. XRPD	2. `Wien2k`	3. α'	4. β'
∠ F1−Zn−F1	180.0°	180.0°	$176.4 \pm 2.0°$	$179.5 \pm 0.3°$
∠ F2−Zn−F2	180.0°	180.0°	$178.7 \pm 0.8°$	$179.4 \pm 0.3°$
∠ F3−Zn−F3	180.0°	180.0°	$178.2 \pm 1.1°$	$179.7 \pm 0.1°$
∠ F1−Zn−F2	90.0°	90.0°	$84.6 \pm 2.6°$	$89.0 \pm 0.7°$
∠ F1−Zn−F3	79.0°	85.7°	$84.7 \pm 2.9°$	$87.7 \pm 0.5°$
∠ F2−Zn−F3	90.0°	90.0°	$88.4 \pm 0.8°$	$89.5 \pm 0.3°$
∠ Zn−F2−Zn	180.0°	180.0°	$145.9 \pm 0.9°$	$156.9 \pm 1.4°$
∠ Zn−F3−Zn	139.7°	145.5°	$141.8 \pm 3.1°$	$148.0 \pm 0.3°$
|F1−Zn| / Å	1.95	2.02	2.01 ± 0.02	1.97 ± 0.00
|F2−Zn| / Å	1.99	1.99	2.08 ± 0.01	2.03 ± 0.01
|F3−Zn| / Å	2.12	2.09	2.11 ± 0.02	2.07 ± 0.00
$\|\psi\|$	0.78	0.30	0.85 ± 0.20	0.27 ± 0.08

applied, but it retains the same symmetry as the unrelaxed XRPD structure. As in structure 1, all FX−Zn−FX have an angle of 180°. The F2 chains are described as having a 180° Zn−F2−Zn angle and the F3 chains are described as having a 145.5° Zn−F3−Zn angle.

A summary of structural parameters for both structures is given in Table 8.1.

8.1.1 Zn electric field gradients

The quadrupolar coupling constant, C_Q on the Zn site was experimentally determined in Ref. 226 to be 8.3 ± 0.1 MHz and the quadrupolar asymmetry parameter, η_Q was determined to be 0.10 ± 0.05. Ab-inito caculations using `Wien2k` are also presented, with $C_Q = -7.7$ MHz and $\eta_Q = 0.64$ for the XRPD-derived structure (1) and $C_Q = 9.0$ MHz and $\eta_Q = 0.06$ for the `Wien2k`-relaxed structure (2).

New electric field gradient calculations have been performed with the `Castep` code[129,146] using a cut-off energy of 50 Ry, the PBE exchange-correlation functional, a single k-

Table 8.2: Zinc quadrupole coupling constants and asymmetry parameters from ab-inito electic field gradient calculations on the proposed structures, using both the `Wien2k` (reported in Ref. 226) code and `Castep` code (this work). An updated `Wien2k` calculation on structure 1 is also presented.[229]

Structure	Code	$\lvert C_Q \rvert$ / MHz	η_Q
1. XRPD	`Wien2k`	7.7	0.64
1. XRPD	`Wien2k` new	18.6	0.75
2. `Wien2k`	`Wien2k`	9.0	0.06
1. XRPD	`Castep`	19.7	0.75
2. `Wien2k`	`Castep`	9.25	0.07
3. α'	`Castep`	12.7 ± 1.9	0.36 ± 0.17
MD mean 1	`Castep`	10.7	0.02
MD mean 2	`Castep`	10.9 ± 0.8	0.23 ± 0.14
4. β'	`Castep`	11.6 ± 0.4	0.52 ± 0.08
Experiment		8.3 ± 0.1	0.10 ± 0.05

point, and ultrasoft pseudopotentials. The pseudopotential describing the Zn atoms treat the 3s and 3p states in the valence. The C_Q and η_Q values are presented in Table 8.2, along with the original `Wien2k` calculations.

The agreement of values calculated for structure 1 between codes is poor, `Castep` predicting $C_Q = 19.7\,\text{MHz}$ compared to $-7.7\,\text{MHz}$ as reported in Ref. 226. The asymmetry parameter η_Q are in reasonable agreement, 0.64 versus 0.75. The agreement between values calculated for structure 2, however, is good and compares well to experiment. `Castep` predicts $C_Q = 9.25\,\text{MHz}$, `Wien2k` predicts $C_Q = 9.0\,\text{MHz}$ and experiment finds $C_Q = 8.3 \pm 0.1\,\text{MHz}$, so both marginally overestimate the quadrupole coupling frequency. The asymmetries are all consistent, being $\eta_Q = 0.06$, 0.07 and 0.10 ± 0.05 respectively.

The cause of the disagreement for structure 1, the XRPD-derived structure, is not clear, however repeats of the calculations[229] using `Wien2k` give a $C_Q = 18.6\,\text{MHz}$ and $\eta_Q = 0.75$, both now consistent with the `Castep` calculations. The `Castep` predictions are hence consistent with the conclusion in Ref. 226 that the `Wien2k`-

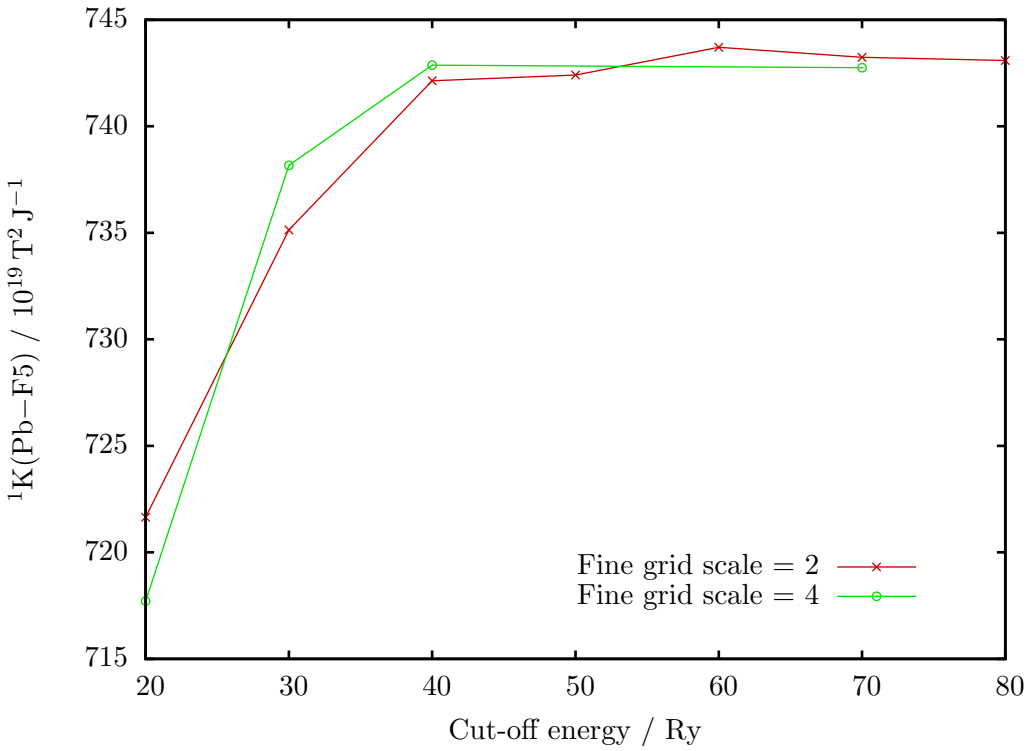

Figure 8.2: Convergence of a ^{1}K(Pb−F) coupling with respect to the plane-wave basis-set cut-off energy and scale of fine augmentation grid used. A energy cut-off of 40 Ry and fine augmentation grid scale of 4 is determined to give good numerical precision.

relaxed structure is most consistent with experiment and most likely provides the best physical description of β-Pb_2ZnF_6.

8.1.2 Pb−F J-coupling

Calculated and experimental[226] J-couplings of all five fluorine sites to the lead site are reported in Table 8.3 for the two β-Pb_2ZnF_6 structures. Calculations were performed using `Castep` with a converged (see Fig. 8.2) energy cut-off of 40 Ry, one k-point $(\frac{1}{4}, \frac{1}{4}, \frac{1}{4})$, ZORA ultrasoft pseudopotentials on the heavy ion (Pb) and Schrödinger ultrasoft pseudopotentials on the lighter ions (Zn and F). The inclusion

Table 8.3: J-couplings of all five fluorine sites to their four nearest lead neighbours in the two β-Pb_2ZnF_6 structures given in Ref. 226 (1 and 2). The mean is of the couplings to the underlined sites, which are the largest equivalent couplings.

Site	J_{iso} / Hz					
F1 (F63)	Pb 17	Pb 19	Pb 20	Pb 21	Mean	
1. XRPD	2339.92	2339.87	733.93	733.95	2340	
2. `Wien2k`	2760.82	2760.99	560.69	560.73	2761	
Experiment					2000	± 200
F2 (F51)	Pb 11	Pb 13	Pb 18	Pb 19	Mean	
1. XRPD	774.25	773.62	774.74	774.41	774	
2. `Wien2k`	815.48	814.74	816.17	815.88	815	
Experiment					1700	± 200
F3 (F59)	Pb 13	Pb 15	Pb 19	Pb 22	Mean	
1. XRPD	91.27	91.34	3077.79	3077.86	3078	
2. `Wien2k`	134.37	134.38	2802.30	2802.13	2802	
Experiment					3000	± 200
F4 (F75)	Pb 18	Pb 19	Pb 27	Pb 29	Mean	
1. XRPD	1994.36	1993.05	1992.39	1991.21	1993	
2. `Wien2k`	2073.63	2072.54	2074.32	2073.28	2073	
Experiment					1800	± 200
F5 (F81)	Pb 17	Pb 19	Pb 27	Pb 30	Mean	
1. XRPD	1523.04	1523.09	1959.45	1958.25	1959	
2. `Wien2k`	1196.11	1196.09	2626.45	2625.38	2626	
Experiment					1800	± 200

of relativity is important for the heavy lead ion, which is in row six of the periodic table.

The two structures are in good agreement with experiment for the couplings to lead from the F1, F3, F4 and F5 sites, the XRPD-derived structure (1) generally being better, there being larger errors of the order 800 Hz on sites F1 and F5 for structure 2. However, the ^{1}J(Pb−F2) coupling has serious disagreements for both structures 1 and 2, being roughly 800 Hz versus the 1700 ± 200 Hz observed in experiment. Exact agreement with experiment shouldn't be expected, as both fluorine and lead are known to be difficult to treat, lead likely needing spin-orbit effects to be taken into account and both requiring better descriptions of the electronic exchance-correlation energy. However, one should expect that the Pb−F couplings have a consistent systematic error. As the F2 site is the fluorine in the ZnF_6 octahedra with a Zn−F2−Zn bond angle of 180°, this is a possible indication of interesting dynamics occuring, poorly explained by a simple high temperature structure with average atomic positions.

8.2 Further structural optimisation

The two structures (1 and 2) determined in Ref. 226 are clearly insufficient for a good description of the J-coupling between the F2 site and the Pb site. A new relaxation has been performed with lower convergence tolerance using the `Castep` code with ultrasoft pseudopotentials, a plane-wave basis set described by a cut-off energy of 50 Ry and a k-point spacing of 0.06 $Å^{-1}$ (giving four k-points) to give structure 3. The forces on the ions were minimised to at most 6 meV/Å. The lattice vectors were fixed at their experimental values and there were no symmetry constraints applied.

After a number of relaxation steps, spontaneous distortion of the fluorine-zinc layer

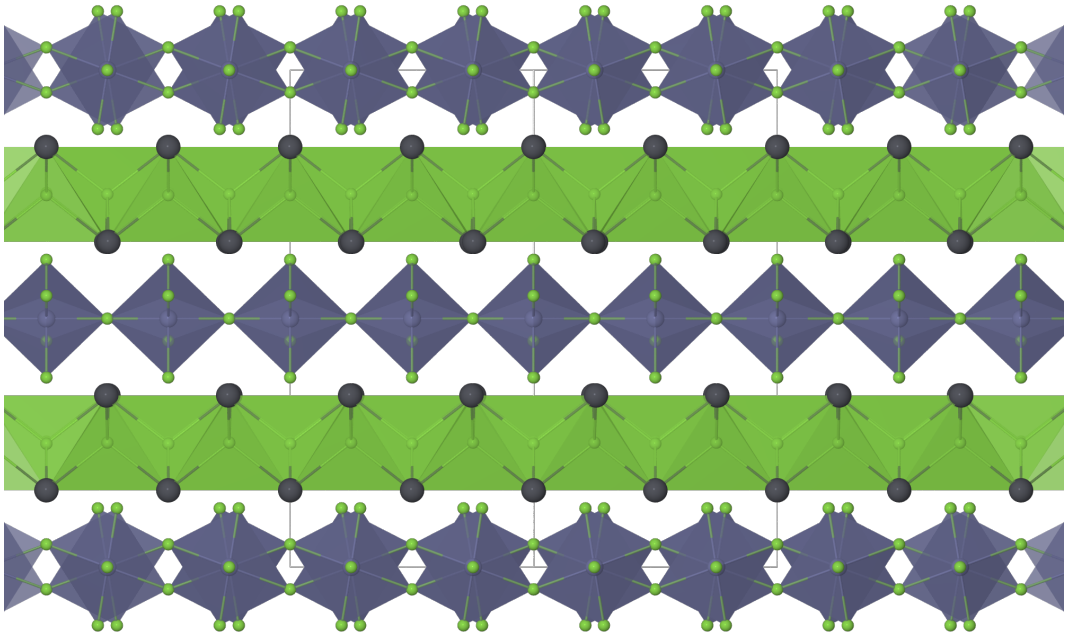

(a) View of β-Pb_2ZnF_6 along the (110) direction.

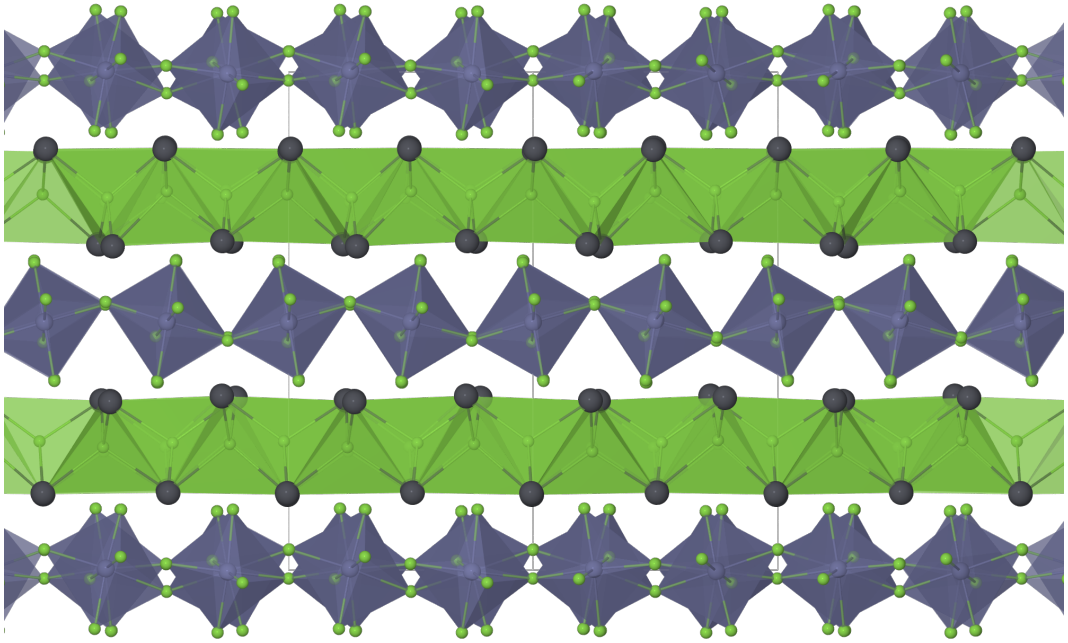

(b) View of α'-Pb_2ZnF_6 along the (110) direction.

Figure 8.3: Views of the β and α' structures along the (110) direction. The F2 chains in the α' structure have distorted from their original 180.0° ∠Zn−F−Zn in the β structure to 145.9° in the α' structure.

F2 chains was observed, see Fig. 8.3 for an illustration. As the DFT relaxation is in effect performed at $T = 0\,\mathrm{K}$ without symmetry constraints, this likely corresponds to a transition to the low-temperature α-Pb_2ZnF_6 structure. However, as we cannot conclusively assert that this is the α structure, lacking experimental data, and considering possibilities such as DFT error or the true α structure having a different unit cell, structure 3 will hence be named α'-Pb_2ZnF_6.

Table 8.1 summarises the structural parameters, bond angles and bond lengths, relating to the ZnF_6 octahedra in the α' structure, along with the other models used. The α' structure no longer has $\angle \mathrm{F}X\mathrm{-Zn-F}X$ exactly equal to 180° nor $\angle$F1−Zn−F2 and $\angle$F2−Zn−F3 precisely equal to 90.0°, appearing to prefer a slight distortion of the octahedra. Most significantly, $\angle$Zn−F2−Zn is no longer 180.0° but rather $145.9 \pm 0.9°$.

We can look at the total energy differences between structures to get an impression of the relative improvement in energetic stability. Based on plane-wave ultrasoft calculations at a 50 Ry cut-off energy and single k-point, the total energy of structure 1 is 2.98 eV above structure 3, and structure 2 is 0.33 eV above structure 3. Divided by the number of ZnF_6 octahedra present in the structure, this is 0.187 eV and 0.021 eV repsectively. The per-octahedron difference between structures 2 and 3 is relatively small, within the range of just-above room temperature thermal motion. The β structure, represented by the XRPD and `Wien2k`-relaxed structures, might hence be a high temperature thermal average, metastable at $T = 0\,\mathrm{K}$.

8.2.1 Zn electric field gradients

The quadrupole coupling constant and asymmetry parameter were predicted in the α' structure using, as before, a cut-off energy of 50 Ry, the PBE exchange-correlation functional, a single k-point, and ultrasoft pseudopotentials. The pseudopotential

Table 8.4: J-couplings of all five fluorine sites to their four nearest lead neighbours in the α'-Pb_2ZnF_6 structure (3) created in this work. The mean is of the couplings to the underlined sites, which are equivalent in the β structure.

Site	J_{iso} / Hz					
F1 (F63)	Pb 17	Pb 19	Pb 20	Pb 21	Mean	
3. α'	3861.99	2313.28	1551.98	175.55	3088	
Experiment					2000	± 200
F2 (F51)	Pb 11	Pb 13	Pb 18	Pb 19	Mean	
3. α'	122.59	215.00	2110.56	3489.01	1852	
Experiment					1700	± 200
F3 (F59)	Pb 13	Pb 15	Pb 19	Pb 22	Mean	
3. α'	84.77	755.63	619.88	4497.28	2559	
Experiment					3000	± 200
F4 (F75)	Pb 18	Pb 19	Pb 27	Pb 29	Mean	
3. α'	1890.99	2445.66	1572.70	2058.29	1992	
Experiment					1800	± 200
F5 (F81)	Pb 17	Pb 19	Pb 27	Pb 30	Mean	
3. α'	1441.20	1690.63	2195.85	2068.86	2132	
Experiment					1800	± 200

describing the Zn atoms treated the 3s and 3p states in the valence. The C_Q and η_Q values are presented in Table 8.2. As ranges of C_Q and η_Q were found, a mean and standard deviation are quoted for both.

Both $C_Q = 12.7 \pm 1.9\,\text{MHz}$ and $\eta_Q = 0.36 \pm 0.17$ systematically overestimate their experimental values, more so than structures 1 and 2. This indicates that, as might be expected, α' does not accurately represent the high-temperature β structure.

8.2.2 Pb−F J-coupling

Although α' likely corresponds to the low temperature structure, we can calculate the J-coupling between the fluorine sites at the lead sites. If the high temperature β structure can be considered to be an average of thermal hopping between α structures, as a simple level of approximation we might take the mean of equivalent

couplings to produce thermally averaged J-couplings. The J-couplings were calculated, as before, with the `Castep` code using a 40 Ry plane-wave cut-off energy, one k-point and ZORA ultrasoft pseudopotentials on the heavy ion (Pb) and Schrödinger ultrasoft pseudopotentials on the lighter ions (Zn and F).

The calculated J-couplings in α', when averaged over couplings equivalent in the β structure, correspond reasonably for sites F2, F4 and F5, although generally systematically larger. However, the couplings to F1 and F3 have inconsistent errors compared to the high-temperature experiment, F1 overestimating by 1,088 Hz and F3 underestimating by 441 Hz. As noted before, while we might not expect exact agreement with experiment due to the level of theory used, we should expect that the error is roughly systematic across all sites.

8.3 Thermodynamic averaging of NMR parameters

It appears that a simple average of equivalent couplings in α' is insufficient to describe the J-coupling in β-Pb_2ZnF_6. The hopping approximation will now be relaxed and the full dynamics of Pb_2ZnF_6 at the appropriate experimental temperature investigated using Born–Oppenheimer molecular dynamics (MD). Previous studies have investigated the effect of temperature on NMR parameters in solids using both phonon calculations and molecular dynamics.[141] The limitations of molecular dynamics were noted, especially the short durations of such simulations. However, as the sites of interest in β-Pb_2ZnF_6 are likely to have highly anharmonic behaviour, due to the suspected hopping, phonon based methods will be insufficient.

MD was performed with the NVT ensemble, giving constant particle number, volume and temperature, at 70 °C, the temperature that the ^{19}F J-coupling experiments were performed at, using the `Castep` code. A Nosé-Hoover[230,231] chain of five ther-

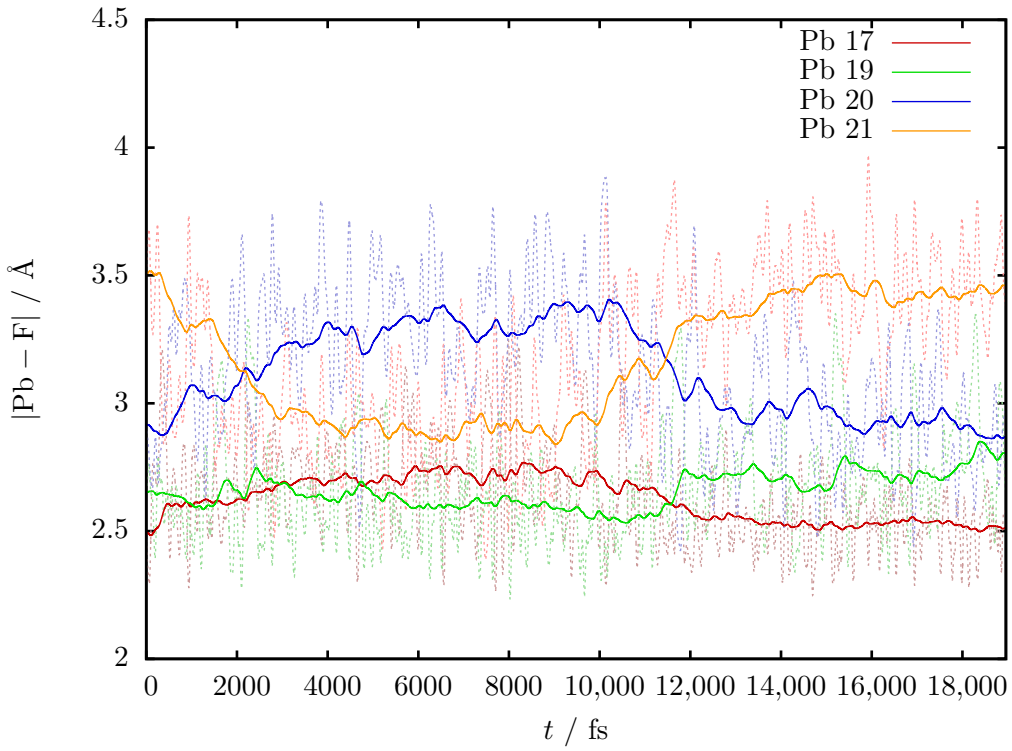

(a) Distance from F1 (F63) to neighbouring lead atoms over time.

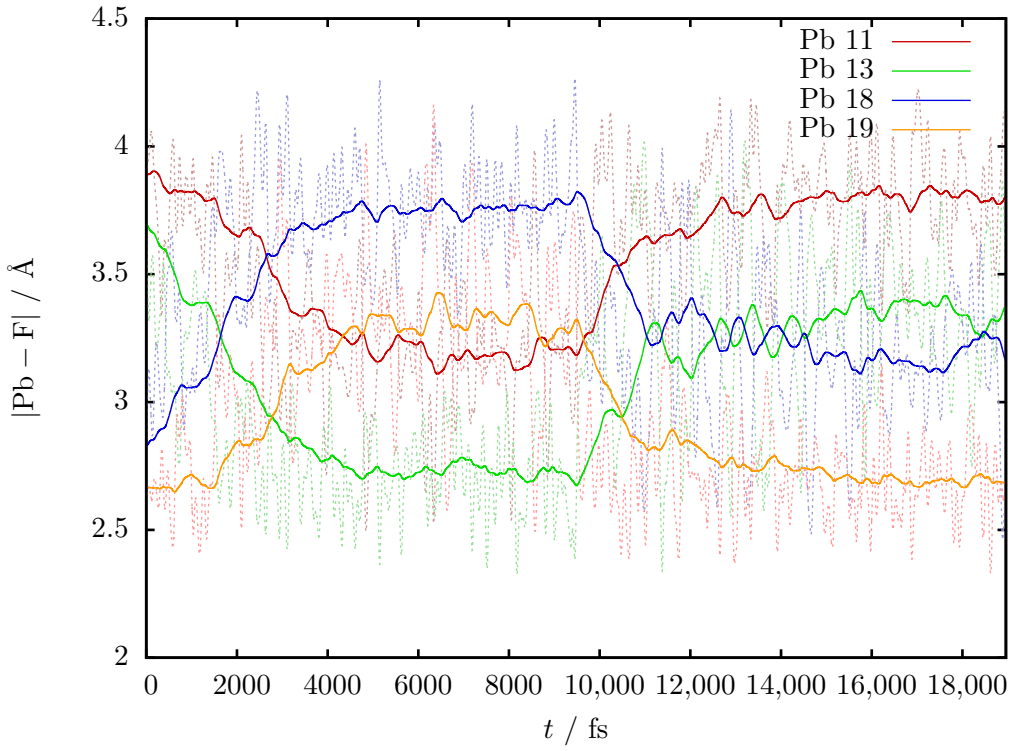

(b) Distance from F2 (F51) to neighbouring lead atoms over time.

Figure 8.4: Distance of atoms representing the five fluorine sites to their four nearest lead atoms over the length of the molecular dynamics simulation. The solid lines are running averages of the form $g_i = f_i(1 - \lambda) + g_{i-1}\lambda$, where $\lambda = 0.999$.

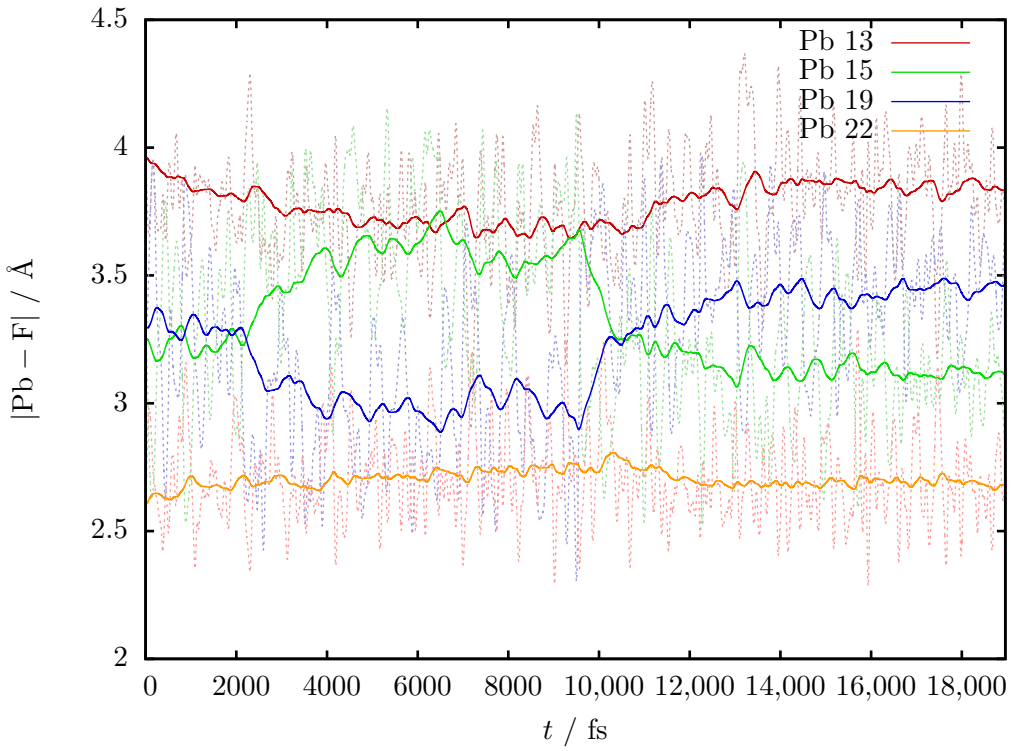

(c) Distance from F3 (F59) to neighbouring lead atoms over time.

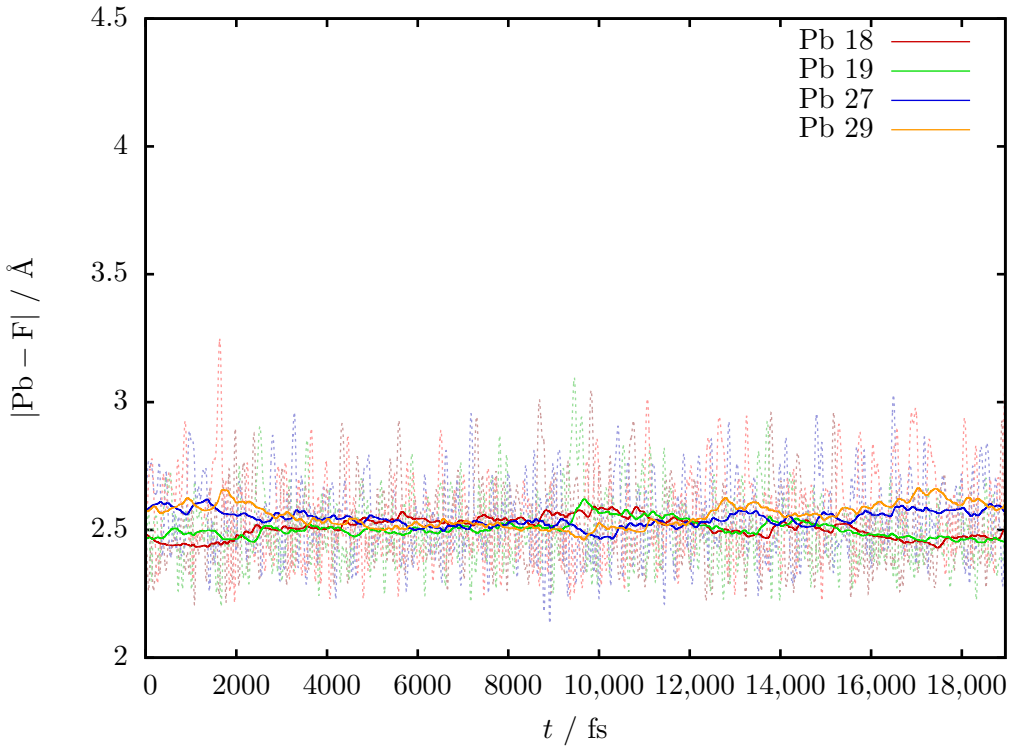

(d) Distance from F4 (F75) to neighbouring lead atoms over time.

Figure 8.4

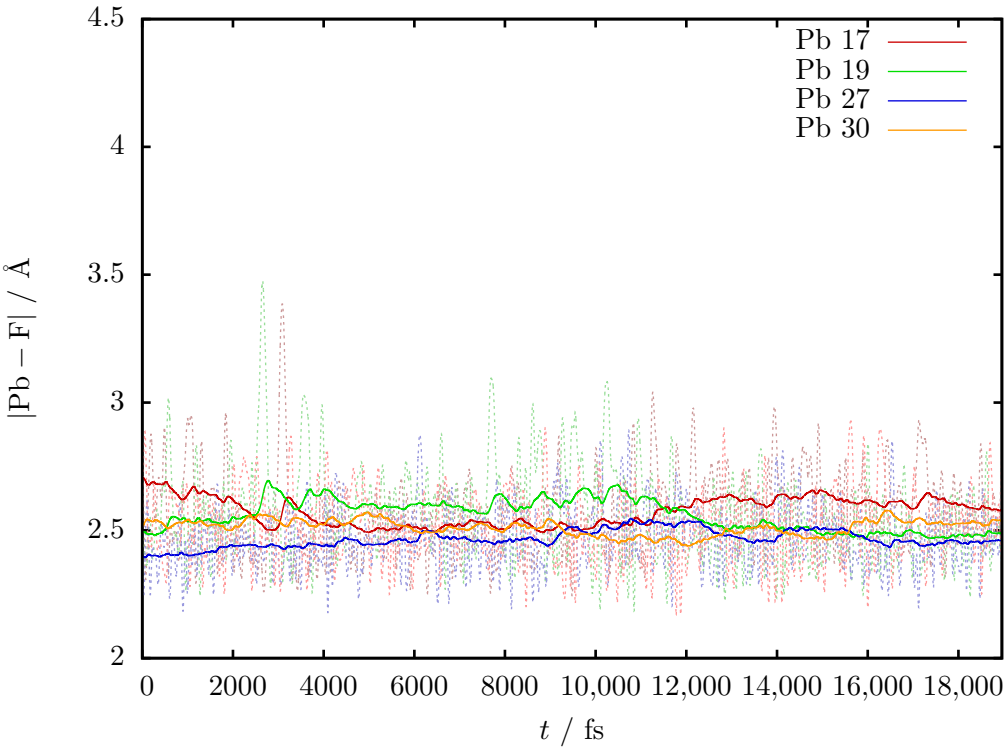

(e) Distance from F5 (F81) to neighbouring lead atoms over time.

Figure 8.4

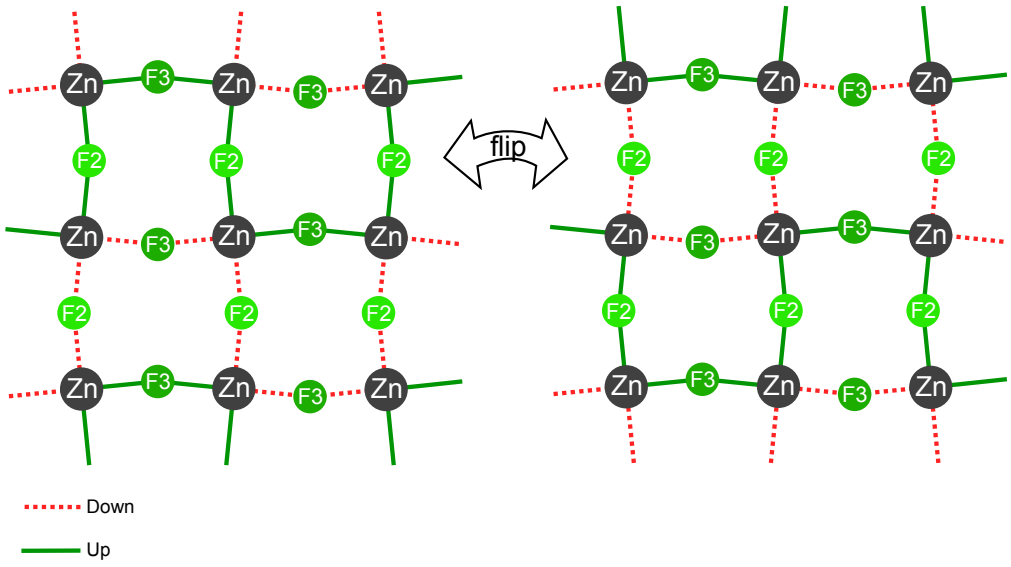

Figure 8.5: Schematic of flipping behaviour observed in the molecular dynamics simulation of Pb_2ZnF_6. The ZnF_6 octahedra are constrained to minimise their distortion and the F3 sites do not change their vertical position.

mostats with a characteristic ionic time of 10 fs was used. The integration time-step was 1 fs for a total time of of 18,960 fs. Electron exchange-correlation was described with the PBE functional and ultrasoft pseudopotentials were used with a plane-wave basis set described by a 50 Ry energy cut-off, with a single k-point. The simulation took 1124 hours of walltime on one node (32 cores) of a Cray XE6 (HECToR) for a total cost of 35,968 CPU core hours.

Fig. 8.4 shows the variation of distances between the fluorine sites and nearest-neighbour lead atoms over time. It can be observed that around 2 ps and 10 ps in, there are large changes in some atomic distances, often occuring in a way that swaps two neighbouring lead atoms. This corresponds to a flip in the orientation of the ZnF_6 octahedra, moving the F2 atoms from above the plane of Zn to below or vice-versa, illustrated in Fig. 8.5. Estimating the rate of this flip occuring should be approached cautiously due to the short simulation time used, and because the small

simulation cell used allows the establishment of long-range order with greater ease than the limit of an arbitrarily large cell. However, this indicates that at 70 °C, such a flip is likely happening in the real system on a timescale of picoseconds, significantly faster than any relevant NMR timescale (microseconds to milliseconds). Dynamics on such faster timescales means that NMR tensors should be thermally averaged to give the observed parameters.

This supports the earlier hypothesis that the β structure is represented by a hopping process between α structures. However, some sites which are considered equivalent in the β structure do not appear to be equivalent in the molecular dynamics samples. The lead atoms shall be referred to by their index in the structure. From the F1 site, Pb 17 and 19 are equivalent, as are Pb 20 and 21, as in the β structure. From the F2 site, Pb 13 and 19 are equivalent, and Pb 11 and 18 are equivalent, whereas in the β structure all the lead neighbours are equivalent. From the F3 site none of the sites appear to be equivalent, and Pb 22 is consistently the closest to the fluorine atom, whereas in the β structure Pb 11 and 13 are equivalent, as are Pb 19 and 22. From the F4 site all the lead atoms are equivalent, swapping in two pairs of Pb 18 and 19 and Pb 27 and 29, as in the β structure. Finally, from the F5 site, Pb 17 and 19 are equivalent, as are Pb 27 and 30, as in the β structure, however sharing a very similar range of bond lengths. What couplings are considered equivalent will affect how we calculate the mean NMR parameters of the sites.

8.3.1 Estimating errors

Configurations from molecular dynamics are serially correlated with some correlation timescale. This means that, in order to get a correct NVT ensemble, the configurations generated by molecular dynamics should be sampled with a temporal separation longer than this correlation timescale, else nearby samples will be too

similar and not add new information to the mean and the estimated error in the mean will be too small. The error in the mean can be corrected for any remaining serial correlation between samples using reblocking analysis,[232] which will now be outlined.

The mean of some property of configuration i, A_i, over a run of N timesteps is

$$\langle A \rangle = \frac{1}{N} \sum_{i=1}^{N} A_i, \tag{8.1}$$

and, assuming independence, the variance in the mean is

$$\sigma^2(\langle A \rangle) = \sigma^2(A)/N, \tag{8.2}$$

where

$$\sigma^2(A) = \frac{1}{N} \sum_{i=1}^{N} (A_i - \langle A \rangle)^2. \tag{8.3}$$

However, the property of configurations might be serially correlated. If the property of configurations has a correlation length of n_c, e.g. it is replicated in blocks of n_c, then the variance in the mean is actually

$$\sigma^2(\langle A \rangle) = n_c \sigma^2(A)/N. \tag{8.4}$$

To find the correlation time we block the sequence of configurations into blocks of

length n and within block j, take the mean

$$\langle A \rangle_j = \frac{1}{n} \sum_i A_i, \tag{8.5}$$

where the sum over i runs only over configurations within the block j.

We can then use these blocked means to estimate the variance

$$\sigma^2(\langle A \rangle_j) = \frac{n}{N} \sum (\langle A \rangle_j - \langle A \rangle)^2. \tag{8.6}$$

In the limit of large n, we expect the block means to be uncorrelated and $\sigma^2(\langle A \rangle_j)$ to be proportional to $\frac{1}{n}$. By taking a limit of n to large block size we can attempt to estimate the true error in the mean. The optimal block size, and hence estimated variance, is determined using the method outlined by Wolff[233] and Lee.[234] The `pyblock` Python package[235] was used to perform the reblocking and choose the optimal block size.

Fully decorrelated sampling will be difficult to achieve with the length of time simulated, as there are only two flips present, and hence a likely total correlation time of tens of picoseconds. However, by averaging between equivalent sites it should be possible to get useful mean values, and instead just ensure sampling at an interval longer than the correlation time of the shorter timescale dynamics between flips.

8.3.2 Zn electric field gradients

The ab-inito C_Q and η_Q in structure 2 were consistent with experiment, structure 3 overestimating by approximately 4 MHz, though with a large standard deviation. By calculating the electric field gradient from sample configurations generated by

the molecular dynamics run we can also verify that that aspect of the molecular dynamics is consistent with experiment. Properties calculated from the molecular dynamics should be taken with caution, especially as it appears that a good sample of the flipping behaviour has not been achieved, and that the EFG experiments were performed at 100 °C rather than 70 °C.

The electric field gradient at every zinc site present has been sampled every 200 fs for 10 ps from the configurations generated by molecular dynamics, discarding the first 1 ps of configurations to allow for thermodynamic equilibriation with the thermostat, to give a total of 51 samples. The electric field gradient calculations were performed, as before, with a cut-off energy of 50 Ry, the PBE exchange-correlation functional, a single k-point, and ultrasoft pseudopotentials. The pseudopotential describing the Zn atoms treated the 3s and 3p states in the valence. The EFG calculations on the 51 samples each took 30 minutes walltime on one node (24 cores) of a Cray XC30 (ARCHER) for a total cost of 612 CPU core hours.

The observed C_Q is found by taking the mean of the EFG tensor, Eqn. 3.82, over the samples and then calculating C_Q using Eqn. 6.12, and similarly so for the asymmetry η_Q. The tensor might also be averaged over all Zn sites present, as they are considered equivalent. However, the principle axis systems of the sites may not be identical, which complicates taking such an average of tensors. With this in mind, Table 8.2 presents two means derived from the molecular dynamics. 'Mean 1' is the C_Q of the mean of the tensors over all samples and all Zn sites, and 'Mean 2' is the mean C_Q of the mean tensors for each Zn site, where the reported error is the standard deviaton of the site C_Q means.

Both methods for taking means of the C_Q give results roughly consistent with experiment, approximately 2 MHz larger than reported but not exhibiting the scale of errors seen in the J-coupling. The asymmetry parameter calculated in 'Mean 1' is of

similar magnitude but smaller than the η_Q observed experimentally, and in 'Mean 2' it is larger than experiment but within one standard deviation.

8.3.3 Pb−F J-coupling

As with the electric-field gradient, the first 1 ps of MD configurations were discarded to allow for thermodynamic equilibriation of the system with the thermostat. After that, sample structures were taken every 200 fs for a total of 10 ps to give 51 samples. On each of these sample structures, J-couplings were calculated for each of the fluorine sites using, as before, a 40 Ry plane-wave cut-off energy, one k-point and ZORA ultrasoft pseudopotentials on the heavy ion (Pb) and Schrödinger ultrasoft pseudopotentials on the lighter ions (Zn and F). The J-coupling calculations on the 5×51 samples each took 4 hours walltime on one node (24 cores) of a Cray XC30 (ARCHER) for a total cost of 24,480 CPU core hours.

Fig. 8.6 plots the sampled isotropic J-coupling between the fluorine sites and neighbouring lead atoms as a function of time. Their mean values are summarised in Table 8.5 along with site averaging. Standard errors for each coupling are given, along with standard errors estimated using a reblocking analysis (Fig. 8.7). The sites have been averaged using the nearest equivalent sites in the β structure to give 'Mean 1' and with the sites determined to be equivalent from Fig. 8.4 to give 'Mean 2'.

The 'Mean 1' set of averages compares reasonably, though with significant underestimations of the experimental number for sites F2 and F3. Site F1 is overestimated by approximately 400 Hz and site F5 by 800 Hz. The 'Mean 2' set of averages compares well, with sites F1, 2, 3 and 4 consistently overestimating experiment by between 200 and 400 Hz. The F5 site is still overestimated by approximately 800 Hz.

The error in the F5 is inconsistent with the apparent systematic error on the other sites, though the coupling between the chosen equivalent pair and the other pair is of very similar magnitude. The mean of all four F5 couplings gives a value of 2012 Hz, consistent with the experimental value of 1800 ± 200 Hz and the systematic error observed on the other sites. Whether or not such an averaging is justified experimentally is unclear, but such complications involving a number of similar magnitude couplings and the assumption of a single experimental coupling could explain the discrepency.

Allowing for errors introduced by the incomplete sampling by the molecular dynamics, this might be considered the set with the best agreement with experiment, having a consistent systematic error.

If the 'Mean 2' set is taken to be the most consistent with experiment, reflecting the local structure of β-Pb_2ZnF_6 at 70 °C the best, it might be concluded that the true local topology doesn't corresponds to that of the proposed β structures (1 and 2), but rather more that of the mean MD structure, structure 4 or β'-Pb_2ZnF_6, illustrated in Fig. 8.8. This is especially seen in site F3, as the β structures have two of the Pb−F couplings as equivalent, but a result more consistent with the systematic errors on the other sites is gained by only considering the largest J-coupling.

The mean structure determined by MD should be taken cautiously because, as noted, full sampling of the observed flips is incomplete and might produce a bias. It can be seen that the F2 chains are averaged to a level position between the Zn atoms, similar to β, but with a small displacement in the layer plane. Table 8.1 gives a summary of structural parameters of the β' structure. The $\angle FX{-}Zn{-}FX$ are all very close to 180°, as in structures 1 and 2 but slightly less so in structure 3.

Of all the structures, the PbF_6 octahedra in β' appear to have the smallest deviation from regular octahedra, which would be the preferred configuration in isolation,[236]

the ∠F1−Zn−F3 angle being 87.7°, as opposed to 79.0°, 85.7° and 84.7° for structures 1, 2 and 3 respectively and the other angles being closer to 90.0°. This distortion can be quantified more rigorously in terms of Ghose and Tsang's polyhedral distortion parameter, Eqn. 6.15, also given in Table 8.1. The β' structure gives the lowest overall distortion of the ZnF_6 octahedra, with a distortion $|\psi|$ of 0.27 ± 0.08, compared to 0.78, 0.30 and 0.85 ± 0.20 for structures 1, 2 and 3 respectively.

Ab-initio EFG calculations on β' are given in Table 8.2, the predicted C_Q overestimating experiment by approximately 3 MHz, more so than the molecular dynamics average. The predicted asymmetry of $\eta = 0.52 \pm 0.08$ is also poor compared to the experimental value of 0.10 ± 0.05. Together these indicate the effect that dynamics has on the EFG, tending to reduce the quadrupole coupling and asymmetry.

The β' structure does not reflect the symmetry of the β structures. In order to be consistent with the structure and symmetry observed in XRPD in Ref. 226, this must somehow be restored. One possibility would be that the material is spatially disordered between two symmetric orientations, hence giving the correct long-range symmetry.

8.4 J-coupling in other similar materials

As a point of comparison for the complex behaviour of couplings in β-Pb_2ZnF_6, two additional materials containing Pb−F J-couplings, with experimental measurements, have been examined to estimate the likely systematic errors present.

$\alpha-PbF_2$ contains two fluorine sites and one lead site. Two structures were used for $\alpha-PbF_2$, one determined experimentally in Ref. 237 and the other where the ionic positions of the experimental structure have been optimised to minimise ionic forces, keeping the lattice vectors constant, using the PBE functional, a 50 Ry energy

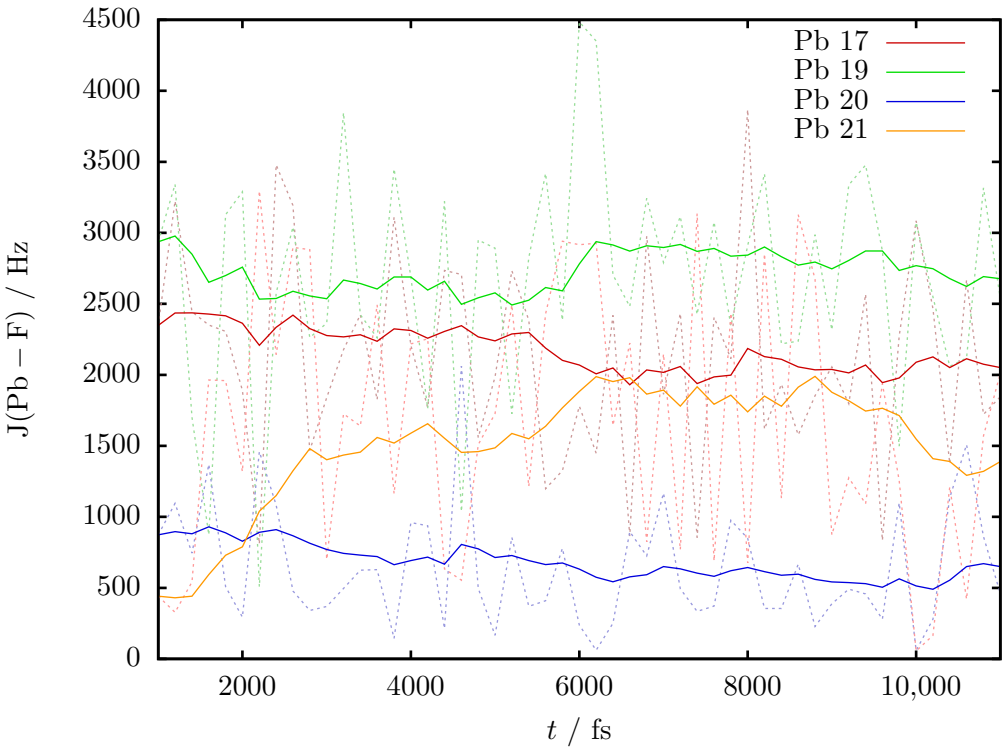

(a) J-coupling from F1 (F63) to neighbouring lead atoms over time.

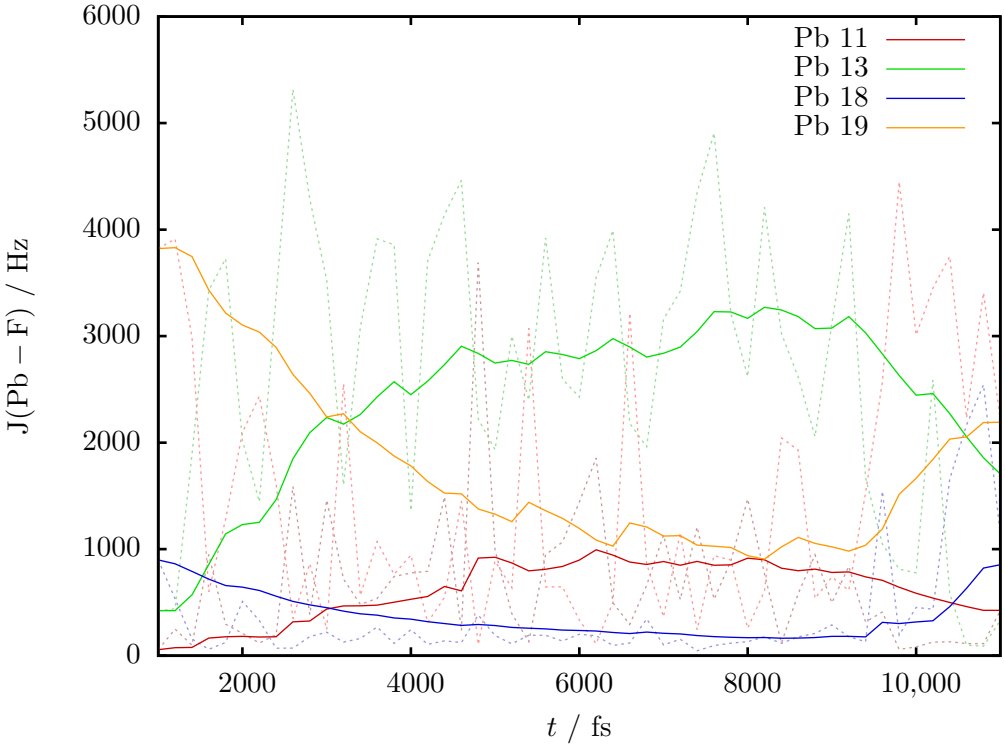

(b) J-coupling from F2 (F51) to neighbouring lead atoms over time.

Figure 8.6: The solid lines are running averages of the form $g_i = f_i(1 - \lambda) + g_{i-1}\lambda$, where $\lambda = 0.9$.

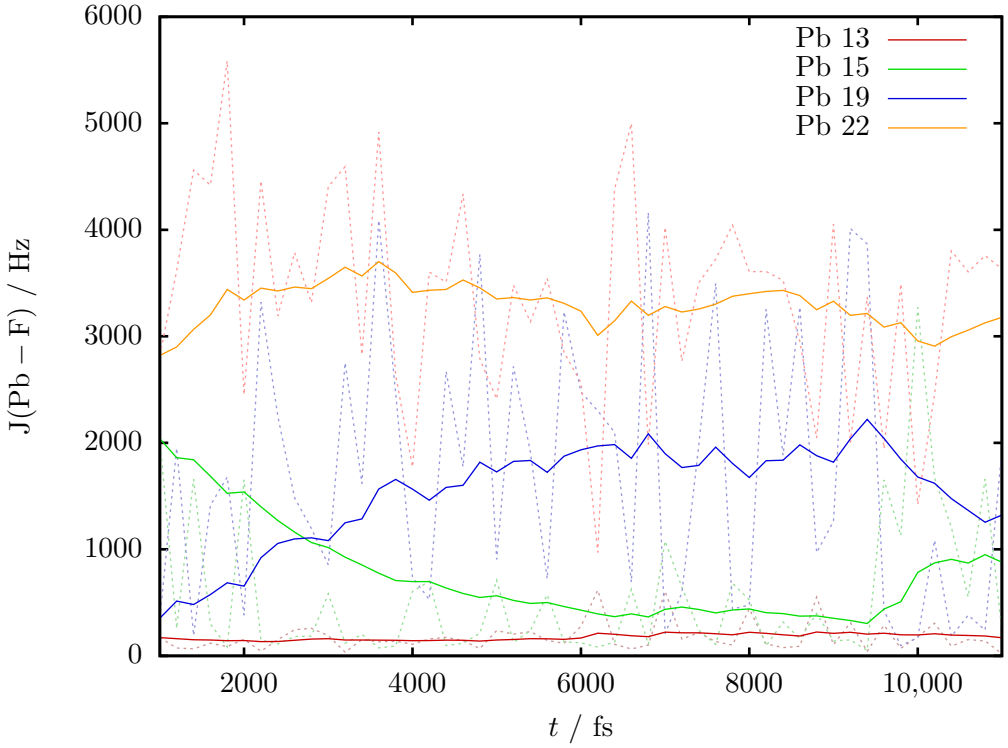

(c) J-coupling from F3 (F59) to neighbouring lead atoms over time.

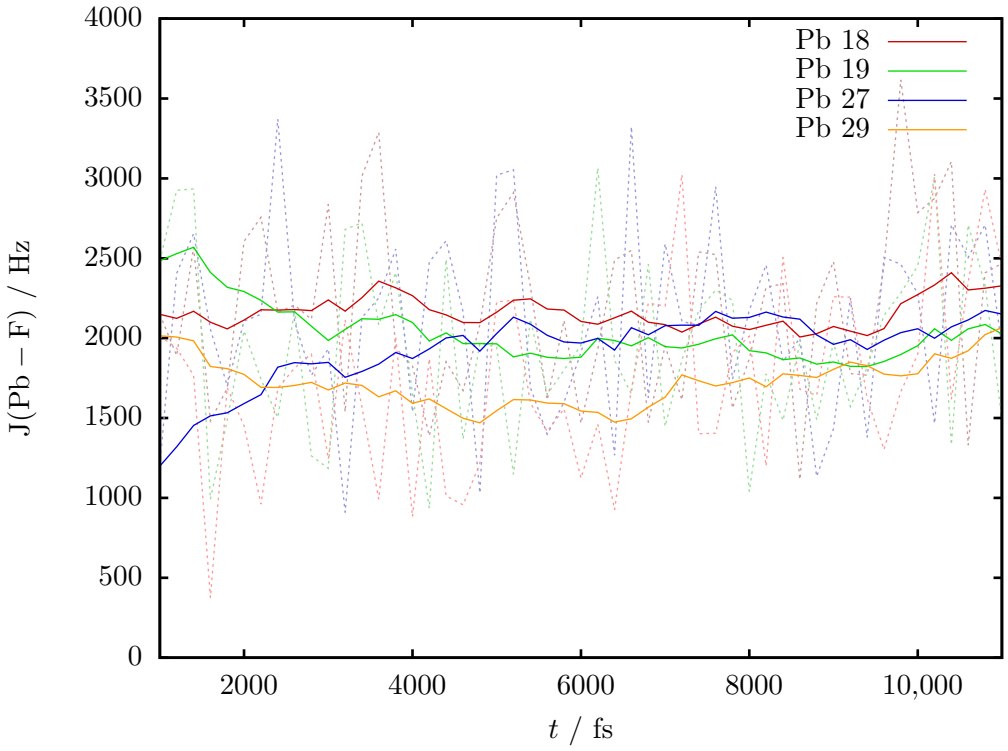

(d) J-coupling from F4 (F75) to neighbouring lead atoms over time.

Figure 8.6

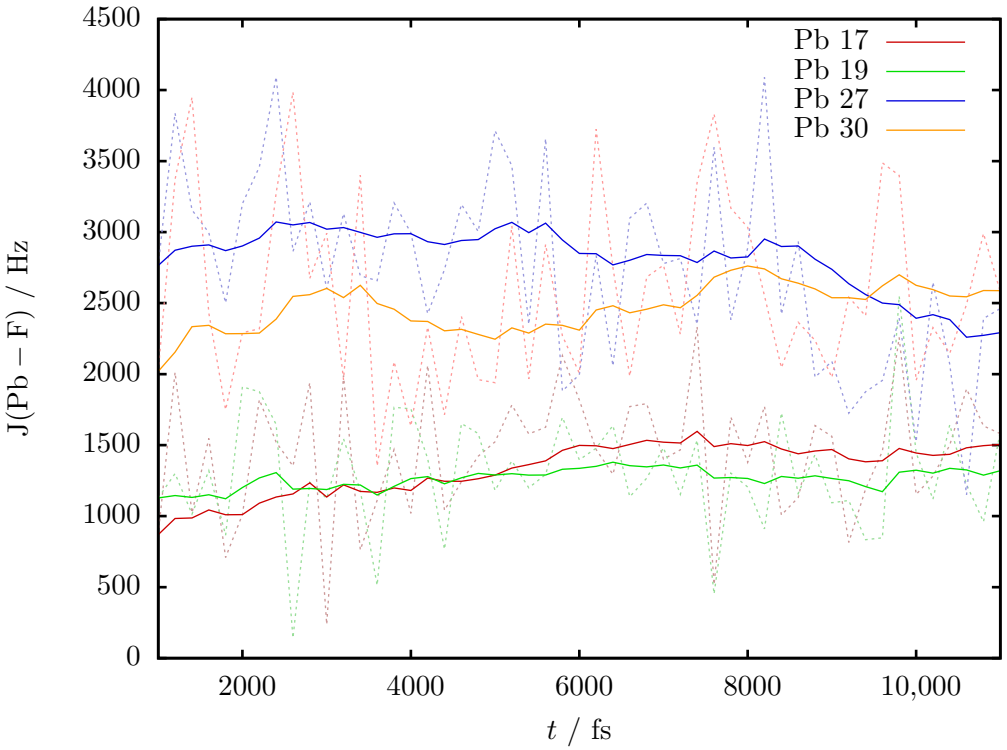

(e) J-coupling from F5 (F81) to neighbouring lead atoms over time.

Figure 8.6

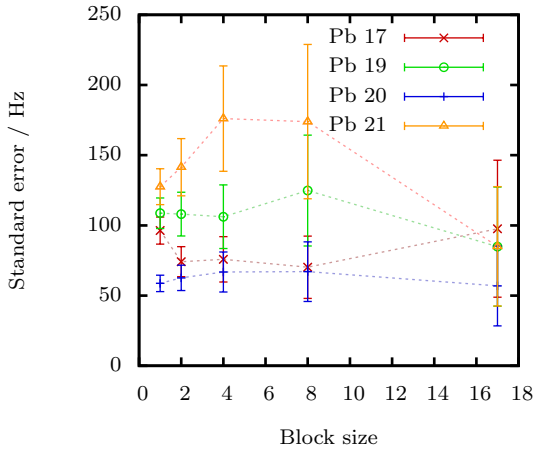

(a) F1 (F63).

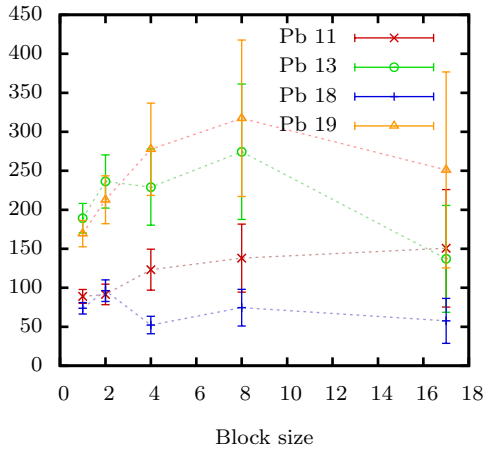

(b) F2 (F51).

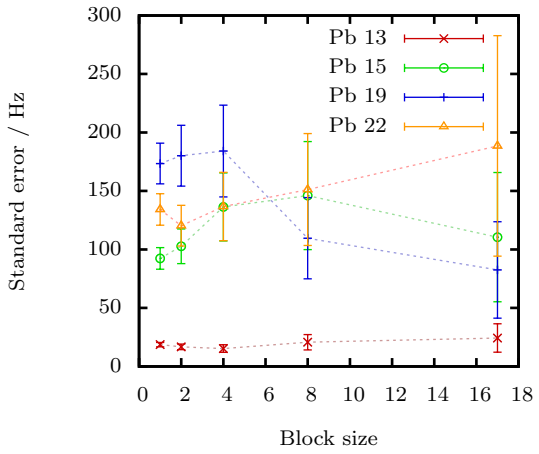

(c) F3 (F59).

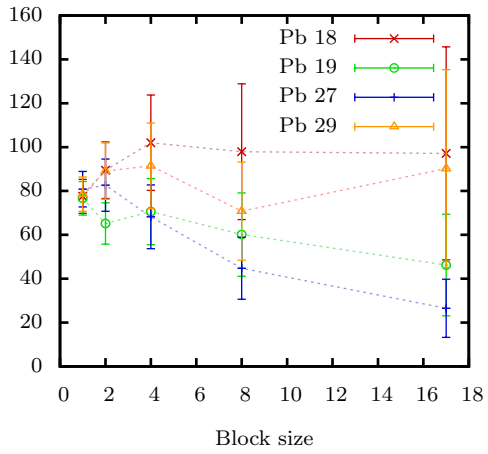

(d) F4 (F75).

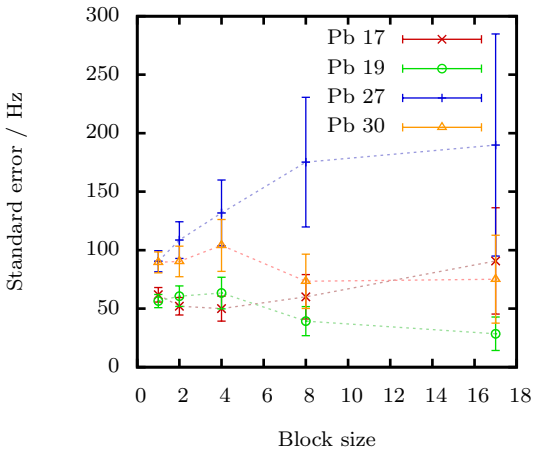

(e) F5 (F81).

Figure 8.7: Reblocking analysis of molecular dynamics data, discussed in Sec. 8.3.1, for each Pb−F J-coupling on each of the flourine sites, performed with the `pyblock` package.[235]

Table 8.5: Mean isotropic J-couplings of all five fluorine sites to their four nearest lead neighbours from samples created from molecular dynamics at 70 °C. 'Mean 1' is of the couplings to the underlined sites, which are equivalent in the β structure, while 'Mean 2' is of the couplings to the starred sites, which are found to be equivalent in the MD bond length data shown in Fig. 8.4.

Site	J_{iso} / Hz					
F1 (F63)	Pb 17*	Pb 19*	Pb 20	Pb 21	Mean 1	Mean 2
MD mean	2121.50	2683.39	642.03	1676.70	2402	2402
Error	95.37	107.59	58.10	126.30		
Re-blocked error	75.79	124.82	67.05	173.93		
Experiment					2,000 ± 200	
F2 (F51)	Pb 11	Pb 13*	Pb 18	Pb 19*	Mean 1	Mean 2
MD mean	679.34	2647.93	365.79	1497.66	1298	2073
Error	88.13	187.34	73.01	167.80		
Re-blocked error	150.61	274.39	52.25	251.14		
Experiment					1,700 ± 200	
F3 (F59)	Pb 13	Pb 15	Pb 19	Pb 22*	Mean 1	Mean 2
MD mean	176.19	553.92	1705.14	3358.24	2532	3358
Error	18.49	91.49	171.78	132.88		
Re-blocked error	15.29	110.51	109.63	151.22		
Experiment					3,000 ± 200	
F4 (F75)	Pb 18*	Pb 19*	Pb 27*	Pb 29*	Mean 1	Mean 2
MD mean	2192.06	1953.03	2097.97	1730.93	1994	1994
Error	76.81	75.94	80.05	77.80		
Re-blocked error	97.89	60.13	68.21	70.80		
Experiment					1,800 ± 200	
F5 (F81)	Pb 17	Pb 19	Pb 27*	Pb 30*	Mean 1	Mean 2
MD mean	1443.65	1297.87	2735.58	2571.12	2653	2653
Error	61.26	55.96	89.64	88.72		
Re-blocked error	50.02	39.31	189.86	73.39		
Experiment					1,800 ± 200	

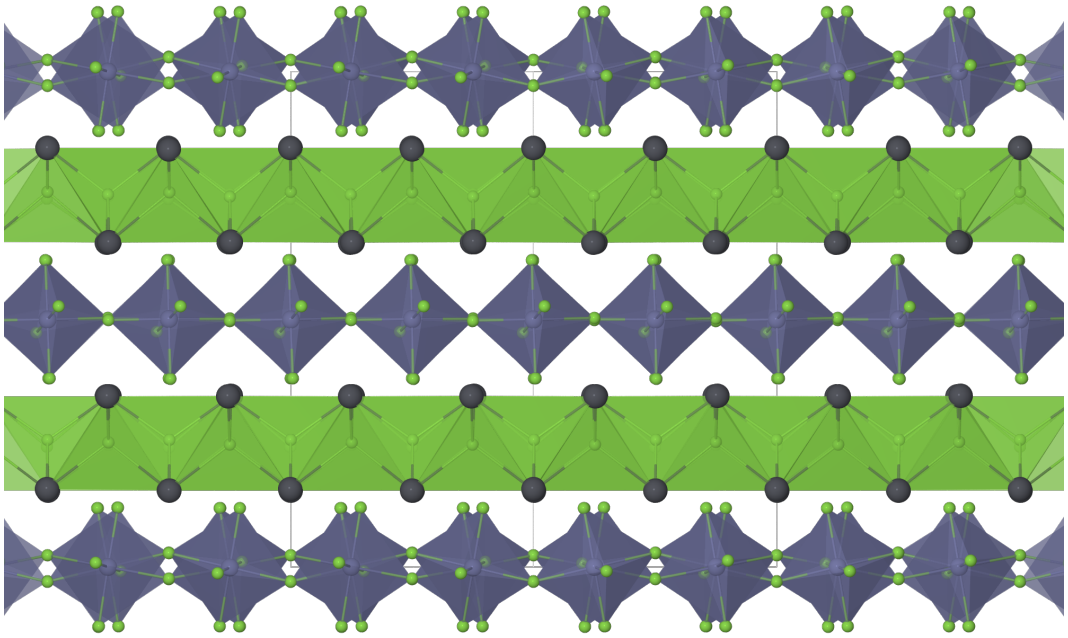

(a) View of the mean structure determined by molecular dynamics along the (110) direction.

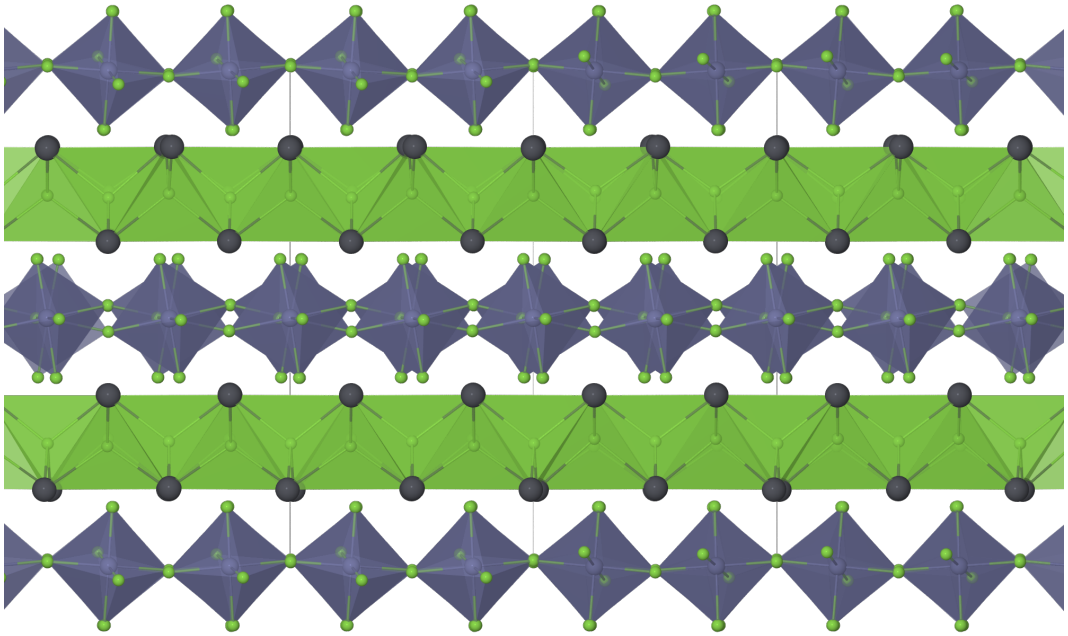

(b) View of the mean structure determined by molecular dynamics along the $(\bar{1}10)$ direction.

Figure 8.8: Views of the mean structure determined by molecular dynamics, named here as β'-Pb_2ZnF_6.

cut-off and a k-point spacing of $0.06\,\text{Å}^{-1}$.

The $\alpha-PbF_2$ J-coupling calculations, shown in Tables 8.6a and 8.6b, find a range of four large couplings, from 2650 to 3950 Hz in the case of the experimental structure, from the F1 site to the Pb site. As noted before, the exact outcome of having a range of similar-sized J-couplings on the experimentally measured value is unclear, but the mean value of approximately 3 kHz is significantly larger than the 2 kHz J-coupling observed in experiment. The F2 site coupling was not measured experimentally.

$\beta-PbF_2$ contains one fluorine sites and one lead site. Only the experimentally determined structure from Ref. 238 was used for $\alpha-PbF_2$, as symmetry enforces zero forces on the ions when the lattice vectors are fixed.

The $\beta-PbF_2$ calculation, shown in Table 8.6c, finds four identical couplings to the closest neighbouring lead atoms, $^1J(Pb-F) = 3108$ Hz. This is larger than the 2600 Hz value measured experimentally in Ref. 239.

Overall, couplings in both structures appear to be significantly overestimated by ab-inito calculation compared to experiment. The magnitude of the systematic error in $\alpha-PbF_2$ and $\beta-PbF_2$ is consistent with the suggested magnitude of systematic error observed in the 'Mean 2' set of MD J-coupling Pb_2ZnF_6 calculations. While the effect of dynamics has been ignored here, these two materials lack the sort of octahedral structures seen in Pb_2ZnF_6 and so we might expect it to be less important.

8.5 Conclusions

Considering the limitations of the techniques used and without further experiments it cannot be definitively asserted which of the proposed models are most consistent with experiment. The nature of the errors in calculated J-coupling, along with

Table 8.6: Calculated and experimental, from Refs. 237 and 239, J-coupling in $\alpha-PbF_2$ and $\beta-PbF_2$.

(a) J-coupling from the F1 site in $\alpha-PbF_2$.

F site	J_{iso} / Hz				
F1 (F19)	Pb 13	Pb 17	Pb 7	Pb 1	Mean
Ref. 237	2650	2656	2820	3950	3019
Ions relaxed	2766	2770	2862	4092	3122
Experiment					2000

(b) J-coupling from the F2 site in $\alpha-PbF_2$.

F site	J_{iso} / Hz					
F2 (F18)	Pb 2	Pb 6	Pb 18	Pb 7	Pb 11	Mean
Ref. 237	1217	1217	2151	2561	2564	1942
Ions relaxed	1097	1098	2181	2703	2706	1957

(c) J-coupling from the F site in $\beta-PbF_2$.

F site	J_{iso} / Hz				
F1 (F1)	Pb 1	Pb 3	Pb 9	Pb 11	Mean
Ref. 239	3108	3108	3108	3108	3108
Experiment					2600

structural effects such as minimisation of the ZnF_6 octahedral distortion by the mean MD structure, suggest that a rich mix of dynamic disorder and spatial disorder could be present in Pb_2ZnF_6.

Despite the lack of a definitive conclusion, this study demonstrates the power of ab-initio J-coupling combined with molecular dynamics to probe and distinguish detailed models of materials. The theoretical techniques developed in this thesis, J-coupling with ultrasoft pseudopotentials and incorporating relativistic effects, brings such a study into the range of reasonable cost with modern computing resources. It should provide a blueprint for future combined theoretical and experimental work investigating the structure of similar materials.

Chapter 9

Conclusions and future work

In this thesis, the plane-wave pseudopotential method for the prediction of NMR J-coupling in condensed matter was developed to allow the use of state-of-the-art ultrasoft pseudopotentials. Furthermore, additional theory was incorporated to include the effects of special relativity on J-coupling, critical, as shown, for heavy elements. The method can now predict experimentally measured J-coupling with favourable accuracy compared to equivalent all-electron, local orbital basis-set quantum chemistry methods. By being able to treat more diverse systems for a lower cost and with greater ease, the method should now see greater use in the wider NMR crystallography community. In addition, several novel studies into compositional disorder, molecular crystals and dynamic disorder have demonstrated the method's power in combination with experiment for the creation and validation of structural models of materials.

The direction of future work is indicated by consideration of the remaining sources of error. The use of approximate exchange-correlation functionals appears to be the main source of error in the systems examined, in agreement with previous studies.[116]

This will be difficult to fix, due to the high computational cost of higher levels of theory, such as hybrid functionals, especially in plane-wave basis sets. Cheaper corrections, such as the DFT+U method,[84] might be considered as a compromise.

The lack of spin-orbit coupling appears to be the next largest source of error in the systems considered. Recent developments in plane-wave pseudopotential codes to allow for the use of two-component spinor wave functions should enable the implementation of PAW J-coupling with spin-orbit effects included.[240–244] An extension to the PAW method to allow for the use of four-component Dirac operators could then be developed, circumventing the need to use the ZORA approximation.

Finally, all the calculations performed in this thesis had to be performed using a supercell, due to the problem of perturbations interacting with their own periodic images. This negates some of the computational advantages of a plane-wave pseudopotential approach using Bloch's theorem, leading to cubic scaling in system size rather than linear scaling in k-points. Development of a method to properly treat the incommensurate magnetic perturbation will allow the efficient treatment of crystals with small primitive unit cells and permit convergence to infinite supercell sizes.

Appendix A

Ab-initio magnetic resonance file format

A.1 Introduction

The aim of this appendix is to describe the motivations for and definition of a standardised output format for magnetic resonance calculations developed during this thesis. It was felt that as more computational codes incorporate the prediction of NMR parameters, especially for solid-state systems, a unified output format would create a common platform for the further development of tools, such as interfaces to spin simulation codes, visualisation tools and general post processing programs useful in the course of research.

It was decided that the format should be machine readable, as simple as possible and provide a complete archival format. The simplicity and machine readability are intended to allow any researcher with a moderate knowledge of a programming language to write their own parser of the format, and so not be reliant on others

doing so, and the completeness of the format is intended to contribute to achieving wider goals relating to scientific reproducibility, e.g. as supplementary information for a journal article, and data mining of simulation output.

These goals were developed into some concrete requirements: allowing the easy extraction of information using standard command-line utilities available in distributions of Linux, such as `grep` and `awk`; ignoring unrecognised elements, allowing later extension; not to specify redundant information, to reduce maintenance; that properties are specified in full Cartesian tensors in well-defined units, leaving tasks such as finding eigenvalues to further processing; including information on atomic positions and, optionally, the crystal lattice for completeness and to allow visualisation; specifying but not requiring the understanding of symmetry operations; to avoid overly expressive languages such as XML, to guarantee easy parsing.

In addition, the following limitations to the standard were recognised: only parameters related to NMR of diamagnetic materials have been specified, the extension to include parameters related to paramagnetic materials should be straight forward; it doesn't include definitions for providing EPR parameters, but could be incorporated in a future backwards-compatible update to the standard; and while the format is designed for processing and archiving, it's not designed for easy querying in a database form. It's assumed a database will perform further transformations into its own desired internal format for indexing.

A.2 Specification

The file format settled on is essentially a series of blocks consisting of rows constraining whitespace-delimited records, with datatype distinguished by tags in the first column. To allow easier recognition by parsers, the file must start with

```
#$magres-abinitio-v1.0
```

the version number 1.0 referring to this standard. Minor version number increases after the period will aim to not break backwards compatibility with existing parsers whereas major version number increases before the period may.

A.2.1 Blocks

Blocks are wrapped with tags:

```
[block]
  ... data ...
[/block]
```

They cannot be nested or overlap. Unrecognised blocks should be ignored, so as to allow other data to be put in the same file. Blocks discussed in this specification are

- `[atoms]` - Atomic coordinates and optional lattice. Must be first block for easy parsing
- `[magres]` - Calculated magnetic resonance parameters
- `[calculation]` - Calculation metadata such as code version and input parameters

The `[atoms]` block should appear before `[magres]` for ease of parsing. The feature of ignoring unrecognised blocks allows codes to include extra blocks of text, such as old magnetic resonance file types that have to be retained for backwards compatibility with existing parsers. Input files could also be kept in extra unrecognised blocks.

A.2.2 Characters and numerical representation

This file format is based on 8-bit ASCII characters but only characters 0–127 should be used outside of comments. Numbers should be written in decimal or scientific notation with double precision (i.e. typically 16 significant figures). Numbers should be written as to be easily parsable by standard string routines (e.g. Fortran, C, Python, Perl, etc.)

A.2.3 Records

A record is a line in the file of arbitrary length and terminated by the line feed character (`\n`). Whitespace (characters recognised by \s in a regex) is ignored at the start and end of a line. One or more whitespace characters separate two entries in a record. Each record has a tag, which is the first entry.

```
lattice 6.0 0.0 0.0 0.0 6.0 0.0 0.0 0.0 6.0
```

In the above record, "`lattice`" is the tag.

A.2.4 Comments

Any characters following a # symbol in a line should be ignored.

A.2.5 Units

Although this specification document will specify the units for each parameter, it's preferable to explicitly define the units used for each kind of tag for discoverability and so as to allow some flexibility and allow parsers to hard-fail when unrecognised units are used. The tag for units is:

```
units <tag> <units>
```

where the units is some case-sensitive string that would make sense to a parser and human, e.g "au" for when atomic units have been used. The strings should be strictly compared, i.e. "J.mol-1" is not the same as "Jmol^-1".

The units tag must appear once or not at all before the first instance of the tag it is describing. Parsers should warn if they do not recognise units. If they have to process quantities with units they don't recognise they should fail.

A.2.6 atoms block

The crystal lattice can be given as the $\mathbf{a}, \mathbf{b}, \mathbf{c}$ unit cell vectors. This is an optional element, however if it is not present it can be assumed that the structure is non-periodic. We will standardise on ångström as the output unit.

```
units lattice Angstrom
lattice a1 a2 a3 b1 b2 b3 c1 c2 c3
```

The atomic positions (for all the atoms in the full crystallographic unit cell) are given in Cartesian coordinates, standardised to ångström as the output unit. These must be present in a file before any magres parameters.

```
units atom Angstrom
atom <atom type> <atom label> <number in atom type> x y z
```

The atom type should be an element symbol (no isotopes, i.e. H rather than D) and the atom label can be any string, e.g. the crystallographic label. If there is no label the element symbol should be given again. Atom types can be specified in any order, but the numbers in the type should be in order and start from one.

If symmetry operators are known, you can specify them with the `symmetry` tag:

```
symmetry <symmetry string>
```

where the symmetry string is in x,y,z notation. As it is undesirable to require basic scripts to know and be able to apply symmetry operators, all non-unique atoms should still be included. An example set of symmetry operations for an alanine crystal structure would be

```
symmetry x,y,z
symmetry x+1/2,-y+1/2,-z
symmetry -x,y+1/2,-z+1/2
symmetry -x+1/2,-y,z+1/2
```

A.2.7 `magres` block

`ms` - Magnetic shielding

The magnetic shielding tensor is defined as the ratio between this induced field, and the external applied field.

$$\mathbf{B}_{\text{in}}(\mathbf{R}) = -\sigma(\mathbf{R}) \cdot \mathbf{B}_{\text{ext}}(\mathbf{R}), \tag{A.1}$$

$\sigma(\mathbf{R})$ is a dimensionless quantity which is reported in parts per million (ppm). It is a rank-2 tensor defined for each atomic site and specified by 9 independent Cartesian components. Note that it is not a symmetric tensor but can be written as the sum of symmetric and antisymmetric tensors.

```
units ms ppm
ms <atom type> <number in atom type> 11 12 13 21 22 23 31 32 33
```

Where the `XY` indices label the components of the tensor like

$$\begin{pmatrix} 11 & 12 & 13 \\ 21 & 22 & 23 \\ 31 & 32 & 33 \end{pmatrix} \tag{A.2}$$

`efg` - Electric field gradient

The Electric Field Gradient (EFG) is a rank-2, symmetric, traceless tensor $V(\mathbf{R})$ given by

$$V(\mathbf{R}) = \frac{\partial \mathbf{E}_\alpha(\mathbf{R})}{\partial r_\beta} - \frac{1}{3}\delta_{\alpha\beta}\sum_\gamma \frac{\partial \mathbf{E}_\gamma(\mathbf{R})}{\partial r_\gamma}, \tag{A.3}$$

where α, β, γ index the Cartesian coordinates x,y,z and $\mathbf{E}(\mathbf{R})$ is the local electric field at the position $\mathbf{R}$. The EFG is recorded in atomic units. Note that 1 a.u. of EFG is approximately $9.717 \times 10^{21}\,\mathrm{V\,m^{-2}}$.

```
units efg au
efg <atom type> <number in atom type> 11 12 13 21 22 23 31 32 33
```

A code might provide the EFG decomposed into theory-dependent contributions with additional tags, e.g. `efg_ions` for just the contribution from the atomic nuclei and cores.

`isc` - Indirect spin-spin coupling (J-coupling)

The indirect spin-spin coupling tensor is obtained from the magnetic field induced at nucleus A due to the perturbative effect of the magnetic moment, $\boldsymbol{\mu}_B$, of nucleus

B,

$$\mathbf{B}_{\mathrm{in}}(\mathbf{R}_{\mathrm{A}}) = K_{\mathrm{A,B}} \cdot \boldsymbol{\mu}_{\mathrm{B}} \tag{A.4}$$

$K_{\mathrm{A,B}}$ is known as the reduced spin coupling tensor. It is a rank-2 tensor, and is given in units of $10^{19}\,\mathrm{T}^2\,\mathrm{J}^{-1}$. The J-coupling tensor is obtained from this using $J_{\mathrm{A,B}} = 2\pi\hbar\gamma_{\mathrm{A}}\gamma_{\mathrm{B}}K_{\mathrm{A,B}}$ where γ_{A} is the gyromagnetic ratio of the nucleus A. Note that K (and hence J) is not symmetric but can be written as the sum of symmetric and antisymmetric tensors. The tensors $K_{\mathrm{A,B}}$ and $K_{\mathrm{B,A}}$ are different. The symmetric part is unchanged on exchanging sites A and B, but the antisymmetric part will change sign.

```
units isc 10^19.T^2.J^-1
isc <atom type A> <number in atom type A> <atom type B> \
  <number in atom type B> 11 12 13 21 22 23 31 32 33
```

A code might provide the K-tensor decomposed into theory-dependent contributions with additional tags.

`sus` - Macroscopic magnetic susceptibility

The Macroscopic Magnetic Susceptibility of the sample. This is a single rank-2 tensor reported in units of $10^{-6}\,\mathrm{cm}^3\,\mathrm{mol}^{-1}$

```
units sus 10^-6.cm^3.mol^-1
sus 11 12 13 21 22 23 31 32 33
```

A.2.8 `calculation` block

The exact content of this section is not precisely defined as applications are not clearly defined, however we suggest it contain sufficient information for a user to reproduce the calculation. For a calculation using a plane-wave pseudopotential code this might include: the date the calculation was performed; the version of computational code used; pseudopotential descriptions; plane wave cut-off energy; k-point sampling.

An example from a recent calculation is given in Section A.2.9. Other possible calculation data to include, for example, would be a list of hashes of the input files for cross referencing in a database.

A.2.9 Example

Below is an example output file from a J-coupling calculation in an ethanol molecule using the `Castep` code, with the C2 atom acting as the perturbation. It has been marginally edited down in order to fit the width of the page better, and so the numbers given do not necessarily reflect the true level of numerical precision. Line continuations are indicated by a backslash.

```
#$magres-abinitio-v1.0
[calculation]
calc_code CASTEP
calc_code_version 8.0
calc_code_hgversion 0b4b78c37491+  \
   Sun, 17 Aug 2014 15:49:55 +0100
calc_code_platform linux_x86_64_gfortran4.8-XT
calc_name ethanol
```

```
calc_comment
calc_xcfunctional PBE
calc_cutoffenergy    680.28462750 eV
calc_pspot H 1|0.8|3.675|7.35|11.025|10UU(qc=6.4,schro)[]
calc_pspot C 2|1.4|9.187|11.025|12.862|20UU:21UU(qc=6,schro)[]
calc_pspot O 2|1.3|16.537|18.375|20.212|20UU:21UU(qc=7.5,schro)[]
calc_kpoint_mp_grid 111
calc_kpoint_mp_offset       0.25000000      0.25000000      0.25000000
[/calculation]
[atoms]
units lattice Angstrom
lattice 6.0 0.0 0.0 0.0 6.0 0.0 0.0 0.0 6.0
units atom Angstrom
symmetry x,y,z
atom H H 1 -8.693E-01 -1.752E-01 -6.490E-01
atom H H 2  1.834E-01 -9.232E-01  5.606E-01
atom H H 3  8.691E-01  1.986E-01 -6.287E-01
atom H H 4 -1.129E+00  9.758E-01  1.565E+00
atom H H 5 -4.377E-01  2.079E+00  3.728E-01
atom H H 6  1.061E+00  6.786E-01  2.298E+00
atom C C 1 -3.000E-03 -3.000E-03 -3.000E-03
atom C C 2 -2.469E-01  1.165E+00  9.383E-01
atom O O 1  8.963E-01  1.459E+00  1.742E+00
[/atoms]
[magres]
units isc 10^19.T^2.J^-1
isc C 2 H 1  2.123E+00 -6.564E-01  2.023E-02 -6.660E-01  1.048E+00 \
```

```
      -3.659E-01  1.885E-02 -3.753E-01  6.520E-01
isc C 2 H 2 -5.540E-01  8.128E-02  1.531E-01  1.697E-01 -9.451E-01 \
      -4.143E-01  4.472E-02 -2.987E-01  3.256E-01
isc C 2 H 3 -3.514E-01  7.002E-01  9.687E-02  5.359E-01 -3.193E-01 \
      -2.326E-01  1.153E-01 -3.419E-01 -9.360E-01
isc C 2 H 4  3.387E+01 -1.290E+00  4.652E+00 -1.302E+00  4.162E+01 \
      6.054E-01  4.812E+00  6.434E-01  3.992E+01
isc C 2 H 5  4.211E+01  2.464E+00 -1.270E+00  2.601E+00  3.545E+01 \
      4.693E+00 -1.341E+00  4.617E+00  3.962E+01
isc C 2 H 6 -3.351E-01  5.655E-01 -5.736E-01  1.023E+00  1.515E+00 \
      -3.789E-02 -8.078E-01 -3.321E-01 -5.116E-01
isc C 2 C 1  2.527E+01 -6.379E+00 -3.906E+00 -6.408E+00  4.555E+01 \
      1.812E+01 -4.008E+00  1.809E+01  3.659E+01
isc C 2 C 2 -3.794E+03  7.100E-01  1.827E+00  7.218E-01 -3.803E+03 \
      6.914E-01  1.851E+00  6.897E-01 -3.802E+03
isc C 2 O 1 -3.094E+01  9.328E+00  2.348E+01  7.332E+00 -6.114E+01 \
      5.442E+00  2.466E+01  6.824E+00 -4.928E+01
[/magres]
```

Appendix B

Magres processing library

B.1 Introduction

This appendix describes a library[245] written, and used, in the Python programming language for the processing of the output of magnetic resonance calculations. It was developed during the course of this thesis' work and was used in numerous places to automate the creation of results from the raw data.

The output of an ab-initio magnetic resonance simulation is relatively modest in terms of pure quantities of data, but can be overwhelming for processing by hand, giving a 3×3 tensor for each of N atoms from a magnetic shielding calculation, the same again for an EFG calculation and $N - 1$ tensors for every J-coupling perturbation site. The recent development of the ab-initio magnetic resonance file format (Appendix A) makes it easy for someone familiar with a programming language to parse the file and load the data into some sort of datastructure for further processing. However, given that there are many common operations then performed, such as measuring bond angles, selecting subsets of atoms, or calculating eigen-

values, it seems sensible to provide an optional support library that supplies this functionality.

The library will be outlined below, along with some practical examples used in the course of this thesis.

B.2 Outline

The Python language allows program code to be grouped together into 'modules', which are isolated namespaces that can be loaded into other Python programs. The modules and their contents are:

`magres.format`

Class, `MagresFile`, and associated helper functions for parsing the ab-initio magnetic resonance file format. For example, reading a file in:

```
f = MagresFile(open("test.magres"))
```

`magres.atoms`

Classes, `MagresAtoms` and `MagresAtomsView`, that hold collections of atoms, with an optional crystal lattice, and with operations such as selecting atoms of different species or within a certain distance of a point. For example, loading a magres file in and building the datastructure:

```
atoms = MagresAtoms.load_magres("test.magres")
```

Selecting the Al15 atom by species and index using the property shortcut:

```
atom = atoms.Al15
```

or selecting all Si atoms present within 3.5Å of the Al15 atom, demonstrating selector chaining:

```
Si_atoms = atoms.species("Si").within(atoms.Al15, 3.5)
```

magres.atom

Class, `MagresAtom`, that describes an atom, including data such as position and species, and acts as a container for other property objects.

```
atom = atoms.Ag1
print atom
print "position =", atom.position
print "isotope =", atom.isotope
print "gamma109 =", atom.gamma
atom.isotope = 107
print "gamma107 =", atom.gamma
```

with the output

```
109Ag1
position = [ 4.06019627  3.70282597  3.64849111]
isotope = 109
gamma109 = -12518634.0
gamma107 = -10889181.0
```

As can be seen, there is support for easily modifying the isotopes of nuclei, which then has knock-on effects in the calculation of nuclear constants such as the gyromagnetic ratio, γ.

magres.ms

Class, `MagresAtomMs`, that holds the magnetic shielding tensor and allows easy computation of derived information, such as eigenvalues, the isotropic shift and the chemical shift anisotropy. For example, the following code prints the isotropic magnetic shielding and anisotropy for every proton in the system:

```
for atom in atoms.species("H"):
  print atom.ms.iso, atom.ms.aniso
```

magres.isc

Class, `MagresAtomIsc`, that holds the reduced J-coupling tensors between two atoms and allows easy computation of derived quantities such as the full J-coupling tensor and the isotropic coupling. The following code prints out the isotropic part of the J tensor between two atoms:

```
print atoms.C2.isc[atoms.O1].J_iso
```

magres.efg

Class, `MagresAtomEfg`, that holds the electric field gradient tensor and allows easy computation of derived information, such as eigenvalues, the quadrupole coupling frequency and the asymmetry. The following code, for example, produces a list of the C_Q of every Al atom in the system:

```
atoms.species("Al").efg.Cq
```

This could then be fed into a plotting system or statistics function.

`magres.constants`

A collection of magnetic resonance data, such as nuclear gyromagnetic ratios and quadrupole moments, and useful functions for operations such as converting a K tensor to a J tensor. For example, the gyromagnetic ratio of ^{35}Cl is obtained by:

```
print magres.constants.gamma["Cl", 35]
```

giving the value of 26241980.0.

`magres.utils`

A collection of utility functions useful in the course of writing scripts using the library, such as a function to find all magnetic resonance output files below a point in a directory hierarchy.

B.3 Examples

B.3.1 Electric field gradients in disordered system

The analysis on gehlenite in Chapter 6 involved ab-initio calculations of electric field gradients in 25 structures per set, followed by extraction of the tensors and structural statistics from every aluminium site present in the material. It's clearly desirable to automate this. Code to perform this will be described below, broken up with explanatory text.

First, the relevant pieces of modules are loaded.

```
from magres.utils import load_all_magres
from matplotlib.pyplot import hist
```

Then, the `.magres` output files are loaded in from the filesystem as a list of `MagresAtoms` objects using the `load_all_magres` utility function.

```
orig_structures = load_all_magres('files/orig')
```

We can do a simple plot of the C_Q data on all the Al sites present, using the `hist` function from the `matplotlib` module.

```
all_Cqs = []

for atoms in orig_structures:
  all_Cqs += atoms.species('Al').efg.Cq

hist(all_Cqs, bins=20)
```

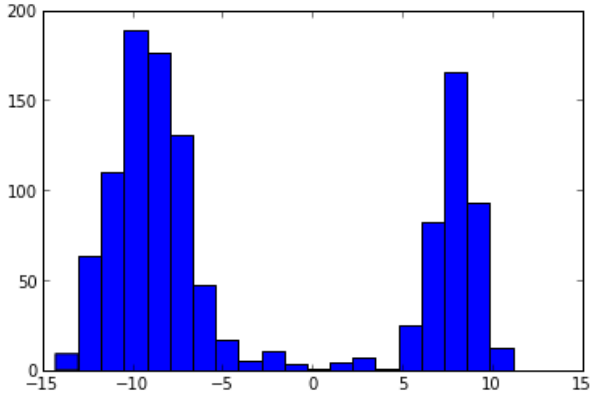

Next, we write a function to bin the C_Q of each aluminium atom by the type of site, T1 or T2, and how many neighbouring silicon atoms there are within 3.5Å.

```
def bin_sites(structures, bins):
  for i, atoms in enumerate(structures):
    for Al_atom in atoms.species('Al'):
      neighbours = atoms.species(['Al', 'Si']).within(Al_atom, 3.5)
      if len(neighbours) == 5:
        site = 'T1'
      else:
```

```
        site = 'T2'
      num_Si = len(neighbours.species('Si'))
      bins[site][num_Si].append(abs(Al_atom.efg.Cq))

Al_Cqs1 = {'T1': {0: [], 1: [], 2: [], 3: [], 4: []},
           'T2': {0: [], 1: []},}
bin_sites(orig_structures, Al_Cqs1)
```

Finally, we can print out a list of statistics about the Al C_Q, broken down by site and n_{Si}.

```
for site in bins:
  for num_si in bins[site]:
    print "Al\%s, n_si=\%d, Cq=\%.2f +- \%.2f" \% (site, num_si, mean(
    bins[site][num_si]), std(bins[site][num_si]))
```

giving the statistics in Table 6.1.

B.3.2 MD sampling of J-coupling

In Chapter 8 a molecular dynamics simulation of Pb_2ZnF_6 is performed, and sample structures are taken. Ab-initio J-coupling calculations are then run on the samples. The following code will extract the J-coupling from every relevant pair of F−Pb, output the J_{iso} as a function of time and calculate the statistics for each Pb site and in total.

As before, we first import the things we need from the modules.

```
import sys
from magres.atoms import MagresAtoms
from magres.utils import find_all
from numpy import mean, std, sqrt
```

Next, we find all the `.magres` output files from the J-coupling calculations and sort them by the sample time.

```
files = find_all(".", ".magres")
def get_time(path):
 return int(path[len("./Pb2ZnF6-MD-"):-7])
files = sorted(files, key=get_time)
f_atom = 81
saught_atoms = [17, 19, 27, 30]
```

Then we iterate over every sample in sequence and extract J_{iso} for each of the couplings we want by indexing into the `.isc` property on each atom and appending the `.J_iso` property into a per-site list.

```
isos = {idx: [] for idx in saught_atoms}
isos['all'] = []

for file in files:
  time = get_time(file)
  if time > 11000:
    break
  atoms = MagresAtoms.load_magres(file)
  atom1 = atoms.get('F', f_atom)
  new_isos = []
  for idx in saught_atoms:
    atom2 = atoms.get('Pb', idx)
    isos[idx].append(atom1.isc[atom2].J_iso)
    isos['all'].append(atom1.isc[atom2].J_iso)
    new_isos.append(atom1.isc[atom2].J_iso)
  print time, idx, " ".join(map(str, new_isos))
```

Finally, statistics are printed out for every site, along with the totals.

```
for idx, isos_ in isos.items():
  if idx != 'all':
```

```
    print >>sys.stderr, "Site =", idx
    print >>sys.stderr, mean(isos_), "+-", std(isos_), "Hz"
    print >>sys.stderr, "Error in mean =", std(isos_) / sqrt(len(isos_
    ))
    print >>sys.stderr

print >>sys.stderr, "Total"
print >>sys.stderr, mean(isos['all']), "+-", std(isos['all']), "Hz"
print >>sys.stderr, "Error in mean =", std(isos['all']) / sqrt(len(
    isos['all']))
```

Giving the data seen in Table 8.5.

Bibliography

[1] Lesage, A. (2009) *Physical Chemistry Chemical Physics*, **11**, 6876.

[2] Ashbrook, S. E. (2009) *Physical Chemistry Chemical Physics*, **11**, 6892.

[3] Florian, P. and Massiot, D. (2013) *CrystEngComm*, **15**, 8623.

[4] Helgaker, T., Coriani, S., Jrgensen, P., Kristensen, K., Olsen, J., and Ruud, K. (2012) *Chemical Reviews*, **112**, 543–631.

[5] Pickard, C. J. and Mauri, F. (2001) *Physical Review B*, **63**, 245101.

[6] Bonhomme, C., et al. (2012) *Chemical Reviews*, **112**, 5733–5779.

[7] Charpentier, T. (2011) *Solid State Nuclear Magnetic Resonance*, **40**, 1–20.

[8] Eichele, K. and Wasylishen, R. E. (1992) *Solid State Nuclear Magnetic Resonance*, **1**, 159–163.

[9] Wu, G. and Wasylishen, R. E. (1993) *The Journal of Chemical Physics*, **98**, 6138–6149.

[10] Vaara, J., Jokisaari, J., Wasylishen, R. E., and Bryce, D. L. (2002) *Progress in Nuclear Magnetic Resonance Spectroscopy*, **41**, 233–304.

[11] Massiot, D., Fayon, F., Deschamps, M., Cadars, S., Florian, P., Montouillout, V., Pellerin, N., Hiet, J., Rakhmatullin, A., and Bessada, C. (2010) *Comptes Rendus Chimie*, **13**, 117–129.

[12] Joyce, S. A. (2004) *First Principles Prediction of Nuclaer Magnetic Resonance J-coupling*. Ph.D. thesis, University of Cambridge.

[13] Joyce, S. A., Yates, J. R., Pickard, C. J., and Mauri, F. (2007) *The Journal of Chemical Physics*, **127**, 204107.

[14] Joyce, S. A., Yates, J. R., Pickard, C. J., and Brown, S. P. (2008) *Journal of the American Chemical Society*, **130**, 12663–12670.

[15] Griffin, J. M., Yates, J. R., Berry, A. J., Wimperis, S., and Ashbrook, S. E. (2010) *Journal of the American Chemical Society*, **132**, 15651–15660.

[16] Bonhomme, C., et al. (2010) *Magnetic Resonance in Chemistry*, **48**, S86–S102.

[17] Hung, I., et al. (2011) *J. Am. Chem. Soc.*, **131**, 1820–1834.

[18] Florian, P., Veron, E., Green, T. F. G., Yates, J. R., and Massiot, D. (2012) *Chemistry of Materials*, **24**, 4068–4079.

[19] Vanderbilt, D. (1990) *Physical Review B*, **41**, 7892.

[20] Pyykkö, P. (1988) *Chemical Reviews*, **88**, 563–594.

[21] Enevoldsen, T., Visscher, L., Saue, T., Jensen, H. J. A., and Oddershede, J. (2000) *The Journal of Chemical Physics*, **112**, 3493–3498.

[22] Autschbach, J. and Ziegler, T. (2000) *The Journal of Chemical Physics*, **113**, 936.

[23] Autschbach, J. and Ziegler, T. (2000) *The Journal of Chemical Physics*, **113**, 9410–9418.

[24] Yates, J. R., Pickard, C. J., Payne, M. C., and Mauri, F. (2003) *The Journal of Chemical Physics*, **118**, 5746.

[25] Purcell, E. M., Torrey, H. C., and Pound, R. V. (1946) *Physical Review*, **69**, 37.

[26] Bloch, F., Hansen, W. W., and Packard, M. (1946) *Physical Review*, **69**, 127.

[27] Proctor, W. G. and Yu, F. C. (1950) *Physical Review*, **77**, 717.

[28] Thomas, H. A. (1950) *Physical Review*, **80**, 901.

[29] Arnold, J. T., Dharmatti, S. S., and Packard, M. E. (1951) *The Journal of Chemical Physics*, **19**, 507.

[30] 1300HSP-01-876, S. N. `http://sdbs.db.aist.go.jp/`.

[31] Hahn, E. L. and Maxwell, D. E. (1951) *Physical Review*, **84**, 1246.

[32] Ramsey, N. F. and Purcell, E. M. (1952) *Physical Review*, **85**, 143.

[33] Ramsey, N. F. (1953) *Phys. Rev.*, **91**, 303.

[34] Andrew, E. R., Bradbury, A., and Eades, R. G. (1958) *Nature*, **182**, 1659.

[35] Antonijevic, S. and Bodenhausen, G. (2005) *Angewandte Chemie International Edition*, **44**, 2935–2938.

[36] Florian, P., Fayon, F., and Massiot, D. (2009) *The Journal of Physical Chemistry C*, **113**, 2562–2572.

[37] Hardy, E. H., Verel, R., and Meier, B. H. (2001) *Journal of Magnetic Resonance*, **148**, 459–464.

[38] Brown, S. P. and Emsley, L. (2004) *Journal of Magnetic Resonance*, **171**, 43–47.

[39] Lai, W. C., et al. (2011) *J. Am. Chem. Soc.*, **128**, 3878–3879.

[40] Brunklaus, G., Chan, J. C. C., Eckert, H., Reiser, S., Nilges, T., and Pfitzner, A. (2003) *Physical Chemistry Chemical Physics*, **5**, 3768.

[41] Scheer, M., Gregoriades, L., Bai, J., Sierka, M., Brunklaus, G., and Eckert, H. (2005) *Chemistry - A European Journal*, **11**, 2163–2169.

[42] Kubo, A. and McDowell, C. A. (1990) *The Journal of Chemical Physics*, **92**, 7156.

[43] Dusold, S., Klaus, E., Sebald, A., Bak, M., and Nielsen, N. C. (2011) *J. Am. Chem. Soc.*, **119**, 7121–7129.

[44] Dusold, S., Milius, W., and Sebald, A. (1998) *Journal of Magnetic Resonance*, **135**, 500–513.

[45] Helluy, X., Marichal, C., and Sebald, A. (2011) *J. Phys. Chem. B*, **104**, 2836–2845.

[46] Fayon, F., King, I. J., Harris, R. K., Evans, J. S., and Massiot, D. (2003) *Comptes Rendus Chimie*, **7**, 351–361.

[47] Fayon, F., King, I. J., Harris, R. K., Gover, R. K. B., Evans, J. S. O., and Massiot, D. (2011) *Chem. Mater.*, **15**, 2234–2239.

[48] Fayon, F., Le Saout, G., Emsley, L., and Massiot, D. (2002) *Chemical Communications*, pp. 1702–1703.

[49] Fayon, F., Massiot, D., Levitt, M. H., Titman, J. J., Gregory, D. H., Duma, L., Emsley, L., and Brown, S. P. (2005) *The Journal of Chemical Physics*, **122**, 194313.

[50] Cadars, S., Lesage, A., Trierweiler, M., Heux, L., and Emsley, L. (2007) *Physical Chemistry Chemical Physics*, **9**, 92.

[51] Fyfe, C. A., Grondey, H., Feng, Y., and Kokotailo, G. T. (2011) *J. Am. Chem. Soc.*, **112**, 8812–8820.

[52] Cadars, S., Brouwer, D. H., and Chmelka, B. F. (2009) *Physical Chemistry Chemical Physics*, **11**, 1825.

[53] Martineau, C., Fayon, F., Legein, C., Buzar?, J., Silly, G., and Massiot, D. (2007) *Chemical Communications*, p. 2720.

[54] Franke, D., Hudalla, C., and Eckert, H. (1992) *Solid State Nuclear Magnetic Resonance*, **1**, 33–40.

[55] Franke, D., Banks, K., and Eckert, H. (2011) *J. Phys. Chem.*, **96**, 11048–11054.

[56] Coelho, C., Azas, T., Bonhomme-Coury, L., Laurent, G., and Bonhomme, C. (2011) *Inorg. Chem.*, **46**, 1379–1387.

[57] Coelho, C., Azais, T., Bonhomme, C., Bonhomme-Coury, L., Boissire, C., Laurent, G., and Massiot, D. (2007) *Comptes Rendus Chimie*, **11**, 387–397.

[58] Eichele, K., Wasylishen, R. E., Grossert, J. S., and Olivieri, A. C. (2011) *J. Phys. Chem.*, **99**, 10110–10113.

[59] Menger, E. and Veeman, W. (1982) *Journal of Magnetic Resonance (1969)*, **46**, 257–268.

[60] Sokolov, F. D., Babashkina, M. G., Safin, D. A., Rakhmatullin, A. I., Fayon, F., Zabirov, N. G., Bolte, M., Brusko, V. V., Galezowska, J., and Kozlowski, H. (2007) *Dalton Transactions*, p. 4693.

[61] Sokolov, F. D., Babashkina, M. G., Fayon, F., Rakhmatullin, A. I., Safin, D. A., Pape, T., and Ekkehardt Hahn, F. (2009) *Journal of Organometallic Chemistry*, **694**, 167–172.

[62] Massiot, D., Messinger, R. J., Cadars, S., Deschamps, M., Montouillout, V., Pellerin, N., Veron, E., Allix, M., Florian, P., and Fayon, F. (2013) *Accounts of Chemical Research*, **46**, 1975–1984.

[63] Ferrara, C., Tealdi, C., Pedone, A., Menziani, M. C., Rossini, A. J., Pintacuda, G., and Mustarelli, P. (2013) *The Journal of Physical Chemistry C*, **117**, 23451–23458.

[64] Charpentier, T., Menziani, M. C., and Pedone, A. (2013) *RSC Advances*, **3**, 10550–10578.

[65] Guerry, P., Smith, M. E., and Brown, S. P. (2011) *J. Am. Chem. Soc.*, **131**, 11861–11874.

[66] Kohn, W. (2003) *Nobel prize lectures*, chap. Electronic Structure of Matter Wave Functions and Density Functionals. World Scientific Publishing Co.

[67] Martin, R. M. (2004) *Electronic Structure: Basic Theory and Practical Methods*, p. 62. Cambridge University Press.

[68] Čížek, J. (1966) *The Journal of Chemical Physics*, **45**, 4256.

[69] Purvis, G. D. (1982) *The Journal of Chemical Physics*, **76**, 1910.

[70] Martin, R. M. (2004) *Electronic Structure: Basic Theory and Practical Methods*, p. 67. Cambridge University Press.

[71] Møller, C. and Plesset, M. S. (1934) *Physical Review*, **46**, 618–622.

[72] Hohenberg, P. and Kohn, W. (1964) *Physical Review*, **136**, B864.

[73] Kohn, W. and Sham, L. J. (1965) *Physical Review*, **140**, A1133.

[74] Sham, L. J. and Kohn, W. (1966) *Physical Review*, **145**, 561.

[75] Ceperley, D. M. and Alder, B. J. (1980) *Physical Review Letters*, **45**, 566.

[76] Perdew, J. P. and Zunger, A. (1981) *Physical Review B*, **23**, 5048.

[77] Perdew, J. P. and Wang, Y. (1992) *Physical Review B*, **45**, 13244.

[78] Perdew, J. P., Burke, K., and Ernzerhof, M. (1996) *Physical Review Letters*, **77**, 3865.

[79] Perdew, J. P. (1991) *Electronic Structure of Solids*, p. 11. Akademie Verlag, Berlin.

[80] Perdew, J. P., Parr, R. G., Levy, M., and Balduz, J. L. (1982) *Physical Review Letters*, **49**, 1691–1694.

[81] Becke, A. D. (1993) *The Journal of Chemical Physics*, **98**, 5648.

[82] Becke, A. D. (1988) *Physical Review A*, **38**, 3098.

[83] Heyd, J., Scuseria, G. E., and Ernzerhof, M. (2003) *The Journal of Chemical Physics*, **118**, 8207–8215.

[84] Anisimov, V. I., Aryasetiawan, F., and Lichtenstein, A. I. (1997) *Journal of Physics: Condensed Matter*, **9**, 767.

[85] Hedin, L. (1965) *Physical Review*, **139**, A796–A823.

[86] Aryasetiawan, F. and Gunnarsson, O. (1998) *Reports on Progress in Physics*, **61**, 237.

[87] Lundqvist, B. I., Andersson, Y., Shao, H., Chan, S., and Langreth, D. C. (1995) *International Journal of Quantum Chemistry*, **56**, 247–255.

[88] Martin, R. M. (2004) *Electronic Structure: Basic Theory and Practical Methods*. Cambridge University Press.

[89] Payne, M. C., Teter, M. P., Allan, D. C., Arias, T. A., and Joannopoulos, J. D. (1992) *Reviews of Modern Physics*, **64**, 1045.

[90] Car, R. and Parrinello, M. (1985) *Physical Review Letters*, **55**, 2471.

[91] Tangney, P. (2006) *The Journal of Chemical Physics*, **124**, 044111.

[92] Gill, P. E., Murray, W., and Wright, M. H. (1981) *Practical optimization*, p. 144. Academic Press London.

[93] Teter, M. P., Payne, M. C., and Allan, D. C. (1989) *Physical Review B*, **40**, 12255.

[94] von Barth, U. and Gelatt, C. D. (1980) *Physical Review B*, **21**, 2222.

[95] Fermi, E. (1936) *Ricerca Scientifica*, **7**, 13–52.

[96] Troullier, N. and Martins, J. (1990) *Solid State Communications*, **74**, 613–616.

[97] Hamann, D. R., Schlter, M., and Chiang, C. (1979) *Physical Review Letters*, **43**, 1494.

[98] Vanderbilt, D. (1985) *Physical Review B*, **32**, 8412.

[99] Laasonen, K., Pasquarello, A., Car, R., Lee, C., and Vanderbilt, D. (1993) *Physical Review B*, **47**, 10142.

[100] Van de Walle, C. G. and Blöchl, P. E. (1993) *Physical Review B*, **47**, 4244.

[101] Blöchl, P. E. (1994) *Physical Review B*, **50**, 17953.

[102] Gonze, X. (1995) *Physical Review A*, **52**, 1096.

[103] Gonze, X. (1997) *Physical Review B*, **55**, 10337–10354.

[104] Baroni, S., Giannozzi, P., and Testa, A. (1987) *Physical Review Letters*, **58**, 1861.

[105] Baroni, S., de Gironcoli, S., Dal Corso, A., and Giannozzi, P. (2001) *Reviews of Modern Physics*, **73**, 515.

[106] Sternheimer, R. M. (1954) *Physical Review*, **96**, 951.

[107] Mahan, G. D. (1980) *Physical Review A*, **22**, 1780.

[108] Snijders, J. and Pyykkö, P. (1980) *Chemical Physics Letters*, **75**, 5–8.

[109] Ziegler, T., Snijders, J., and Baerends, E. (1980) *Chemical Physics Letters*, **75**, 1–4.

[110] Ziegler, T., Snijders, J. G., and Baerends, E. J. (1981) *The Journal of Chemical Physics*, **74**, 1271–1284.

[111] Pyykkö, P., Pajanne, E., and Inokuti, M. (1973) *International Journal of Quantum Chemistry*, **7**, 785–806.

[112] Aucar, G. A., Saue, T., Visscher, L., and Jensen, H. J. A. (1999) *The Journal of Chemical Physics*, **110**, 6208.

[113] Visscher, L., Enevoldsen, T., Saue, T., Jensen, H. J. A., and Oddershede, J. (1999) *Journal of Computational Chemistry*, **20**, 1262–1273.

[114] Wolff, S. K., Ziegler, T., van Lenthe, E., and Baerends, E. J. (1999) *The Journal of Chemical Physics*, **110**, 7689.

[115] Bryce, D. L., Wasylishen, R. E., Autschbach, J., and Ziegler, T. (2002) *Journal of the American Chemical Society*, **124**, 4894–4900.

[116] Moncho, S. and Autschbach, J. (2010) *Journal of Chemical Theory and Computation*, **6**, 223–234.

[117] Autschbach, J. (2012) *The Journal of Chemical Physics*, **136**, 150902–150902–15.

[118] Dirac, P. A. M. (1928) *Proceedings of the Royal Society of London. Series A*, **117**, 610–624.

[119] Darwin, C. G. (1928) *Proceedings of the Royal Society of London. Series A*, **118**, 654–680.

[120] Lenthe, E. v., Baerends, E. J., and Snijders, J. G. (1993) *The Journal of Chemical Physics*, **99**, 4597.

[121] Van Lenthe, E. (1996) *The ZORA Equation*. Ph.D. thesis, Vrije University, Amsterdam.

[122] Sadlej, A. J., Snijders, J. G., van Lenthe, E., and Baerends, E. J. (1995) *The Journal of Chemical Physics*, **102**, 1758.

[123] Lévy-Leblond, J.-M. (1967) *Communications in Mathematical Physics*, **4**, 157–176.

[124] Helgaker, T., Jaszuski, M., and Ruud, K. (1999) *Chemical Reviews*, **99**, 293–352.

[125] Mauri, F., Pfrommer, B. G., and Louie, S. G. (1996) *Physical Review Letters*, **77**, 5300.

[126] Lee, A. M., Handy, N. C., and Colwell, S. M. (1995) *The Journal of Chemical Physics*, **103**, 10095.

[127] Grant, D. M., Harris, R. K., and Haeberlen, U. (1996) *Encyclopedia of NMR*, vol. 1, p. 368. Wiley, England.

[128] Keith, T. A. and Bader, R. F. W. (1992) *Chemical Physics Letters*, **194**, 1–8.

[129] Profeta, M., Pickard, C., and Mauri, F. (2003) *J. Am. Chem. Soc.*, **125**, 2541–548.

[130] Yates, J. R. (2010) *Magnetic Resonance in Chemistry*, **48**, S23–S31.

[131] Wodyski, A., Repisk, M., and Pecul, M. (2012) *The Journal of Chemical Physics*, **137**, 014311.

[132] Ashbrook, S. E., Berry, A. J., Frost, D. J., Gregorovic, A., Pickard, C. J., Readman, J. E., and Wimperis, S. (2011) *J. Am. Chem. Soc.*, **129**, 13213–13224.

[133] Ashbrook, S. E., Le Poll?s, L., Gautier, R., Pickard, C. J., and Walton, R. I. (2006) *Physical Chemistry Chemical Physics*, **8**, 3423.

[134] Cadars, S., Lesage, A., Pickard, C. J., Sautet, P., and Emsley, L. (2011) *J. Phys. Chem. A*, **113**, 902–911.

[135] Gervais, C., et al. (2007) *Journal of Magnetic Resonance*, **187**, 131–140.

[136] Hoffmann, A., Sebastiani, D., Sugiono, E., Yun, S., Kim, K. S., Spiess, H. W., and Schnell, I. (2004) *Chemical Physics Letters*, **388**, 164–169.

[137] Pourpoint, F., Gervais, C., Bonhomme-Coury, L., Azas, T., Coelho, C., Mauri, F., Alonso, B., Babonneau, F., and Bonhomme, C. (2007) *Applied Magnetic Resonance*, **32**, 435–457.

[138] Salager, E., Day, G. M., Stein, R. S., Pickard, C. J., Elena, B., and Emsley, L. (2011) *J. Am. Chem. Soc.*, **132**, 2564–2566.

[139] Uldry, A., et al. (2011) *J. Am. Chem. Soc.*, **130**, 945–954.

[140] Yates, J. R., Dobbins, S. E., Pickard, C. J., Mauri, F., Ghi, P. Y., and Harris, R. K. (2005) *Physical Chemistry Chemical Physics*, **7**, 1402.

[141] Dumez, J.-N. and Pickard, C. J. (2009) *The Journal of Chemical Physics*, **130**, 104701–104701–8.

[142] Yates, J. R., Pickard, C. J., Payne, M. C., Dupree, R., Profeta, M., and Mauri, F. (2011) *J. Phys. Chem. A*, **108**, 6032–6037.

[143] Yates, J. R., Pham, T. N., Pickard, C. J., Mauri, F., Amado, A. M., Gil, A. M., and Brown, S. P. (2011) *J. Am. Chem. Soc.*, **127**, 10216–10220.

[144] Alkorta, I., Elguero, J., Mó, O., Yáñez, M., and Del Bene, J. E. (2005) *Chemical Physics Letters*, **411**, 411–415.

[145] Alkorta, I., Elguero, J., Mó, O., Yáñez, M., and Del Bene, J. E. (2004) *Molecular Physics*, **102**, 2563–2574.

[146] Clark, S. J., Segall, M. D., Pickard, C. J., Hasnip, P. J., Probert, M. J., Refson, K., and Payne, M. (2005) *Z. Kristall.*, **220**, 567–570.

[147] Sahakyan, A. B., Shahkhatuni, A. A., Shahkhatuni, A. G., and Panosyan, H. A. (2008) *Magnetic Resonance in Chemistry*, **46**, 63–68.

[148] Del Bene, J. E. and Elguero, J. (2007) *Magnetic Resonance in Chemistry*, **45**, 484–487.

[149] Yates, J. R., Pickard, C. J., and Mauri, F. (2007) *Physical Review B*, **76**, 024401.

[150] Dal Corso, A. (2001) *Physical Review B*, **64**, 235118.

[151] Sychrovsk, V., Grfenstein, J., and Cremer, D. (2000) *The Journal of Chemical Physics*, **113**, 3530–3547.

[152] Lantto, P., Vaara, J., and Helgaker, T. (2002) *The Journal of Chemical Physics*, **117**, 5998.

[153] Sadoc, A., Body, M., Legein, C., Biswal, M., Fayon, F., Rocquefelte, X., and Boucher, F. (2011) *Phys. Chem. Chem. Phys.*, **13**, 18539–18550.

[154] Helgaker, T., Jaszuski, M., Ruud, K., and Grska, A. (1998) *Theoretical Chemistry Accounts*, **99**, 175–182.

[155] Bryce, D. L. and Wasylishen, R. E. (2000) *Journal of the American Chemical Society*, **122**, 3197–3205.

[156] Bryce, D. L. and Wasylishen, R. E. (2000) *Journal of the American Chemical Society*, **122**, 11236–11237.

[157] Lantto, P. and Vaara, J. (2001) *The Journal of Chemical Physics*, **114**, 5482–5490.

[158] Vaara, J., Kaski, J., and Jokisaari, J. (1999) *The Journal of Physical Chemistry A*, **103**, 5675–5684.

[159] Lantto, P., Kaski, J., Vaara, J., and Jokisaari, J. (2000) *Chemistry A European Journal*, **6**, 1395–1406.

[160] Shenderovich, I. G., Smirnov, S. N., Denisov, G. S., Gindin, V. A., Golubev, N. S., Dunger, A., Reibke, R., Kirpekar, S., Malkina, O. L., and Limbach, H.-H. (1998) *Berichte der Bunsengesellschaft fr physikalische Chemie*, **102**, 422–428.

[161] Barszczewicz, A., Helgaker, T., Jaszunski, M., Jorgensen, P., and Ruud, K. (1995) *Journal of Magnetic Resonance, Series A*, **114**, 212–218.

[162] Vaara, J., Kaski, J., Jokisaari, J., and Diehl, P. (1997) *The Journal of Physical Chemistry A*, **101**, 5069–5081.

[163] Vaara, J., Kaski, J., Jokisaari, J., and Diehl, P. (1997) *The Journal of Physical Chemistry A*, **101**, 9185–9185.

[164] Kaski, J., Lantto, P., Rantala, T. T., Schroderus, J., Vaara, J., and Jokisaari, J. (1999) *The Journal of Physical Chemistry A*, **103**, 9669–9677.

[165] Kaski, J., Lantto, P., Vaara, J., and Jokisaari, J. (1998) *Journal of the American Chemical Society*, **120**, 3993–4005.

[166] Kaski, J., Vaara, J., and Jokisaari, J. (1996) *Journal of the American Chemical Society*, **118**, 8879–8886.

[167] Pyykkö, P., Pajanne, E., and Inokuti, M. (1973) *International Journal of Quantum Chemistry*, **7**, 785–806.

[168] Khandogin, J. and Ziegler, T. (1999) *Spectrochimica Acta Part A: Molecular and Biomolecular Spectroscopy*, **55**, 607–624.

[169] Pyykkö, P. (1977) *Chem. Phys*, **22**, 289.

[170] Adamo, C. and Barone, V. (1999) *The Journal of Chemical Physics*, **110**, 6158–6170.

[171] Autschbach, J. (2009) *ChemPhysChem*, **10**, 22742283.

[172] Vosko, S. H., Wilk, L., and Nusair, M. (1980) *Canadian Journal of Physics*, **58**, 1200–1211.

[173] Pye, C. C. and Ziegler, T. (1999) *Theoretical Chemistry Accounts*, **101**, 396–408.

[174] Mann, B. E. (1973) *Journal of the Chemical Society, Dalton Transactions*, p. 20122015.

[175] Young, C. G., Kober, E. M., and Enemark, J. H. (1987) *Polyhedron*, **6**, 255–259.

[176] Fischer, E., Knauss, L., Keiter, R., and Verkade, J. (1972) *Journal of Organometallic Chemistry*, **37**, C7–C10.

[177] Caldarelli, S., Catalano, D., Di Bari, L., Pasquali, M., Veracini, C. A., and Leoni, P. (1990) *Gazzetta Chimica Italiana*, pp. 211–213.

[178] Keiter, R. L. and Verkade, J. G. (1969) *Inorganic Chemistry*, **8**, 2115–2120.

[179] Banck, J. and Schwenk, A. (1975) *Zeitschrift fr Physik B Condensed Matter*, **20**, 75–80.

[180] Eujen, R. and Lagow, R. J. (1978) *Journal of the Chemical Society, Dalton Transactions*, p. 541.

[181] Hawk, R. M. and Sharp, R. R. (1974) *The Journal of Chemical Physics*, **60**, 1009–1017.

[182] Schumann, C. and Dreeskamp, H. (1970) *Journal of Magnetic Resonance (1969)*, **3**, 204–217.

[183] Clark, R. J. H., Davies, A. G., Puddephatt, R. J., and McFarlane, W. (1969) *Journal of the American Chemical Society*, **91**, 1334–1339.

[184] McFarlane, W. (1967) *Molecular Physics*, **13**, 587–588.

[185] Brown, A. J., Howarth, O. W., and Moore, P. (1976) *Journal of the Chemical Society, Dalton Transactions*, pp. 1589–1592.

[186] Wu, G., Kroeker, S., and Wasylishen, R. E. (1995) *Inorganic Chemistry*, **34**, 1595–1598.

[187] Sebald, A. and Wrackmeyer, B. (1985) *Journal of Magnetic Resonance (1969)*, **63**, 397–400.

[188] Kretschmer, M., Pregosin, P. S., Favre, P., and Schlaepfer, C. W. (1983) *Journal of Organometallic Chemistry*, **253**, 17–30.

[189] Paonessa, R. S. and Trogler, W. C. (1982) *Journal of the American Chemical Society*, **104**, 1138–1140.

[190] Xu, Q., Heaton, B. T., Jacob, C., Mogi, K., Ichihashi, Y., Souma, Y., Kanamori, K., and Eguchi, T. (2000) *Journal of the American Chemical Society*, **122**, 6862–6870.

[191] Hao, N., McGlinchey, M. J., Sayer, B. G., and Schrobilgen, G. J. (1982) *Journal of Magnetic Resonance (1969)*, **46**, 158–162.

[192] Benn, R., Michael Bch, H., and Reinhardt, R.-D. (1985) *Magnetic Resonance in Chemistry*, **23**, 559–564.

[193] Rochon, F. D. and Buculei, V. (2004) *Inorganica Chimica Acta*, **357**, 2218–2230.

[194] Goggin, P. L., Goodfellow, R. J., Haddock, S. R., Knight, J. R., Reed, F. J. S., and Taylor, B. F. (1974) *Journal of the Chemical Society, Dalton Transactions*, p. 523.

[195] Musco, A., Pontellini, R., Grassi, M., Sironi, A., Meille, S. V., Ruegger, H., Ammann, C., and Pregosin, P. S. (1988) *Organometallics*, **7**, 2130–2137.

[196] Maliarik, M., Glaser, J., and Tth, I. (1998) *Inorganic Chemistry*, **37**, 5452–5459.

[197] Berg, K. E., Blixt, J., and Glaser, J. (1996) *Inorganic Chemistry*, **35**, 7074–7081.

[198] Zechmann, C. A., Boyle, T. J., Pedrotty, D. M., Alam, T. M., Lang, D. P., and Scott, B. L. (2001) *Inorganic Chemistry*, **40**, 2177–2184.

[199] Loewenstein, W. (1954) *American Mineralogist*, **39**, 92.

[200] Kodama, N., Tanii, Y., and Yamaga, M. (2000) *Journal of Luminescence*, **8789**, 1076–1078.

[201] Kodama, N., Takahashi, T., Yamaga, M., Tanii, Y., Qiu, J., and Hirao, K. (1999) *Applied Physics Letters*, **75**, 1715–1717.

[202] Simondi-Teisseire, B., Viana, B., Vivien, D., and Lejus, A. M. (1996) *physica status solidi (a)*, **155**, 249–262.

[203] Simondi-Teisseire, B., Viana, B., Lejus, A.-M., Benitez, J.-M., Vivien, D., Borel, C., Templier, R., and Wyon, C. (1996) *IEEE Journal of Quantum Electronics*, **32**, 2004–2009.

[204] Zhang, Q., Wang, J., Zhang, M., and Su, Q. (2008) *Applied Physics B*, **92**, 195–198.

[205] Lejus, A. M., Pelletier-Allard, N., Pelletier, R., and Vivien, D. (1996) *Optical Materials*, **6**, 129–137.

[206] Navrotsky, A., Peraudeau, G., McMillan, P., and Coutures, J.-P. (1982) *Geochimica et Cosmochimica Acta*, **46**, 2039–2047.

[207] Solvang, M., Yue, Y. Z., Jensen, S. L., and Dingwell, D. B. (2005) *Journal of Non-Crystalline Solids*, **351**, 499–507.

[208] Engelhardt, D., G.; Michel (1987) *High-Resolution Solid-State NMR of Silicates and Zeolites*. John Wiley and Sons: Chichester, U.K.

[209] Putnis, A. and Angel, R. J. (1985) *Physics and Chemistry of Minerals*, **12**, 217–222.

[210] Putnis, A., Fyfe, C. A., and Gobbi, G. C. (1985) *Physics and Chemistry of Minerals*, **12**, 211–216.

[211] Vega, A. J. (1996) *The Journal of Physical Chemistry*, **100**, 833–836.

[212] Dubinsky, E. V. and Stebbins, J. F. (2006) *American Mineralogist*, **91**, 753–761.

[213] Stebbins, J. F., Zhao, P. D., Lee, S. K., and Cheng, X. (1999) *American Mineralogist*, **84**, 1680.

[214] Stebbins, J. F, Lee, S. K., and Oglesby, J. V. (1999) *American Mineralogist*, **84**, 983–986.

[215] Thayaparam, S., Dove, M., and Heine, V. (1994) *Physics and Chemistry of Minerals*, **21**.

[216] Ghose, S. and Tsang, T. (1973) *American Mineralogist*, **58**, 748–55.

[217] Townes, C. H. and Dailey, B. P. (1949) *The Journal of Chemical Physics*, **17**, 782–796.

[218] Liu, C. W., Pan, H., Fackler, J. P., Wu, G., Wasylishen, R. E., and Shang, M. (1995) *Journal of the Chemical Society, Dalton Transactions*, p. 3691.

[219] Subramanian, R. R., Anandan, S. S., Kwek, K. H., Low, K. S., Shanmuga Sundara Raj, S., Fun, H.-K., Razak, I. A., Hanna, J. V., and Ng, S. W. (2000) *Acta Crystallographica Section C Crystal Structure Communications*, **56**, e292–e294.

[220] Belaj, F., Trnoska, A., and Nachbaur, E. (1998) *Acta Crystallographica Section C Crystal Structure Communications*, **54**, 727–728.

[221] Hanna, J. V. and Ng, S. W. (2000) *Acta Crystallographica Section C Crystal Structure Communications*, **56**, 24–25.

[222] Ng, S. W. (1995) *Zeitschrift fr Kristallographie*, **210**, 206–209.

[223] Ng, S. W. (1998) *Acta Crystallographica Section C Crystal Structure Communications*, **54**, 743–744.

[224] Bowmaker, G. A., Effendy, Hanna, J. V., Healy, P. C., King, S. P., Pettinari, C., Skelton, B. W., and White, A. H. (2011) *Dalton Transactions*, **40**, 7210–7218.

[225] Miranday, J.-P., Jacoboni, C., and De Pape, R. (1981) *Journal of Non-Crystalline Solids*, **43**, 393–401.

[226] Martineau, C., Fayon, F., Legein, C., Buzaré, J.-Y., Body, M., Massiot, D., and Goutenoire, F. (2008) *Dalton Transactions*, pp. 6150–6158.

[227] Bureau, B., Silly, G., Buzar, J. Y., Emery, J., Legein, C., and Jacoboni, C. (1997) *Journal of Physics: Condensed Matter*, **9**, 6719.

[228] Bureau, B., Silly, G., and Buzar, J. Y. (1999) *Solid State Nuclear Magnetic Resonance*, **15**, 79–89.

[229] Martineau, C. personal communication.

[230] Nosé, S. (1984) *The Journal of Chemical Physics*, **81**, 511–519.

[231] Hoover, W. G. (1985) *Physical Review A*, **31**, 1695–1697.

[232] M. P. Allen and D. J. Tildesley (1987) *Computer Simulations of Liquids*, p. 192, Oxford University Press.

[233] Wolff, U. (2004) *Computer Physics Communications*, **156**, 143–153.

[234] Lee, R. M., Conduit, G. J., Nemec, N., Lpez Ros, P., and Drummond, N. D. (2011) *Physical Review E*, **83**, 066706.

[235] Spencer, J. (2014), pyblock. `https://github.com/jsspencer/pyblock`.

[236] Pauling, L. (1960) *The Nature of the Chemical Bond*, p. 147, Cornell University Press.

[237] Wang, F. and Grey, C. P. (1995) *Journal of the American Chemical Society*, **117**, 6637–6638.

[238] Sears, R. E. J., Guo, Q. Z., and Mackey, H. J. (1984) *The Journal of Chemical Physics*, **80**, 5448–5452.

[239] Martineau, C. (2009) ^{19}F$-^{207}$Pb J-coupling in $\beta-PbF_2$, unpublished slides.

[240] Hemstreet, L. A., Fong, C. Y., and Nelson, J. S. (1993) *Physical Review B*, **47**, 4238–4243.

[241] Theurich, G. and Hill, N. A. (2001) *Physical Review B*, **64**, 073106.

[242] Theurich, G. and Hill, N. A. (2002) *Physical Review B*, **66**, 115208.

[243] Dal Corso, A. and Conte, A. M. (2005) *Physical Review B*, **71**, 115106.

[244] Dal Corso, A. (2010) *Physical Review B*, **82**, 075116.

[245] Green, T. F. G. (2012–2014), magres-format. `https://github.com/tfgg/magres-format`.